

Coordinated Research Project
“Accelerator Simulation and
Theoretical Modelling of Radiation
Effects” (CRP SMORE)

Institute Reports

CONTENTS

ATOMIC-LEVEL MODELLING AND MODELLING-ORIENTED EXPERIMENTS IN FE-CR ALLOYS

1. Introduction	6
2. Development of an advanced iron chromium potential	6
3. Atomistic study of dislocation/defect interaction.....	8
4. Advanced atomistic kinetic monte carlo simulations in Fe-Cr alloys.....	9
5. Positron annihilation on neutron-irradiated Fe-Cr alloys.....	12
6. Concluding remarks	13

VERY HIGH DOSE IRRADIATION INDUCED RADIATION DAMAGE AND SYNERGISTIC EFFECT ON FORMATION OF VACANCY CLUSTERS IN CLAM

1. Background.....	17
2. Experiment	17
3. Results	21
4. Discussion.....	24
5. Conclusions	25

SYNERGISTIC EFFECTS ON SWELLING IN MODEL FERRITIC STEELS UNDER HIGH-DOSE IRRADIATION

1. Background.....	27
2. Results	27
3. Modelling	33
4. Discussion	34
5. Conclusions	35

MULTISCALE MODELLING OF MECHANICAL BEHAVIOUR OF FE-CR ALLOYS: FROM THE ATOMIC TO THE CONTINUUM LEVEL

1. Introduction	37
2. Atomic simulations.....	37
3. Transition to the continuum level.....	42
4. DD simulations of precipitation strengthening	43
5. Conclusions	45

NUMERICAL MODELLING OF MECHANICAL BEHAVIOUR OF IRRADIATED STRUCTURAL MATERIALS: A MULTI-SCALE APPROACH

1. Introduction	47
2. Atomistic simulations of irradiation hardening.....	47
3. Dislocation dynamics simulation of irradiation hardening	52
4. Micro-mechanical modeling of miniature tests.....	55
5. Conclusions	57

IRRADIATION TOLERANCE AND ION-IRRADIATION EFFECTS ON NANO-OXIDE DISPERSION STRENGTHENED STEELS

1. Background	59
2. Results	59
3. Discussion	66
4. Conclusions	67

SIMULATION OF NEUTRON DAMAGE EFFECTS IN EXPERIMENTS ON STEELS IRRADIATED WITH NEUTRONS OR KRYPTON IONS

1. Experimental results	70
2. EBSD-studies of martensite transformation in 12Cr18Ni10Ti after cold deformation and irradiation with Kr ions (E=1.56 MeV/nucleon).....	77
3. Conclusions	83

COMPUTATIONAL AND EXPERIMENTAL APPROACH TO RADIATION EFFECTS ON FE-CR MODEL ALLOYS

1. Background.....	84
2. Electron irradiation of Fe-Cr model alloys.....	84
3. Ion irradiation of Fe-Cr model alloys.....	87
4. Conclusions	93

NON-DESTRUCTIVE CHARACTERIZATION OF OXIDE DISPERSION STRENGTHENED STEELS

1. Introduction	95
2. Materials	96
3. Experimental techniques	97
4. Results	100
5. Conclusions	107

INFLUENCE OF IRRADIATION EFFECTS ON MECHANICAL PROPERTIES OF AUSTENITIC STAINLESS STEEL

1. Introduction	110
2. Small punch test	110
3. Materials used in the investigation	112
4. Determination of calibration curves	112
5. Results of measurements after irradiation	117
6. Scanning electron microscope observations.....	118
7. Summary	119

IRRADIATION OF STRUCTURAL MATERIALS BY HEAVY IONS AND THEORETICAL MODELLING OF SWELLING AND RADIATION-INDUCED SEGREGATION PHENOMENA

1. Introduction	122
2. Experimental investigations	123
3. Theoretical modelling.....	125
4. Main Conclusions.....	132

INVESTIGATION OF PHYSICAL MECHANISMS OF RADIATION-INDUCED PROCESSES IN STRUCTURAL MATERIALS FOR FISSION AND FUSION REACTORS USING ACCELERATORS OF CHARGED PARTICLES AND THEORETICAL MODELING

1. Introduction	136
2. Experimental results	139
3. Theoretical modelling.....	143
4. Conclusion, Remarks and Summary	148

EXAMINATION OF FE-CR BINARY AND ODS ALLOYS BY POSITRON ANNIHILATION SPECTROSCOPY AND OTHER TECHNIQUES

PAPER 1. DIFFERENT CHROMIUM CONTENT AND THERMAL ANNEALING INFLUENCE ON ION IMPLANTED FE-CR MODEL ALLOYS

1. Introduction	153
2. Materials treatment	153
3. Results	154
4. Conclusions	157

PAPER 2. STUDY OF RESIDUAL STRESS AND VACANCY DEFECTS IN OXIDE DISPERSION STRENGTHENED STEELS

1. Introduction	160
2. Experiment	160
3. Results	162
4. Discussion & Conclusion	164

DEFECT FORMATION AND BINDING ENERGIES IN FE-CR ALLOYS AS A FUNCTION OF CR CONCENTRATION: A SIMULATION STUDY

1. Background.....	167
2. Results	168
3. Discussion	172
4. Conclusions	175

EXPERIMENTAL STUDIES OF FUNDAMENTAL MATERIALS PROPERTIES AND IRRADIATION BEHAVIOR USING SUB-SIZED SAMPLES AND MICRO-TESTING

1. Introduction	178
2. Experimental	179
3. Results	181
4. Conclusions	186

SIMULATION AND STUDIES OF HIGH DOSE RADIATION DAMAGE IN CORE STRUCTURAL MATERIAL WITH THE USE OF CHARGE PARTICLE ACCELERATORS AND HIGH-TECH INSTRUMENTATION

1. Introduction	188
2. Results	188
3. Conclusions	199
4. Recommendations	200

ION BEAM IRRADIATIONS ON STRUCTURAL MATERIALS FOR NUCLEAR APPLICATION

1. General introduction.....	202
2. Ion beam irradiation on a Cu single crystal and post-irradiation indentation in cross section with a detailed analysis of the indents in a TEM.....	203
3. Small scale mechanical testing and local electrode atom probe measurements on novel materials for nuclear application	207
4. Low energy Ion beam irradiation of ODS alloy PM2000 and post-irradiation indentation creep and TEM characterization.....	209
5. Atom Probe Tomography analysis after ion beam irradiation on PM2000.....	210
6. List of direct collaborative efforts developed during the SMoRE CRP.....	211

**DUAL AND TRIPLE ION-BEAM IRRADIATIONS OF FE, FE(CR) AND
FE(CR)-ODS FINAL REPORT: IAEA SMORE CRP#**

1.	Rationale for the project	213
2.	Overview of the initial project plan.....	214
3.	Modification and deviations from initial plan.....	215
4.	Results	216
5.	Conclusions	224
6.	Recommendations	224

ATOMIC-LEVEL MODELLING AND MODELLING-ORIENTED EXPERIMENTS IN FE-CR ALLOYS

L. MALERBA, G. BONNY, N. CASTIN, M. LAMBRECHT, D. TERYTYEV
Structural Materials Modelling and Microstructure,
Institute for Nuclear Materials Science,
Boeretang,
Belgium
Email: lmalerba@sckcen.be (corresponding author)

Abstract

Fe-Cr alloys are model materials suitable for the study of the processes governing radiation effects in high-Cr ferritic/martensitic steels, which are candidate structural materials for several components of future nuclear reactors. This report overviews the work performed at SCK•CEN as contribution to the SMoRE CRP of the IAEA, to develop multiscale models describing nanostructural evolution and radiation-hardening processes in Fe-Cr alloys. The report is divided in four parts: (i) development of an advanced interatomic potential for Fe-Cr alloys suitable for radiation damage studies; (ii) application of the interatomic potential in molecular dynamics simulations of dislocation/defect interactions; (iii) application of the interatomic potential in advanced atomistic kinetic Monte Carlo models for thermal ageing simulations and calculation of diffusion coefficients of radiation defects; (iv) positron annihilation spectroscopy characterization of neutron-irradiated Fe-Cr model alloys, as part of a programme of modelling-oriented experiments.

1. INTRODUCTION

High-chromium ferritic-martensitic steels (~9–12 at. % Cr) are candidate structural materials for advanced nuclear reactors. A first approximation to describe such steels in a modelling framework is the Fe-Cr binary alloy.

The addition of chromium to iron influences significantly the response to irradiation [1]. For example, it has been shown that swelling in Fe-Cr is about one order of magnitude lower than in pure Fe for the same dose [2–6]. Even in the absence of irradiation, the Fe-Cr system exhibits a number of peculiarities. For example, the mixing enthalpy exhibits a change of sign [7–10], being negative below a critical concentration of ~10 at.% Cr and positive above it, indicating large solubility and a tendency to partial ordering for Cr in Fe, even at low temperature.

In a multiscale modelling framework, the first step to study a given model alloy is the development of a suitable interatomic potential. Section 2 highlights how a suitable Fe-Cr potential was developed. This potential can then be used for atomistic studies with molecular dynamics (MD) codes, as well as for the parameterization of atomistic kinetic Monte Carlo (AKMC) models. MD can be used for example to study the interaction between radiation-defects and dislocations, in order to inform dislocation dynamics models that, in turn, can be used to estimate the consequent strengthening at single-crystal level.

In Section 3 the main results of MD studies of this type performed to study the interaction between dislocations and radiation defects are recalled (see also joint EDF R&D / SCK•CEN Report in this volume). AKMC models are especially suited to model microchemical phenomena such as precipitation and segregation. In Section 4, results obtained in Fe-Cr with an AKMC model based on the use of artificial neural networks (ANN) to calculate properly the energy barriers are overviewed. Finally in Section 5 the results of the use of positron annihilation spectroscopy (PAS) on neutron-irradiated Fe-Cr alloys, as part of a wider modelling-oriented experimental effort, are summarised.

2. DEVELOPMENT OF AN ADVANCED IRON CHROMIUM POTENTIAL

2.1 Background and fitting procedure

To date, two Fe-Cr interatomic potentials exist which are capable of reproducing the change of sign of the heat of mixing as a function of composition: the two-band model (2BM)

potential developed in [11] (OLS) and the concentration dependent model (CDM) potential developed in [12] (CAR). Both formalisms are adaptations of the embedded atom method [13], in which local concentration dependence is introduced. Both potentials, however, suffer from important drawbacks regarding the description of thermodynamic, point-defect, and dislocation properties. We have hence developed a new 2BM potential to correct those shortcomings, while keeping the known useful qualities of both potentials. Details on formalism and fitting methodology are given in [14]. Here we only sketch the main ideas and recall a few key features of the potential developed.

For pure Fe, we chose the potential number 2 from [15], which is accepted to be one of the best available [16], while the pure Cr potential and the mixed Fe-Cr interactions were newly fitted. The main reason to fit a new potential for pure Cr was to provide a better description of dislocation properties in this metal. The material properties considered in the fit for pure Cr were the correct stability of different crystallographic structures, the cohesive energy, the equilibrium lattice constant, the elastic constants (for cubic lattice structures) [26], and the vacancy formation energy.

In addition, the formation energy of self-interstitial configurations, the vacancy migration energy and, most importantly, the $\{110\}\langle 111 \rangle$ gamma surface cut and the $\frac{1}{2}\langle 111 \rangle$ screw-dislocation core structure were included in the fit. The mixed interactions were fitted simultaneously to all properties of interest. The mixing enthalpy was fitted in the whole concentration range using a variance expansion as described in [18]. The Cr-Cr and Cr-vacancy interaction energies up to second nearest neighbour were fitted, as well as the Cr-vacancy migration energy in Fe, using DFT reference values as guides [10].

We also fitted the excess vibrational entropy, computed in the harmonic approximation [19], to a value as close as possible to the experimental one [20,21]. Finally, the potential was adjusted in the short distance region to reproduce the DFT-obtained binding energy of the mixed $\langle 110 \rangle$ Fe-Cr dumbbell. Tabulations of the potential obtained containing up to 5000 points are available on-line at: <http://www.ctcms.nist.gov/potentials/> or upon request to the authors.

2.2 Main properties of the potential

The main improvements to be achieved with the present potential as compared to the OLS and CAR potentials concern correct structure for the $\frac{1}{2}\langle 111 \rangle$ screw-dislocation core and miscibility gap closer to CALPHAD's, i.e. closing at an acceptable temperature (differently from CAR), while removing the symmetrical shape predicted by OLS. Fig. 1 shows, via differential displacement maps [22], that while OLS predicts a three-fold symmetry screw-dislocation core, ours gives a compact core, as in DFT [23]. In Fig. 2 the CALPHAD miscibility gap [24, 25] is compared to the prediction of our potential and OLS (from Monte Carlo simulations in the semi-grand canonical ensemble [26]), as well as of CAR (from free energy calculations using a thermodynamic integration technique [27]). Large Cr solubility at low temperature, due to the negative heat of mixing, is well reproduced by all potentials. OLS underestimates the critical temperature at which the gap closes by ~ 200 K, while our potential overestimates it by roughly the same amount. CAR, on the other hand, gives a critical temperature above the melting point. On the Cr-rich side, the little Fe solubility at low temperature is well reproduced by both our potential and CAR, while OLS predicts high Fe-solubility. As far as interaction energy between Cr atoms and point-defects, it has been verified that our potential is equivalent to OLS, which in this respect performs very well.

In practice, the main improvement as compared to OLS is that no modification of the screw dislocation core structure occurs during the interaction with Cr precipitates, avoiding that in

MD simulations such core transformation will manifest itself as emission of kink pairs in the $\{112\}$ plane, causing cross-slip movement instead of stable glide [23].

In summary, the newly developed Fe-Cr potential reaches the goal of removing the main shortcomings of previously existing ones, while conserving their “good” properties. Both this and OLS potentials were used in the simulations reported in the following sections.

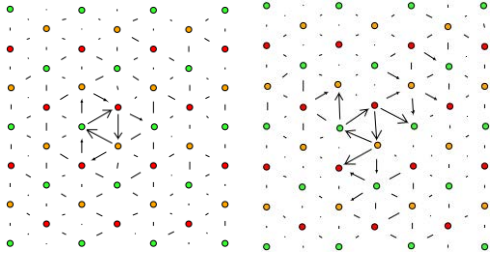


FIG. 1. Comparison of screw component maps obtained with our potential (left) and OLS (right).

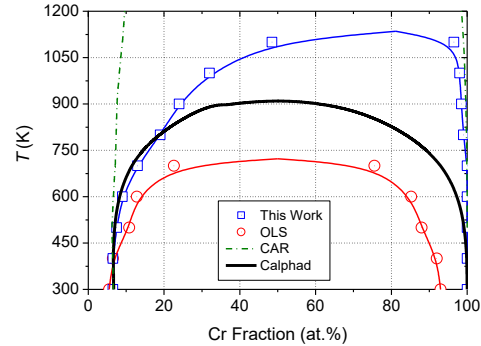


FIG. 2. Comparison of phase diagrams resulting from different potentials against a CALPHAD calculation. Curves for OLS and our potential are from [57], for CAR and CALPHAD from [54] & [55], respectively.

3. ATOMISTIC STUDY OF DISLOCATION/DEFECT INTERACTION

3.1 Background and methodology

The defects that can be considered responsible for the strengthening of Fe-Cr alloys under irradiation are prismatic dislocation loops of interstitial nature, with Burgers vector $\frac{1}{2}\langle 111 \rangle$ or $\langle 100 \rangle$, as well as, above $\sim 9\%$ Cr, Cr-rich precipitates [2, 3, 28, 29], the formation of which is enhanced by irradiation within the miscibility gap of the Fe-Cr system (Fig. 2). So, MD simulations of edge dislocation motion were performed in presence of both these classes of defects, exploring different defect configurations, sizes, temperatures, and also strain rates, in concentrated Fe-Cr alloys with different composition, namely 5, 10 and 15 at. %Cr. The simulations were performed following the methodology developed in [30].

3.2 Interaction of edge dislocations with radiation-produced defects in Fe-Cr

For results of studies of the interaction of an edge and also a screw dislocation in pure Fe with dislocation loops and voids, see [31–38]. These studies clarified the mechanisms of interaction and provided values for the corresponding critical resolved stress, τ_C . Loops can be absorbed or not depending on type of loop, temperature and strain-rate: if absorbed, they are stronger obstacles than when they are not. However, if apparent sizes (i.e. diameters) are compared, voids are stronger obstacles than loops (Fig. 3). In Fe-10%Cr the mechanisms of interaction between the dislocation and the defects did not change. No difference in the critical resolved shear stress is found between Fe and Fe-Cr in the case of loops. In the case of voids, for large sizes, the strength seems to increase in Fe-Cr as compared to Fe. The effect of the matrix is essentially only to add the friction stress.

A number of experiments suggest the possibility that in Fe-Cr alloys under irradiation Cr atoms segregate at dislocation loops, or that α' precipitates on them [39–44]. Recent Metropolis Monte Carlo (MMC) studies performed with the 2BM potentials of Section 2

support this possibility [45]. Therefore, the interaction of edge dislocations with $\frac{1}{2}\langle 111 \rangle$ loops enriched with Cr, extracted from MMC simulations, has also been studied. Fig. 4 shows the stress-strain curves relative to the interaction of the same type of dislocation with the same type of loop under the same conditions, with the only difference of increasing Cr content in the neighborhood of the loop. All calculations have been performed in pure Fe matrices. Clearly, a non-negligible effect exists, as the critical resolved stress increases to different degrees in presence of Cr-enrichment. The effect of enrichment should be noticeable (depending on loop size and strain-rate) if the test temperature is "high enough" to have absorption and if the irradiation temperature is "not too high", to have enrichment, but for the moment it is not obvious how to assign precise values to these two limiting temperatures.

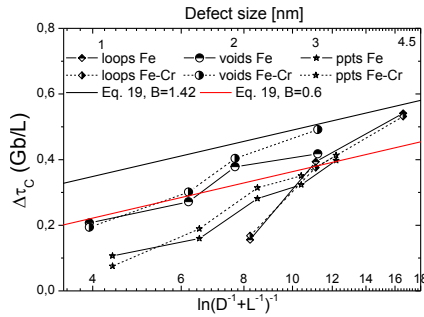


FIG. 3. Comparison in terms of normalized strength of the effect of radiation-produced defects and precipitates on edge dislocation glide versus size, in Fe and in Fe10% Cr.

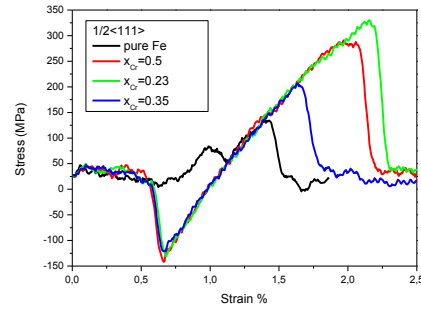


FIG. 4. Stress-strain curves during the interaction of an edge dislocation with a $\frac{1}{2}\langle 111 \rangle$ loop at 450 K with varying levels of Cr-enrichment.

3.3 Discussion: radiation strengthening in Fe-Cr alloys

All experimental studies available agree on the fact that Fe-Cr alloys containing from a few fractions of %Cr up to 15-20% Cr harden more under irradiation in the same conditions than pure Fe [4, 28, 39, 46–49]. This fact still lacks of clear explanation. Void swelling is suppressed by adding Cr [2,-6], so the additional irradiation hardening in Fe-Cr should be explained chiefly on the basis of the loop-dislocation interaction. Moreover if, in addition to irradiation-produced defects, α' precipitates are formed, hardening will be higher [50].

Under specific conditions, $\frac{1}{2}\langle 111 \rangle$ loops can be considered stronger obstacles than $\langle 100 \rangle$ loops. Since in Fe-Cr the appearance of $\langle 111 \rangle$ loops is favoured over $\langle 100 \rangle$ loops [4, 29], this fact alone may partly explain a higher irradiation hardening in Fe-Cr. The higher strength of decorated loops as obstacles for dislocations (Fig. 4) may be a further reason. Finally, simply the presence of a higher density of invisible defects (small loops) in Fe-Cr as compared to Fe, due to the slowing-down effect of Cr on small loops [44, -147], may also provide an explanation for higher hardening.

4. ADVANCED ATOMISTIC KINETIC MONTE CARLO SIMULATIONS IN FE-CR ALLOYS

4.1 Background and methodology

AKMC methods are widespread tools to study diffusion-controlled microstructural and microchemical evolution in alloys during thermal ageing and under irradiation [54–63]. Most of the physics is contained in the energy barriers associated with the migration jumps of the point-defects, E_m , which must embody both the thermodynamics and the kinetics of the

system studied. We have developed in [64–66] a method that constructs a mathematical regression of the energy barriers as functions of the local atomic environment (LAE) with an artificial neural network (ANN) [67]. Reference cases are calculated by the nudged elastic band method (NEB) [68, 69], using an interatomic potential, so all necessary atomic neighbours can be taken into account, together with chemical and strain field effects. Instrumental for a successful application of this methodology was the development of an ANN training scheme called *gradually improving accuracy constructive algorithm* (GIACA) [66].

4.2 Application to thermal annealing of Fe-Cr alloys

The GIACA has been applied to predict with an ANN the E_m of single-vacancies in 615 atom LAEs containing both Fe and Cr atoms. The ANN predictions have been verified to be very satisfactory (small error, small bias, high correlation), so the ANN can be considered as a very good (and much faster) substitute to the NEB method. These barriers have been used in our AKMC model to simulate thermal annealing processes in Fe-Cr, following for the rest the guideline of several published works [59–61]. The alloy is initially a random solid solution; one vacancy is introduced in the system with periodic boundary conditions. With time, atoms are progressively re-arranged by the diffusing vacancy toward the final equilibrium for the working temperature. If the model is thermodynamically correct, Cr atoms will cluster and eventually precipitate in Fe, if present in concentrations above their solubility limit, in accordance with the corresponding phase diagrams (see Fig. 2). In addition, AKMC models are expected to predict correctly also the kinetics of the precipitation process. The details of how the simulation was performed can be found in [66].

Fig. 5 shows how the kinetics of the precipitation process in Fe-20%Cr at 500°C as predicted by the present ANN-based AKMC model compares with experimental measurements. These were obtained under the same conditions and for the same material, by Jaquet [70], Novy *et al.* [71], and Bley [72]. For the comparison, the simulation time had to be suitably renormalized, to take into account the fact that, due to the smallness of the simulation volume, the concentration of vacancies in the simulation is larger than in reality (the problem is discussed e.g. in [56, 59]). In Fig. 5, the results obtained using a more heuristic approach are shown as well. With the latter, while the predicted average cluster radius is in agreement with the experiments, the final cluster density is overestimated by almost an order of magnitude. On the contrary, in the present ANN-based AKMC, the results on size are overall good, especially considering the discrepancy existing between different experimental data-sets, and the cluster density is in much better agreement with the experiments than using the other approach, too.

4.3 Application to study the diffusivity of radiation-induced defects

Here we show that ANN trained using the GIACA and based on properly obtained NEB values can be also used to predict the energy barriers of single self-interstitials migrating in a concentrated Fe-Cr alloy. In addition, by including other point-defects in the LAE, it is possible to describe the formation of clusters, as well.

It is known that the Fe-Cr mixed dumbbell is stable and, in a dilute alloy, migrates faster than the Fe-Fe dumbbell (see [73, 74] for experiments, [75] for DFT calculations). More in general the interaction between dumbbell and multiple Cr atoms can be very strong [10, 76], with the effect that, in concentrated alloys, configurational traps may exist [77]. These are local configurations around the dumbbell in which the dumbbell/Cr interaction is so strong that the self-interstitial is practically trapped. As discussed in [78], although between traps the mixed dumbbell migrates faster than the Fe-Fe dumbbell; the correlation of diffusion jumps around

configurational traps reduces the effective diffusivity of dumbbells. This is reflected in significant changes in the resistivity recovery peaks under isochronal annealing, as compared to iron or dilute Fe-Cr alloys [79].

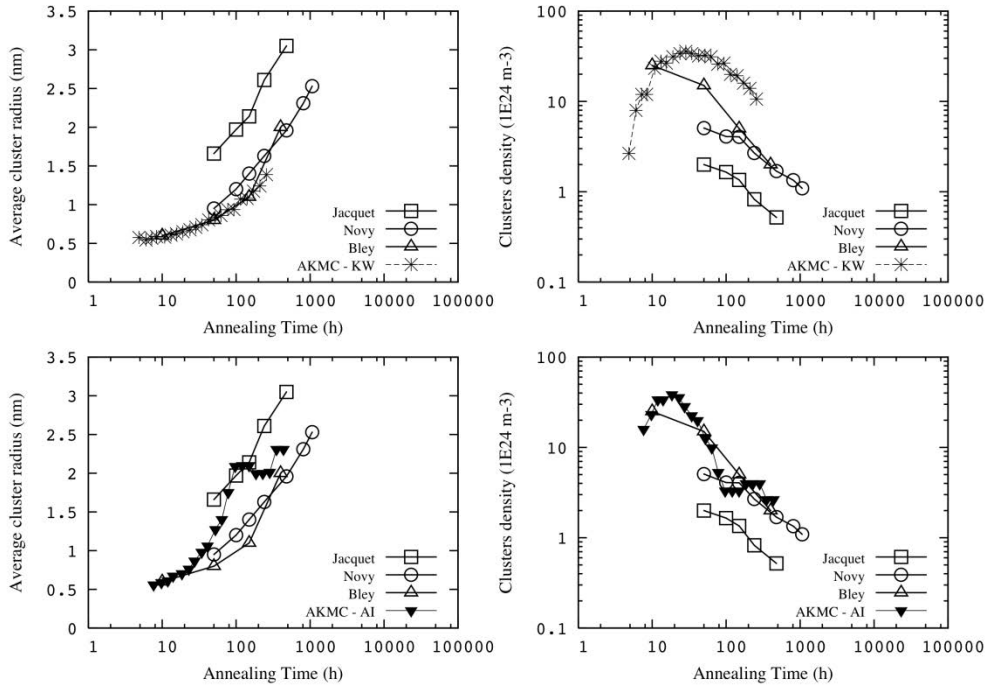


FIG. 5. Comparison of experimental average cluster radius (left) and cluster density (right) with results from Fe-20%Cr AKMC thermal annealing simulations at 500°C, using two different migration energy calculation methods: a heuristic one (above) and ANN (below). The experimental values are from [70–72].

However, it is impossible to study and determine quantitatively by MD the diffusivity of self-interstitials in Fe-Cr alloys, because the time spent by the dumbbell in configurational traps exceeds the affordable timeframe of these simulations. The present ANN-based AKMC model solves this problem. Using established techniques to determine the jump frequency, ν , and the diffusion coefficient, D , of point-defects and their clusters at a given temperature from long enough atomistic simulations [80–82], and interpolating the data-points versus temperature with Arrhenius laws, the corresponding migration energies (E_m^V and E_m^D) and pre-factors (ν_0 and D_0) can be obtained. The two migration energy values will coincide only if all jumps contribute to diffusion. In this case, though, many jumps are needed to produce actual diffusion, because the diffusing species is trapped during its motion. Consistently, Fig. 6 shows that the migration energy of the dumbbell *between traps*, deduced from the jump frequency decreases with increasing Cr content; however, the *effective* migration energy deduced from the diffusion coefficient is significantly higher, because of the presence of configurational traps.

By training the ANN including vacancies in the LAE the energy barriers for single vacancy migration calculated with the ANN will implicitly take into account the existence of a binding energy with other vacancies. This enables the model to describe correctly the formation of vacancy clusters, as well as their stability and mobility. A study of stability and mobility of vacancy and vacancy-solute clusters in Fe and Fe-Cu alloys was already carried out using an ANN-based AKMC model in [81,82].

Here the study performed for Fe-Cr alloys is reported. In these alloys the interaction between solute atoms and vacancies is extremely weak [1, 83], so solute-vacancy clusters will not form and vacancy-cluster stability and mobility is expected to be the same as in Fe. However, this extrapolation from dilute to concentrated alloys needs to be verified. The ANN-based AKMC model developed here allows this verification. Fig. 7 shows the result of calculations of diffusion coefficients of clusters of up to 10 vacancies at different temperatures for three Cr contents (0, 5 and 10 %Cr), following the methodology described in [82]: with the minor exception of the cluster of 9 vacancies, the presence of Cr in solid solution up to 10% does not affect the migration of the vacancy clusters.

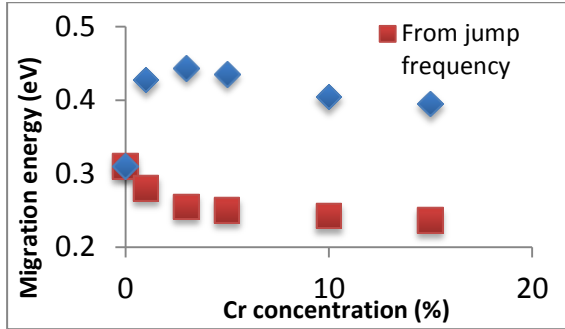


FIG. 6. Migration energy of the dumbbell versus Cr content deduced from diffusion coefficient and jump frequency, as calculated from AKMC simulations at different temperatures.

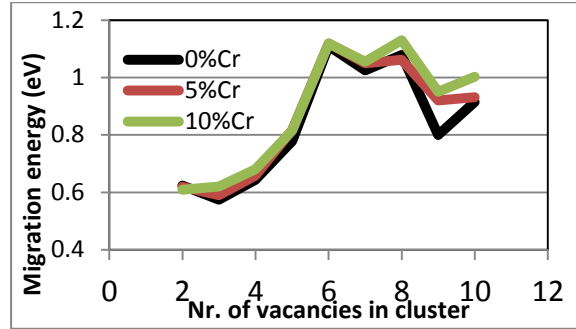


FIG. 7. Migration energy of vacancy clusters up to size 10 in pure Fe and Fe-Cr, from AKMC simulations at different temperatures.

5. POSITRON ANNIHILATION ON NEUTRON-IRRADIATED FE-CR ALLOYS

5.1 Background

As support to modelling, neutron irradiated (0.06, ~0.6 and >1 dpa) Fe-Cr alloys of increasing Cr content (2.5, 5, 9 and 12%Cr – nominal) are being thoroughly characterized, using a combination of microstructural examination techniques, in addition to testing their mechanical properties [28, 84–87]. Here, the results of positron annihilation spectroscopy (PAS) are recalled (see [88] for details).

5.2 Results

PAS is especially sensitive to vacancy-type defects. The results of PAS suggest that Cr addition delays or even inhibits vacancy cluster formation. Further analysis to estimate the concentration of single vacancies in absolute terms in the Fe-Cr alloys irradiated to 0.06 dpa, along with the concentration of vacancies in pure iron irradiated to 0.025 dpa under similar conditions, shows that the addition of Cr to Fe makes the concentration of vacancies an order of magnitude lower (Fig. 8). The concentration of vacancies does increase with Cr addition, but in absolute terms this increase remains a minor effect. The low concentration of vacancies is in itself an explanation of the absence, or low occurrence, of clusters in the alloys, since the reaction rate of two single vacancies to form di-vacancy scales as the square of single vacancy concentration.

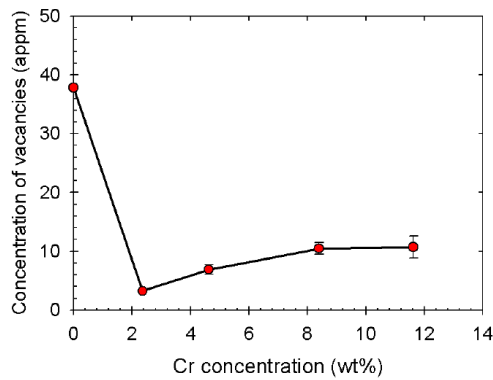


FIG. 8. The concentration of vacancies that remain in the irradiated Fe-Cr alloys after 0.06 dpa, compared to the total amount of vacancies in irradiated Fe (0.025 dpa).

At higher dose the concentration of vacancies could not be deduced because lifetime measurements could not be performed due to activation, but the normalized coincidence Doppler broadening spectra suggest that more and/or bigger vacancy clusters have been formed, as compared to the lower dose. From the S-W factor plot one can deduce that the largest mean size of vacancy clusters is likely not to exceed 2–3 vacancies, in the alloy with the least Cr, and is certainly smaller for the other alloys.

As a matter of fact, the highest value of this parameter in the Fe-Cr alloys irradiated to 0.6 dpa is of the same magnitude as the value in pure Fe irradiated to a dose about *25 times* lower (0.025 dpa). So, these results, although quantitatively less complete, confirm the observations made at lower dose: the addition of Cr to Fe decreases the amount of surviving vacancies and retards the nucleation/growth of vacancy clusters. It is important to note that at 0.6 dpa a clear non-monotonic behaviour is observed for both the *S* and the *W* parameters. Between 5 and 9 wt.% of chromium, *S* reaches a minimum, while *W* shows a maximum. This non-monotonic trend of the *S* parameter is fully consistent with the dependence of void swelling measured in Fe-Cr alloys of different Cr content, irradiated to much higher dose and temperature [2–6]. It also consistent with the non-monotonic slowing-down of self-interstitial clusters as a function of Cr content found in MD simulations [51–53]. It is therefore argued that there is a direct connection between the latter and the former: reduced diffusivity of self-interstitial clusters will lead to enhanced recombination with decrease of vacancy population. For a full discussion, see [88].

6. CONCLUSION

In this report we have overviewed the work of development and application of a new potential for the Fe-Cr binary alloy which, within a relatively simple EAM-like approach, provides satisfactory results. We have indeed shown how such potential can be exploited for the study of the interaction between dislocations and radiation defects, using numerically intensive MD techniques. Much work is needed, because many different cases need to be simulated and looked at in detail to derive the general trends, but eventually this work will allow the parameterisation of dislocation dynamics models capable of predicting the strengthening of irradiated Fe-Cr alloys at single crystal level. The same potential also allowed the study of the microchemical evolution of Fe-Cr binary alloys under thermal ageing, reproducing closely experimental results of density and size of Cr-rich precipitates. For this purpose, an AKMC technique that implies a high level of complexity and a long developmental effort had to be used. This technique, however, bears the promise of allowing also the study of the nanostructure evolution under irradiation in a near future.

Overall, the use of advanced simulation tools revealed many details on mechanisms acting at the nanoscopic scale in Fe-Cr alloys. Concerning thermodynamics, the identification of a region of negative mixing enthalpy led to the revision of the Fe-Cr phase diagram. Concerning point-defect properties, probably the most important fact is the recognition of the affinity of Cr in Fe for self-interstitials and its complete transparency to vacancies. These two facts have consequences that are now being progressively brought into ever more refined models, and provide hints to understand experimental observations. The agreement between the expectation from simulation results and the results of PAS examination of Fe-Cr alloys in terms of suppression of vacancy clusters formation in presence of Cr is an important example.

REFERENCES

- [1] MALERBA, L., CARO, A., WALLENIIUS, J., J. Nucl. Mater. **382** (2008) 112.
- [2] LITTLE, E.A., J. Nucl. Mater. **87** (1979) 11
- [3] LITTLE, E.A., STOW, D.A., Metal Science **14** (1980) 89.
- [4] POROLLO, S., DVORIASHIN, A., VOROBYEV, A., KONOBEV, Y., J. Nucl. Mater. **256** (1998) 247.
- [5] GARNER, F.A. TOLOCZKO, M.B., SENCER, B.H., J. Nucl. Mater. **276** (2000) 123.
- [6] KONOBEV, Y., DVORIASHIN, A., POROLLO, S., GARNER, F.A., J. Nucl. Mater. **355** (2006) 124.
- [7] OLSSON, P., ABRIKOSOV, I.A., VITOS, L., WALLENIIUS, J., J. Nucl. Mater. **321** (2003) 84.
- [8] OLSSON, P., ABRIKOSOV, I.A., WALLENIIUS, J., Phys. Rev. B **73** (2006) 104416.
- [9] KLAVER, T.P.C., DRAUTZ, R., FINNIS, M.W., Phys. Rev. B **74** (2006) 094435.
- [10] OLSSON, P., DOMAIN, C., WALLENIIUS, J., Phys. Rev. B **75** (2007) 014110.
- [11] OLSSON, P., WALLENIIUS, J., DOMAIN, C., NORDLUND, K., MALERBA, L., Phys. Rev. B **72** (2005) 214119; *ibid.* **74** (2006) 1(E).
- [12] CARO, A. CROWSON, D.A., CARO, M., Phys. Rev. Lett. **95** (2005) 75702.
- [13] DAW, M.S. BASKES, M.I., Phys. Rev. B **29** (1984) 6443.
- [14] BONNY, G., PASIANOT, R.C., TEREITYEV, D., MALERBA, L., Philos. Mag. **91** 12 (2011) 1724.
- [15] MENDELEV, M.I., HAN, S., SROLOVITZ, D.J., ACKLAND, G.J., SUN, D.Y., ASTA, M., Philos. Mag. **83** 35 (2003) 3977.
- [16] MALERBA, L., *et al.*, J. Nucl. Mater. **406** (2010) 19.
- [17] KITTEL, C., Introduction to Solid State Physics, John Wiley & Sons, New York, (1996).
- [18] BONNY, G. PASIANOT, R.C., MALERBA, L., Philosophical Magazine **89** 34–36 (2009) 711.
- [19] VAN DE WALLE, A., CEDER, G., Reviews Modern Phys. **74** (2002) 11.
- [20] FULTZ, B., ANTHONY, L., ROBERTSON, J.L., NICKLOW, R.M., SPOONER, S., MOSTOLLER, M., Phys. Rev. B **52** (1995) 3280.
- [21] SWAN-WOOD, T.L., DELAIRE, O., FULTZ, B., Phys. Rev. B **72** (2005) 024305.
- [22] VITEK, V., Crystal Lattice Defects **5** (1974) 1.
- [23] TEREITYEV, D., BONNY, G., DOMAIN, C., PASIANOT, R.C., Phys. Rev. B **81** (2010) 214106.
- [24] BONNY, G., TEREITYEV, D., MALERBA, L., J. Phase Equil. & Diff. **31** (2010) 439.
- [25] ANDERSSON, J., SUNDMAN, B., Calphad **11** (1987) 83.
- [26] BONNY, G., PASIANOT, R.C., ZHURKIN, E.E., HOU, M., Comp. Mater. Sci. **50** (2011) 2216.

- [27] BONNY, G., ERHART, P., CARO, A., PASIANOT, R.C., MALERBA, L., CARO, M., *Model. & Simul. Mater. Sci. & Eng.* **17** (2009) 025006.
- [28] MATIJASEVIC, M., ALMAZOUZI, A., *J. Nucl. Mater.* **377** (2008) 147.
- [29] GELLES, D.S., in 14th International Symp. on the Effects of Radiation on Materials (PACKAN, N.H., STOLLER, R.E., KUMAR, A.S., Eds.), American Society for Testing and Materials, Andover, MA (1988) 73.
- [30] OSETSKY, Y.N., BACON, D.J., *Model. & Simul. Mat. Sci. & Eng.* **11** (2003) 427.
- [31] BACON, D.J., OSETSKY, Y.N., RONG, Z., *Philos. Mag.* **86** 25–26 (2006) 3921.
- [32] NOMOTO, A., SONEDA, N., TAKAHASHI, A., ISHINO, S., *Mater. Trans.* **46** (2005) 463.
- [33] OSETSKY, Y.N., BACON, D.J., *Mater. Sci. & Eng. A* **400–401** (2005) 374.
- [34] TEREPTYEV, D., MALERBA, L., BACON, D.J., OSETSKY, Y.N., *J. Physics: Cond. Matter* **19** (2007) 456211.
- [35] TEREPTYEV, D., BACON, D.J., OSETSKY, Y.N., *J. Physics: Conde. Matter* **20** (2008) 445007.
- [36] TEREPTYEV, D., GRAMMATIKOPOULOS, P., BACON, D.J., OSETSKY, Y.N., *Acta Mater.* **56** (2008) 5034.
- [37] TEREPTYEV, D., BACON, D.J., OSETSKY, Y.N., *Philos. Mag.* **89** 9 (2009) 1.
- [38] TEREPTYEV, D., OSETSKY, Y.N., BACON, D.J., *Scripta Mater.* **62** (2010) 697.
- [39] SUGANUMA, K., KAYANO, H., *J. Nucl. Mater.* **118** (1983) 234.
- [40] OHNUKI, S., TAKAHASHI, H., TAKEYAMA, T., *J. Nucl. Mater.* **122–123** (1984) 317.
- [41] YOSHIDA, N., YAMAGUCHI, A., MUROGA, T., MIYAMOTO, Y., KITAJIA, K., *J. Nucl. Mater.* **155–157** (1988) 1232.
- [42] NEKLYUDOV, I.M., VOYEVODIN, V.N., *J. Nucl. Mater.* **212–215** (1994) 39.
- [43] WAKAI, E., HISHINUMA, A., KATO, Y., YANO, H., TAKAKI, S., ABIKO, K., *J. Physique IV* **5** (1995) 277.
- [44] TEREPTYEV, D., KLIMENKOV, M., MALERBA, L., *J. Nucl. Mater.* **393** (2009) 30.
- [45] ZHURKIN, E.E., TEREPTYEV, D., HOU, M., MALERBA, L., BONNY, G., *J. Nucl. Mater.* **417** (2011) 1082.
- [46] OKADA, A., KAWAGUCHI, N., HAMILTON, M., HAMADA, K., YOSHIIE, T., ISHIDA, I., HIROTA, E., *J. Nucl. Mater.* **212–215** (1994) 382.
- [47] OKADA, A., MAEDA, H., HAMADA, K., ISHIDA, I., *J. Nucl. Mater.* **271–272** (1997) 133.
- [48] MATIJASEVIC, M., VAN RENTERGHEM, W., ALMAZOUZI, A., *Acta Mater.* **57** (2009) 1577.
- [49] SUGANUMA, K., KAYANO, H., YAJIMA, S., *J. Nucl. Mater.* 105 (1982) 23.
- [50] TEREPTYEV, D., BONNY, G., MALERBA, L., *Nucl. Instr. & Meth. B* **267** (2009) 3155.
- [51] TEREPTYEV, D., MALERBA, L., BARASHEV, A.V., *Philos. Mag. Lett.* **85** 11 (2005) 587.
- [52] TEREPTYEV, D., OLSSON, P., MALERBA, L., BARASHEV, A.V., *J. Nucl. Mater.* **362** (2007) 167.
- [53] TEREPTYEV, D., MALERBA, L., BARASHEV, A.V., *Philos. Mag.* **88** 1 (2008) 21.
- [54] LE BOUAR, Y., F. SOISSON, F., *Phys. Rev. B* **65** (2002) 094103, and refs. therein.
- [55] SOISSON, F., *J. Nucl. Mater.* **249** (2006) 235.
- [56] SOISSON, F., FU, C-C., *Phys. Rev. B* **76** (2007) 214102.
- [57] VINCENT, E., BECQUART, C.S., DOMAIN, C., *Nucl. Instr. Meth. Phys. Res. B* **255** (2007) 78.

- [58] VINCENT, E., BECQUART, C.S., DOMAIN, C., J. Nucl. Mater. **382** (2008) 154.
- [59] VINCENT, E., BECQUART, C.S., PAREIGE, C., PAREIGE, P., DOMAIN, C., J. Nucl. Mater. **373** (2008) 387;
- [60] BONNY, G., TEREITYEV, D., MALERBA, L., Comput. Mater. Sci. **42** (2008) 107.
- [61] BONNY, G., TEREITYEV, D., MALERBA, L., VAN NECK, D., Phys. Rev. B **79** (2009) 104207.
- [62] BECQUART, C.S., DOMAIN, C., *physica status solidi (b)* **247** (2010) 9.
- [63] SOISSON, F., BECQUART, C.S., CASTIN, N., DOMAIN, C., MALERBA, L., VINCENT, E., J. Nucl. Mater. **406** (2010) 55, and references therein.
- [64] CASTIN, N., DOMINGOS, R.P., MALERBA, L., Int. J. Comput. Intell. Syst. **1** 4 (2008) 340.
- [65] CASTIN, N., MALERBA, L., Nucl. Instr. Meth. Phys. Res. B **267** (2009) 3148.
- [66] CASTIN, N., MALERBA, L., J. Chem. Phys. **132** (2010) 074507.
- [67] BISHOP, C. M., Neural networks for pattern recognition, Clarendon Press, Oxford, (1995).
- [68] JÓNSSON, H., MILLS, G., JACOBSEN, K.W., in Classical and quantum dynamics in condensed phase simulations (BERNE, B.J., CICCOTTI, G., COKER, D.F., Eds.), World Scientific, Singapore (1998).
- [69] HENKELMAN, G., JÓNSSON, H., J. Chem. Phys. **113** (2000) 9901.
- [70] JACQUET, V., PhD dissertation, Ecole polytechnique, Paris, France (2000).
- [71] NOVY, S., PAREIGE P., PAREIGE, C., J. Nucl. Mater. **384** (2009) 96.
- [72] BLEY, F., Acta Metal. Mater. **40** (1992) 1505.
- [73] MAURY, F., LUCASSON, P., LUCASSON, A., FAUDOT, F., BIGOT, J., J. Phys. F: Met. Phys. **17** (1987) 1143
- [74] ABE, H., KURAMOTO, E., J. Nucl. Mater. **271&272** (1999) 209.
- [75] OLSSON, P., J. Nucl. Mater. **386–388** (2009) 86.
- [76] KLAVER, T.P.C., OLSSON, P., FINNIS, M.W., Phys. Rev. B **76** (2007) 214110.
- [77] NIKOLAEV, A.L., J. Phys.: Condens. Mat. **11** (1999) 8633; NIKOLAEV, A.L., Philos. Mag. **87** 31 (2007) 4847.
- [78] TEREITYEV, D., OLSSON, P., KLAVER, T.P.C., MALERBA, L., Comp. Mater. Sci. **43** (2008) 1183, and refs. therein.
- [79] BENKADDOUR, A., DIMITROV, C., DIMITROV, O., Mater. Sci. Forum **15–18** (1987) 1263; DIMITROV, C., BENKADDOUR, A., CORBEL, C., MOSER, P., Ann. Chime. France **16** (1991) 319.
- [80] OSETSKY, Y.N., Defects and Diffusion in Metals **188** (2001) 71.
- [81] DJURABEKOVA, F., MALERBA, L., DOMAIN, C., BECQUART, C.S., Nucl. Instr. & Meth. B **255** (2007) 47.
- [82] PASCUET, M.I., CASTIN, N., BECQUART, C.S., MALERBA, L., J. Nucl. Mater. **412** (2011) 106.
- [83] MOSLANG, A., GRAF, H., BALZER, G., RECKNAGEL, E., WEIDINGER, A., WICHERT, T. GRYNSZPAN, R.I., Physical Review B **27** (1983) 2674.
- [84] HEINTZE, C., ULBRICHT, A., BERGNER, F., ECKERLEBE, H., J. Phys.: Conf. Series **247** (2010) 012035.
- [85] ULBRICHT, A., HEINTZE, C., BERGNER, F., ECKERLEBE, H., J. Nucl. Mater. **407** (2010) 29.
- [86] MATIJASEVIC, M., LUCON, E., ALMAZOUZI, A., J. Nucl. Mater. **377** (2008) 101.
- [87] MATIJASEVIC, M., Ph.D. dissertation, University of Ghent, Belgium (2007).
- [88] LAMBRECHT, M., MALERBA, L., Acta Mater. **59** (2011) 6547.

VERY HIGH DOSE IRRADIATION INDUCED RADIATION DAMAGE AND SYNERGISTIC EFFECT ON FORMATION OF VACANCY CLUSTERS IN CLAM

SHENGYUN ZHU*, YONGNAN ZHENG*, YI ZUO*, DAQING YUAN*, PING FAN*, DONGMEI ZHOU*, QIAOLI ZHANG*, BAOQUN CUI*, LIHUA CHEN*, WEISHENG JIANG*, YICAN WU**, QUNYING WANG**, LEI PENG**, XINZHONG CAO***, BAOYI WANG***, LONG WEI***

* China Institute of Atomic Energy, P.O. Box 275–50, Beijing 102413, China

** Institute of Plasma Physics, CAS, P.O. Box 1126, Hefei, Anhui 230031, China

*** Institute of High Energy Physics, CAS, Beijing 100039, China

Abstract

A triple beam irradiation facility, a double-stop positron lifetime spectrometer with four LaBr₃ scintillation detectors and a coincidence Doppler broadening energy spectrometer have been established, which will play an important role in investigating radiation damage in nuclear energy structural materials. Simultaneous and sequential irradiations of gold, hydrogen and helium ions were performed on the China low activation martensitic (CLAM) steel. The dose and temperature dependencies of radiation damage in the CLAM steel were measured after ion irradiation, and show that the size of vacancy clusters increases with the increasing irradiation dose up to 85 dpa and that the variation of the vacancy cluster size with irradiation temperature has a peak at ~500°C. The obtained results show clearly the synergistic effect of displacement damage and hydrogen and helium on the formation of radiation damage, which suppresses the radiation damage in the present case.

1. BACKGROUND

Investigation of radiation damage induced by very high dose irradiation in the CLAM steel has been pursued with the development of advanced structural materials for nuclear energy facilities of Generation IV. These structural materials are required to work in extreme environments of high dose, high temperature, etc for decades without failure and withstand constant bombardment by neutrons coupled with transmutations resulting from the (n, α) and (n, p) nuclear reactions, producing high dpa levels and large amounts of helium and hydrogen. To study these phenomena accelerator facilities for simulation of high dose neutron irradiations by heavy ion irradiation and for simultaneous irradiation with hydrogen and helium have been developed.

The present work is directed toward the development of techniques of acceleration simulation using simultaneous irradiation by triple beams to investigate the irradiation dose and temperature dependencies of radiation damage and the synergistic effect of high displacement damage, hydrogen and helium on the formation of vacancy clusters in the CLAM.

2. EXPERIMENT

2.1 Development of CLAM steel

The CLAM steel has been developed in China [1–5], the chemical composition of which was optimized based on the compositions of the EUROFER97, F82H, JLF-1 ORNL9Cr-2WVTa steels. Table 1 shows the chemical composition of the CLAM steel. This steel is considered to be a promising candidate for structural materials used for nuclear energy facilities of the Generation IV.

TABLE 1. CHEMICAL COMPOSITION OF CLAM (HEAT 0408D) IN WT%

Element	C	Cr	W	V	Ta	Mn	Y	Fe
Content	0.10	9.00	1.50	0.20	0.15	0.45	0.20	Bal.

Previously, the microstructure, physical and mechanical properties of the steel were tested and measured, and its radiation properties were examined by variety of irradiations, using electron irradiation to different doses at 450°C, 80 MeV ^{19}F ions to a dose of 10.0 dpa at 1.0 dpa/h, neutrons to 0.02 dpa at 250°C and by plasma exposure in the HT-7 Tokamak facility. The steel's compatibility with LiPb liquid metal and its coating and joining properties have also been tested. Fig. 1 shows a comparison of positron annihilation lifetimes and their intensities in the CLAM, F82H and T91 steels before and after 80 MeV ^{19}F irradiation to 10 dpa.

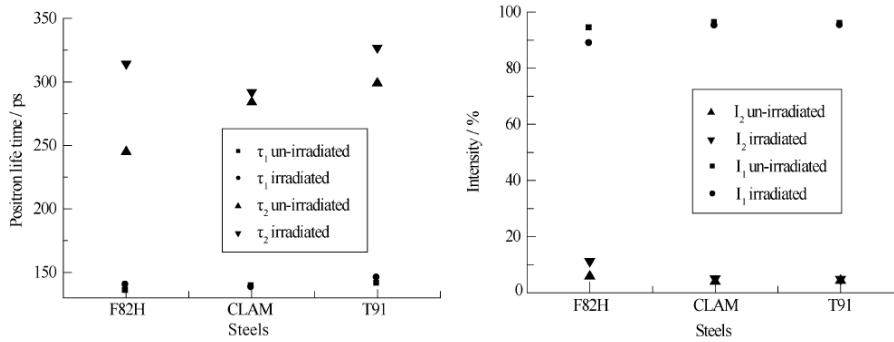


FIG. 1. Comparison of positron annihilation lifetimes (left) and their intensities (right) in CLAM, F82H and T91 before and after irradiation of 80MeV ^{19}F ions.

Fig. 2 shows neutron-induced hardening and embrittlement in the CLAM steel. These results demonstrate that CLAM possesses good properties similar to those for the other RAFM steels such as EUROFER97, F82H, T91, and JLF-1 steels and therefore is a potential structural material for Generation IV nuclear energy facilities.

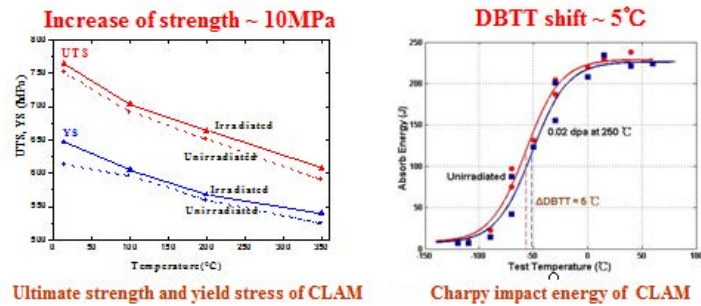
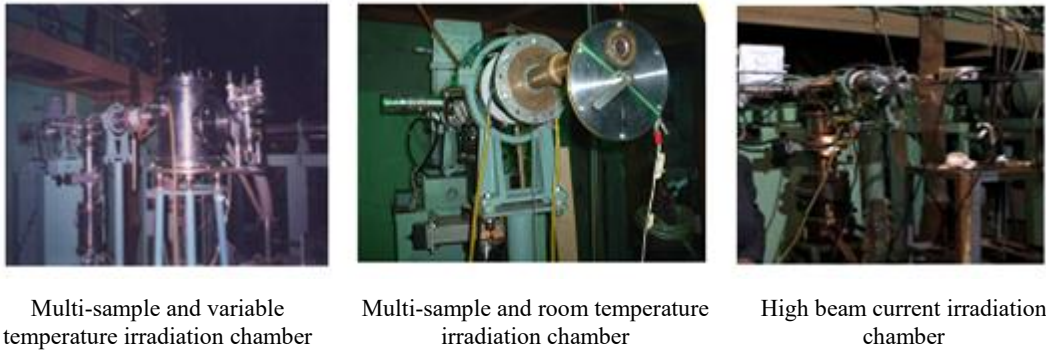


FIG. 2. Neutron irradiation induced hardening and embrittlement.

2.2 Accelerator simulation and radiation damage characterization

2.2.1 Heavy ion irradiation simulation

The heavy ion irradiation facilities were established at the China Institute of Atomic Energy using the HI-13 tandem accelerator that is able to provide the heavy ions with mass up to Au [6–9]. As shown in Fig.3 three irradiation chambers were constructed and installed at the beam terminal of the HI-13 tandem accelerator for heavy ion irradiations up to a few hundreds of dpa with an accuracy of ± 0.01 dpa. One chamber is a multi-sample and variable temperature irradiation chamber in which six samples can be mounted that are irradiated in turn without breaking vacuum, with a temperature range up to 800°C with accuracy of $\pm 10^\circ\text{C}$. The second chamber is the high beam current irradiation chamber that cools the sample directly by flowing water during irradiation. The third chamber is a room-temperature and multi-sample irradiation chamber.



Multi-sample and variable temperature irradiation chamber

Multi-sample and room temperature irradiation chamber

High beam current irradiation chamber

FIG. 3. Heavy ion irradiation chambers established at HI-tandem accelerator.

2.2.2 Triple beam irradiation of heavy ion, hydrogen and helium

A triple beam irradiation facility composed of an existing HI-13 tandem accelerator, a 250 kV implanter of hydrogen and helium and a triple beam irradiation chamber was constructed as shown in Fig. 4 for triple beam irradiations of heavy ion, hydrogen and helium [10–16]. The implanter of 250 kV is capable of providing a mixed beam of hydrogen and helium with a maximum beam current of 50 μ A. The gas flows of hydrogen and helium are controlled by two gas flow controllers and independently measured by two flow meters, so that the ratio of hydrogen to helium ions in a mixed beam can be adjusted easily to a desired value for simultaneous triple beam irradiations. The irradiation chamber can install six samples that are then irradiated one by one without breaking vacuum. The sample can be heated up to 1100°C with an accuracy of $\leq \pm 10^\circ\text{C}$. A more advanced triple beam irradiation facility with an existing HI-13 tandem accelerator, a 250 kV H implanter and a 500 kV He implanter is nearing completion.

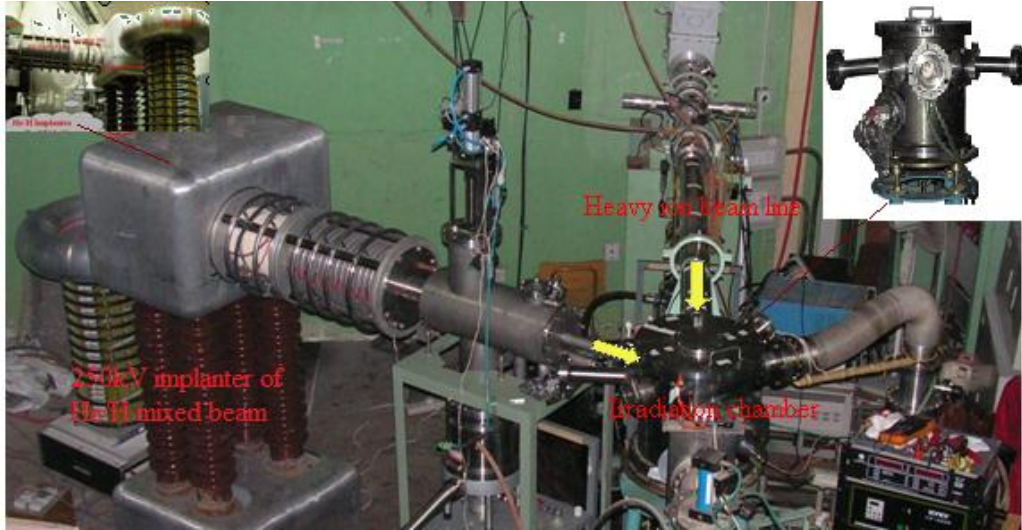


FIG.4. Triple beam irradiation facility with a 250kV implanter of He-H mixed beam.

2.2.3 Positron annihilation spectroscopy

Positron lifetime and Doppler broadening measurements were performed to characterize the radiation damage produced in this work [17]. Because the implantation ranges of heavy ion, hydrogen and helium in triple beam irradiations are very short in the CLAM steel, the slow-positron depth profiling measurements were then performed to detect the created radiation damage.

2.2.3.1 Four LaBr₃ detector positron lifetime spectrometer



FIG.5. Four LaBr₃ detector positron lifetime spectrometer with & without Pb shielding.

To perform lifetime measurements for high level radioactive samples a brand new positron annihilation spectrometer composed of four LaBr₃ scintillation detectors has been constructed and used for lifetime measurements of both radioactive and non-radioactive samples throughout this work [18–19]. Fig. 5 illustrates the four LaBr₃ scintillation detector (PMT1-4) positron lifetime spectrometer with (left) and without (right) lead shielding. The energy and time resolutions of the spectrometer are $\sim 2\%$ and 180ps, respectively. To suppress background brought in by radioactive samples a double-stop method is adopted, the principle of which is that the 1.27MeV γ -ray is detected by a detector (e.g. PMT1) as a start signal, while a pair of 0.511MeV γ rays are detected coincidentally by two detectors (e.g. PMT2 and PMT4) as a stop signal. To enhance the detection efficiency four lifetime spectra (PMT1-PMT2+PMT4, PMT3-PM2+PMT4, PMT2-PMT1+PMT3 and PMT4-PMT1+PMT3 in Fig. 5) are recorded simultaneously.

2.2.3.2 Coincidence Doppler broadening energy spectrometer

To suppress the background and raise the ratio of peak to valley a coincidence Doppler broadening spectrometer was established and used to characterize the defects [20]. Fig. 6 shows the spectrometer, detection principle and Doppler broadening spectra.

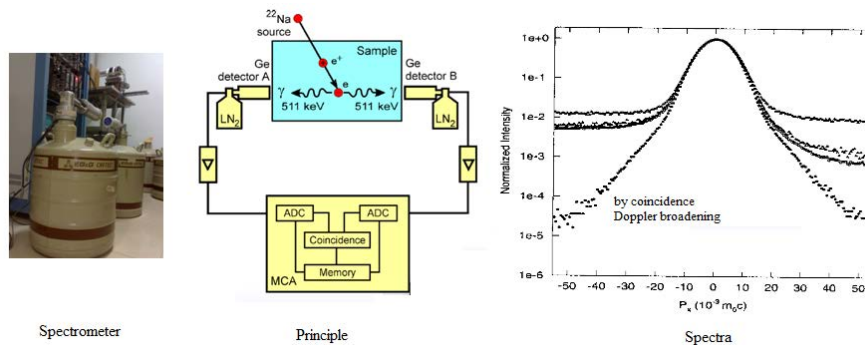


FIG. 6. Coincidence Doppler broadening energy spectrometer.

2.2.4 Slow positron beam facility

In the triple beam irradiations the ranges of the implanted ions in stainless steels are very short (less than 1 μm). Therefore, the mono-energetic slow positron beams were employed for depth profiling measurements of the S and W parameters [21]. The slow positron beam facility is based on the 1.3 GeV Linac of Beijing Electron-Positron Collider (BEPC) and can provide the mono-energy slow positron beams up to 30 keV with an intensity of $6 \times 10^5 \text{ e}^+ \text{ s}^{-1}$.

3. RESULTS

3.1 Dose dependence of radiation damage in CLAM steel

Radiation damage produced by high dose irradiations in the CLAM steel was investigated by heavy ion irradiation simulation and by using the positron annihilation lifetime and Doppler broadening techniques. The size of the CLAM samples was $\phi 15 \text{ mm} \times 0.5 \text{ mm}$. The samples were mechanically polished to a mirror-like surface. The irradiations were carried out using 80 MeV fluorine ions from the HI-13 tandem accelerator. The dose dependence was determined at room temperature up to 85 dpa with a damage rate of 2.1 dpa h^{-1} .

Positron lifetime and Doppler broadening measurements were conducted at room temperature. The Doppler broadening was analyzed with either the S parameter or W parameter. Besides the source components, all the measured positron lifetime spectra were fitted well with two lifetime components τ_1 and τ_2 with a fitting variance 1.3. The short lifetime τ_1 is a weighted average of annihilation lifetimes of the free positrons and the positrons trapped at mono- and di-vacancies and also dislocations. The long lifetime τ_2 is associated with vacancy clusters or voids. The larger the vacancy clusters, the longer the lifetime τ_2 . The relative intensities of τ_1 and τ_2 are I_1 and I_2 with $I_1+I_2=1$. The dose dependences of the positron annihilation lifetimes τ_1 and τ_2 , their intensities I_1 and I_2 and the S parameters are shown in Fig. 7.

3.2 Temperature dependence of radiation damage in CLAM steel

The dependence of radiation damage on irradiation temperature in the CLAM steel was measured in the irradiation temperature region from room temperature to 700°C at a dose of 15 dpa with a damage rate of 2.1 dpa h^{-1} . Most of experimental details are the same as in the dose dependence measurement.

The dependencies of the lifetimes τ_1 and τ_2 and the S parameter on irradiation temperature are shown in Fig. 8.

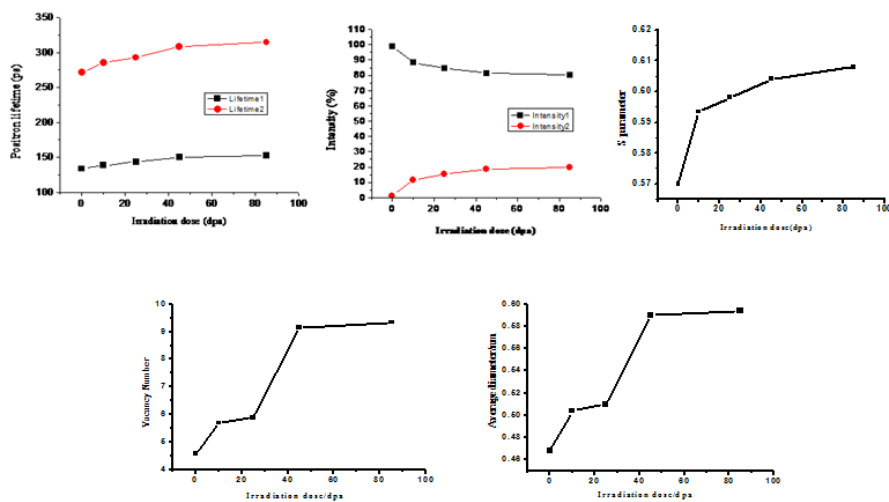


FIG.7. Dose dependences of positron lifetimes and their intensities and S parameters in CLAM.

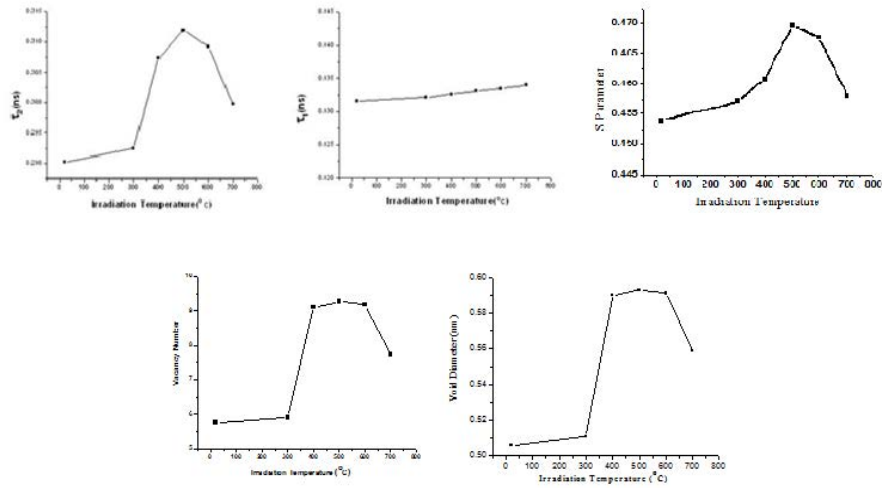


FIG.8. Irradiation temperature dependencies of positron lifetimes and S parameters in CLAM.

3.3 Triple beam irradiation of CLAM steel

The triple beam irradiations were carried out at room temperature with the triple beam irradiation facility shown in Fig. 4. The irradiation parameters are listed in Table 2. Fig. 9 shows the depth distributions of displacement for 100 keV H, 200 keV He and 70 MeV Au ions in the whole range (A) and in the range from 0 to 600 nm (B), the depth distributions of the total and respective displacements (C) and the depth distributions of the total displacement and the hydrogen and helium concentrations (D) for the irradiation fluence C. The experiment was designed to investigate the synergistic effect in the depth between 0 and 300 nm and the helium and hydrogen effects in the depth between 300 and 600 nm. The slow-positron depth profiling measurements of Doppler broadening were performed at room temperature to characterize the radiation damage produced.

The depth profiles of the S and W parameters are shown in Fig. 10 for unirradiated and simultaneously irradiated to the fluences B and C samples. Fig. 11 shows the depth profiles of the S and W parameters for the unirradiated and sequentially and simultaneously irradiated to the fluence B samples.

TABLE 2. TRIPLE BEAM IRRADIATION PARAMETERS

	Energy/keV	Irradiation fluence /cm ⁻² A	Irradiation fluence /cm ⁻² B	Irradiation fluence /cm ⁻² C
Hydrogen	100	0	2.42×10^{16}	4.84×10^{16}
Helium	200	0	7.89×10^{15}	1.66×10^{16}
Gold	70000	0	5.37×10^{13}	1.07×10^{14}

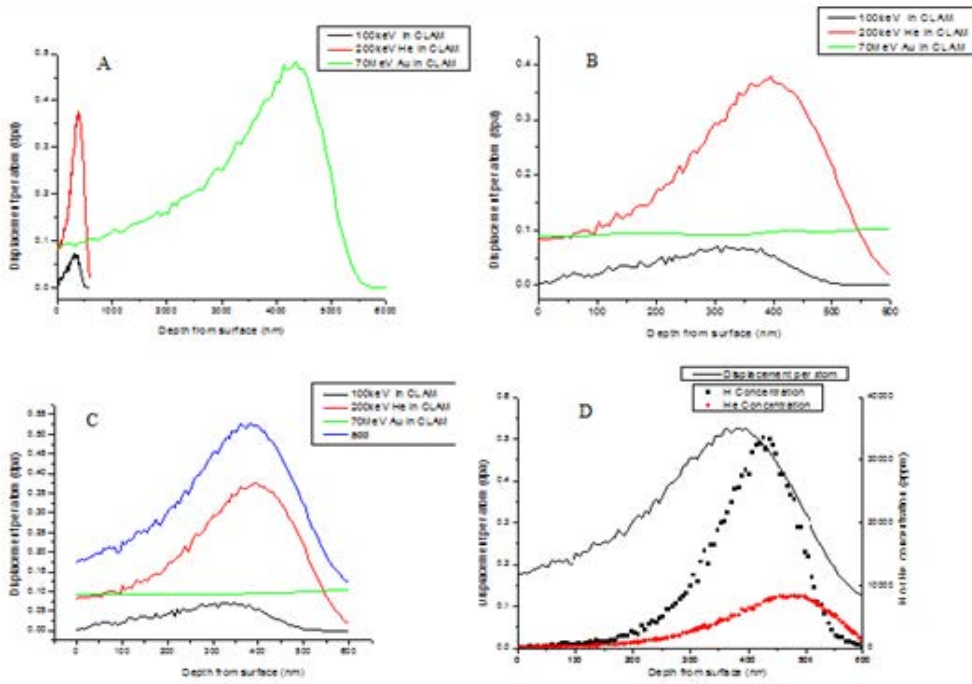


FIG. 9. Distributions of displacements and H and He concentrations for irradiation fluence C: A and B: Depth distributions of displacement for H (black), He (red) and Au (green) ions in whole range (A-till 6000 nm) and range (B-before 600 nm), C: Depth distributions of total (violet), and respective (H-black, He-red, Au-green) displacements, D: Distributions of total displacement (solid line) and H (black dots) and He (red dots) concentrations.

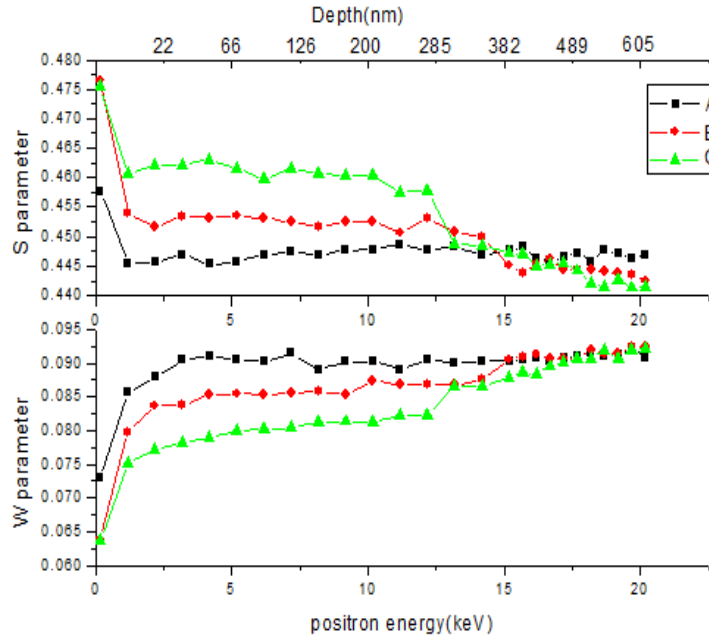


FIG. 10. Depth profiles of S and W parameters for the unirradiated (A) and simultaneously irradiated to fluences B and C samples.

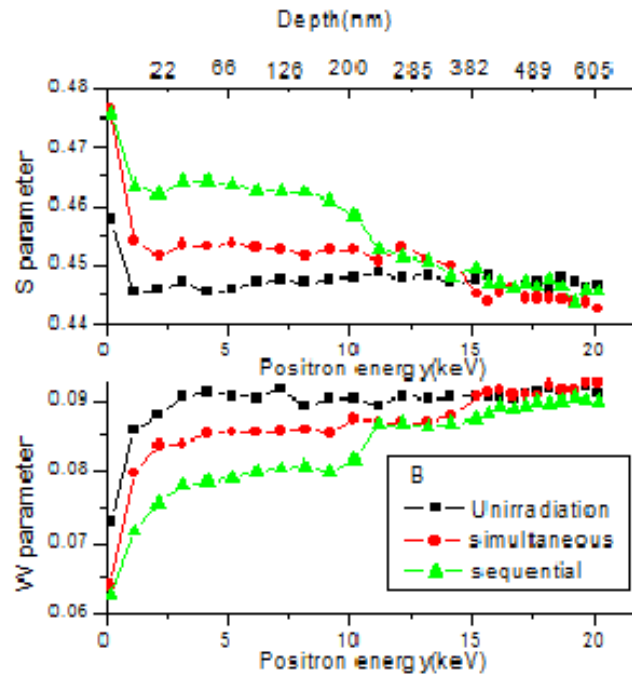


FIG. 11. Depth profiles of S and W parameters for unirradiated and sequentially and simultaneously irradiated to fluence B samples.

4. DISCUSSION

4.1 Dose and temperature dependencies of radiation damage in CLAM steel

As shown in Fig. 7, the positron lifetimes τ_1 and τ_2 , the intensity I_2 and the S parameters increase with the increasing irradiation dose. The increase of τ_1 means increasing concentrations of mono- and di-vacancies and dislocations, and the increases of τ_2 , S and I_2 illustrate that both the size and concentration of the formed vacancy clusters increase with increasing irradiation dose.

Fig. 8 exhibits a very slow increase of the lifetime τ_1 with increasing irradiation temperature and a peak-structured variation of the lifetime τ_2 and the S parameter with irradiation temperature, the peak temperature of which is at $\sim 500^\circ\text{C}$. This observed peak structure can be understood empirically. At lower temperatures the created defects are less mobile and the probability to form larger clusters is small, and at higher temperatures defect annealing occurs. Thus, there is a peak in a certain temperature between them, e.g. $\sim 500^\circ\text{C}$ for the CLAM steel.

The number of vacancies and the average diameter of the vacancy cluster can be deduced from the measured lifetime τ_2 . The obtained results are drawn in Figs 7 and 8. It can be seen that the vacancy clusters contain 9 vacancies with an average diameter of 0.60 nm at the maximum irradiation dose of 85 dpa and at the peak temperature of $\sim 500^\circ\text{C}$ and that the changes of the vacancy cluster size with irradiation temperature and dose are considerably small, giving clear evidence that the CLAM steel does have good radiation resistance.

4.2 Radiation damage induced by triple beam irradiation in CLAM steel

The triple beam irradiations of gold, hydrogen and helium generated in the CLAM steel samples produced vacancy type defects, which caused an increase of the S parameters or the decrease of the W parameters with respect to the un-irradiated sample. For the simultaneous irradiations, as shown in Fig. 10, the S parameter of the sample irradiated to the high fluence

C is greater than those of the sample irradiated to the low fluence B in the depth up to 300 nm. This indicates that the higher dose irradiations generated larger vacancy clusters, leading to the greater S parameters. This behavior is similar to that of pure heavy ion irradiation.

Fig. 11 shows the depth profiles of the S and W parameters for unirradiated and simultaneously and sequentially irradiated to the fluence B samples. The S parameters of the samples irradiated simultaneously and sequentially to the fluence B are much greater than those of the un-irradiated samples, indicating the production of vacancy clusters by both irradiations. As shown in Fig. 11, the S parameters for the simultaneous irradiation are smaller than those for the sequential irradiation in the implantation depth up to 300nm. This is due to the synergistic effect of hydrogen and helium that reduces the S parameters. The implanted helium and hydrogen atoms are mobile during the simultaneous irradiation and are subsequently trapped by vacancies. They are eventually located inside the vacancy clusters or voids [22]. The hydrogen and helium filling lowers the available positron trap volume and leads to a significant reduction of the S parameter, resulting in smaller S parameters for the simultaneous irradiation than those for the sequential irradiation. This demonstrates that the synergistic effect suppresses the radiation damage in the present case.

It can be seen from Fig. 9 that both the concentrations of helium and hydrogen peaked in the depth region between 300 nm and 600 nm. As shown in Figs 10 and 11 all the measured S parameters for both simultaneous and sequential irradiations to the irradiation fluences B and C are closed to the S parameters of the un-irradiated sample in this region. This is attributed to the helium and hydrogen effects. The concentrations of helium and hydrogen are so high that all the produced vacancy clusters or voids are filled with the hydrogen and helium. This greatly reduces the S parameters to those of the un-irradiated sample.

5. CONCLUSIONS

The CLAM steel was developed with superior physical, mechanical and radiation-resistant properties, which make it a potential candidate of structural materials for Generation IV nuclear energy facilities.

The dose and temperature dependences of radiation effects in the CLAM steel were measured, which revealed that the size of the vacancy clusters created in the CLAM steel increases with increasing irradiation dose and that the variation of the vacancy cluster size with irradiation temperature has a peak at $\sim 500^{\circ}\text{C}$. The absolute amplitudes of the vacancy cluster size changes produced in the CLAM steel with temperature and dose are relatively small, indicating the CLAM steel does have a good radiation resistance.

The simultaneous and sequential irradiations of gold, hydrogen and helium ions were performed on the CLAM steel. The slow-positron depth profiling measurements of the S and W parameters exhibit clearly the synergistic effect of displacement damage and hydrogen and helium on the formation of radiation damage, which suppresses the radiation damage in the present case. At very high concentrations of helium and hydrogen the positron annihilation Doppler broadening S parameters for the irradiated samples are reduced to those for the un-irradiated samples due to the helium and hydrogen effects i.e. the vacancy clusters or voids are filled with the hydrogen and helium.

ACKNOWLEDGEMENT

This project was supported in part by the State Major Basic Research Development Program in China under Grant No. 2007CB209900 and by National Natural Science Foundation of China under Grant No. 91126002. The support given by the IAEA under the SMoRE-CRP No. 15165/R0 is greatly acknowledged. Sincere thanks are extended to all participants within this SMoRE project for collaboration and discussions.

REFERENCES

- [1] SHAOJUN LIU, QUNYING HUANG, CHUNJING LI, et al., Fusion Engineering and Design 84(2009)1214
- [2] YANFEN LIU, QUNYING HUANG, YICANWU, et al., Fusion Engineering and Design 82(2007)2683
- [3] Q. HUANG, C. LI, Y. LI, et al., Chin. Journal of Nuclear Science& Engineering 27(2007)41
- [4] Y. XIN, J. QIU, X. JIA, et al., Nuclear Instrument & Methods B 267 (2009) 3166
- [5] Q.Y. HUANG, Y.C. WU, J.G. LI, et al., Journal of Nuclear Materials, 386–388(2009)400
- [6] ZHU SHENGYUN, ZHENG YONGNAN, POLAT AHMAT, et al., J. of Nuclear Materials 343 (2005)325
- [7] YONGNAN ZHENG, YI ZUO, YONGJUN XU, et al., Problems of Atomic Science and Technology, 2009, 4 August 89–96
- [8] YONGNAN ZHENG, YI ZUO, DAQING YUAN, et al., Nuclear Physics A, 834 (2010) 761
- [9] S. ZHU, T. IWATA, Y. XU, et al., Modern Physics Letters B18(2004)881
- [10] M.J. FLUSS, LLNL-CONF-415877
- [11] A. MÖSLANG, Workshop Proc., vol. 2007, OECD Nuclear Energy Agency, Germany, 2007.
- [12] M. ANDO, E. WAKAI, T. SAWAI, et al., Nuclear Instruments and Methods B **266** (2008) 3178.
- [13] H. TANIGAWA, K. FURUYA, S. JITSUKAWA, et al., Journal of Nuclear Materials, **329** (2004) 1137.
- [14] E. WAKAI, M. ANDO, T. SAWAI, et al., Journal of Nuclear Materials, **356** (2006) 95.
- [15] K. KIKUCHI, K. FURUYA, M. SATO, et al., Journal of Nuclear Materials, 307–**311** (2002) 278.
- [16] CHEN LIHUA, CUI BAOQUN MA RUIGANG, et al, Nuclear Technique **33** (2010)1 in Chinese.
- [17] S. ZHU, Y. XU, Z. WANG, et al., Journal of Nuclear Materials **343** (2005) 330.
- [18] H. SAITO, Y. NAGASHIMA, T. KURIHARA AND T. HYODO, Nucl. Instr. Meth. **A487** (2002) 612.
- [19] YI ZUO, DAQING YUAN, YONGNAN ZHENG, et al., Nuclear Physics A, **834** (2010) 767.
- [20] S. VAN PETEGEM, B. VAN WAEYENBERGE, D. SEGERS, et al., Nucl. Instr. Meth. **A513**(2003) 622.
- [21] BAOYI WANG, XINGZHONG CAO. RUNSHENG YU, et al., Mat. Sci. Forum 445–4 **46** (2004) 513
- [22] X. H. RAJAINMAKI, S. LINDEROTH, H.E. HANSEN, et al, Phys. Rev. **38** (1988) 1087.

SYNERGISTIC EFFECTS ON SWELLING IN MODEL FERRITIC STEELS UNDER HIGH-DOSE IRRADIATION

A. BARBU¹, L. BECK¹, E. BORDAS¹, D. BRIMBAL¹, B. DÉCAMPS², C. C. FU¹, J. HENRY¹, H. MARTIN¹, E. MARTINEZ¹, E. MESLIN¹, S. MIRO¹, Y. SERRUYS¹, P. TROCELLIER¹, F. WILLAIME¹

¹ CEA, Nuclear Energy Division (DEN), Department of Materials for Nuclear Energy (DMN), F-91191 Gif-sur-Yvette, France

² Centre de Spectrométrie Nucléaire et de Spectrométrie de Masses (CSNSM/IN2P3/CNRS), Orsay University, Orsay, France

Abstract

The capabilities of the Jannus facility are presented, along with some recent representative experimental results. A brief review is also presented of supporting modelling efforts.

1. BACKGROUND

The work performed by CEA (France) in the framework of the SMoRE Coordinated Research Project (CRP) concerns model ferritic steels under irradiation. It is based on the one hand on irradiations using the Jannus multiple ion-beam irradiation facility, and subsequent structural characterization of ferritic steels (ranging from pure Fe to oxide dispersion-strengthened (ODS) ferritic steels) and on the other hand on the multi-scale modelling of Fe and model Fe-Cr alloys using *ab initio* methods and kinetic models.

2. RESULTS

2.1 Experiment

2.1.1 The Jannus facility [1,2]

The JANNUS multi-ion beam irradiation platform is a joint project between the French Atomic Energy and Alternative Energies Commission (CEA) through the Nuclear Energy Direction (DEN) and the National Institute for Nuclear Science and Technology (INSTN) at Saclay, the National Center for Scientific Research (CNRS) through the Nuclear Spectrometry and Mass Spectrometry (CSNSM) and Paris-Sud University at Orsay. The JANNUS platform includes two sites. At CSNSM Orsay, a 200 kV TEM is coupled with two ion accelerators for in-situ observation of the modifications of material microstructure and properties induced by ion irradiation (see Fig. 1).

At CEA Saclay, a triple beam facility was designed mainly for the simultaneous production by ion beams of nuclear recoil damage and concomitant generation of nuclear reaction products (see Fig. 2). Two accelerators were already available at the beginning of the SMoRE CRP: a 3 MV Pelletron with ECR source and a 2.5 MV Van de Graaff accelerator. A new 2 MV tandem accelerator was installed at the end of 2009 (see Fig. 3). It is equipped with a SNICS II (Source of Negative Ions by Cesium Sputtering). The overall JANNUS design allows a large range of irradiation, implantation, in situ TEM and ion beam analysis conditions and of dual or triple beam combinations.

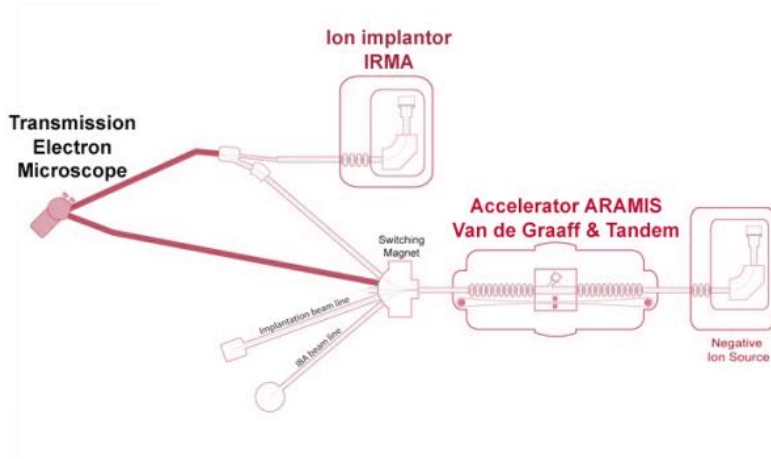


FIG. 1. Schematic representation of the Jannus-Orsay facility, located at Orsay and managed by the "Centre de Spectrométrie Nucléaire et de Spectrométrie de Masse" (CSNSM) belonging to CNRS-IN2P3-Université Paris-Sud 11. The facility couples a 2 MV Tandem accelerator (ARAMIS) and a 190 kV ion implanter (IRMA) to a 200 kV Transmission Electron Microscope (TEM FEI Tecnai G² 20).

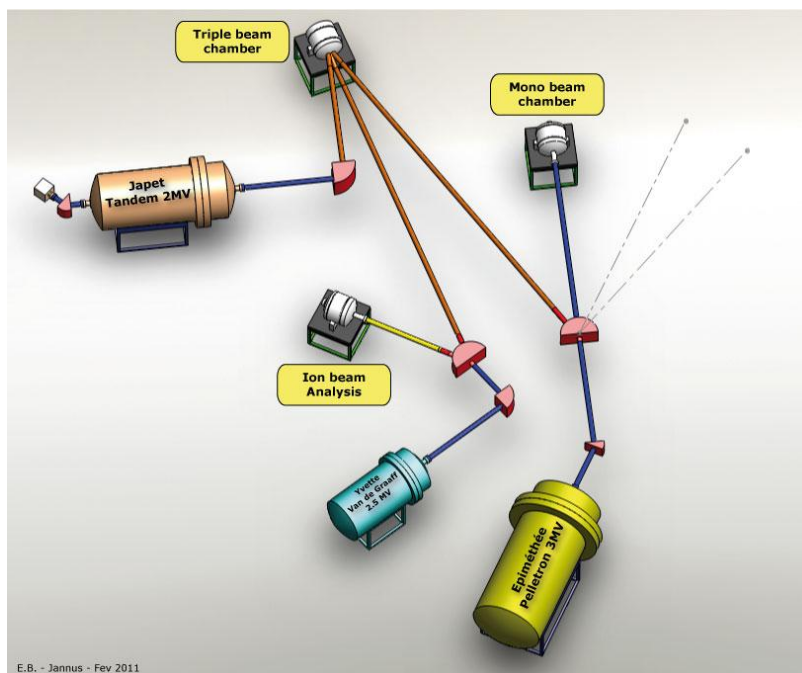


FIG. 2. Schematic representation of the Jannus-Saclay facility. This facility is managed by the "Service de Recherches de Métallurgie Physique" (SRMP) from the Nuclear Energy Division of the CEA. It couples a 3 MV Pelletron accelerator (ÉPIMÉTHÉE) equipped with a multi-charged ECR ion source and a 2.5 MV single ended Van de Graaff accelerator (YVETTE) managed by the Institut National des Sciences et Techniques Nucléaires (INSTN). A third ion accelerator, JAPET (2 MV tandem) was connected to the previous ones in 2009.



FIG. 3. Picture of the third ion accelerator, JAPET (2 MV tandem) installed in the Jannus-Saclay facility in Nov. 2009.

Calls for proposals of experiments on this facility have been issued every year since Dec. 2008. As shown in Fig. 4, in the period covered by the present CRP, the number of operating days has increased greatly. The Jannus-Saclay facility has greatly benefited, firstly from the technical point of view, from exchanges with Michael Fluss and his collaborators from Lawrence Livermore National Laboratory (LLNL) and in particular Scott Tumey in the framework of this CRP. It is indeed with these collaborators, that a number of "premieres" were achieved. One can mention in particular: the first use of degrader foils to obtain homogeneous implantation profiles, the first use of an optical pyrometer to measure the temperature at the surface of the specimen during irradiation, improvements in the regulation of the temperature, etc. These technical improvements have allowed performing the first dual beam irradiation and the second triple beam irradiation, as well as a series of other irradiations on Fe(Cr) alloy and ODS steel. These samples included ODS steels from Prof. A. Kimura (Institute of Advanced Energy, Kyoto University, Gokasho, Japan) also obtained in the framework of this CRP. Extensive TEM characterizations were performed by Luke L. Hsiung from LLNL using a Phillips CM300 field-emission transmission electron microscope (accelerating voltage of 300 kV). The results are described in the LLNL report. They have been the object of two papers [3, 4].

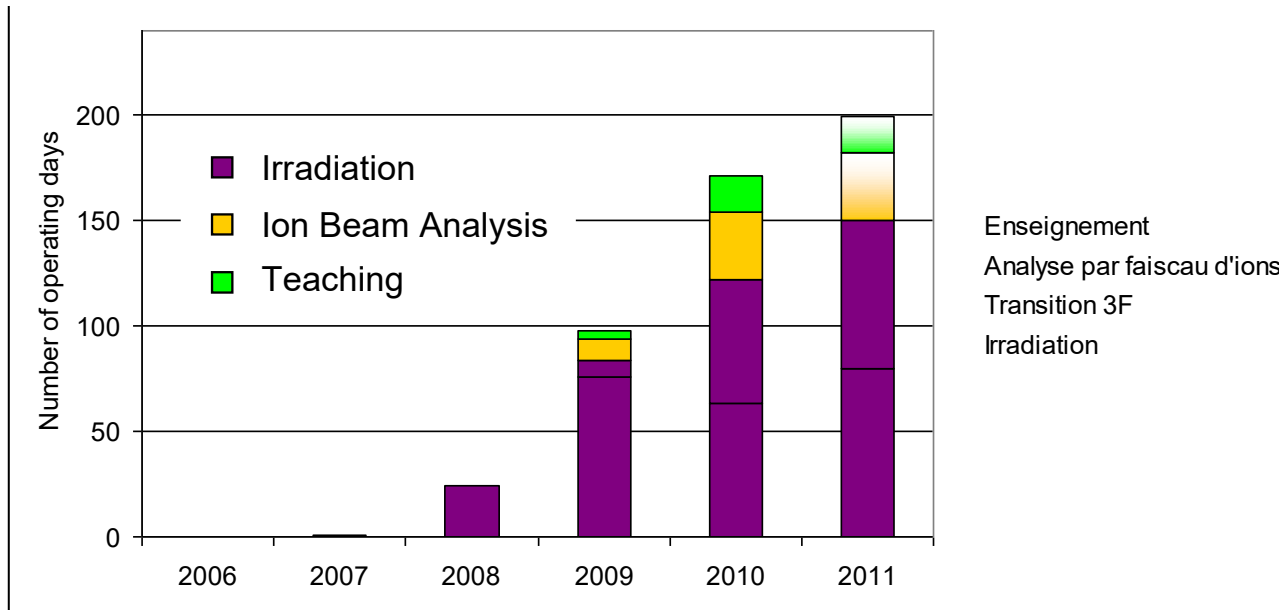


FIG. 4. Evolution of the number of operating days per year at the Jannus-Saclay facility (based on an extrapolation for 2011).

2.1.2. Dual-beam irradiation of α -iron: Heterogeneous bubble formation on dislocation loops

In order to study the effect of helium on the evolution of the microstructure during the irradiation, the Jannus-Orsay platform has been used. This new installation enables the dual beam irradiation of transmission electron microscopy (TEM) samples inside a microscope, a FEI TECNAI G2 20 Twin. Helium implantation and heavy-ion irradiation are performed simultaneously. This special configuration allowed us to discover a peculiar correlation between helium bubbles and dislocation loops which to our knowledge has not been observed previously [5].

The high purity iron used for these experiments was fabricated at the ‘Ecole des Mines de Saint-Etienne’. The average grain size in the as-received material was 180 μm , and the dislocation density was $10^{12}/\text{m}^2$. Slices 1 mm thick were cut from the as-received bars. These slices were then polished mechanically to 90 μm . Discs with a diameter of 3 mm were then punched out from the slices. Finally, samples were electro-polished in a Tenupol 5 with a 5% perchloric acid- 95% methanol electrolyte, at 40°C in order to produce thin foils suitable for TEM investigations.

For the helium implantation, 15 keV He^+ ions were used, and the damage cascades were created with 1 MeV Fe^+ ions. The two ion beams struck the sample surface with an incidence of about 45°, and the angle between the two beams was 45°. During dual beam irradiations, it was not possible to continuously film the evolution of the microstructure, because the 15 keV He^+ beam would be deviated if the objective lens was turned on. So the microstructure was examined at a dose of $1.1 \cdot 10^{18} \text{ Fe}^+/\text{m}^2$ (0.3 dpa) and $1.9 \cdot 10^{18} \text{ He}^+/\text{m}^2$ (180 appm He) and at the final dose, $3.1 \cdot 10^{18} \text{ Fe}^+/\text{m}^2$ (0.92 dpa) and $6.9 \cdot 10^{18} \text{ He}^+/\text{m}^2$ (540 appm He). The irradiations were performed at 500°C and the observations at 25°C. The maximum irradiation dose reached was 0.92 dpa, according to SRIM (Stopping and Ranges of Ions) calculations (taking $E_d = 40 \text{ eV}$ for the threshold displacement energy for iron), with helium content at the end of the irradiation of 540 appm. The damage rate was close to $3.4 \cdot 10^{-4} \text{ dpa/s}$, and the helium implantation rate was close to 0.2 appm He/s, these are the average values of the distributions shown in Fig. 5. The average is taken between 0 and 160 nm, since the specimen is 160 nm wide.

The high implantation value was chosen in order to understand the mechanisms. It was not determined whether the objects were bubbles or cavities (i.e. we did not attempt to determine the He content inside them), but for clarity we shall call them bubbles. Special imaging conditions have been used to obtain clear images of bubbles associated to dislocations. Generally, the specimen is oriented far from any Bragg condition and extensive through-focus series are taken to reveal the presence of bubbles. In our case, Bragg conditions are closer in order to visualize contrast from dislocations. For negative defocus (under focus of the objective lens), bubbles appear as white dots surrounded by a dark fringe while for positive defocus (over focus), the dots are dark and the fringe is white. The size of the bubbles may be estimated by measuring the size of the dots in the through-focus series.

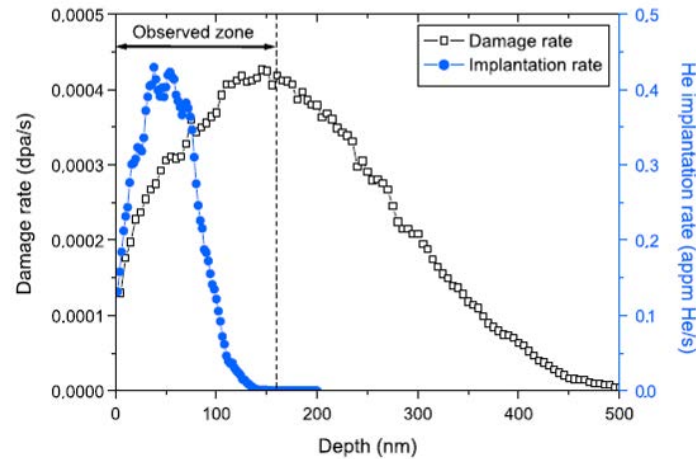


FIG. 5. Damage rate and implantation rate variations throughout the specimen thickness, according to SRIM.

After dual beam irradiation to 0.3 dpa (180 appm He), dislocation loops were present homogeneously throughout the foil, with a density of $5.5 \pm 0.3 \cdot 10^{20} \text{ m}^{-3}$. The average size of the loops was 32 nm. No bubbles were detected at this dose. Once the higher damage level (0.92 dpa and 540 appm He) was reached, even larger dislocation loops (average size: 75 nm) were observed throughout the specimen, with a density of $7.3 \pm 0.6 \cdot 10^{20} \text{ m}^{-3}$. Most dislocation loops have $\langle 100 \rangle$ type Burgers vectors and are situated in $\{100\}$ type planes. By imaging the dislocation loops alternately in and out of focus, it was discovered that small bubbles (average size: 5.0 nm) are present heterogeneously in the matrix: they are mostly situated inside dislocation loops (Fig. 6). Smaller bubbles are located close to or on the dislocation cores. Very few bubbles are located in the matrix outside the dislocation loops. However, since some loops may be invisible it is not clear whether these bubbles are situated in dislocation loops or not. Bubbles of similar sizes are also located on grain boundaries. The images are taken near a $\{131\}$ pole, for $sg > 0$ and with $\langle 110 \rangle$ diffraction vector.

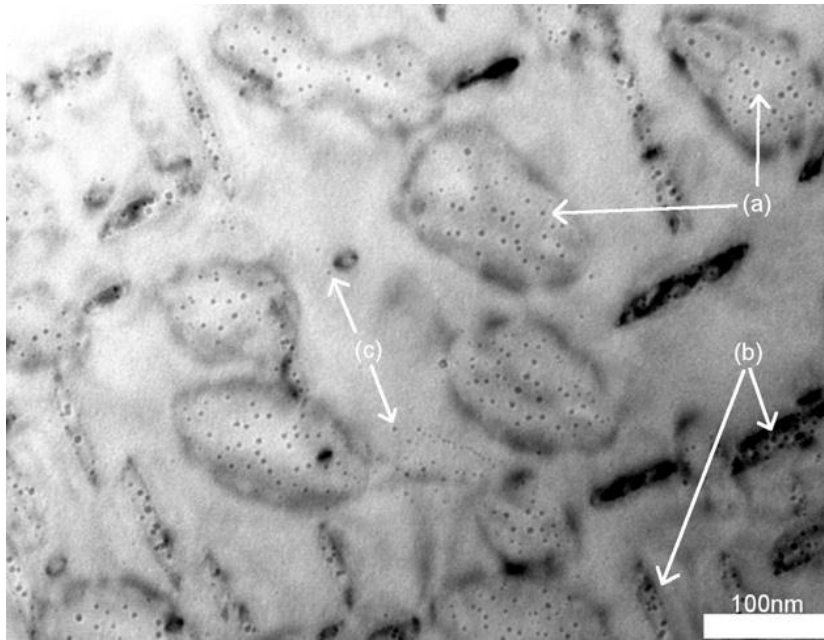


FIG. 6. Bubbles and dislocation loops in α -Fe irradiated at 500°C to 0.92 dpa and 540 appm He .

The Jannus-Saclay facility has greatly benefited, firstly from the technical point of view, from exchanges with Michael Fluss and his collaborators from LLNL and in particular Scott Tumey in the framework of this CRP. It is indeed with these collaborators, that a number of "premieres, were achieved. One can mention in particular: the first use of degrader foils to obtain homogeneous implantation profiles, the first use of an optical pyrometer to measure the temperature at the surface of the specimen during irradiation, improvements in the regulation of the temperature, etc. These technical improvements have allowed performing the first dual beam irradiation and the second triple beam irradiation, as well as a series of other irradiations on Fe(Cr) alloy and ODS steel. These samples included ODS steels from Prof. A. Kimura (Institute of Advanced Energy, Kyoto University, Gokasho, Japan) also obtained in the framework of this CRP. Extensive TEM characterizations were performed by Luke L. Hsiung from LLNL using a Phillips CM300 field-emission transmission electron microscope (accelerating voltage of 300 kV). The interpretation of the results have benefited from interaction The results are described in the LLNL report. They have been the object of two papers [4, 5].

2.1.3. First triple beam irradiation

The first triple beam irradiation in the Jannus-Saclay facility was successfully performed in March 2010 on a Fe-12Cr model alloy and its ODS analogue (0.3% Y₂O₃) at room temperature. The following beams were employed: ⁵⁶Fe⁸⁺ at 24 MeV, ⁴He⁺ at 1.9 MeV and a proton beam at 600 keV. The irradiation dose was 7 dpa for an helium concentration of 100 appm/dpa and an H/He ratio of 4. Fig. 7 shows the superposition of the profiles of radiation damage, and He, H and Fe implantation. The post-irradiation characterizations are still in progress.

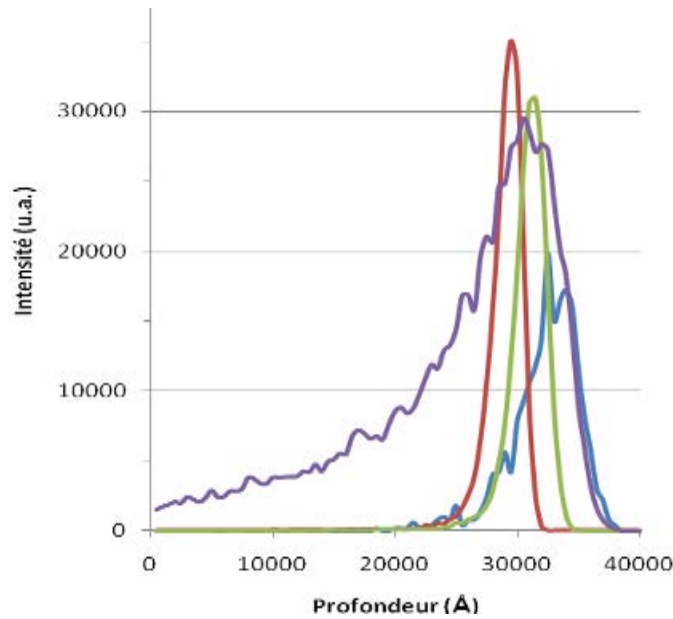


FIG. 7. Superposition of the profiles of implantation of He (in red), H (in green), and Fe (in blue) and vacancy distribution (in purple) created by the Fe ions in the Fe-12Cr ODS steel.

3. MODELLING

We have performed density functional theory calculations to study the effect of Cr on the formation of He-vacancy (He_nV_m) clusters in a dilute FeCr system. The calculations were performed using the SIESTA code. All the calculations are spin polarized, and they include the recent implementation of noncollinear magnetism. Spin-orbit coupling effects are not considered. All the results were obtained using the generalized gradient approximation (GGA) exchange-correlation functional in the Perdew-Burke-Ernzerhof (PBE). Complementary GGA calculations have also been carried out using more robust DFT implementations involving planewave basis sets, for validation for some of the relevant cases. We used the PWSCF code using the projector augmented wave (PAW) potential.

We have compared the formation energies of vacancies, substitutional Helium, He_{sub} , interstitial Helium at tetrahedral and octahedral sites, He_{tet} and He_{oct} , in Fe and Cr and observe a remarkable difference between them. These results led us to hypothesize that there would be an effect of Cr in He accumulation. To check the hypothesis of the Cr effect on Fe we have started performing calculations in dilute alloys in which we have studied the variation of He properties close to a Cr atom. In the case of He_{sub} we observe, as happens with vacancies, a weak attraction with a Cr atom. The relaxation volume in both cases is small. On the other hand, Cr repels both He_{tet} and He_{oct} .

In our calculations the He atom in an octahedral site becomes unstable near a Cr atom falling to a tetrahedral site without any barrier. A Cr atom is ejected from its lattice site, creating a Frenkel pair, when a cluster with 5 helium atoms agglomerates around it (see Fig. 8). The binding energy between an interstitial Cr and a He_5V cluster is 0.28 eV which would lead to the decoration of these clusters. On the other hand, the dissociation energies of He or V from He_nV_m complexes do not change significantly with respect to the pure Fe case, with a crossover around $n/m \approx 1.3$.

Fitting functions can be used in mesoscale calculations such as object kinetic Monte Carlo or rate theory models. Studies with several Cr atoms have been carried out. In substitutional sites, helium seems to screen the Cr-Cr repulsion. We have found several configurations in

which Cr atoms preferred to cluster at a 3nn distance of each other around the He_nV_n complexes rather than being far apart in the matrix. On the other hand, when the cluster is formed by interstitial He, the Cr atoms are always strongly repelled.

These data suggest the existence of two different regimes depending on the He-V ratio. When He atoms are mostly interstitials (high n/m ratio), bubbles will mostly form far from the Cr atoms due to the Cr-He_{int} repulsion while when the n/m ratio is low (mostly substitutional He), the V-Cr attraction may prevail inducing the formation of He_nV_m clusters close to Cr atoms. For this last case-scenario, the binding energies are small and therefore we expect this effect to decrease as temperature increases.

We have studied the diffusion paths for He_{tet} and He_{sub} close to a Cr atom. Concerning the migration of a He_{tet} the main result is the difference in the energy barrier for this species to jump close to a Cr atom, the highest value being 0.12 eV when moving from the 2nn to the 1nn of Cr, while in pure Fe the energy barrier is around 0.06 eV. For substitutional He there exist two main diffusion mechanisms, the dissociative mechanism and the vacancy mechanism. We have found that the diffusion properties of the dissociative mechanism are slightly modified by the presence of Cr.

We have obtained a value for the dissociation energy of a substitutional He into a He_{tet} and a V of 2.45 eV when the original substitutional He is at a 1nn site of Cr, which compared to the 2.36 eV value in pure Fe indicates that there is a lower probability of this mechanism to take place in the presence of Cr. We have also analyzed the vacancy mechanism.

We have studied the most stable configurations for the HeV_2 complex nearby a Cr and calculated the energy landscape of the different pathways. These most stable configurations are the ones with the vacancies at a 1nn distance which have a binding energy V- He_{sub} of 0.71 eV, while in pure Fe the value is 0.78 eV. At a 2nn the binding energy becomes 0.28 eV and it is negligible beyond that distance. A weak trapping effect of the HeV_2 cluster by the Cr is observed since there are barriers around a Cr atom which are lower than in pure Fe (1.08 eV) and lower than the exiting paths (1.14–1.25 eV).

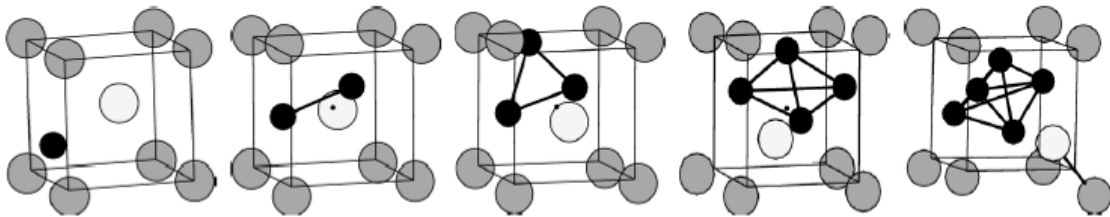


FIG. 8. Relaxed configurations of interstitial He_n clusters close to a Cr atom containing 1, 2, 3, 4 and 5 He_{int} atoms. Fe atoms in grey, He atoms in black and Cr atoms in white.

4. DISCUSSION

4.1. Dual-beam irradiation of α -iron: Heterogeneous bubble formation on dislocation loops

It is well known that at high temperatures, helium bubbles nucleate at interfaces and dislocations. However, most previous experiments with high appm He/dpa ratios were performed on industrial steels, presenting a complex microstructure prior to irradiation. A good example is the implantation of 23 MeV alpha particles at 550°C up to 0.5 at.% He in two martensitic steels by Henry et al.. In this experiment, bubbles appeared on the various defects present: prior austenitic grain boundaries, lath boundaries, dislocations, and carbide–

matrix interfaces. In one irradiation of pure iron, Arakawa et al. have noticed the presence of a few cavities in the vicinity of dislocation loops.

Theoretical calculations justify the fact that helium is trapped at the dislocation loop cores, that interstitial helium atoms are mobile along dislocation cores, and that helium clusters or helium-vacancy clusters may nucleate near the cores of dislocation loops. We have observed that bubbles are located on the dislocation lines but also on the full disc constitutive of the loops. This and the previously mentioned theoretical results suggest the following mechanism: (i) helium atoms are trapped at the dislocation core, (ii) the mobility of the trapped helium atom in the dislocation core results in the nucleation of small helium clusters, (iii) the dislocation loops grow by preferential absorption of self-interstitial atoms and leave the clusters behind them, (iv) these clusters are stable as helium is highly insoluble in iron as in most metals, and grow by absorption of vacancies and helium atoms.

The last step in the process (iv) is of course justified by the fact that vacancy and interstitial helium binding energies to helium-vacancy clusters are positive, according to *ab initio* and molecular dynamics calculations. The proposed mechanism is consistent with the fact that the bubbles observed near the dislocation loop lines are smaller than the bubbles observed inside the dislocation loop.

We have performed a dual beam irradiation of high purity iron in the new Jannus facility at 500°C. The high helium implantation rate has caused the nucleation and growth of helium bubbles inside dislocations loops. These experiments have given us more insight into the mechanisms at work in iron when helium and damage cascades are both present.

4.2 Cr interactions with He and vacancies in dilute FeCr alloys from first principles

According to the present DFT results, the presence of Cr does not seem to much modify the dynamics of bubble formation in an α -Fe matrix [6]. However, this statement will have to be confirmed by performing larger scale calculations that may use the results of this study as fitting parameters for the chosen model.

5. CONCLUSIONS

The Jannus-Orsay and Jannus-Saclay facilities are now fully in operation. During this CRP, the first dual-beam irradiation (He+Fe) with *in situ* TEM observation was performed at Jannus-Orsay, and the first triple beam (He+H+Fe) was performed at Jannus-Saclay. The *in situ* or *post-mortem* TEM observations of He bubble formation in a series of ferrite-type materials (ranging from pure Fe to Fe-Cr alloys, and ferritic ODS steels) has provided further insight into the fate of helium in these materials.

Density Functional Theory methods are very powerful tools to generate predictive atomic-scale data on the energetics of He in Fe-Cr dilute alloys. These data, which cannot be deduced from experiments, are the basis of a multi-scale approach to predict the fate of He in Fe-Cr ferritic materials. The issue of ODS-steels has not been addressed yet because of the difficulty to model within DFT the details of yttrium-titanium oxide nano-precipitates.

REFERENCES

- [1] Y. SERRUYS et al., "JANNUS: experimental validation at the scale of atomic modelling", C. R. Physique **9** (2008) 437–444.
- [2] Y. SERRUYS et al., "JANNUS: A multi-irradiation platform for experimental validation at the scale of the atomistic modeling", J. Nucl. Mater. **386–388**, pp. 967–970, (30 April 2009).

- [3] L. HSIUNG , M. FLUSS, S. TUMEY, J. KUNTZ, B. EL-DASHER, M. WALL, B. CHOI, A. KIMURA, F. WILLAIME, Y. SERRUYS, "HRTEM study of oxide nanoparticles in K3-ODS ferritic steel developed for radiation tolerance", *Journal of Nuclear Materials* **409** (2011) 72–79.
- [4] L. HSIUNG, M. FLUSS, S. TUMEY, B. CHOI, Y. SERRUYS, F. WILLIAMS, AND A. KIMURA, "Formation mechanism and the role of nanoparticles in Fe-Cr ODS steels developed for radiation tolerance," *Phys. Rev., B* **82**,184130, (2010).
- [5] D. BRIMBAL, B. DÉCAMPS, A. BARBU, E. MESLIN, J. HENRY, "Dual-beam irradiation of α -iron; Heterogeneous bubble formation on dislocation loops", *Journal of Nuclear Materials* **418** (2011) 313–315.
- [6] E. MARTINEZ and C. C. FU, "Cr interactions with He and vacancies in dilute FeCr alloys from first principles", *Phys. Rev. B* **84**, 014203 (2011).

MULTISCALE MODELLING OF MECHANICAL BEHAVIOUR OF FE-CR ALLOYS: FROM THE ATOMIC TO THE CONTINUUM LEVEL

G. MONNET
EDF – R&D, MMC
Avenue des Renardières, 77818 Moret-sur-Loing,
France

D. TARENTYEV
SCK-CEN, Nuclear Material Science Institute
Boeretang 200, B-2400 Mol,
Belgium

Abstract

In this paper, we report results of a multiscale modelling of mechanical properties of Fe-Cr alloys starting from the atomistic and ending with the continuum level approach. The multiscale modelling scheme aims at the construction of a complete characterization of the material's behaviour in order to establish a crystalline law accounting for the available physical data. Firstly, Molecular Dynamics (MD) simulations were used to investigate the dislocation motion in Fe-Cr solid solution varying Cr content. These simulations enable the determination of the critical stress for the motion of a dislocation as a function of Cr content and temperature. Secondly, the interaction of dislocations with Cr precipitates, induced by irradiation at elevated temperature, is studied by MD and Dislocation Dynamics (DD) simulations. The applied multiscale simulation approach allowed for MD results to be used directly in DD simulations to predict the corresponding strengthening in the range of experimental strain rates. We show how MD output can be used to determine (i) the absolute resistance of a Cr precipitate as a function of its size and (ii) the thermal activation parameters enabling the introduction of temperature effects on dislocation unpinning. These results are then used in DD simulations to compute the strengthening associated with a random array of Cr precipitates. Results show a strong effect of temperature and spatial distribution on the strengthening induced by Cr precipitates.

1. INTRODUCTION

Fe-Cr based steels are expected to play an important role in the next nuclear power plant generation. The mechanical behaviour is complex and it essentially depends on the content of major alloying elements [1]. In addition, the microstructure is found to evolve strongly under irradiation [2, 3]: decomposition into Fe-rich and Cr-rich phase (α') [4], large density of dislocation loops, decoration of radiation defects by Cr, etc. To rationalize the impact of Cr content, binary Fe-Cr alloys were developed, irradiated and characterized. Their microstructure and mechanical behaviour were reported in a number of experimental investigations [5]. But the origin of the radiation induced strengthening remains a challenge for the scientific community.

In this paper we propose a multiscale approach for modelling and simulating the mechanical behaviour of Fe-Cr alloys from the atomic to the continuum level. In the following section, we present atomic simulations including Molecular Statics (MS) and Molecular Dynamics (MD) results. In Section 3, we analyse MS and MD results in view of the determination of relevant parameters for the continuum scale approach. In Section 4, we show how these parameters can be applied in Dislocation Dynamics (DD) simulations for the determination of the strengthening associated with the Cr precipitates. Finally, we draw conclusions.

2. ATOMIC SIMULATIONS

2.1 MD simulations

To study the movement of dislocations in Fe-Cr alloys we apply the model developed by Osetsky and Bacon [6]. The principal axes x , y and z of the simulated body-centred cubic crystal were oriented along the [111], [112] and [110] directions, respectively. The initially straight edge dislocation with slip plane x - y was created along the y direction and had Burgers vector $\mathbf{b} = \frac{1}{2}[111]$ parallel to the x axis. Periodic boundary conditions were applied along the x and y directions. A glide force on the dislocation was generated by the relative displacement of the rigid blocks in the x direction, which corresponds to simple shear strain ε_{xz} . The

corresponding resolved shear stress induced by the applied deformation was calculated as $\tau_{xz} = F_x/A_{xy}$, where F_x is the total force in the x direction and A_{xy} is the xy cross-section area of the box. Static calculations were performed using a combination of conjugate gradient and quasi-dynamic relaxation algorithms to achieve a convergence of the forces lower than 0.001 eV/Å.

The interatomic potential for bcc Fe-Cr developed by Bonny et al. [7, 8] was used. The integration of Newton's equations was performed using the velocity Verlet scheme at constant time step varying from 0.5 to 2 fs, depending on temperature. All calculations were done in the microcanonical (NVE) ensemble. No additional temperature control was applied, for the temperature increase over the simulation time was negligible.

2.2 Movement of a $\frac{1}{2}\langle 111 \rangle\{110\}$ edge dislocation in random Fe-xCr alloys at 0 K

A set of static calculations was performed to reveal the minimum size (i.e. dislocation length) of the system at which the critical stress for the dislocation to move does not vary significantly depending on the geometrical parameters of the simulation crystal. It was found that the response of the stress on the applied strain does not vary anymore if the height of the box (Z period) exceeds ~ 10 nm and spacing between periodically repeated dislocation lines (X period) is longer than 12.5nm. We therefore fixed these sizes and vary only dislocation length. A set of simulations where the dislocation length (L_D) was varied from 10 up to 42nm has shown that the maximum critical stress (τ_C) measured after the dislocation has passed a substantial distance saturates for $L_D \sim 20$ nm. A comparison of the stress-strain response (henceforth τ - γ) in Fe – 5 and 10% Cr alloys for the dislocations with $L_D=21$ and 42nm is shown in Fig. 1 a and b, respectively. For both dislocation sizes, the critical stress τ_c for the 5% and the 10% Cr alloys is found to be close to 150 MPa and 225 MPa, respectively. Thus, the parametric study has been performed in the crystals with $L_D = 21$ nm, $L_X = 12.5$ nm and $H_Z=10$ nm.

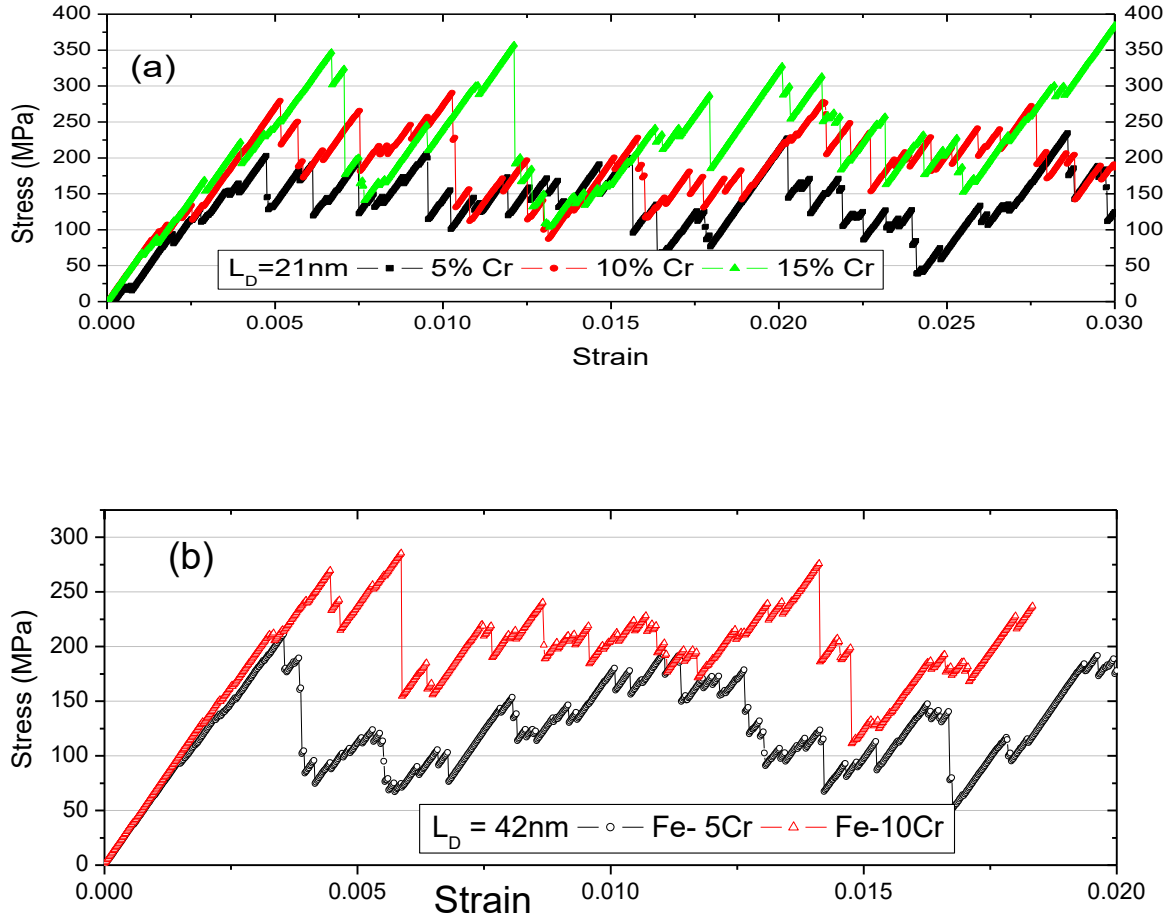


FIG. 1. Stress-strain plot for the dislocation with (a) $L_D = 21\text{nm}$ and (b) $L_D = 42\text{nm}$ in the Fe-5Cr and Fe-10Cr crystals, calculated at $T=0\text{ K}$.

The effect of temperature on the τ - γ response of the dislocation loaded at various temperatures is presented in Fig. 2. The loading rate in all simulation was $\dot{\gamma}=10^7\text{ s}^{-1}$. In all cases, it can be seen that, with increasing T , the flow stress (τ_c) decreases down to about 50–100 MPa depending on Cr content. In simulations at $T=100\text{ K}$ and 300 K most of the peaks, seen in statics (i.e. at 0 K), are reproduced with a lower amplitude. At $T=600\text{ K}$, on the other hand, a number of peaks vanish suggesting that some configurations contributing at low temperature do not offer any resistance at $T=600\text{ K}$ and above.

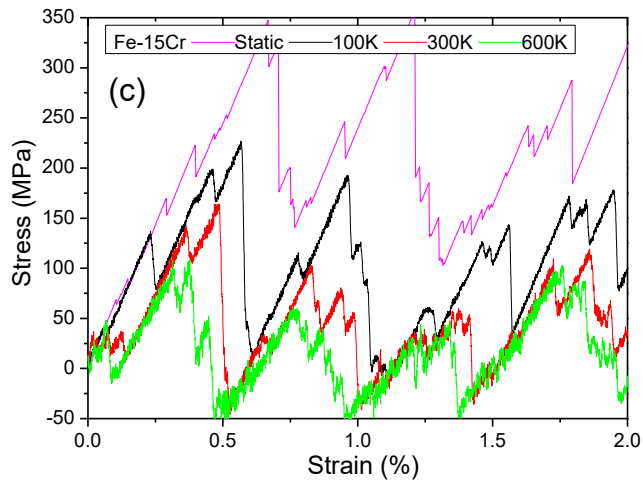
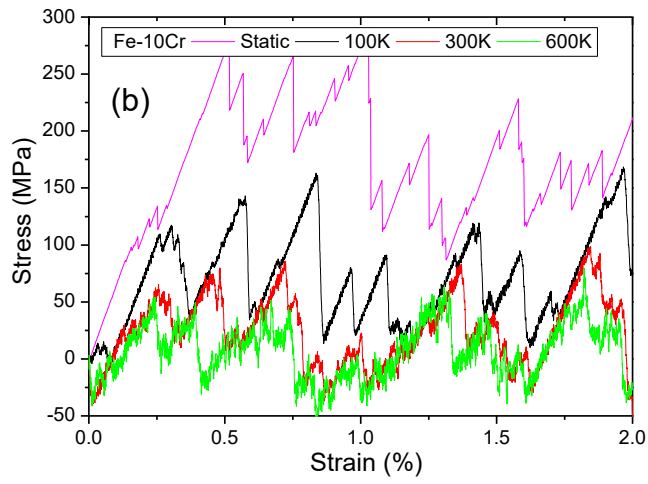
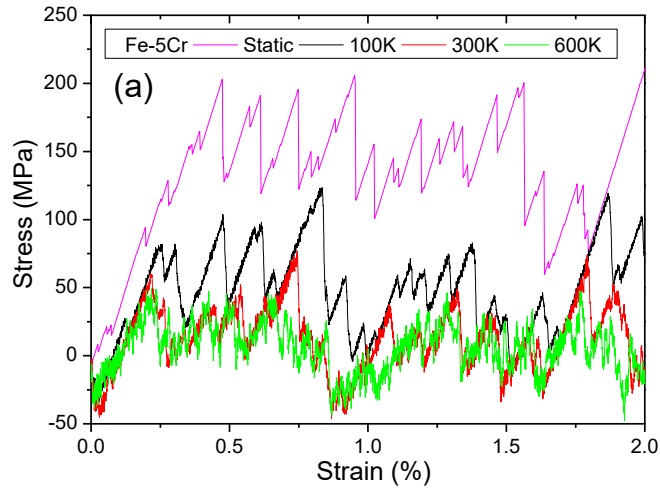


FIG. 2. Stress-strain plot for the dislocation with $L_D = 21$ nm in Fe-Cr alloys containing (a) 5%Cr, (b) 10%Cr and (c) 15%Cr, calculated at $T=0, 100, 300$ and 600 K.

2.3 Interaction of a dislocation with Cr precipitates

The interaction of the edge dislocation with pure Cr precipitates was simulated at different temperatures [9]. The sample is first relaxed by minimizing its energy using the conjugated gradient method at constant volume. The relaxed structure is then thermalized for 2 ps and after that shear deformation is applied. To model deformation, the shear stress resulting from an imposed shear strain at a constant rate is calculated at each time step from the internal force acting on atoms in the upper region of the sample. The imposed strain rate is $1 \times 10^7 \text{ s}^{-1}$.

The critical stress τ_c corresponding to the dislocation release, was determined by checking the obtained $\tau-\gamma$ curve at the unpinning moment, revealed by means of dislocation core visualization tools.

The following general interaction mechanism was revealed in the simulations: (i) initially, the dislocation was repelled by the precipitate; (ii) under increasing τ , it bowed around the precipitate and (iii) finally cut it, so τ_c was reached just before the dislocation entered the precipitate. As soon as the dislocation enters the precipitate, it is pinched off almost immediately.

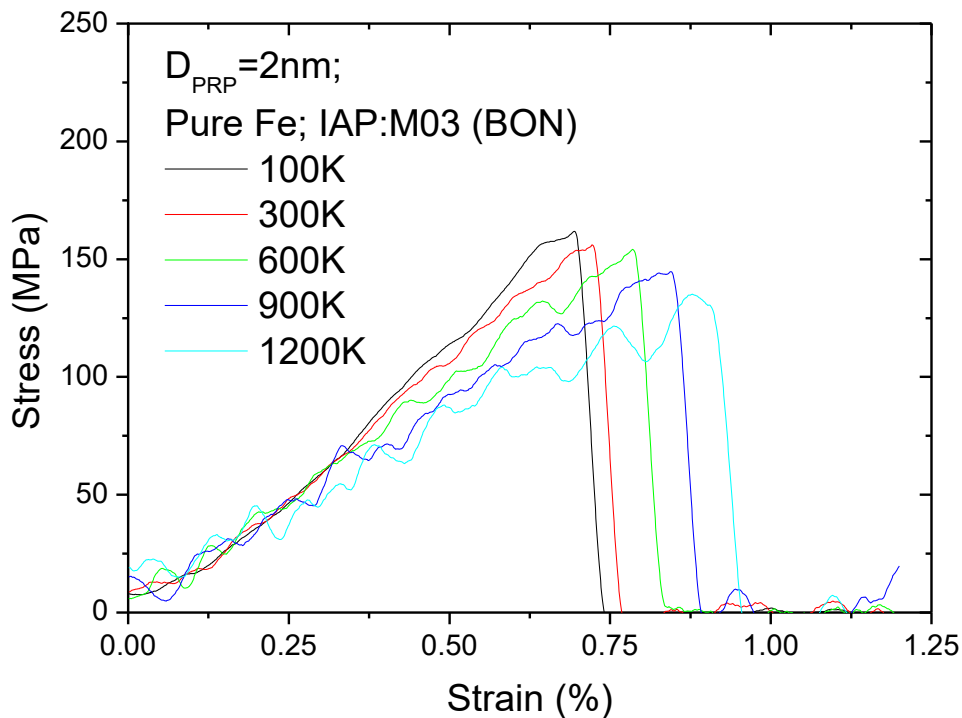


FIG. 3. $\tau-\gamma$ curves obtained for pure Fe containing 2nm Cr precipitates. MD simulations were performed at $T=100-1200 \text{ K}$.

The stress-strain curves corresponding to the interaction of the edge dislocation with a 2nm Cr precipitate are shown in Fig. 3 for different temperature. In all the cases, τ_c monotonically decreases with temperature.

3. TRANSITION TO THE CONTINUUM LEVEL

In order to carry out DD simulation in Fe-Cr alloys, the mobility laws for dislocations should be established first. MD simulations of dislocation motion in Fe-Cr presented above allow one to deduce these important parameters. As can be seen from Fig. 2, the threshold stress for the dislocation motion reaches a thermal plateau beyond 300 K. This stress is called in the following the friction stress τ_f . From these MD results, we estimate the friction stress to be equal to 30, 40, and 70 MPa for 5, 10 and 15%Cr, respectively. Consequently, when the effective stress is lower than the τ_f , dislocation segments do not move in DD simulations.

Interaction with Cr precipitates can be analyzed on the continuum level, following the energy-stress decomposition presented in [10, 11]. The analysis is based on the concept of the effective stress exerted on dislocation segments in contact with the Cr precipitate. Depending on temperature, the probability of unpinning is a function of the effective stress only. The activation energy per dislocation length versus effective stress obtained from MD simulations is shown in Fig. 4.

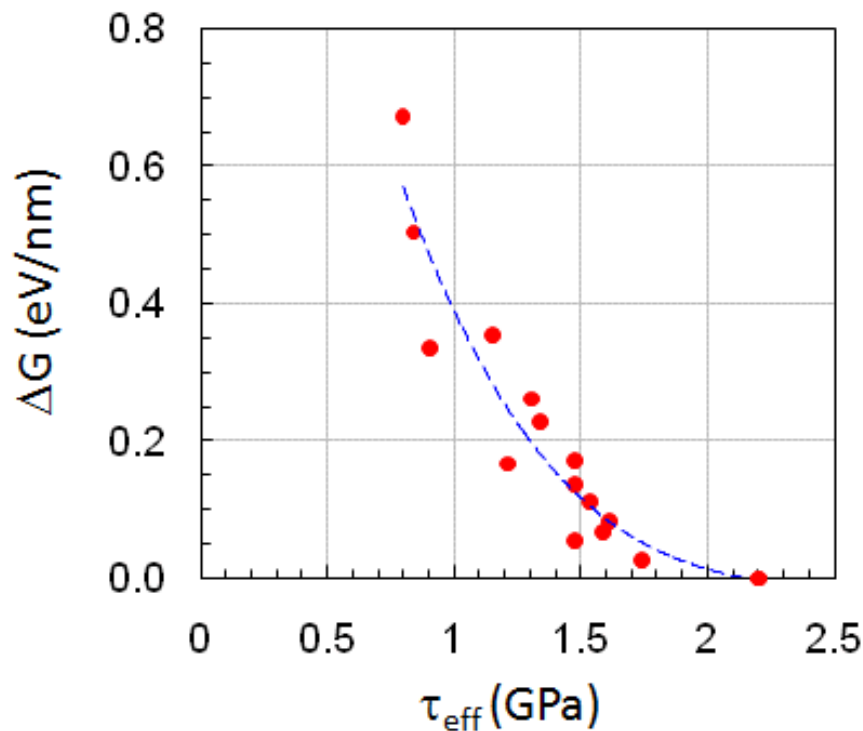


FIG. 4: Evolution of the activation energy as a function of the effective stress for the shearing of pure Cr precipitates in iron.

We can see that the activation energy decreases strongly with the effective stress. For stresses larger than 2.2 GPa, no thermal activation is needed for the shearing process to occur. On the other hand, for stresses lower than 0.7 GPa, the activation energy steeply rises up. In DD simulations, this feature is reflected by preventing dislocation segments to penetrate the precipitates until the effective stress reaches 0.7 GPa.

The unpinning probability due to the thermal activation, as obtained from MD data, is integrated in the DD code via a Monte Carlo scheme. In the next section, we show how these results enable the determination of the strengthening associated with Cr precipitation.

4. DD SIMULATIONS OF PRECIPITATION STRENGTHENING

4.1 Validation of the transition method

Before performing large scale DD simulations, we validate the implementation of the thermally activated unpinning of the dislocation from Cr precipitates. Hence, we apply DD simulations in the same conditions as employed in MD calculations, i.e. the same strain rate, box dimensions, dislocation character, temperature, precipitate size and its position. If the transition method captures the physics involved in the interaction process, DD simulations should predict the same value for the unpinning stress. In Fig. 5 the comparison between MD and DD results is shown, which clearly demonstrates a good agreement between the two methods. Hence, we conclude that the established mobility rules can be applied for massive DD simulations.

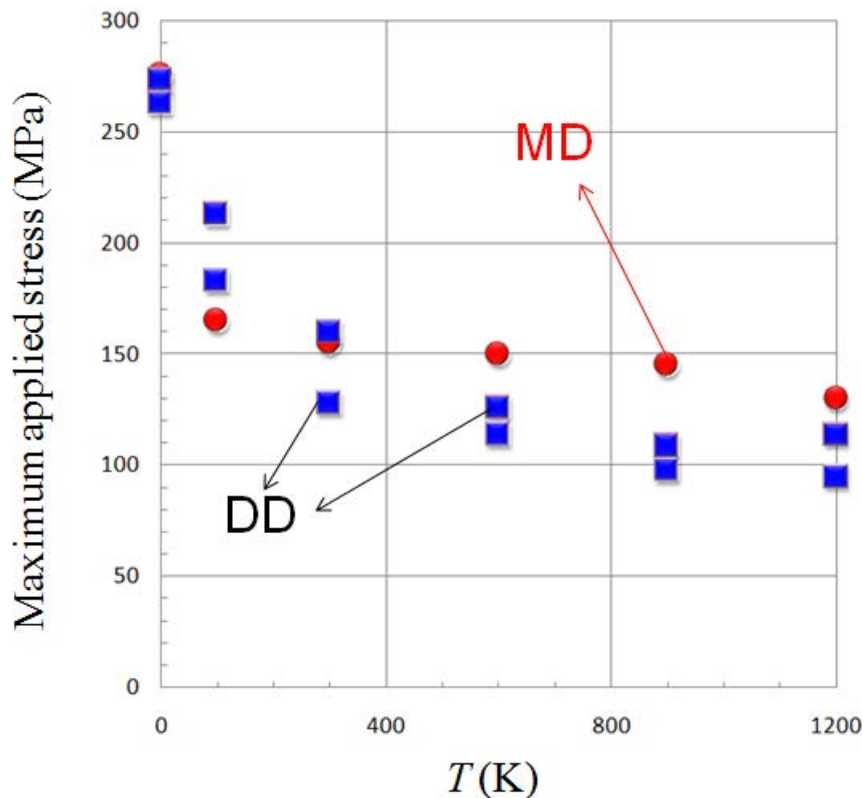


FIG. 5. Comparison between the maximum applied stresses found in MD and DD simulations needed to unpin the dislocation from a 2nm Cr precipitate.

4.2 Massive DD simulations of precipitate strengthening

In the next step, a large DD simulation contains almost 10^4 randomly distributed Cr precipitates. Periodic boundary conditions are applied in order to form an infinite edge dislocation, as can be seen in Fig. 6. The simulation box dimensions are: 10 nm perpendicular to the slip plane, 1 μm along the dislocation line and 1 μm in the direction of the Burgers vector. The average planar spacing between precipitates is 10 nm. For the sake of simplicity, all precipitates are chosen to have size of 2 nm. A fixed strain rate is chosen in order to ensure a fixed average dislocation velocity of 2 m/s, to comply with the dislocation velocity in experimental mechanical tests.

At 0 K, the motion of the dislocation is jerky. Often, unpinning from a strong configuration enables the dislocation to sweep a large area of the slip plane. The movement becomes smoother with increasing temperature.

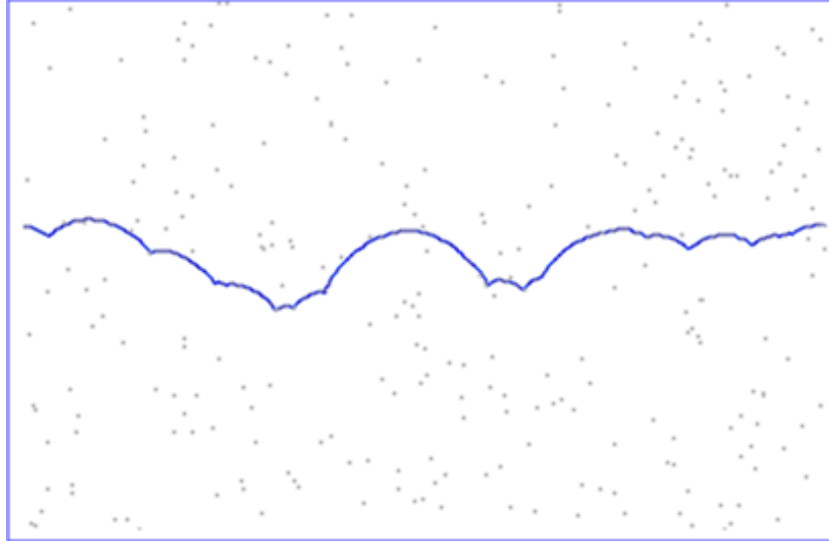


FIG. 6. Snapshot of the infinite edge dislocation interacting with a randomly-distributed 2nm Cr precipitates.

The flow stress, computed by the DD code, as a function of temperature is then used to calculate the strengthening $\Delta\tau$ associated with Cr precipitates by subtracting the friction stress of the corresponding Fe-Cr alloy. The strengthening induced by Cr precipitates alone is presented in Fig. 7.

Two important remarks follow from Fig. 7. Firstly, the precipitation strengthening goes down strongly with increasing temperature from 0 K up to 300 K and then does not change, so that above room temperature it reaches a plateau of 15 MPa. Secondly, the computed strengthening is much lower than the Orowan stress at all temperatures. For instance, the Orowan critical stress for a regular square array of Cr precipitates at 0 K is 250 MPa, while the DD simulations predict only 60 MPa for the random distribution.

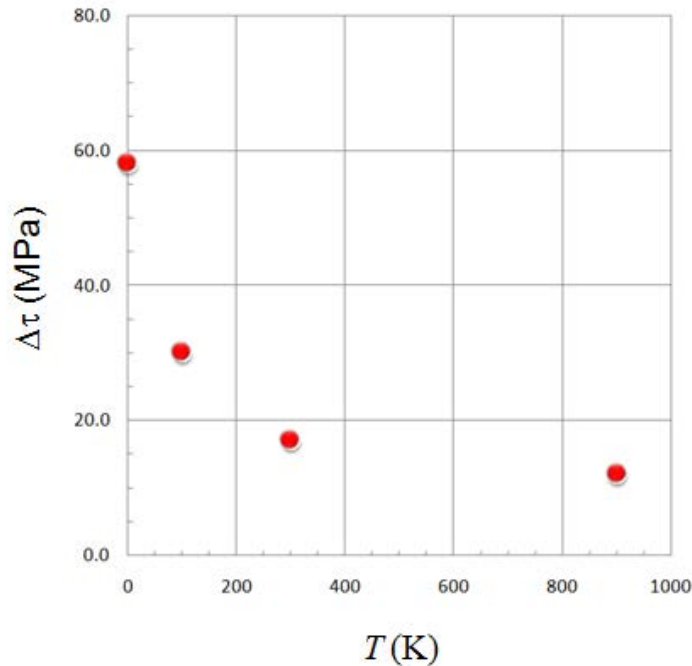


FIG. 7. Evolution of the strengthening induced by Cr precipitates as a function of temperature.

5. CONCLUSIONS

Based on the calculations performed and results obtained so far, we can draw the following conclusions:

- (i) Equilibrium properties of defect free Fe-xCr (x=5,10,15%Cr) matrix are very close to those in Fe, in terms of cohesive energy, lattice unit, shear modulus and stacking fault energy for a {110} plane. The dislocation core energy and radius for both edge and screw dislocations are also essentially the same in Fe and in the Fe-Cr alloys.
- (ii) Adding 5, 10 and 15%Cr in the Fe matrix leads to an increase of the flow stress for the edge dislocation from 80 MPa in pure Fe up to 200, 270 and 350 MPa, in the Fe-Cr alloys, respectively.
- (iii) Finite temperature simulations have shown that the flow stress decreases with temperature down to about 50 MPa in Fe-5%Cr and Fe-10%Cr alloys and down to 100 MPa in Fe-15%Cr.
- (iv) The interaction of an edge dislocation with a square array of coherent pure Cr precipitates with size up to 2.5 nm was studied using atomistic simulations at varying temperature from 0 to 1200 K. The critical stress needed to unpin the dislocation and the breakaway dislocation line shapes were determined.
- (v) The dislocation was observed to shear Cr precipitates, which indicates that these coherent precipitates are of finite strength.
- (vi) A transition method is applied to deduce the activation energy for shearing the Cr precipitates. It is shown that no thermal activation unpinning is possible for the effective stress lower than 0.7 GPa, while shearing is athermal if the effective stress larger than 2.1 GPa.
- (vii) Results of the transition method were successfully used in DD simulation, enabling the latter to reproduce results of MD simulations addressing the interaction of an edge dislocation with a regular array of Cr precipitates.
- (viii) DD calculations have shown that the strengthening induced by Cr precipitation is much lower than the Orowan stress for a regular array of Cr precipitates. The strengthening is attributed to the Cr precipitation, estimated here by the DD method, is not enough to explain the experimentally measured hardening in the irradiated Fe-Cr alloys.

REFERENCES

- [1] KOHYAMA A., HISHINUMA A., GELLES D., KLUEH R., DIETZ W., EHRLICH K., J. Nucl. Mater. **233–237** (1996) 138.
- [2] OKADA A, KAWAGUCHI N, HAMILTON ML, HAMADA K, YOSHIIE T, ISHIDA I, HIROTA E, J. Nucl. Mater. **212–215** (1994) 382.
- [3] OKADA A, MAEDA H, HAMADA K, ISHIDA I, J. Nucl. Mater. **271&272** (1999) 133.
- [4] HEINTZE C., ULBRICHT A., BERGNER F., ECKERLEBE H., Journal of Physics: Conference Series 247 (2010) 012035.
- [5] M. MATIJASEVIC, A. ALMAZOUZI, J. Nucl. Mater. **377** (2008) 147.
- [6] OSETSKY Y.N., BACON D.J., Modelling and Simulation in Mat. Sci. Eng. **11** (2003) 427.
- [7] BONNY G., PASIANOT R.C., TERENCEV D., MALERBA L., Philosophical Magazine **91** (2011) 1724.

- [8] TERENTYEV D., BONNY G., DOMAIN C., PASIANOT R.C., Physical Review B **81** (2010) 214106.
- [9] TERENTYEV D., BONNY G., MALERBA L., Acta Materialia **56** (2008) 3229.
- [10] MONNET G., OSETSKY Y., BACON D., Philosophical Magazine **90** (2010) 1001.
- [11] MONNET G., Philosophical Magazine **91** (2011) 3810.

NUMERICAL MODELLING OF MECHANICAL BEHAVIOUR OF IRRADIATED STRUCTURAL MATERIALS: A MULTI-SCALE APPROACH

P.V. DURGAPRASAS, B.K. DUTTA, RAJEEV KAPOOR AND A.K. PAWAR
Bhabha Atomic Research Centre
Trombay, Mumbai,
India
Email: pvd@barc.gov.in

Abstract

Multi-scale material modeling methodology has been used to understand properties of irradiated materials with a focus to ferritic/martensitic steels. The complete description of failure and its numerical modelling requires knowledge of length scales ranging from nano to meso to micro length scales. For the irradiated materials, there are other governing defects like irradiation-induced defect clusters which control motion of dislocations under external loads. At the atomic scale, motion and interaction of dislocations with irradiation induced defects in Fe, Fe-Cr and Fe-Cr-He systems was studied using MD simulations. The output of MD simulations such as friction stress, critical resolved shear stress was passed on to next higher length scale-dislocation dynamics simulations. With the dislocation dynamics simulations, the flow stress for Fe and Fe-Cr alloys in the presence of voids and bubbles was determined. Finally, at the micro-length scale, a combined numerical and experimental methodology showing the use of small punch (SP) tests is presented which can be used to understand fracture behavior of irradiated materials. SP tests have been carried out on T91 material and micro-mechanical Gurson parameters have been determined.

1. INTRODUCTION

The proposed structural materials to be used in future Generation-IV fission reactors and fusion reactors are expected to operate at temperatures above 500 °C and see damage up to 100–200 dpa. Some of the candidate materials for such applications are ferritic/martensitic steels, ODS materials, etc. There is an ongoing exercise all over the world to determine the properties of such materials subjected to severe radiation environments through both experimental and theoretical investigations. Experimental investigations include reactor and accelerator irradiation, high resolution microscopic examinations, small scale/miniature specimen tests, etc., whereas the theoretical studies involve multi-scale methods covering atomistic to dislocation dynamics to micro-mechanical analyses.

Multi-scale material modelling (MMM) methodology is being widely employed to understand the above mechanisms and to determine irradiated material properties. The current research in MMM is largely devoted to find suitable numerical models and linking mechanisms from one-scale to another. In the present work, the MMM methodology was used to understand properties of irradiated materials with a focus to ferritic/martensitic (FM) steels. At the atomic length scale, MD simulations of the dislocation-defect interactions in Fe, Fe-Cr and Fe-Cr-He systems were carried out to understand the irradiation induced hardening. The outputs of atomistic simulations were then passed to the next length scale of modelling, dislocation dynamics. At this scale, flow curves for Fe and Fe-Cr alloys were determined by using the combined effect of motion and interaction of dislocations with the defects and the required stress and strain fields of dislocations were obtained from elasticity theory. At the micro-scale, a methodology is presented showing combined use of experimental and micro-mechanical modelling of small punch tests to determine fracture behaviour of irradiated materials. Out of the three length scale studies mentioned in this work, some of the results of atomistic and DD simulations were reported in [1].

2. ATOMISTIC SIMULATIONS OF IRRADIATION HARDENING

Atomistic studies of defect interactions in Fe and Fe-Cr alloys provide the basis for understanding property degradation in FM steels. There is an ongoing effort all over the world to understand radiation hardening in steels using molecular dynamics simulations. In this work, MD simulations of motion and interaction of edge dislocations (ED) with irradiation induced defects in Fe and a Fe-10% Cr system are presented. The effect of irradiation on edge

dislocation motion in Fe and Fe-Cr was taken into account by considering a) voids b) helium bubbles and c) helium as substitutional and interstitial atoms in Fe-Cr alloy. The results of atomistic simulations were passed onto next length scale such as dislocation dynamics simulations.

2.1 MD simulations: Computational details

The MD simulations are carried out for edge dislocation-defect interactions in Fe, Fe-10%Cr and Fe-10%Cr-1%He alloys. The Fe-Fe potential by Mendeleev et al [2] was used in various simulations is used for Fe-Fe atomic interactions. The concentration dependent two elements Fe-Cr potential given in Stukowski et al [3] was used for Fe-Cr interactions. The Fe-He [4], Cr-He [5] and He-He [6] potentials were employed from various published papers to analyze the Fe-Cr-He crystal system. For studying MD simulations of motion of dislocations with ternary potential, the Fe-Cr-He ternary potential given by Caro [7] has been employed. The ternary potential is used to determine the friction stress for motion of ED in Fe-10%Cr and Fe-10%Cr-x%He systems for different temperatures. One of the active slip systems $\langle 111 \rangle$ $\{110\}$ is taken for simulation of edge dislocation motion in alpha iron having bcc lattice structure. The directions of BCC lattice $\langle 111 \rangle$, $\langle 110 \rangle$ and $\langle 112 \rangle$ were oriented along x, y, and z direction. The simulation domain under simple shear was considered to study the mobility of the ED with the dislocation and dislocation-defect interactions.

The simulation domain has a size of $20 \times 9 \times 10 \text{ nm}^3$ and contained approximately 140,000 atoms in the mobile region. The Cr and He atoms were randomly distributed in Fe-10%Cr and Fe-10%Cr-1%He systems using different random number seeds. Different sizes of voids and bubbles were used in the simulations of interaction of ED with irradiation induced defects in Fe and Fe-10%Cr matrices. For studies with ternary potential, the He atoms were considered as being both substitutional and interstitial in Fe-Cr matrix. The following definitions are used here: The dislocation motion in otherwise defect free crystal occurs at a stress value known as friction stress which is defined by the maximal stress; i.e. the average of peak values in the shear stress-strain (τ - γ) plot. The resistance for dislocation motion due to an obstacle is defined as critical resolved shear stress CRSS, i.e. the maximum stress required to overcome the obstacle. In the following section, various results obtained from the present MD simulation are given.

2.2 MD simulations: Case studies, results and discussions

2.2.1. Mobility of edge dislocations in pure Fe, Fe-10%Cr and Fe-10%Cr-1%He

The mobility of the ED in the absence of irradiation induced defects is investigated in this section. Under the applied external load the dislocation starts to move in its slip plane. The flow stress required to move the dislocation in its slip plane was found to be 81 MPa. Similarly, the flow stress for edge dislocations to move in Fe-10%Cr alloy matrix was also determined. The analyses were carried out for different random distributions of chromium atoms. The τ - γ plot for different random distributions of Cr is shown in Fig. 1(a). The peaks in the τ - γ plot are amplified due to the presence of Cr atoms and are less regular in comparison to pure Fe.

This is due to the pinning and releasing of the dislocation by a cluster of two or more chromium atoms. This analysis shows the hardening effect due to the presence of Cr atoms in pure Fe. A pair of solute atoms in nearest neighbor configuration or a cluster of solute atoms lying on the adjacent planes above and below the geometric slip plane act as strong obstacles to gliding dislocation. The average of maximal flow stress is 130 MPa as shown by the dotted line in the figure. The alloy matrix Fe-10%Cr with 1% helium was used to assess the effect of

irradiation on the dislocation mobility. The τ - γ plots for Fe-10%Cr system with different random distribution of He are shown in Fig. 1(b). In the presence of 1%He, the peak stress values are more amplified and the stress required moving the dislocation increases significantly. The dotted line shows the average of maximal friction stress at 230 MPa.

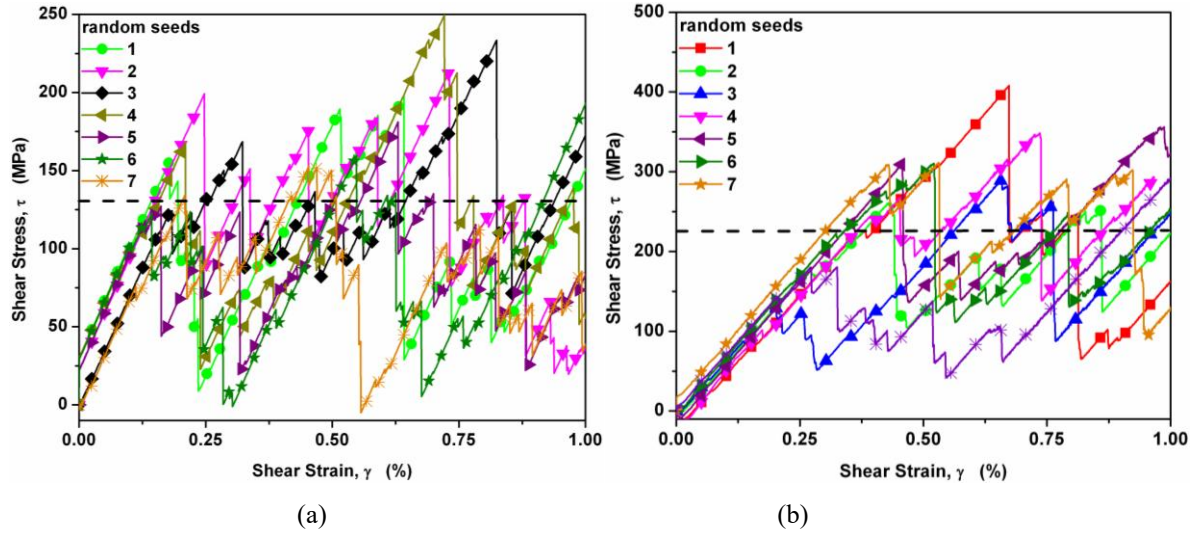


FIG. 1. Shear stress-strain (τ - γ) plots for with different random number of seeds for (a) Fe-10%Cr and (b) Fe-10%Cr-1%He.

2.2.2 Dislocation-Void interaction in pure Fe, Fe-10%Cr and Fe-10%Cr-1%He

The MD simulation of the interaction of edge dislocations with voids was carried out to determine the CRSS. The voids were considered by removing the atoms falling within a spherical volume of given diameter. Fig. 2(a) shows τ - γ plot for interaction of an edge dislocation with different void diameters in pure Fe. The initial drop in stress corresponds to attraction of the dislocation by the void. The dislocation is pinned by the void until the stress exceeds the critical stress value CRSS. To study the effect of temperature a similar study has been carried out at 523K to find the CRSS required overcoming the defects. The τ - γ plots for various void sizes in pure Fe at 523K are shown in Fig. 2(b).

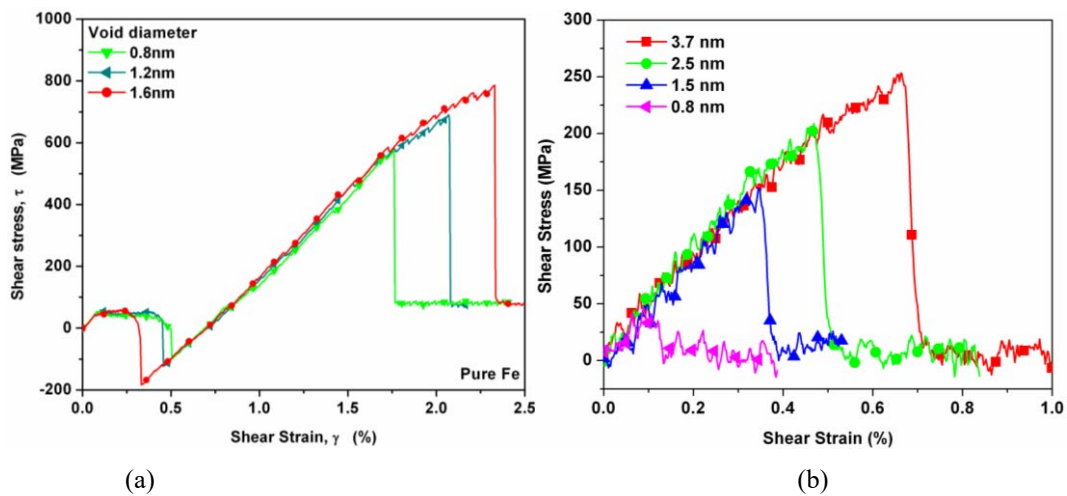


FIG. 2. Shear stress-strain (τ - γ) plots for ED-void interaction in pure Fe at (a) 10 K and (b) 520 K.

Similarly, the interaction of ED with voids was studied in Fe-10%Cr system. The 10% Cr atoms were randomly distributed in the Fe matrix and the corresponding τ - γ plot for Fe-10%Cr is shown in Fig. 3(a). The presence of Cr atoms seems to decrease the CRSS for smaller size voids and to have a softening effect on the strength of the void. This has been checked for various distributions of Cr atoms and this observation has been found to be consistent. Out of the three cases (0.8, 1.2 and 1.6nm) reported here, there is a softening effect of Cr atoms for a 0.8nm void. A transition from softening to strengthening has been observed for a 1.2nm void, whereas the CRSS is noticeably higher in the case of a 1.6nm void.

The effect of irradiation induced He in FM steels on the interaction of ED with a void was considered by randomly placing the substitutional He atoms in the Fe-10%Cr matrix. The τ - γ plot for Fe-10%Cr-1%He is shown in Fig. 3(b). The CRSS values are found to be 687 MPa, 750 MPa and 950 MPa for 0.8 nm, 1.2 nm and 1.6 nm voids, respectively. In comparison to pure Fe and Fe-10%Cr, a significant increase in CRSS is observed due to the presence of 1% He. The initial dislocation-void configuration and the bowed dislocation due to pinning by a 1.6 nm void in Fe-10%Cr-1%He are shown in Fig. 4(a) and (b) respectively.

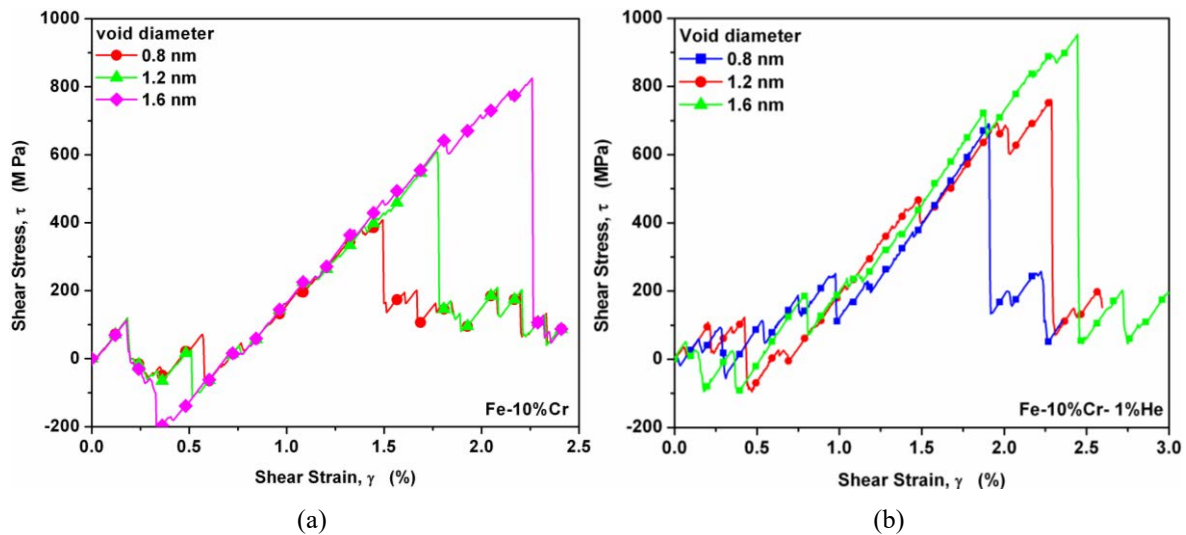


FIG. 3. Shear stress-strain (τ - γ) plots for ED interacting with different sizes of voids in a) Fe-10%Cr and b) Fe-10%Cr-1%He.

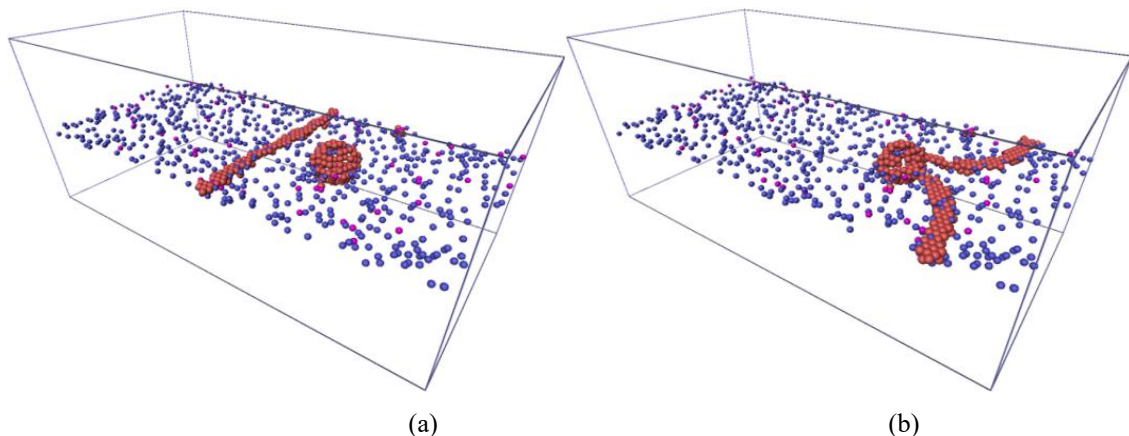


FIG. 4. Interaction of ED with 1.6 nm void (void surface atoms plotted) in Fe-10%Cr-1%He; (a) initial dislocation-void configuration, (b) bowed out dislocation line after pinning by void (Cr atoms-blue color, He atoms-magenta color). Fe atoms other than those on the dislocation line are not shown here.

2.2.3 Dislocation-He bubble interaction in pure Fe and Fe-10%Cr

Bubbles of size 0.8nm, 1.2nm and 1.6nm were inserted by replacing Fe lattice atoms with He atoms in a spherical volume of given diameter, resulting in bubbles of type 1He-1V pair. The τ - γ plots for an edge dislocation interacting with helium bubbles in pure Fe is shown in Fig. 5(a). It is seen that He bubbles of 1He-1V type are weaker obstacles in comparison to the voids of same size as highlighted in [9]. The dislocation-bubble interaction behavior is similar to that of the dislocation void interaction as described above. A similar exercise was carried out for the interaction of edge dislocations with helium bubbles in the Fe-10%Cr system and the corresponding τ - γ curves are shown in the Fig. 5(b). The simulation shows that the CRSS for an edge dislocation interacting with He bubble (1He-1V) is comparable to that of a void. The CRSS for the 1.6 nm diameter bubbles is almost same as that of the void in Fe-10%Cr, but for 0.8 and 1.2 nm bubbles it is 157 and 129 MPa greater than that of the void.

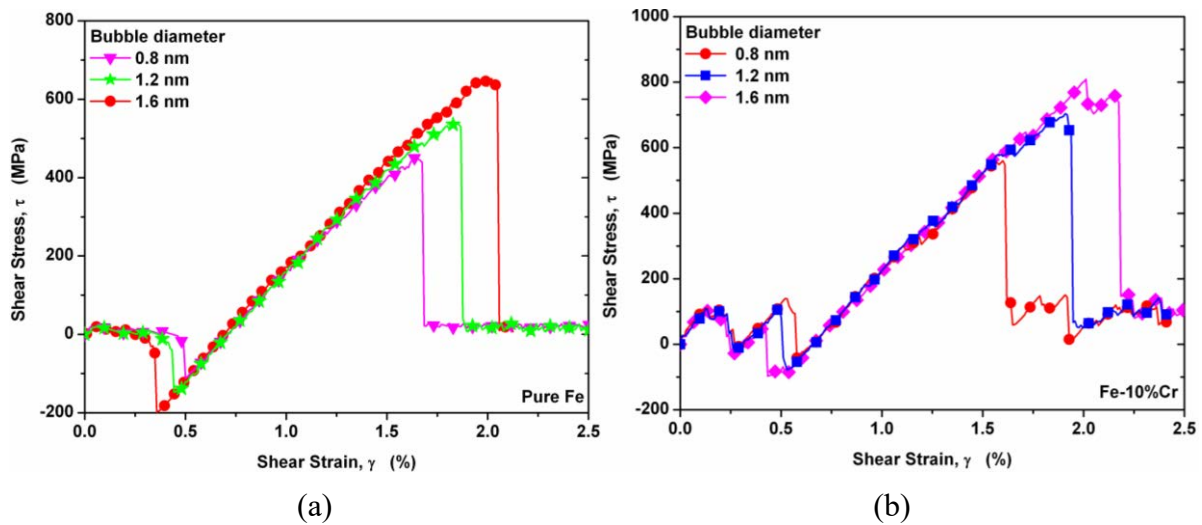


FIG. 5. Shear stress-strain (τ - γ) plots for ED-bubble interactions in (a) pure Fe and (b) Fe-10%Cr.

2.2.4 Study of dislocation mobility in Fe-Cr and Fe-Cr-He systems using ternary potential

MD simulations were carried out to understand the mobility of a dislocation in the Fe-Cr and Fe-Cr-He systems using the ternary potential. The Cr atoms were placed as substitutional atoms in Fe matrix, whereas the He was considered to be at a) substitutional and b) interstitial positions in the Fe-Cr matrix. He substitutional and interstitial atoms are referred as He_{sub} and He_{int} , respectively. A comparison of the friction stress for ED in Fe-10%Cr, Fe-10%Cr-1% He_{sub} , Fe-10%Cr-1% He_{int} for different temperatures is shown in Fig.6. To study the effect of the concentration of substitutional He with ternary potential, studies of motion of ED in Fe-10%Cr- $x\%$ He_{sub} was carried out. The variation of maximal shear stress/friction stress with respect to temperature for $x\%$ He_{sub} is as shown in Fig. 7(a). The rate of change of friction stress tends to decrease for higher He content as shown in this figure. Similar studies of the effect of interstitial He on dislocation motion in Fe-Cr matrix were carried out.

The variation of maximal shear stress/friction stress with respect to temperature for He_{int} content are as shown in Fig. 7(b). In the presence of He in interstitial position, the peak stress values are much amplified in comparison to Fe-Cr with 1% He substitutional. Even at higher temperatures (up to 100 K), the friction stress is higher, which can be attributed to formation of small clusters of He in case of Fe-10%Cr- $x\%$ He.

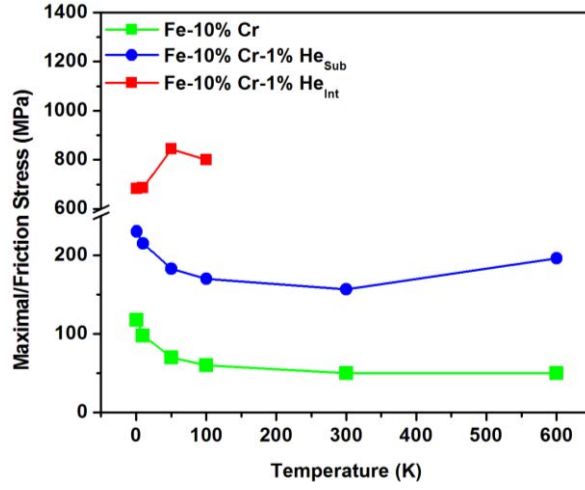


FIG. 6. Comparison of friction stress for ED in Fe-10%Cr, Fe-10%Cr-1%He_{sub}, Fe-10%Cr-1%He_{int} for different temperatures (using the ternary potential).

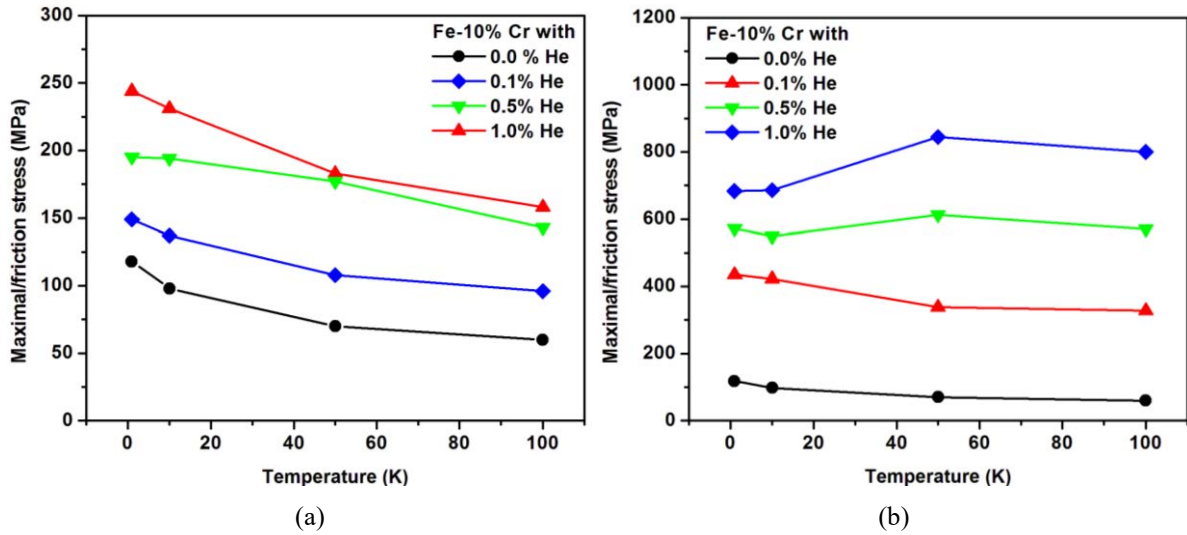


FIG. 7. Friction stress for motion of ED in Fe-10%Cr-x%He using the ternary potential as function of temperature with (a) He as substitutional and (b) He as interstitial.

3. DISLOCATION DYNAMICS SIMULATION OF IRRADIATION HARDENING

The plastic deformation of irradiated materials is governed by the motion and interaction of dislocations with irradiation induced defects. To understand property degradation of irradiated FM steels, it thus becomes necessary to study dislocation-defect interactions at the meso scale using dislocation dynamics simulations. In this work, the three dimensional dislocation dynamics (DD) simulations were carried out to estimate the flow stress of Fe and Fe-10%Cr crystals by using the critical resolved shear stress (CRSS) values obtained from the MD simulations.

The computational domain was assumed as isotropic and elastic, with a shear modulus of 83.6 GPa, Poisson's ratio of 0.33 and a Burger's vector of 0.248nm which corresponds to pure iron. The domain considered in the present DD simulation had a volume of $7 \times 8 \times 9 \mu\text{m}^3$ with periodic boundary conditions. The x, y, z directions correspond to [100], [010] and [001] crystallographic directions respectively. The initial microstructure was generated by straining the crystal having 48 dislocation nucleation sources with random (edge, screw or mixed) character. An equal number of sources in each slip system of slip family $\langle 111 \rangle \{110\}$ were

considered to be active in iron at low temperatures. The initial microstructure consists of a dislocation density of $9 \times 10^{11} \text{ m}^{-2}$. A drag coefficient of $10^{-4} \text{ Pa}\cdot\text{s}$ was used in the simulations. The tensile loading was applied by specifying a strain rate of 100 s^{-1} along the $\langle 001 \rangle$ direction. The cross-slip behavior of screw dislocations were not considered in the present simulations. A discretization length of $0.25 \text{ }\mu\text{m}$ and a time step size of $3.5 \times 10^{-11} \text{ s}$ was used in all simulations. For studying the effect of irradiation induced defects, an obstacle density (either voids or bubbles) of $2 \times 10^{21} \text{ m}^{-3}$ was used. The voids and bubbles are considered as obstacles of diameter d with spherical volume having a friction stress τ_{shear} as given in [10]. To bridge the length scales, the computed CRSS values from MD simulations of dislocation-defect interactions was used to find the friction stress τ_f for input to DD simulations. For this bridging, the scaling law described by Sylvain [11] were used to calculate τ_f from τ_{CRSS} as given below:

$$\tau_f = \tau_{CRSS} \times \frac{l}{d} \quad (1)$$

where l is the distance between the obstacle and d is the diameter of the obstacle.

3.1 DD simulations: Case studies, results and discussion

The DD simulations were carried out to estimate the flow stress for a) the Fe, Fe-10% Cr and Fe-10%Cr-1%He alloy systems and, b) the Fe, Fe-10%Cr alloy system in the presence of irradiation induced defects with selected case studies. The presence of effect of Cr and He in Fe was taken into account by using the threshold friction stresses τ_f as derived from MD simulations. As a first approximation, it was assumed that the friction stress obtained for edge dislocation was applicable for all dislocation characters, i.e. edge, screw and mixed. The friction stresses for the materials considered in the present simulations were taken from MD simulations at 80, 130 and 230 MPa for Fe, Fe-Cr and Fe-Cr-He systems respectively. The irradiation induced obstacles were randomly distributed in the Fe and Fe-10%Cr crystals and overlapping of these obstacles was avoided in all cases. The stress required to shear the obstacle was dependent on the size and type of the obstacles. The shear resistance or stress needed for dislocation segments to overcome obstacles was also taken from MD simulations using equation (1). Various results obtained from the present DD simulations are presented in the following sections.

3.1.1 Flow stress for Fe, Fe-10%Cr and Fe-10%Cr-1%He without irradiation induced obstacles

The initial microstructure of dislocations used for subsequent straining is shown in Fig. 8(a). The tensile stress vs. total strain (σ - ϵ) behavior obtained from DD simulations for Fe, Fe-10%Cr and Fe-10%Cr-1%He system without irradiation obstacles is shown in Fig. 8 (b). The figure shows the linear elastic region followed by the plastic deformation of the crystal. Flow stress values of 115 MPa, 235 MPa and 480 MPa were obtained for Fe, Fe-10%Cr and Fe-10%Cr-1%He respectively. The junctions are formed due to the interaction of dislocations of different slip planes resulting in pinning of the dislocations. These junctions need higher stresses to unlock the dislocations such that the dislocation starts to move in its slip plane under the action of an external load. The hindering of dislocation motion by junction formation contributes to the strain hardening of the materials.

The strain hardening due to pinning of dislocations at junctions is computable by DD analysis in the case where computation is continued to higher strains. The maximum strain, for which computation was carried out in the present case is of the order of 0.2% which is essentially enough to assess the change in flow stress due to the presence of obstacles of different

strength. The simulations show a flow stress increase of 120 MPa for Fe-10%Cr and 365 MPa for Fe-10%Cr-1%He in comparison with that of pure Fe.

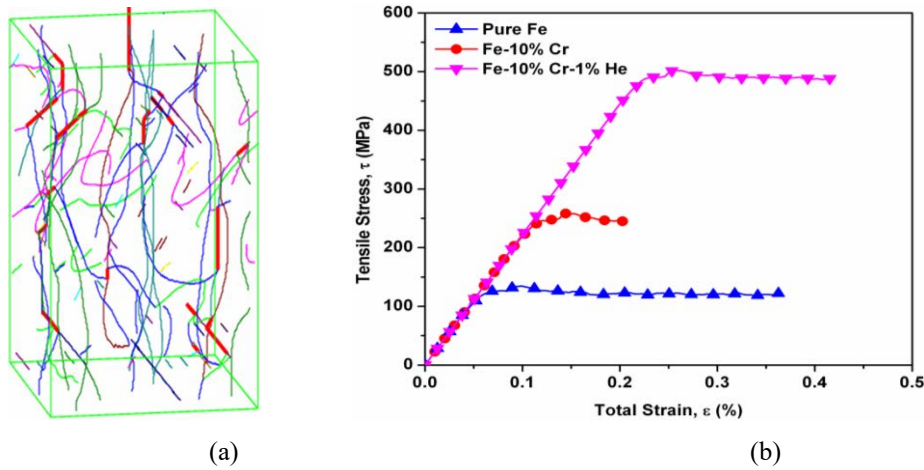


FIG. 8. a) Initial dislocation microstructure in DD simulations of Fe without obstacles; b) Tensile stress vs. total strain for Fe, Fe-10%Cr and Fe-10%Cr-1%He.

3.1.2 Flow stress for Fe, Fe-10%Cr with irradiation induced voids

In this section the DD simulations were performed to determine the flow stress variation of Fe and Fe-10%Cr in the presence of different sized voids. The simulation conditions were the same as that defined in the previous section. The σ - ϵ plots for Fe and Fe-10%Cr with different void diameters are shown in Fig. 9. The simulations were stopped as the σ - ϵ plot started to indicate a plateau region. It can be observed that an increase in diameter of the void at a given obstacle density increases the flow stress of the material. Approximate increases in flow stress of 20MPa for 0.8nm, 35MPa for 1.2nm and 50MPa for 1.6nm void were observed in both crystals considered.

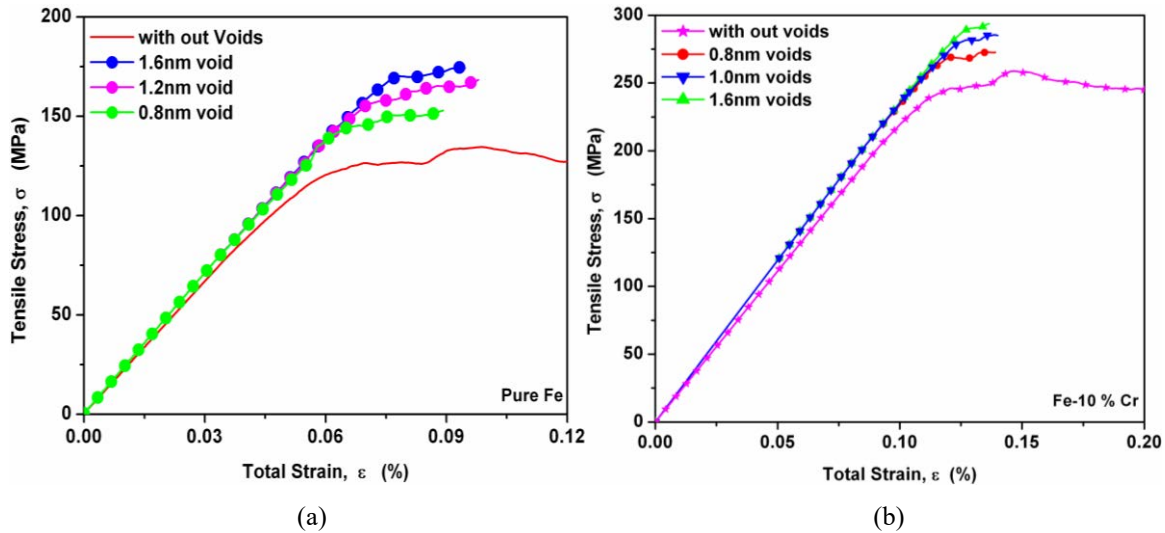
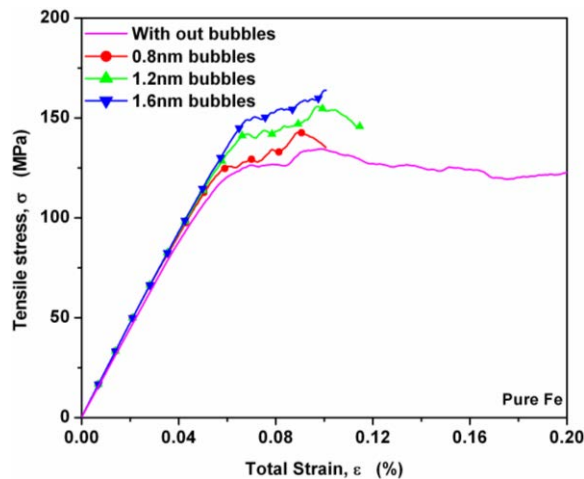


FIG. 9. Tensile stress vs. total strain plots for a) pure Fe and, b) Fe-10%Cr at different void sizes.

3.1.3 Flow stress for Fe with irradiation induced bubbles

In this case, DD simulations were performed to determine the flow stress variation in pure Fe with different sizes of helium bubbles due to irradiation. We considered the same simulation

conditions as used before. The σ - ϵ plot for Fe with different bubble diameters is shown in Fig. 10. The similar hardening behavior is obtained in the present case as observed in case of voids. Approximate increases in the flow stress of 10 MPa for 0.8nm, 25 MPa for 1.2nm and 35 MPa for 1.6nm bubbles was observed. In all simulations, the obstacles lying on the slip planes were sheared by the dislocations.



(a)

FIG. 10. Tensile Stress vs. total strain (σ - ϵ) plots for pure Fe in the presence of bubbles of different size.

4. MICRO-MECHANICAL MODELING OF MINIATURE TESTS

The materials used in fission and fusion reactors undergo high energy particle irradiation, which results in changes in material properties. To understand the irradiation effects, post-irradiation material testing was carried out on the samples taken from reactor surveillance capsules. Limited availability of the irradiated material from both reactors and accelerators resulted in an evolution of innovative testing methods including small specimen testing techniques. Small punch (SP) testing is one popular method used to determine material properties. SP tests use small TEM sized disks to evaluate the mechanical behaviour of the materials. Most of such analyses using SP have been based purely on experimental tests and only a few previous studies have used numerical SP tests to determine the mechanical behavior of materials.

Campitelli [12] compared experimental and finite element simulations of SP tests and made an assessment of the stress-strain behavior for Eurofer97 irradiated with 590 MeV protons to 0.5 dpa at 150°C. Chang et.al [13] investigated the characterization of ductile fracture resistance (J-R) curves by the SP testing technique in conjunction with finite element analyses incorporating the well-known micro-mechanical damage models for unirradiated materials. In our present work, a methodology has been established to determine the fracture resistance curves of irradiated materials using experimental SP tests in conjunction with numerical analyses.

4.1 Small punch test methodology to obtain mechanical behavior of irradiated materials

A methodology has been established to determine stress-strain behaviour of irradiated materials using experimental small punch tests in conjunction with numerical SP test simulations. The methodology comprises the following steps: a) comparison of experimental load-displacement data and numerical simulations of SP tests to determine the Gurson damage parameters and the friction factor between the ball and the specimen, b) using these

parameters and an appropriate shift in the stress-strain curve (which will be described in the following sections) to account the effect of irradiation, the load-displacement data of SP test was obtained for irradiated materials, c) compare the numerical and experimental load-displacement data of irradiated samples, the stress-strain data of irradiated samples was obtained. Finally, the fracture properties such the J-R curve can be evaluated for irradiated materials by employing the stress-strain data and damage parameters for standard specimens. In the present work, Gurson material damage parameters are derived for T91 FM steel by using combined experimental and numerical SP results.

4.2 Experimental details of SP test for T91 material

The small punch experiments were carried out on thin samples of ferritic/martensitic steel T91 procured from SCK-CEN, Belgium. A schematic diagram of the experimental setup of the small punch testing is shown in Fig. 11(a). The experimental setup parameters, the lower die hole diameter D , ball radius R , thickness of the specimen t , upper die hole diameter d are given in Table 1. The specimen was kept between the upper and lower die. The upper die contained a central hole for ball and plunger movement. The upper and lower die centres were aligned concentrically with the specimen centre. The load displacement curves obtained from the experiments are shown in Fig. 11(b). Four samples were tested having a thickness around 0.23mm. The load displacement curves can be divided into four regions as i) the initial elastic region, which is governed by the elastic properties of the material, ii) the plastic bending region, iii) the membrane stretching region where nonlinear strain hardening of part of the material begins, and finally iv) the plastic instability region which is governed by void nucleation, growth and coalescence.

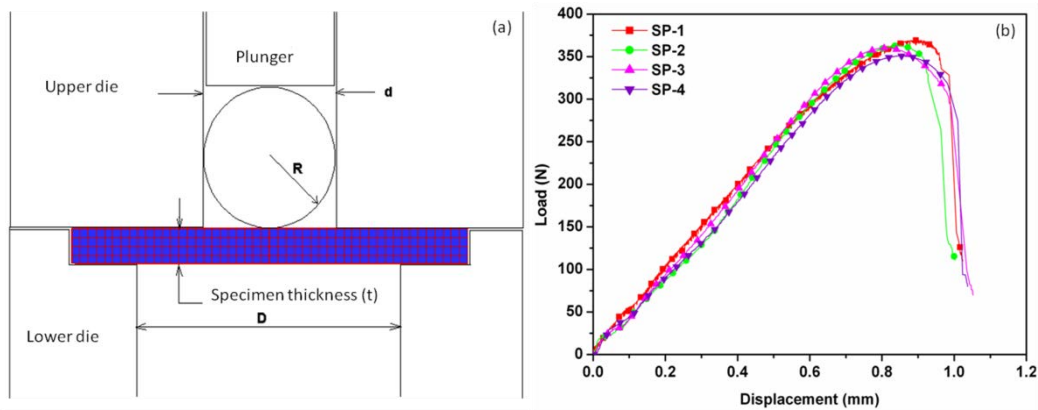


FIG. 11. a) Schematic diagram of SP experimental setup and b) Load displacement curves for four T91 samples.

TABLE. 1. SMALL PUNCH TEST SETUP PARAMETERS (ALL DIMENSIONS IN MM)

Material	t	R	d	D
T91	0.234	0.500	1.000	1.500

4.3 Numerical simulation of Small punch tests

Numerical simulation of Small punch tests or simulation of the SP test, the established micro-mechanical damage GTN model (Gurson-Tvergaard-Needleman) was utilized. The ductile damage model employs a yield potential represented in terms of a single damage quantity i.e. the void volume fraction (f). The GTN model was initially proposed by Gurson [14] and later modified by Tvergaard and Needleman [15]. In the present work, systematic FE analysis was

performed on the SP tests of miniature disks of T91 material. Micro mechanical parameters were obtained by combined use of numerical simulation of SPT and experimental load displacements described in the above section. The small punch specimen of diameter 3mm with thickness of 0.234mm was used for T91 material. Discretization (FE model) of the geometry was done with Axi-symmetric 8 node quadrilateral elements. The FE model of T91 consisted of 104 elements with 373 nodes, with a mesh size of 0.058 mm. In Fig. 11(a), the FE model of the SPT specimen for T91specimen is shown. A relative sliding between ball and specimen was taken into consideration. The deformed shape and contour plot of the Von-Mises stress for the SP specimen is shown in Fig. 12(a). The comparison of one of the experimental and simulated load displacement curves to determine the GTN parameters is shown in Fig. 12(b). The Gurson damage parameters obtained from the present analysis are tabulated in Table.2.

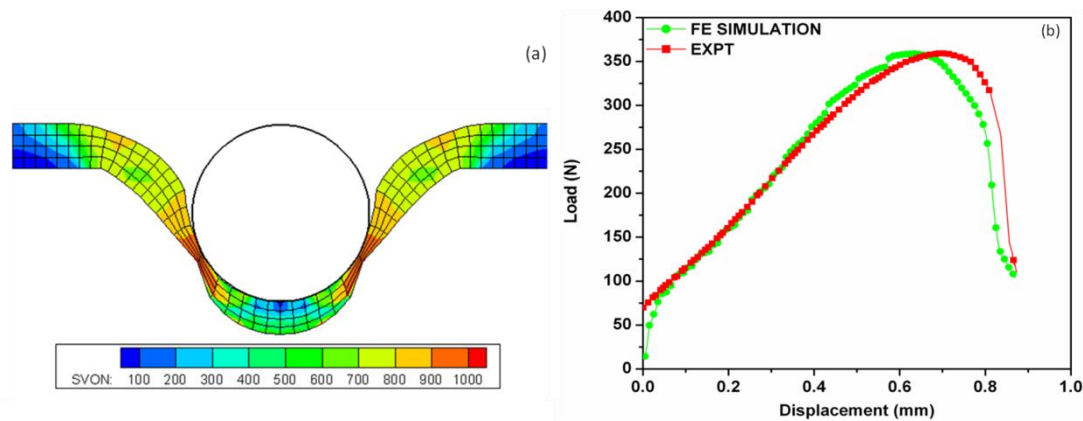


FIG. 12. (a) Deformed shape and contour plots of the Von-Mises stress and (b) Simulated and Experimental load displacement curves for T91.

TABLE.2. FRICTION FACTOR AND DAMAGE PARAMETERS OBTAINED FROM THE PRESENT STUDY (FOR DESCRIPTION OF PARAMETERS REFER TO [14, 15]).

Material	μ	f_0	f_c	f_f	f_n	q_1	q_2	q_3	S_n	ϵ_n
T91	0.400	0.0008	0.05	0.2	0.002	1.50	1.00	2.25	0.3	0.1

The stress strain data for irradiated materials can be generated by using the guidelines given in Tanguy [16] in conjunction with the SP tests. The Gurson parameters determined in the above analysis were used in the analysis. A shifted stress-strain curve from that of unirradiated material was assumed in the numerical analysis. The stress-strain curve with best matching of experimental and simulated SP results was then used in determination of the J-R curve. The experimental details of SP tests on unirradiated samples to ascertain the Gurson micro-mechanical parameters are reported in [17]. Presently, experiments of T91 irradiated samples are in progress.

5. CONCLUSIONS

Multi-scale material modeling methodology has been used to study the mechanical behaviour of irradiated materials with a focus to ferritic/martensitic steels. MD simulations were used to determine the friction stress of dislocations and the effect of irradiation induced defects on motion of dislocations in Fe, Fe-10%Cr and Fe-10%Cr-1%He systems. The CRSS required to overcome such defects was found for different sizes of voids and He bubbles. Motion of dislocations with a ternary Fe-Cr-He potential were also studied. The CRSS determined from

MD simulations was passed as input to DD simulations to study the flow behavior of the Fe, Fe-Cr and Fe-Cr-He systems. A methodology showing use of combined experimental and micro-mechanical analysis of small punch testing was presented to study the effect of irradiation on continuum properties of materials. As a part of this methodology, Gurson damage parameters were determined for unirradiated T91 material supplied by SCK-CEN, Belgium. Similar analyses on irradiated T91 are currently in progress.

ACKNOWLEDGEMENTS

The authors would like to thank Dr. L. Malerba (SCK-CEN, Belgium) for providing the T91 material for carrying out the SP experiments listed in this work.

REFERENCES

- [1] N. NAVEEN KUMAR et.al., *Computational Materials Science* 53 (2012) 258–267.
- [2] M. I. MENDELEV, D. J. SROLOVITZ, G. J. ACKLAND, D. Y. SUN, M. ASTA., *Philosophical Magazine*, **83** (2003) 3977.
- [3] A. STUKOWSKI, BABAK SADIGH, P. ERHART, A. CARO., *Modeling and Simulation in Materials Science and Engineering*", **17** (2009) 75–105.
- [4] T. SELETSKAIA, YU. N OSETSKY, R. E. STOLLER, G. M. STOCKS., *Journal of Nuclear Materials*, **367–370** (2007) 355–360.
- [5] D. TERYTYEV, N. JUSLIN, K. NORDLUND, N. SANDBERG., *Journal of Applied physics*, **105** (2009)103506.
- [6] R. A. AZIZ, ALEC R. JANZEN, MICHAEL R. MOLDOVER., *Physical Review Letters*, **74** (1995) NUM 9.
- [7] A. CARO et al., *Journal of Nuclear Materials* (2011), doi:10.1016/j.jnucmat.2011.07.010
- [8] YU. N. OSETSKY, D.J. BACON, "An atomic level model for studying the dynamics of edge dislocations in metals", *Modeling and Simulation in Materials Science and Engineering*, **11** (2003) 427–446.
- [9] C. KOHLER, P. KIZLER, S. SCHMAUDER., *Modeling and Simulation in Materials Science and Engineering*, **13** (2005) 35–45.
- [10] G. MONNET., *Philosophical Magazine*, **86** 36 (2006)5927–5941.
- [11] SYLVAIN QUEYREAU., Ph.D. thesis, Univ. Pierre et Marie Curie Paris, 2008.
- [12] E. N. CAMPITELLI, P. SPATIG, J. BERTSCH, C. HELLWIG, "Assessment of irradiation-hardening on Eurofer 97 and Zircaloy 2 with punch tests and finite-element modeling", *Materials Science and Engineering A* **400–401** (2005) 386–392.
- [13] Y-S. CHANG, J-M. KIM, J-B. CHOI, Y-J. KIM, M-C. KIM, B-S.LEE, "Derivation of ductile fracture resistance by use of small punch specimens", *Engineering Fracture Mechanics* **75** (2008) 3413–3427.
- [14] A. L. GURSON, "Continuum of ductile rupture by void nucleation and growth: Part I–Yield criteria and flow rules for porous ductile media", *Journal of Engineering Materials Technology* **99** (1977) 2–55.
- [15] V. TVERGAARD, A. NEEDLEMAN, "Analysis of the cup-cone fracture in a round tensile bar", *Acta Metall.* **32** (1984) 157–169.
- [16] B. TANGUY, C. BOUCHET, S. BUGAT, J. BENSON, "Local approach to fracture based prediction of ΔT_{56j} and $\Delta T_{K_{Ic100}}$ shifts due to irradiation for an A508 Pressure vessel steel", *Engineering Fracture Mechanics* **73** (2006) 191–206.
- [17] N. NAVEEN KUMAR et.al, "Ascertaining the micro-mechanical damage parameters of T91 ferritic/martensitic steel using a small punch test", *Transactions of International Conference on Structural Mechanics in Reactor Technology (SMiRT 21)*, 2011, India.

IRRADIATION TOLERANCE AND ION-IRRADIATION EFFECTS ON NANO-OXIDE DISPERSION STRENGTHENED STEELS

A. KIMURA
Institute of Advanced Energy, Kyoto University,
Gokasho, Uji, Kyoto,
Japan
Email: kimura@iae.kyoto-u.ac.jp

Abstract

Radiation tolerance of nano-oxide dispersion strengthened steels was assessed by investigating phase stability and He-bubble formation behavior under irradiation at elevated temperatures. Ion irradiation experiments were performed with 6.4 MeV Fe ions at 650°C up to a nominal displacement damage of 60 dpa, which corresponds to 180 dpa at the peak position. Microstructural examinations were carried out using TEM and EDX. No significant change in grains and grain boundaries as well as morphologies of complex oxides was detected after the ion irradiation up to 60 dpa at 650°C. The complex oxides of the ODS steels are considered to be highly stable in the irradiation environment. Energy-degraded helium ions were simultaneously implanted into the steels to the amount of 1000 appm. Microstructural observations showed that helium cavities formed on dislocations, precipitations, lath boundaries, and prior austenitic boundaries in F82H implanted with 1000 appm He. On the other hand, helium cavities were distributed in the matrix of 9Cr-ODS steel. It was revealed that oxide particles in the 9Cr-ODS steel act as effective trapping sites for helium. He implantation was carried out by a cyclotron with a beam of 50 MeV α -particle up to 1000 appm at ~550°C. In the case of F82H, a ferritic-martensitic (F/M) steel the ductile-brittle transition temperature (DBTT) shift induced by the He implantation was about 60°C, and the brittle fracture mode changed from cleavage to grain boundary fracture in the He-implanted area. In contrast, no DBTT shift or fracture mode change was observed in He-implanted 9Cr-ODS and 14Cr-ODS steels. It can be concluded that the radiation tolerance of ODS steels stems from their high capacity for trapping point defects and defect clusters and also helium at interfaces of the oxide particles and the matrix. Fine dispersion morphology increases the interface area and therefore trapping sites, which may account for the observed radiation tolerance of the ODS steels.

1. BACKGROUND

Oxide dispersion strengthened (ODS) steels based on ferritic/martensitic (F/M) steels have been developed to improve creep strength at elevated temperatures. Many ODS steels have been developed [1–8]. The “Super ODS Steels” R&D program was started in Japan in 2005 to develop new fuel cladding material for next generation nuclear systems. The objective of the program is to produce an excellent cladding material having good performance with 1) high strength at temperatures up to 700°C, 2) high resistance to neutron irradiation up to 200 dpa and 3) high resistance to corrosion in coolants such as super critical pressurized water (SCPW) and lead-bismuth eutectic (LBE) [9–11]. For high corrosion resistance, high levels of chromium (>14 wt %) and aluminum-added ODS steels are considered to be such candidates for advanced cladding material. Since the high performance of ODS steels stems from the finely dispersed nano-scaled oxide particles [12–16], phase stability of the particles under irradiation is hopefully inevitable. The objective of this research is to assess the phase stability of oxide particles in the Al-added ODS steels under heavy ion-irradiation and to investigate the cavity formation or swelling behavior of ODS steels irradiated with a dual ion-beam. Another objective of this research is to assess the efficiency of He trapping by nano-scaled oxide particles by comparing the effects of He-implantation on the impact fracture behavior between a conventional martensitic steel (F82H) and ODS F/M steels.

2. RESULTS

2.1 Experiment

Chemical compositions of the materials used in this research are shown in Table 1 (where HT-heat treatment). The base material was a 16Cr-4Al-0.1Ti-0.35Y₂O₃ ODS ferritic steel, which was designated as SOC-1. Titanium- and zirconium-added new ODS steels were produced from the base. The pre-alloyed powders were prepared at KOBELCO Ltd. These powders were mechanically alloyed with Y₂O₃ powder in either an argon or helium gas atmosphere. The mixed powders were consolidated by a hot extrusion method at 1150°C.

Subsequently, the consolidated ODS steels were heat treated at 1050°C for 1 h followed by air cooling. The disk-shaped specimens, with a diameter of 3 mm and a thickness of 0.25 mm, were cut and their surfaces were polished by mechanical polishing and electropolishing.

The dual-beam material irradiation facility for energy technology (DuET) at the Institute of Advanced Energy, Kyoto University, was used for this research. Test specimens were irradiated with 6.4 MeV Fe³⁺ ions by using a 1.7 MeV tandem accelerator. The irradiation temperature range was from 300°C to 650°C. The nominal dose rate and the dose of ion-irradiation were 5×10^{-4} dpa/s and up to 60 dpa at a depth of approximately 600 nm from the surface, respectively. TEM investigation was performed using a JEOL JEM2010 and a JEM2200FS with EDX. Nano-indentation tests were carried out to measure the irradiation hardening using ELIONIX ENT-1100a [17, 18].

TABLE 1. CHEMICAL COMPOSITIONS OF THE STEELS TESTED IN THIS RESEARCH

Materials	C	Cr	Al	W	Si	Mn	Ni	Ti	Zr	Y ₂ O ₃	HT
SOC-1	0.02	16.11	3.44	0	0.02	0.03	-	0.1	-	0.35	a
SOC-5	0.02	15.95	0	0	0.01	0.01	-	0.1	-	0.35	a
SOCP-1	0.031	14.7	3.3	1.9	0.02	0.02	-	-	0.6	0.35	a
SOCP-3	0.045	13.6	0	1.9	0.03	0.03	-	0.15	-	0.35	a
14Cr-	0.04	13.64	4.12	1.65	0.033	0.06	-	0.28	-	0.38	a
9Cr-ODS	0.14	8.67	-	1.96	0.05	0.05	0.06	0.23	-	0.34	b
F82H	0.09	7.71	-	1.95	0.11	0.16	0.02	0.01	-	-	c

a) Normalized at 1323K, 1h, AC

b) Normalized at 1323K, 1h, AC; tempered at 1073K, 1h,

c) Normalized at 1313K, 0.5h, AC; tempered at 1023K, 1h, AC

The materials used in the evaluation of helium embrittlement were F82H steel and two types of ODS steel which were either 9Cr- or 14Cr-ODS steels [19, 20]. Miniaturized Charpy V-notch (CVN) specimens for Charpy impact test were machined to 1.5 × 1.5 × 20 mm, 0.3 mm in notch depth, 0.08 mm in notch root radius and 30° in notch angle. Helium ion implantation was performed using 50 MeV α-particles from the AVF cyclotron in Tohoku University. The projected range of 50 MeV He ions in a Fe-9Cr steel was calculated to be about 380 μm by the TRIM code [21]. A tandem-type energy degrader system was used to obtain uniform depth distribution of He atoms in the specimens. Nominal He concentration was about 1000 appm, which was calculated from the beam current. The average displacement damage produced by the He ions was about 0.28 dpa. The implantation temperature was 550 ± 10°C. Vickers hardness tests on the irradiated area, instrumented impact tests, and fracture surface analysis were carried out after He implantation.

2.2 Phase stability assessment

2.2.1 Effect of irradiation temperature

The results of nano-indentation test are shown in Fig. 1. The micro hardness after the irradiation at 300°C increases with increasing dose, and appears to saturate at 5–10 dpa. At 500°C, alloy SOC-1 keeps almost the same hardness up to 10 dpa, and a softening was observed at 650°C. According to the results of neutron irradiation experiments, small irradiation hardening was also observed after the irradiation at 500°C, which is in contrast to that of reduced activation ferritic steels (RAFS) showing almost no change in the tensile strength. The mechanism of relatively low hardening in the ODS steel after irradiation at 500°C is considered to be due to the higher thermal stability of dislocation loops that cause hardening. At 300°C, fine dislocation loops were induced by ion-irradiation. At 500°C, these dislocation loops grow and incorporate into the original existing dislocation network. The

main contributors to the irradiation hardening are considered to be dislocation loops and precipitates.

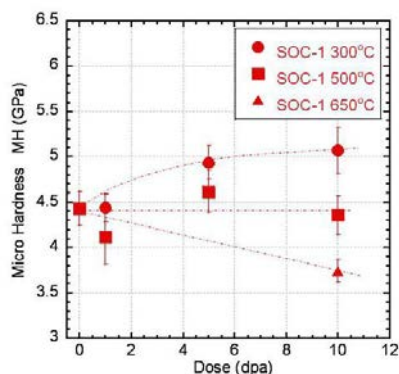


FIG. 1. Irradiation hardening of SOC-1 investigated by nano-indentation [3].

2.2.2 Phase stability of nano-particles under ion-irradiation at 650°C

In the ODS steels, fine dispersed oxide particles strongly contribute to high temperature strength. Alternation of chemical compositions of the steel affects the dispersion morphology of oxide particles through the changes in the type of oxide as well as their structure in the steel. TEM-EDX analysis indicated that SOC-1, which is a 16Cr-4Al-0.1Ti-0.35Y₂O₃ ODS steel, is strengthened by (Y, Al) complex oxides. SOC-5 contains no Al and has (Y, Ti) oxides but no (Y, Al) oxides. SOCP-1 is strengthened by (Y, Zr) complex oxides without any addition of Ti. The oxides in SOCP-3 are so fine that the characterization by TEM is difficult, but they are considered to be (Y, Ti) complex oxides because of the chemical compositions of SOCP-3. SOCP-3 contains 2 wt% W, while SOC-5 doesn't. Furthermore, the processing condition is different between the steels.

Fig. 2 shows the TEM images of dispersed oxides in the ODS steels before and after irradiation at 650°C up to 60 dpa at 600 nm depth, which correspond to 180 dpa at the peak position. At any depth, no significant irradiation-induced changes in the dispersion morphology of oxide particles, such as the size and number density of oxides, were detected by TEM examination irrespective of steel composition. The size distributions of dispersed oxides in the TEM images are summarized in Fig. 3. Fig. 4 shows the comparison of averaged size among the steels.

Finally, in this research, we observed no significant change in the dispersion morphology of oxide particles irrespective of steel compositions or type of oxide particle during ion-irradiation up to 60 dpa (180 dpa at a peak position) at 650°C. However, it is also expected that irradiation tolerance might be controlled by the coherency between oxide particles and matrix since the interfaces can absorb point defects and their clusters, and contribute as a sink of defect structures. It is thought that the strain field surrounding oxide particles will be the most important factor of radiation tolerance. Therefore coherency measurements are critical to assess the effectiveness of oxide particles as a defect structure absorber.

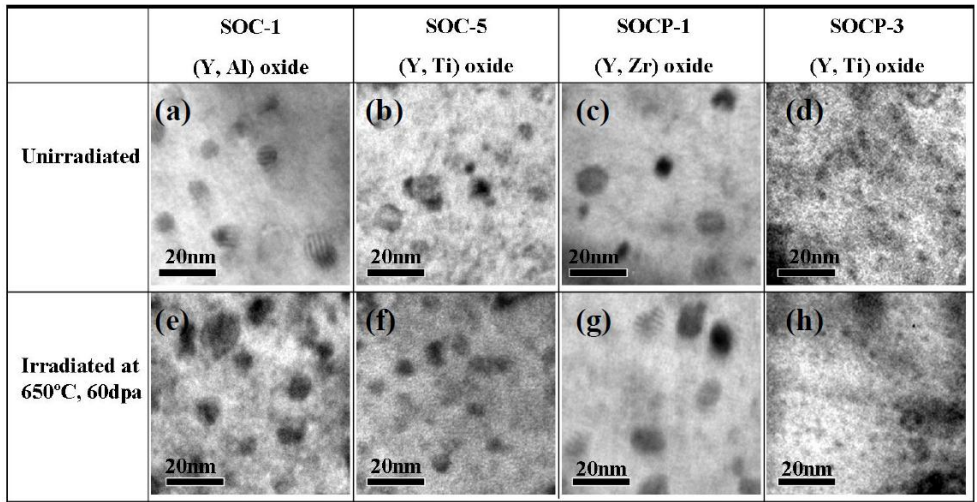


FIG. 2. TEM images of complex oxides on the Super ODS steels [3].

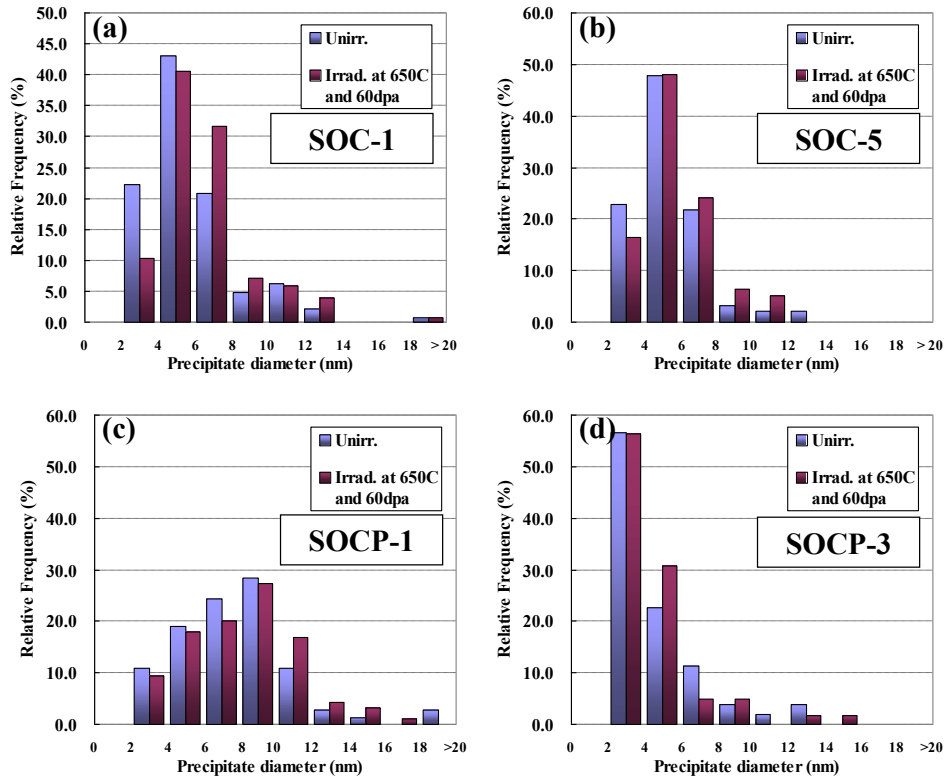


FIG. 3. Size distribution histograms of (a) SOC-1, (b) SOC-5, (c) SOCP-1, and (d) SOCP-3, before and after irradiation at 650 °C to 60 dpa [3].

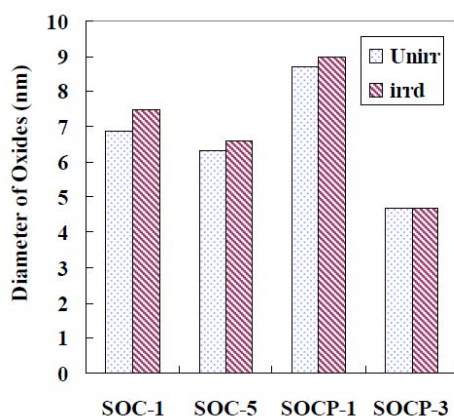


FIG. 4. Average diameter of oxides in unirradiated and irradiated Super ODS steels [3].

2.3 Helium induced swelling behaviour

2.3.1 Void swelling

Fig. 5 shows microstructures of a) F82H and b) 9Cr ODS steel after ion-irradiation at 550°C up to 0.4 dpa with 1000 appm helium implantation. Aligned cavities along dislocations are observed in the helium implanted region of the F82H steel, while they are scarce in the 9Cr-ODS steel where voids distribute more homogeneously in the matrix. TEM images of F82H show that cavities were formed on a) the interfaces between precipitates (carbides) and matrix, b) line dislocations, c) lath boundaries, and d) prior austenitic grain boundaries. The aligned networks of cavities in Fig. 5 are considered to be formed at line dislocations. Fig. 5(a) also showed the formation of cavities at grain boundaries, suggesting possible degradation of fracture toughness through intergranular embrittlement in F82H steel. In the 9Cr-ODS steel helium cavities were dispersed in the matrix and some cavities were also observed on dislocations. There was no formation of cavities at grain boundaries in the ODS steel.

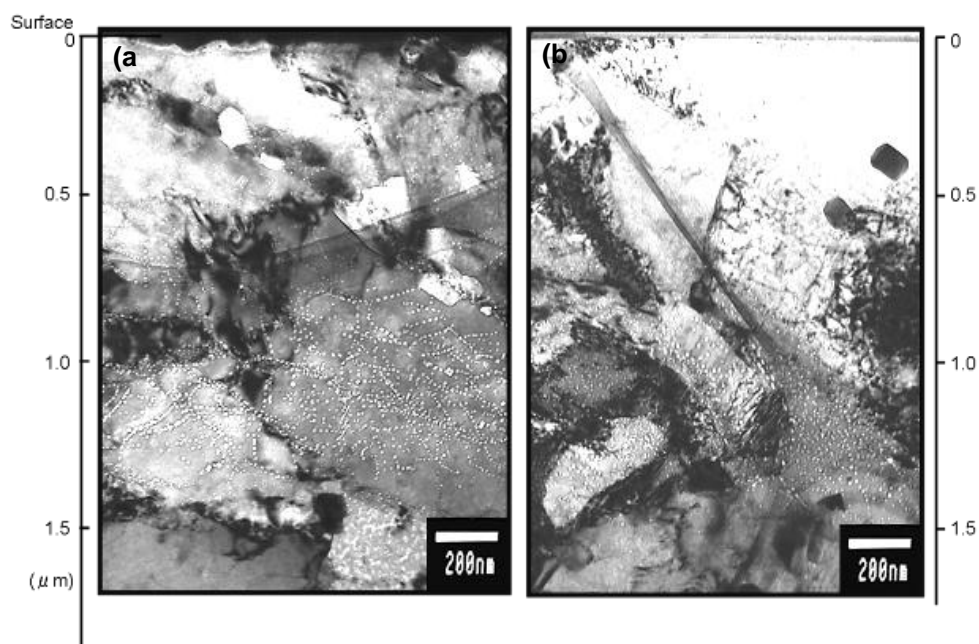


FIG. 5. Cross-sectional TEM images in ion-irradiated steels. (823K, 0.4dpa, 1000appmHe)
(a) F82H (b) 9Cr-ODSS.

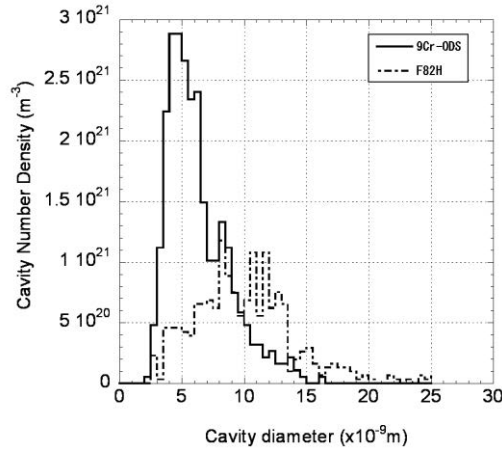


FIG. 6. Helium cavity size distribution in ion-irradiated F82H steel and 9Cr-ODS steel.

TABLE 2. SWELLING IN ION-IRRADIATED STEELS.

Material	Mean cavity diameter, nm	Cavity density, m ⁻³	Swelling, %
F82H	9.80	1.60×10^{22}	1.23
9Cr-ODS	6.07	2.67×10^{22}	0.49

Size distributions of helium cavities in F82H and 9Cr-ODS steel are shown in Fig. 6. F82H showed a broad distribution up to several tens of nm. On the other hand, 9Cr-ODS steel showed a narrower and smaller distribution of cavities with higher density. Table 2 shows the mean cavity diameter, number density, and swelling in both of the steels implanted up to 1000 appm He. It is noted that the mean size and number density of cavities in the 9Cr-ODS steel is smaller than that of the F82H steel. Swelling values are 1.23% in the F82H steel and 0.49% in the 9Cr-ODS steel. These results reveal that the interface of nano-oxide particles/matrix in the 9Cr-ODS steel captured helium to distribute uniformly in the matrix of the 9Cr-ODS steel, and suppressed the formation of coarse cavities both in the matrix and at grain boundaries.

The results of impact tests with using sub-sized specimens of F82H, 9Cr-ODS and 14Cr-ODS steels are shown in Fig. 7 [22]. The Charpy impact energy vs. temperature curves of F82H before and after He implantation revealed that the DBTT was shifted by 70°C after 1000 appm He implantation. The Vickers hardness test results indicate a slight hardening ($\Delta H_v = 40$) in the He-implanted area of these specimens. Fig. 8 shows a SEM micrograph of the He-implanted specimens that underwent brittle fracture at -60°C. The grain boundary surface was observed only from the bottom of the notch to a depth of about 400 μm , which corresponds to the He-implanted region. No grain boundary fracture was observed in the He-implantation range.

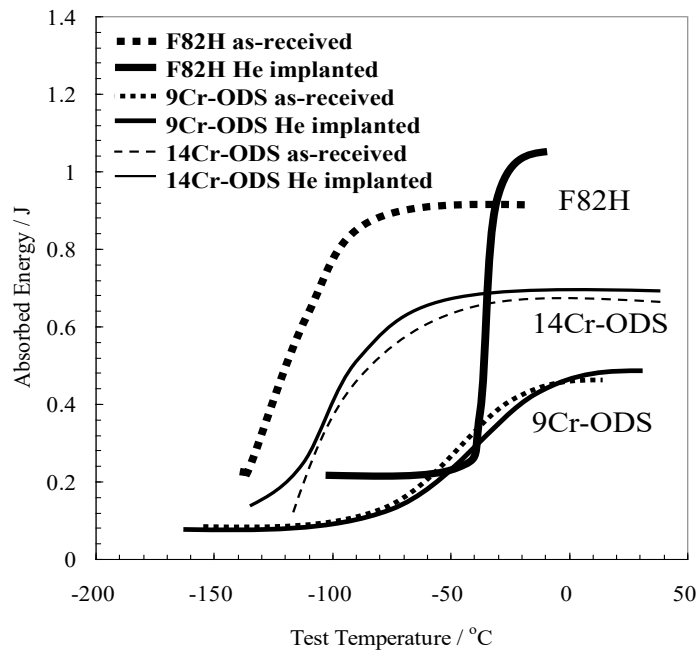


FIG. 7. Summary of Charpy impact energy vs. temperature curves [22].

In contrast to F82H, it can be seen that the implantation of 1000 appm of He had almost no effect on the DBTT of 9Cr-ODS steel. Fig. 8 (b) shows the fracture surface of the He-implanted specimen that ruptured in a brittle manner at -120°C . The fracture mode in both the He-implanted and un-implanted regions of the 9Cr-ODS steel was cleavage, and no grain boundary type surface was observed. The hardness of the He-implanted area decreased relative to the un-implanted area ($\Delta H_v = -100$), indicating the possibility of irradiation-induced recovery of the dislocation structure. Fig. 8(c) shows TEM micrographs of a He-implanted 9Cr-ODS, which was irradiated by 3MeV He implantation to 1000 appm at 550°C using the dynamitron-type accelerator at Tohoku University. An arrow in the figure shows a grain boundary. Fine bubbles were uniformly distributed in the matrix, and no bubble segregation on grain boundaries was observed. These indicate that the He trapping capacity induced by oxide particles is still effective after the He implantation up to 1000 appm at 550°C . This type of bubble distribution is due to the fine oxide particles and fine grain structure of the ODS steels.

The DBTT of both the as-received and He-implanted 14Cr-ODS steel was -100°C . No fracture mode change due to He implantation was observed. The DBTT of 14Cr-ODS steel did not change upon the He implantation but a slight decrease of hardness ($\Delta H_v = -15$) was observed in the He-implanted area. From the view point of microstructure, the 9Cr-ODS steel has martensitic structure and the 14Cr-ODS steel has ferritic structure. Both specimens have fine and dense oxide particles [19, 20]. Yutani et al., showed He bubble trapping behavior on the fine oxide particles after ion irradiation. These results reveal that fine and dense oxide particles in the ODS steels have enough trapping capacity of He to 1000appm at around 600°C .

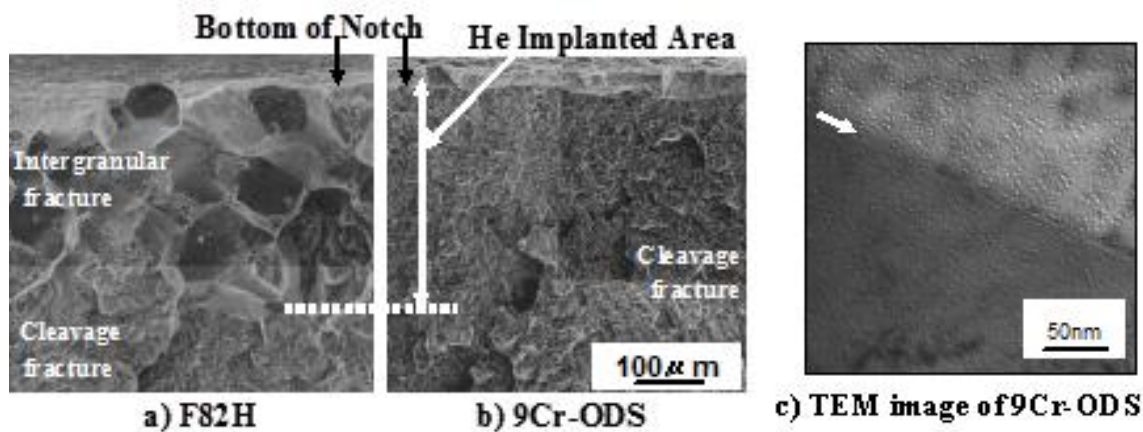


FIG. 8. Typical fracture surfaces for He-implanted impact test specimen of a) F82H tested at -60°C , b) 9Cr-ODS steel tested at -120°C and TEM image of a grain boundary of 9Cr-ODS steel [22].

3. DISCUSSION

There are some published reports on the irradiation effects on ODS alloys. Monnet et al. reported that fine oxides disappeared after the heavy neutron irradiation over 60 dpa in Phénix reactor [23]. Allen et al. investigated the irradiation effects on (Y, Ti) oxide particles by 5 MeV Ni ion-irradiation up to 150 dpa at 700°C , and reported a reduction of the particle size [24]. On the other hand, an atom probe tomography research by Pareige et al. indicated high thermal stability of nano-clusters in 12YWT against 150 keV Fe ion-irradiation up to 0.7 dpa at 300°C [25]. Our previous research also showed the stability of (Y, Al) and (Y, Ti) oxides up to 150 dpa at 670°C [26].

Although there is not so many research of neutron irradiation effect at higher temperature, a recent neutron irradiation research by McClintock et al. reported that the 14YWT alloy had a superior irradiation resistance up to 1.5 dpa at 670°C [27]. Irradiation effects on the microstructure of ODS steels were investigated by an ion-irradiation experiment and TEM observation. Irradiation temperature was from 300°C to 650°C , and the nominal dose of ion-irradiation was up to 60 dpa. TEM examination revealed that the ODS steels used in this current research have different types of dispersed oxides, SOC-1 has (Y, Al) oxides, SOC-5 and SOCP-3 have (Y, Ti) oxides, SOCP-1 has (Y, Zr) oxides. At 300°C , dense dislocation loops were formed by ion-irradiation in addition to the originally existed dislocations induced during hot-extrusion. Over 500°C , dislocation loops were not formed but were incorporated with the existing dislocations. The size distribution of complex oxides before and after ion-irradiation was compared, and any significant modification could not be detected. Microstructural evolution did not occur up to 60 dpa at 650°C , indicating that the dispersed oxides in the ODS steels are stable at the tested conditions.

Helium implantation experiments at high concentration ($\sim 1000\text{appm}$) were performed for the F82H and ODS steels to compare cavity formation behaviour. In the irradiation experiment, the cavities are formed on dislocations and at grain boundaries in RAF F82H steel, but the cavities in the ODS steel were mainly formed at the interfaces of oxide particles and matrix. Based on the microstructural observation after helium implantation, intergranular fracture in the RAF steel is considered to be due to the formation of many cavities on prior austenitic boundaries. It was confirmed that helium atoms are trapped by oxide particles in the ODS steels. Oxide particles act as trapping sites for suppression of swelling and intergranular embrittlement as a result of preventing helium from transport and gathering at grain boundaries.

The effect of high-concentrations of He implanted at 550°C on the impact fracture behaviour of 9Cr- and 14Cr-ODS steels was compared to that of F82H using high-energy α -particle irradiation by accelerators. Almost no increase in DBTT and no intergranular fracture due to He implantation was observed in 9Cr- and 14Cr-ODS steels, while F82H showed both a DBTT increase and intergranular fracture. The finely dispersed oxides and fine grain size or large grain boundary area in these ODS steels are considered to effectively behave as He trapping sites. Suppression of irradiation hardening and grain boundary degradation are anticipated for ODS steels up to 1000 appm He at around 550°C.

4. CONCLUSIONS

Radiation tolerance of nano-oxide dispersion strengthened steels was assessed by investigating the phase stability and He-bubble formation behaviour under ion irradiation at elevated temperatures.

1) No significant change in grains and at grain boundaries as well as changes in morphology of complex oxides was detected after ion irradiation up to 60 dpa (180 dpa at a peak position) at 650°C. The stable complex oxides are considered to provide microstructural stability of the ODS steels in the irradiation environment.

2) Energy-degraded helium ions were simultaneously implanted into the steels at 1000 appm. Microstructural observations showed that helium cavities were formed on dislocations, precipitations, lath boundaries, and prior austenitic boundaries in F82H. On the other hand, helium cavities were distributed in the matrix of 9Cr-ODS steel. It was revealed that oxide particles in the 9Cr-ODS steel act as effective trapping site for helium.

3) He implantation was carried out by a cyclotron with a beam of 50 MeV α -particles up to 1000 appm at around 550°C. In the case of F82H, the ductile-brittle transition temperature (DBTT) was shifted by He implantation by 60°C, and the brittle fracture mode was changed from cleavage to grain boundary fracture in the He-implanted area. In contrast, no DBTT shift or fracture mode change was observed in He-implanted 9Cr-ODS and 14Cr-ODS steels.

It can be concluded that the radiation tolerance of ODS steels stems from the high capacity for trapping point defects, their clusters and helium at interfaces of oxide particles and the matrix. Refining dispersion morphology increases the interface area and therefore trapping sites, which appears to produce radiation tolerance of the ODS steels.

REFERENCES

- [1] R. L. KLUEH, et al., "Tensile and creep properties of an ODS ferritic steels", *Journal of Nuclear Materials* **307–311** (2002) 772–777.
- [2] S. UKAI, et al., "Characterization of high temperature creep properties in recrystallized 12Cr-ODS ferritic steels claddings", *Journal of Nuclear Science and Technology* **39** (2002) 872–879.
- [3] H. KISHIMOTO, et al., "Super ODS Steels R&D for fuel cladding of next generation nuclear systems, Ion-irradiation effects at elevated temperatures", *Proc. of 2009 International Congress on Advances in Nuclear Power Plants*, 9219 (2009) 1–8.
- [4] M. J. ALINGER, et al., "On the role of alloy composition and processing parameters in nanocluster formation and dispersion strengthening in nanostructured ferritic alloys", *Acta Materialia* **57** (2009) 392–406.
- [5] D. S. GELLES, "Microstructural examination of commercial ferritic alloys at 200 dpa", *Journal of Nuclear Materials* **233–237** (1996) 293–298.

- [6] B. DUBIEL, et al., "Correlation of the microstructural and the tensile deformation of Incoloy MA956", *Journal of Materials Processing Technology* **53** (1995) 121–130.
- [7] A. CZYRSKA-FILEMONOWICZ, B. DUBIEL, "Mechanically alloyed, ODS alloys: structure properties", *Journal of Materials Processing Technology* **64** (1997) 53–64.
- [8] M. KLIMENKOV, et al., "New insights into the structure of ODS particles in the ODS-Eurofer alloy", *Journal of Nuclear Materials*, in press.
- [9] A. KIMURA, et al., "Fuel cladding materials R&D for high burn-up operation of advanced nuclear energy systems", *Proceedings of Int. Congress on Advances in Nuclear Power Plants, ICAPP'06*, 2229–2237 (2006).
- [10] H. S. CHO, et al., "Corrosion properties of ODS steels in super-critical water environment", *Journal of Nuclear Materials* **329–333** (2004) 387–391.
- [11] P. HOSEMANN, H.T. THAU, A.L. JOHNSON, S.A. MALOY, N. LI, "Corrosion of ODS steels in lead–bismuth eutectic", *Journal of Nuclear Materials* **373** (2008) 246–253.
- [12] S. UKAI, et al., "R&D of ODS ferritic martensitic steels for FBR", *Journal of Nuclear Materials* **258–263** (1998) 1745–1749.
- [13] S. UKAI, M. FUJIWARA, "Perspective of ODS alloys application in nuclear environments" *Journal of Nuclear Materials* **307–311** (2002) 749–757.
- [14] S. UKAI, et al., "Tube manufacturing trials by different routes in 9CrW-ODS martensitic steels", *Journal of Nuclear Materials* **329–333** (2004) 356–361.
- [15] N. AKASAKA, et al., "Microstructural changes of neutron irradiated ODS ferritic and martensitic steels", *Journal of Nuclear Materials* **329–333** (2004) 1053–1056.
- [16] S. YAMASHITA, et al., "Effect of mechanical alloying parameters on irradiation damage in ODS steels", *Journal of Nuclear Materials* **283–287** (2000) 647–651.
- [17] M. ANDO, et al., "Evaluation of hardening behavior of ion irradiated reduced activation ferritic/Martensitic steels by an ultra-micro-indentation technique", *Journal of Nuclear Materials* **307–311** (2002) 260–265.
- [18] Y. KATOH, et al., "Radiation and helium effects on microstructures, nano-indentation properties and deformation behaviour in ferrous alloys", *Journal of Nuclear Materials* **323** (2003) 251–262.
- [19] S. UKAI, et al., "Development of 9Cr-ODS martensitic steel claddings for fuel pins by means of ferrite to austenite phase transformation", *J. Nuclear Science and Technology* **39**, No.7, (2002) 778–788.
- [20] H.S. CHO, A. KIMURA, S. UKAI, M. FUJIWARA, "Corrosion properties of oxide dispersion strengthened steels in super-critical water environment", *Journal of Nuclear Materials* **329–333** (2004) 387–391.
- [21] J. P. BIERSACK, J. F. ZIEGLER, TRIM85 Program, IBM Corp., Yorktown, NY, 1985.
- [22] A. HASEGAWA, et al., "Effects of helium on ductile-brittle transition behavior of RAFAE after high concentration He implantation at high temperature", *Journal of Nuclear Materials* **386–388** (2009) 241–244.
- [23] I. MONNET, et al., "Microstructural investigation of the stability under irradiation of ODS ferritic steels", *Journal of Nuclear Materials* **335** (2004) 311–321.
- [24] T.R. ALLEN, et al., "Radiation response of a 9Cr ODS steel to heavy ion-irradiation", *Journal of Nuclear Materials* **375** (2008) 26–37.
- [25] P. PAREIGE, et al., "Stability of nanometer-sized oxide clusters in mechanically-alloyed steel under ion induced displacement cascade damage conditions", *Journal of Nuclear Materials*, in press.
- [26] H. KISHIMOTO, et al., "Heavy-ion irradiation effects on the morphology of complex oxide particles in ODS ferritic steels", *Journal of Nuclear Materials* **367–370** (2007) 179–184.

- [27] D. A. McCLINTOCK, et al., "Mechanical properties of neutron irradiated nano-structured ferritic alloy14YWT", Journal of Nuclear Materials, in press.

SIMULATION OF NEUTRON DAMAGE EFFECTS IN EXPERIMENTS ON STEELS IRRADIATED WITH NEUTRONS OR KRYPTON IONS

DR. OLEG P. MAKSIMKIN
Institute of Nuclear Physics,
National Nuclear Center,
Kazakhstan
maksimkin@inp.kz

Abstract

In the first portion of our SMORE activity, studies of changes induced by irradiation in microstructure, density and microhardness of ferritic-martensitic steel 12Cr13Mo2NbVB, also designated as EP-450, were performed. The obtained results show that radiation and thermal exposure lead to phase recrystallization of this initially two-phase or "duplex" steel and also show dissolution of pre-existing carbides. As a result, optical micrographs show an increase in volume fraction of ferrite with increasing irradiation temperature with the volume fraction of ferrite increasing three times compared to the unirradiated condition. Also observed were strongly correlated changes of density, microhardness and irradiation-induced swelling of steel which showed maximum values at 380°C and 61 dpa. In the second portion of our effort investigations proceeded on the stainless steel 12Cr18Ni10Ti in the original, strained and irradiated states using ^{84}Kr ions, $E=1,56$ MeV/nucleon, at doses of $1 \cdot 10^{15}$ ion/ cm^2 and $4 \cdot 10^{15}$ ion/ cm^2 using magnetometry, X-ray structure analysis and SEM investigations with EBSD analysis. Application of the EBSD technique allowed us to determine the microstructural differences in non-irradiated and irradiated samples, especially the α -phase and ϵ - phase was formed in the near-surface layer.

1. EXPERIMENTAL RESULTS

1.1 EP-450 ferritic-martensitic steel irradiated in BN-350 reactor

Microstructural changes and mechanical properties were investigated of 12Cr13Mo2NbBV (EP-450) ferritic-martensite stainless steel of the following composition: C-0.13; Cr-12.83; Ni-0.14; Mo-1.62; Nb-0.45; Si-0.4; Mn-0.34; V-0.16 (wt. %). This material was used as the hexagonal-shaped wrapper of a fuel assembly removed in 1992 from the core active region of the BN-350 nuclear reactor located in Aktau, Kazakhstan.

In the "hot" chamber of the BN-350 reactor the changes in shape S (corner to corner) and R (flat to flat) of the wrapper were determined by means of specially designed device (Fig.1) which was moved along the hexagonal duct and fuel assembly. The fuel assembly was stored in water for 8 years and then removed so that samples could be cut from it. These samples of size (50 × 10 × 2 mm) were cut from «+375 mm», «+75 mm» and «-375 mm» levels, measured from the core midplane. The samples then were transported by railway from Aktau to the Institute of Nuclear Physics in Almaty to perform our investigations. In the "hot" chamber of VVR-K reactor the steel plates were cut into smaller samples for investigation. Particularly, for metallography samples of 5x10x2 mm were cut from the region close to the corner edge of hexagonal wrapper. The outer surface of the wrapper was studied. Sample preparation included grinding, polishing and electropolishing. The characteristics of the investigated samples are given in Table 1.

TABLE 1. PARAMETERS OF IRRADIATION OF STEEL SAMPLES

Distance from midplane, mm	Maximum damaging dose, dpa	Irradiation temperature, °C	Sample weight, g	Activity level, $\mu\text{R}/\text{sec}$
+375	40	420	0.8014	293
+75	61.6	380	0.8412	383
-375	40.3	300	0.8746	449

1.2 Study of EP-450 steel samples irradiated in BN-350 reactor

It is known that the initial microstructure of ferrite-martensitic steels is determined by its chemical composition and heat treatment parameters, allowing to produce duplex steels with both ferrite grains and sorbite (tempered martensite) grains. Tsykanov et al. showed that the ratio ferrite/sorbite=1 arises after water quenching from 1059°C and subsequent tempering at 750–770°C for 1 hour in vacuum [1]. The same ratio of ferrite and sorbite grains was observed in after austenization at 1050°C and subsequent air cooling and followed by annealing at 720°C for 1 hour [2]. Additionally, the same ferrite/sorbite ratio was observed after austenization at 1050°C (30 min) and annealing at 720°C for 1 hr [3]. The ferrite grain size was 10–30 microns.

After austenization at 1050°C (30 min) and tempering at 780–800°C for 40 min, however the ferrite/sorbite ratio was 1:5.7 [2], and after heat treatment (1050°C, 30 min + 850°C 5 sec) the volume fraction of ferrite grains was 30–40% (i.e. ferrite/sorbite = 1:1.5) [4], demonstrating that the ratio is variable and sensitive to the processing conditions.

It was also shown in earlier studies that ferrite-martensite steels during neutron irradiation developed significant structural changes and phase transformations, which were primarily determined by the initial state of the alloy and by the irradiation conditions [4].

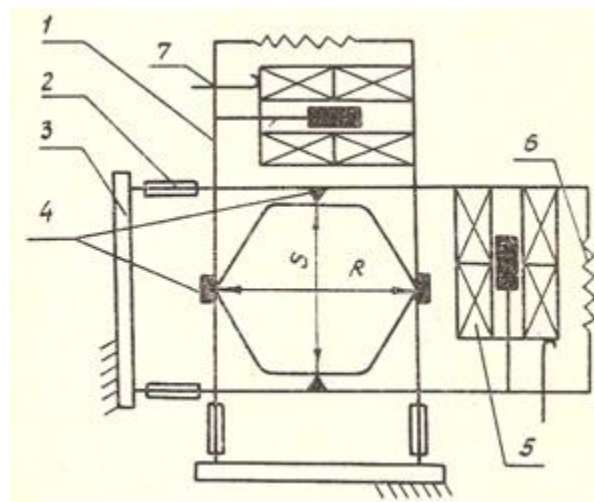


FIG. 1. The scheme of measuring device: 1 – lever arms; 2 – bracket; 3 – flat spring; 4 – probes; 5 – differential transformer transducer; 6 – spring; 7 – tuning screw. Changes in R are primarily a measure of swelling and changes in S are a measure of both swelling and irradiation creep.

Studies of radiation-induced microstructural changes, strength and density were performed. Both optical (Neophot-2) and electron (JEM 100CX) microscopy was used to characterize the samples. Weighing of the irradiated samples in both air and water to determine density change was carried using a VLR-20 scale (± 0.05 mg accuracy). Microhardness was determined using the PMT-3 device with a 50 g load on the indenter ($\pm 3\%$). To perform microhardness measurements for the different phases (ferrite, sorbite), the surface of a steel sample was first etched to reveal grain boundaries between the two grain types.

Fig. 2 shows the distribution of shape changes along the wrapper. It can be seen that the amount of shape change reaches a maximum in the middle of the fuel assembly. Fig. 3 and 4 illustrate steel microstructures at different magnifications which are characterized by ferrite (bright) and sorbite (dark) grains. Micrographs obtained at low magnification (x200, Fig. 3)

show that ferrite-sorbite structure present in steel for all levels of the fuel assembly, but the volume fraction of the components (ferrite/sorbite) is different. The volume fraction measurements were performed using the line intercept method for micrographs taken at magnification of $\times 200$.

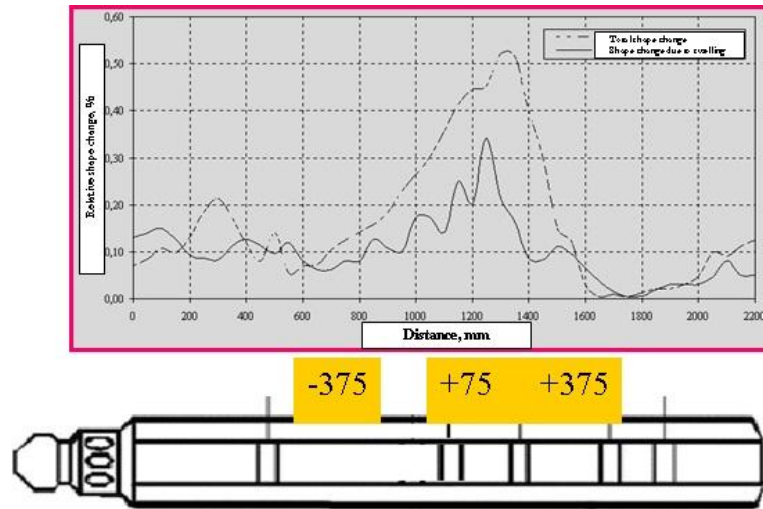


FIG.2. Shape changes in wrapper of fuel assembly made of EP-450 steel. The upper curve is a measure of creep plus swelling while the lower curve is a measure of swelling only.

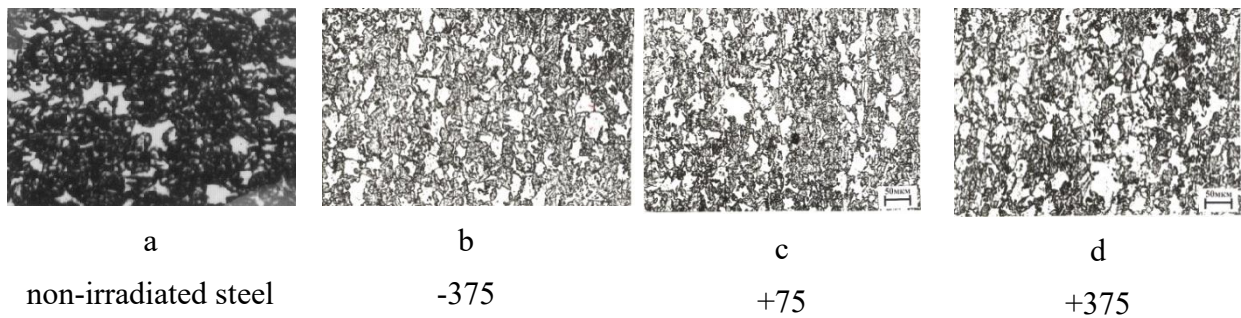


FIG.3. Microstructure before irradiation and after irradiation at different elevations and irradiation conditions ($\times 200$).

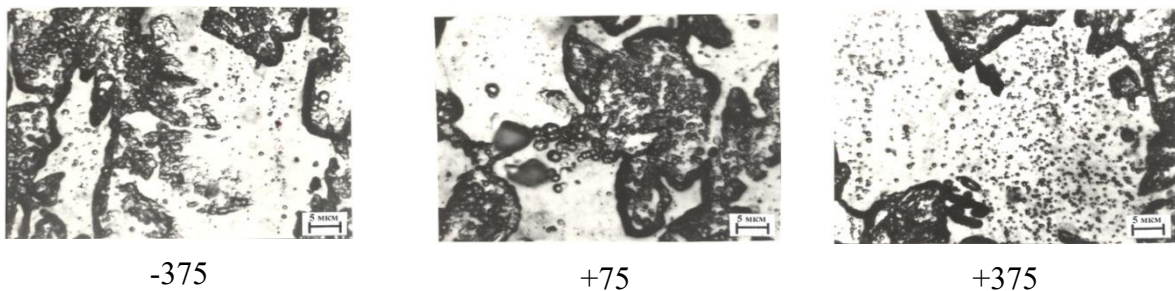


FIG.4. Microstructure observed at different elevations and irradiation conditions ($\times 2000$).

Metallographic investigations showed that 12Cr13Mo2NbBV steel microstructure for non-irradiated and irradiated samples differs significantly (Fig. 3). The ratio of ferrite/sorbite in the non-irradiated steel is 1:1.551 or only 39% ferrite (Fig. 3a), while for the irradiated steel this ratio shifts towards ferrite phase with increasing elevation and corresponding irradiation

temperature (Table 3). It is worth noting that ferrite grains in the non-irradiated steel are well-defined, while sorbite grains are in general smaller with the grain boundaries not fully formed.

Fig. 4 shows the following microstructural changes in ferrite and sorbite grains:

- a) A large number of fine spherical precipitates were formed in ferrite (presumably $Me_{23}C_6$). An increase in irradiation temperature (up to $\sim 420^\circ C$) results in a rise in ferrite volume fraction.
- b) Sorbite contained globular second phase particles of various diameters ($\sim 1 \div 2$ microns); carbides were also observed at phase interfaces. The density of globular particles in sorbite grains decreases with temperature increase (up to $\sim 420^\circ C$). The ratios of ferrite/sorbite, obtained from experiments, and the mean grain size of ferrite are given in Table 3.

TABLE 3. GRAIN SIZE CHANGES AND FERRITE/SORBITE RATIOS IN THE EP-450 FERRITE-MARTENSITIC STEEL

Distance from midplane, mm	Ferrite/sorbite raio	Mean grain size of ferrite, μm
+375	3.55:1	42 (dmax ~ 90)
+75	2.44:1	36 (dmax ~ 70)
-375	2.14:1	30 (dmax ~ 40)
initial	1:1.55	20 (dmax ~ 25)

Microstructural studies of irradiated steel at high magnifications have revealed the presence of macro-chains of cementite phase, which are located not only in the matrix of both ferrite and sorbite grains but also at grain boundaries (Fig. 5). Some of these precipitates are continuous, while others are aligned but separated from each other. An interesting fact is that second phase particle chains were observed only at faces of the wrapper and not on corners of the wrapper.



FIG. 5. Chains of carbide inclusions (x2000).

Microhardness measurements $H\mu$ of steel samples showed that prior to irradiation $H\mu=280$ kg/mm^2 (ferrite + sorbite), while the microhardness of ferrite did not exceed 225 kg/mm^2 . Neutron irradiation resulted in increase of microhardness (Table 4). At «-375» level the total microhardness of the steel (ferrite + sorbite) was 355 kg/mm^2 , while the hardness of only ferrite was 365 kg/mm^2 . From the obtained results the effect of radiation hardening was determined for each of these structural constituents.

TABLE 4. MICROHARDNESS OF FERRITE AND SORBITE, AND THE MEAN MICROHARDNESS FOR THE EP-450 STEEL AT DIFFERENT LEVELS

Distance from midplane, mm	Mean H_{μ} , kg/mm^2	H_{μ} of components kg/mm^2	
		ferrite	sorbite
+375	280	280	280
+75	418	412	382
-375	355	365	354
Initial	280	225	282

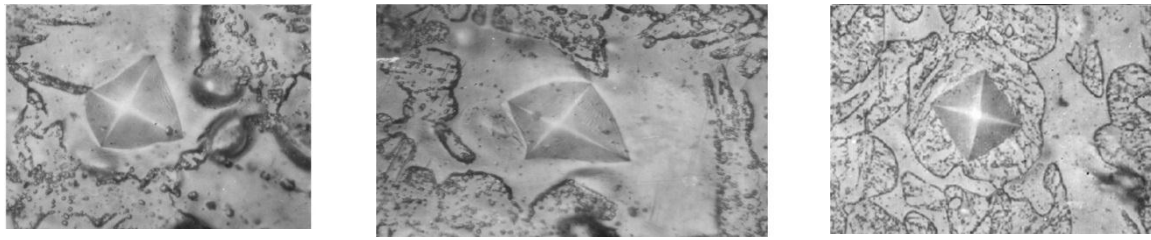
Ferrite hardening: $225\Delta H_{\text{ferrite}} = 365 - 225 \cdot 100\% \approx 60\%$. The hardening induced by sorbite could be obtained from the relationship: $2H_{\text{total}} = H_{\text{ferrite}} + H_{\text{sorbite}}$. For non-irradiated steel: $2 \cdot 285 = 225 + H_{\text{sorbite}}$, $H_{\text{sorbite}} \approx 340 \text{ kg/mm}^2$. At the same time for irradiated steel: $2 \cdot 355 = 365 + H_{\text{sorbite}}$, or $H_{\text{sorbite}} \approx 340 \text{ kg/mm}^2$. It follows that the irradiation-induced hardness of sorbite did not change, while that for ferrite lead to a 60% increase at the level «-375».

It was determined that at the «+75 mm» level H_{μ} of ferrite had a much greater range in values, but for more than 50% measurements the mean value is 412 kg/mm^2 . Moreover, only at this level were strain lines observed around some indenter marks. It was also noticed that marks from the indenter in ferrite grains of the irradiated steel frequently have an irregular shape (Fig. 6). The strong distortions were observed at level «-375 mm» from the midplane. An increase in temperature leads to a decrease of distortion level. Taking as a unit of distortion the difference between diagonal sizes of indenter mark, it is obtained that at the level «-375 mm» the angle distortion decreases to $\sim 25\%$, at «+75 mm» to 10% and at «+375 mm» to $\sim 5\%$.

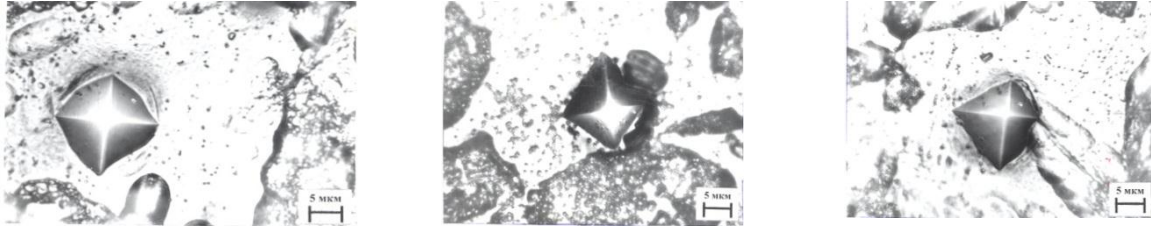
The distorted indentations in ferrite are proposed to result from gradients in carbon across the grain as they grow from the disintegration of sorbite grains and the release of carbon from dissolving carbides in the sorbite.

TEM investigations of the sample cut from the «-375mm» level revealed the presence of vacancy voids (Fig. 7), which volume fraction and size distribution results in swelling which does not exceed 0.2% .

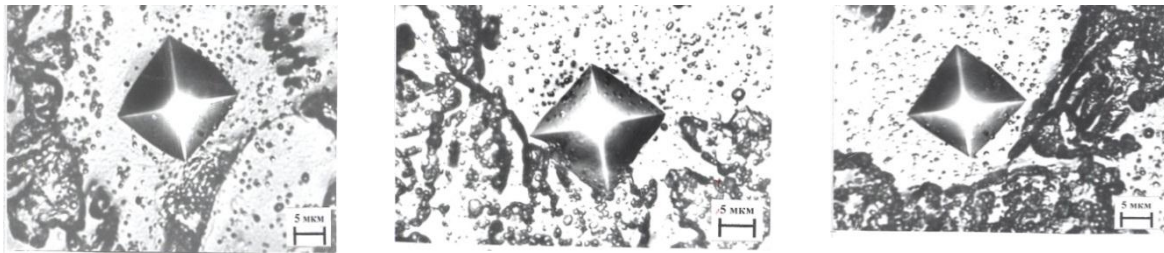
Fig. 8 shows that both damaging dose and irradiation temperature influence microhardness (H_{μ}), density (ρ), volume fraction of ferrite phase (ϕ) and amount of shape changes (S) in the EP-450 ferrite-martensite steel. It could be seen that the maximum values for H_{μ} , ρ and S were obtained for the «+75» level close to the midplane.



(a)



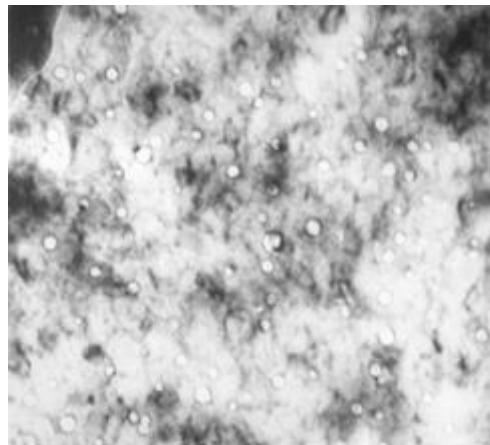
(b)



(c)

FIG.6. Indenter marks at microhardness measurements of steel samples cut from different levels: a – «-375»; b – «+75»; c – «+375».

All indentations shown were made (Fig. 6) in ferrite grains, with the exception of the right hand-side micrograph of 6a for the «-375mm» level (sorbite grain).



x 50000

FIG. 7. Voids observed in EP-450, irradiated in BN-350 reactor to 40.3 dpa at 300 °C.

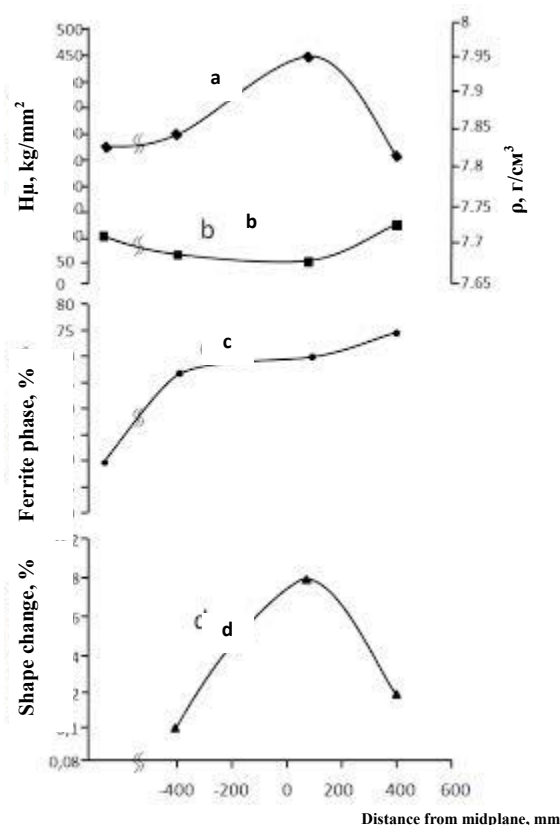


FIG. 8. Changes in microhardness (a), hydrostatic density (b), volume fraction of ferrite (c) and shape changes due to swelling with the distance from midplane of fuel assembly.

1.3 Conclusions for EP-450 portion of work

The EP-450 steel microstructure remains dual phase (ferrite-sorbite) during irradiation in response to changes in dose and temperature, but the following changes were observed:

- the volume fraction of ferrite increases due to irradiation-induced breakup of sorbite and possible dissolution of carbide particles in ferrite with the temperature increase;
- temperature increase (up to 420 °C) leads to a more than double increase of the mean grain size of ferrite, and a large number of fine carbides (<1 micron) are formed in the ferrite matrix;
- two types of ferrite should be distinguished: primary (without inclusions) and secondary ferrite with a large distribution of carbides in it;
- ferrite has the major effect on radiation-induced hardening of EP-450 steel at «-375 mm» and «+75 mm» levels, at which the products of sorbite breakup are dissolved. In the initial condition, sorbite plays the major effect to determine hardness at the given heat treatment;
- distortion of indenter marks was observed in ferrite grains of the irradiated steel. The temperature increase results in a decrease of irregular shape marks and the level of distortion decreases from 25 to 5%.

2. EBSD-STUDIES OF MARTENSITE TRANSFORMATION IN 12CR18NI10TI AFTER COLD DEFORMATION AND IRRADIATION WITH KR IONS (E=1.56 MEV/NUCLEON)

It is well known that highly-alloyed austenite stainless steels widely used for construction of fast nuclear reactors are metastable and long-term radiation and stresses or strains results in development of α -phase. As formation of this phase leads not to only changes in crystal lattice (fcc \rightarrow bcc) but also affects the magnetic, mechanical and corrosion properties, studies of $\gamma\rightarrow\alpha$ transformation are of great importance for irradiated materials and require special attention. Literature review showed that there are many data sources on mechanisms and characteristics of $\gamma\rightarrow\alpha$ transformation in irradiated materials. The phenomenon of martensite transformations in reactor steels was often observed after irradiation with high-energy particles and as a result of plastic deformation.

Diffusionless $\gamma\rightarrow\alpha'$ transformations taking place during cold deformation of stainless steel was frequently investigated by means of electron microscopy, X-ray analysis and by measuring magnetic properties. It is worth noting that not only the volume fraction of α' -phase was measured, but also its distribution along deformed parts of samples. However, from results of these measurements it was not clear what microstructural changes are responsible for an increase of magnetic characteristics.

The use of X-ray analysis at low (up to 2–3%) values of ferromagnetic α -phase is limited to the low sensitivity of this method, while TEM requires damage of investigated sample what may non-applicable for most cases. It could be concluded that to investigate mechanisms of $\gamma\rightarrow\alpha'$ transformation it is required to use more sensitive methods for analysis, which would be able to detect even slight changes in microstructure and in phase composition of the material by combining these results with the data on changes of elements' composition and local orientations of crystals.

Electron backscatter diffraction (EBSD) is one of these methods and it combines strengths of both electron microscopy and structural analysis. This technique is used to investigate a wide range of crystalline materials and, particularly, aimed at texture determination, orientations of crystallites and properties of grain boundaries. The present work gives experimental results of EBSD studies on structural and phase transformations in austenite Cr-Ni steel induced by deformation and irradiation with high-energy particles.

2.1 Experimental samples and methods

As an object for this research samples of 12Cr18Ni10Ti stainless steel (austenization at 1050°C for 30 minutes) as well as samples irradiated with high-energy Kr ions at accelerator DC-60 were chosen. Irradiation was performed on four flat samples (aimed for mechanical testing) of a thickness of 300 microns and fixed in a specially designed holder (Fig. 9) and placed in vacuum chamber (10^{-4} Pa). The irradiation temperature did not exceed 100°C and forced water cooling was provided for the “target”. Irradiation was performed in two stages. First, the samples #02 and #15 were irradiated to fluence of $4\cdot 10^{15}$ ion/cm² (E=1,56 MeV/nucleon), while the samples #05 and #09 were irradiated to $1\cdot 10^{15}$ ion/cm². After a year the above mentioned samples were reirradiated at the same conditions and the final maximum fluence was $9\cdot 10^{15}$ ion/cm² for the samples #02 and #15 and for the samples #05 and #09 it was $6\cdot 10^{15}$ ion/cm².

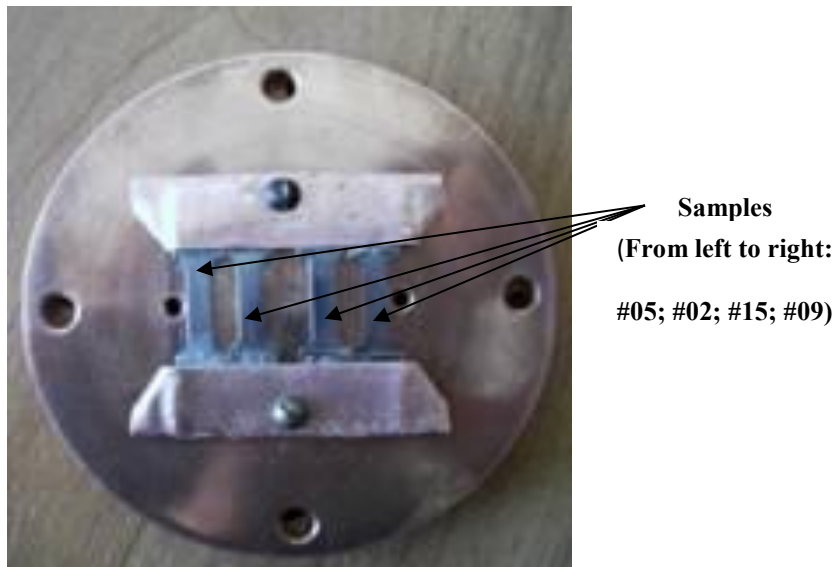


FIG. 9. Copper holder for irradiation of samples in vacuum chamber of DC-60 accelerator.

After irradiation the amount of ferromagnetic phase in the initially non-magnetic steel was determined using a Feritoscope MP-30 microanalyzer (accuracy $\sim 0.01\%$). X-ray analysis of phase composition for the initial, deformed and irradiated steel samples was performed using a D8 ADVANCE (Bruker AXS GmbH) using $\text{Co K}\alpha$ -irradiation and a scintillation detector. Data was acquired at scan rate $2^\circ/\text{min}$ at rotation rate of ~ 60 revolutions/min to get the best diffraction patterns of present phases in steel. Accuracy for θ and 2θ angles was $\pm 0.005^\circ$.

Investigations of irradiated surfaces as well as phase analysis was made using JSM-7500F SEM with HKL EBSD detector. The EBSD technique was used to obtain texture characteristics. This method gives maximum resolution of 200 nm while its accuracy to determine crystal orientation is about 1° . In this work determination of crystallographic orientations was performed with the step size of 0.05 microns for the area of 310×230 microns (scanning time ~ 4 hours).

The main difficulty when using EBSD is sample preparation. There are certain requirements to the surface quality as the sample is tiled and even a small relief may result in deterioration of EBSD map, i.e. to reduce phase recognition. For the investigated steel samples indexing was in the range of 60–85%.

2.2 Deformation-induced $\gamma \rightarrow \alpha'$ martensite transformation

Fig. 10a shows typical microstructure of deformed stainless steel, where slip lines, twins and α' -phase martensite plates are observed.

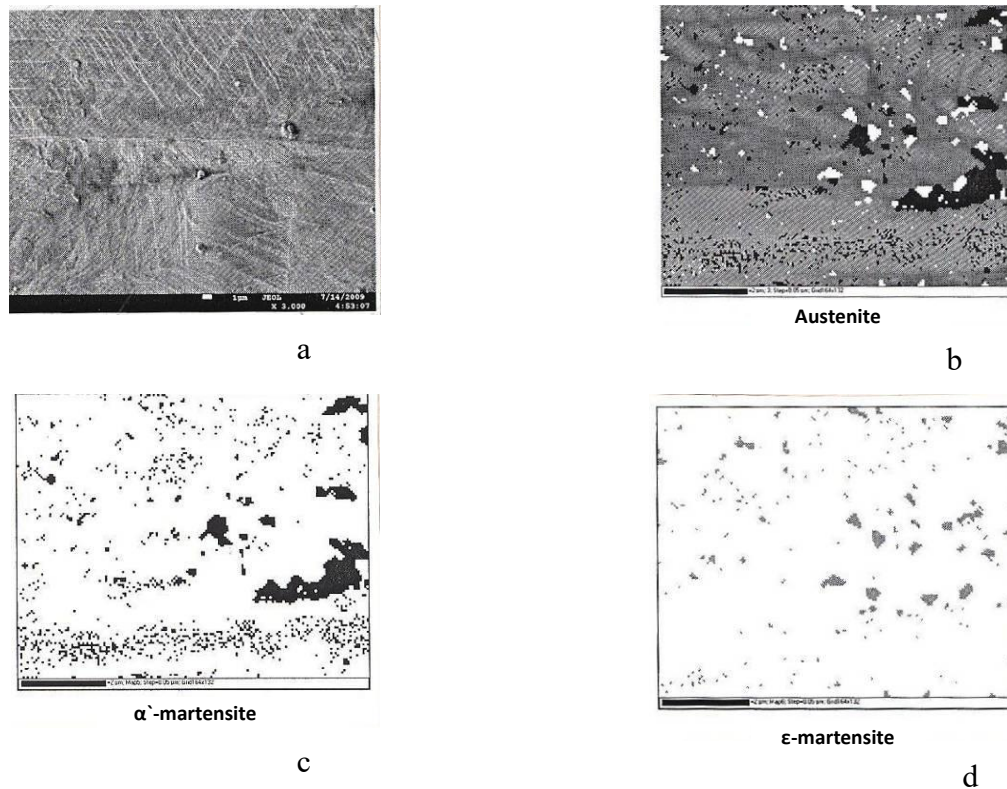


FIG. 10. FIG. 10. a)-Surface of a 12Cr18Ni10Ti steel sample after tensile testing at 20°C; b), c) and d)- EBSD maps for the deformed steel sample.

EBSD maps of the steel sample (Fig. 10b, c, d) show that material has three phases: austenite matrix has inclusions of ϵ -phase (fcc) as well as deformation-induced α' -martensite. This also was confirmed by measurements of magnetic phase and from literature sources. The mean size of deformation-induced α' -martensite was about several microns and this also agrees with many experimental works. In addition, fine distributed particles of α' - martensite (~ 10 nm) are present in austenite grains. In other words, the austenite matrix contains α' - martensite particles of both micron and sub-micron sizes.

2.3 Irradiation-induced (^{84}Kr) $\gamma \rightarrow \alpha'$ martensite transformation

Fig. 11 shows micrographs of steel surface irradiated with four different fluences of ^{84}Kr ($E=1.56$ MeV/nucleon). It could be seen that after irradiation ($F_1=1 \cdot 10^{15}$ ion/cm 2) carbides and nitrides as well as gas blisters could be distinguished on the surface. It is likely that their appearance was caused by the following reasons:

- appearance of carbides and nitrides arising an increased rate of ion etching of austenite compared to that for harder particles;
- Gas blisters arising from Kr atoms and their agglomeration at near-surface layer.

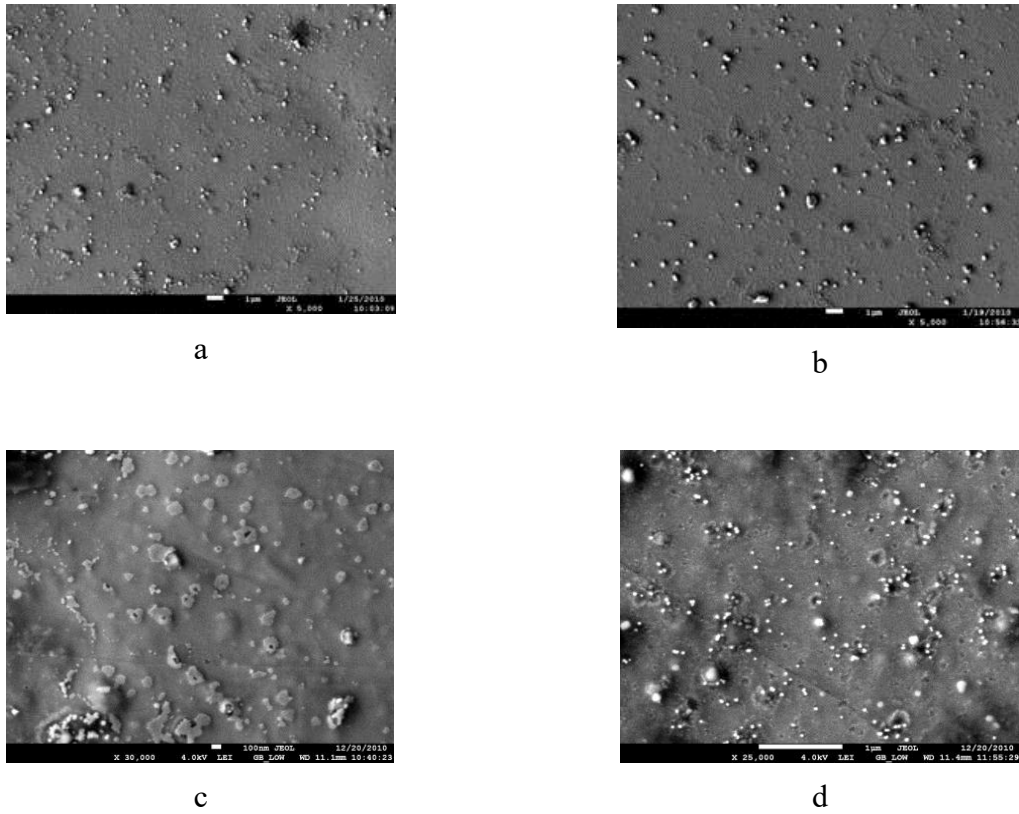


FIG. 11. Micrographs of 12Cr18Ni10Ti steel after irradiation with ^{84}Kr with energy 1.56MeV/nucleon at fluence: a) $1 \cdot 10^{15}$; b) $4 \cdot 10^{15}$; c) $6 \cdot 10^{15}$; d) $9 \cdot 10^{15}$ ion/cm².

The average carbide (nitride) particle size was 100–200 nm. Blisters as opposed to carbides (nitrides) have a circular shape with mean diameter was about 20–60 nm. An increase of irradiation dose to $4 \cdot 10^{15}$ ion/cm² leads to an intensive rupture of blisters and to surface erosion (Fig. 11b).

Fig. 12 shows distribution of second phase particles in 12Cr18Ni10Ti steel samples irradiated with different fluence of high energy ions of Kr. It is seen that a higher fluence leads to an increase of amount of snowflakes, and originally flat and polished surface transforms into the one covered with small spots. This fact should be taken seriously into consideration when using austenite steels as a construction material for the first wall of fusion reactor.

EDS analysis confirmed that small circle particles observed inside grains are carbides (Table 5).

TABLE 5. EDS ANALYSIS OF CARBIDE PARTICLES (SAMPLE № 05, $F_T=6 \cdot 10^{15}$ ION/CM²)

Element	C	Al	Si	Ti	Cr	Mn	Fe	Ni	Total
Weight %	24.2	0.3	0.5	0.4	14.2	0.8	51.9	7.4	100

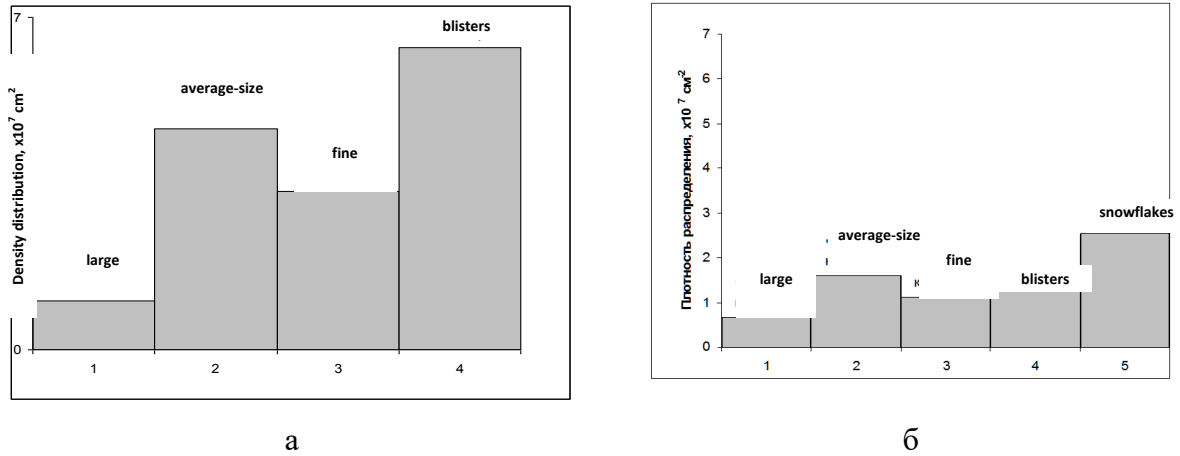


FIG. 12. Distribution of second phase particles in 12Cr18Ni10Ti steel irradiated with ^{84}Kr (1.56 MeV/nucleon) a) $F_1=1 \cdot 10^{15} \text{ ion/cm}^2$; б) $F_2=4 \cdot 10^{15} \text{ ion/cm}^2$.

Magnetic measurements (as well as X-ray analysis) of steel samples prior to and after irradiation with Kr ions did not show a presence of magnetic phase in the samples irradiated to fluence $4 \cdot 10^{15} \text{ ion/cm}^2$ (Fig. 13.). Taking into account the fact that depth of penetration for magnetic field of the probe is high ($\sim 1\text{mm}$) and the sensitivity of X-ray is low for the investigated amount of magnetic phase, EBSD technique was used to study its quantity and morphology.

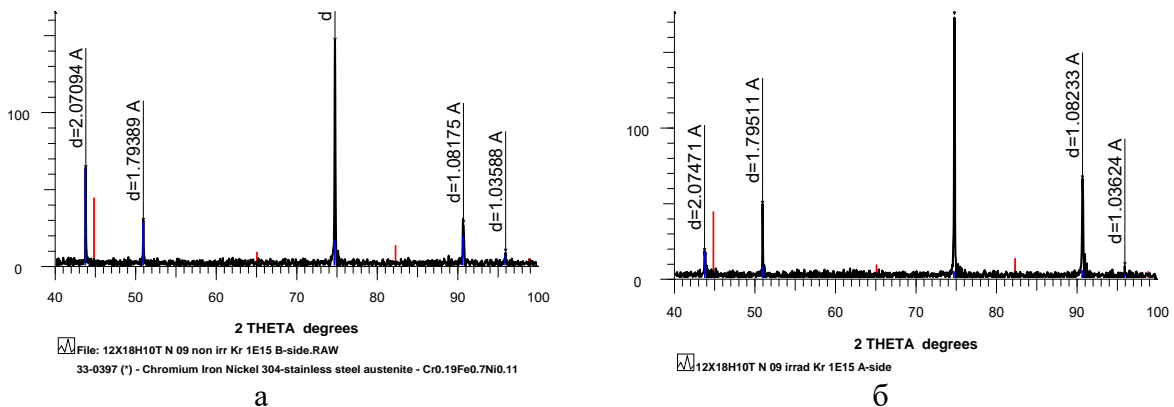


FIG. 13. X-ray diffraction profiles of 12Cr18Ni10Ti austenite stainless steel: a) initial; б) irradiated with ^{84}Kr ($4 \cdot 10^{15} \text{ ion/cm}^2$).

Fig. 14a presents an EBSD micrograph showing a rippled surface and inhomogeneously distributed blisters. Comparison of this figure with Fig. 14b shows that the blister density differs for various grains. The phase distribution map (Fig. 14c) shows that irradiation of 12Cr18Ni10Ti steel with heavy high energy particles leads to development of two martensite phases (α and ϵ). The α -phase is characterized by its small size (less than 0.1 microns) while an insignificant amount of large particles is also present. Moreover, the bcc phase is forming predominantly in regions without blisters and in the [001] grains close to grain boundaries. In contrast, ϵ -martensite originates in grains with [111] orientation.

It is worth noting that during phase transformations the grain orientation does not change with fluence. Fig. 15 gives evidence that the grain orientation could be the major factor which determines what type of defect structure would be formed: blisters on (101) or α -phase on (001).

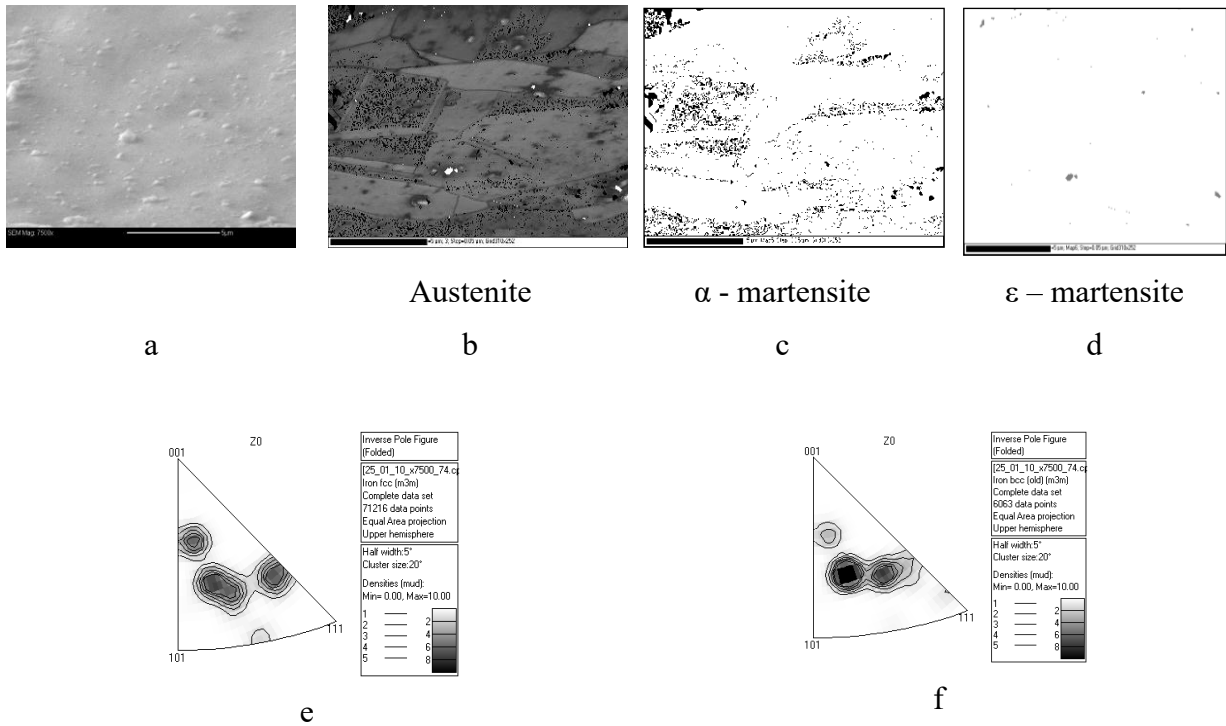


FIG.14. a)-Surface, b)-f)- EBSD phase maps for the 12Cr18Ni10Ti steel sample irradiated with 84Kr at $F_1=1 \cdot 10^{15}$ ion/cm² (step size 0.05 microns) (x7500).

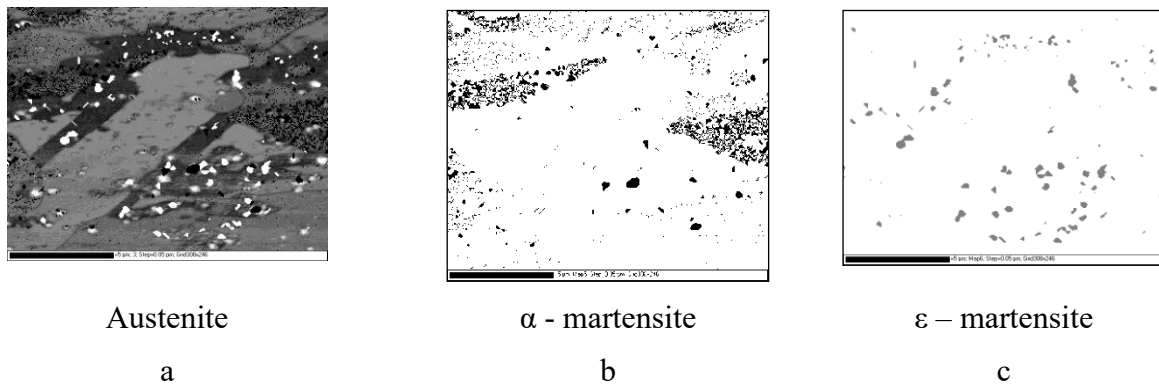


FIG.15. EBSD phase map for the 12Cr18Ni10Ti steel sample irradiated with ⁸⁴Kr at $F_2=4 \cdot 10^{15}$ ion/cm² (step size 0.05 microns)

The amount of α -martensite in the sample irradiated with the fluence of $1 \cdot 10^{15}$ ion/cm² was about 8% (ϵ -martensite – 1%), while that in the sample irradiated with the fluence of $4 \cdot 10^{15}$ ion/cm² the percentage of α -phase was 9% (ϵ -martensite – 2%). After re-irradiation of the samples with Kr ions (total fluence is $9 \cdot 10^{15}$ ion/cm²), the results of investigation showed the presence of magnetic phase in the austenite matrix. EBSD maps also confirmed the presence of both ϵ and α phases.

The martensite phase formed during low temperature irradiation by heavy ions is mainly finely dispersed, i.e. processes of formation prevail over those of growth. Early studies of $\gamma \rightarrow \alpha'$ transformation mechanisms during deformation of irradiated with neutrons

12Cr18Ni10Ti steel showed that irradiation mainly influences origination of α -phase rather than its growth. One of the explanations could be related to hardening of irradiated lattice by irradiation-induced defects.

3. CONCLUSIONS

Although alloy 12Cr18Ni10Ti is initially fully austenitic in its normal use both deformation and radiation, especially when conducted at low temperatures can give rise to magnetic phases. When introduced by ion irradiation some tools may not be sufficiently sensitive to confirm the presence and accurately measure the amount of these phases. When coupled with EBSD techniques, however, it is possible to see the development of two martensite phases (α and ε), and to study the factors that determine their relative abundance. Especially surprising is the role of grain orientation on which phase predominates.

REFERENCES

- [1] TSYKANOV, V.A., NEUSTROYEV, V.S., SHAMARDIN, V.K. et al. "Radiation studies of structural materials irradiated BOR-60", Transactions of Nuclear Science and Technology: Nuclear Materials Science». Volume 1 (18), 1985, p. 45.
- [2] AGEEV, V.S., SHAMARDIN, V.K., KONOBEYEV, A.N. et al., " Influence of structure and phase composition on 1Cr13Mo2NbVB steel; mechanical properties in initial, Aged and irradiated states", Effect of Radiation on Materials, ASTM STP 1046 Volume 1, 1990, p. 98.
- [3] AGEEV, V.S., VOEVODIN, V.N., ZELENSKIY, V.F., MATVEENKO, B.V. et al. "Structural and phase transformations in the irradiated 1Cr13Mo2NbVB steel" VANT, Nuclear Materials Science, 1985, № 1(18), pp. 83–87.
- [4] PANCHENKO, V.L., AVERIN, S.A., KOZLOV A.V. "Microstructural studies of ferrite-martensite 1Cr13Mo2NbBV steel after high-dose irradiation in BN-600". VANT, Nuclear Materials Science, 1999, 3(75), pp. 111–116.

COMPUTATIONAL AND EXPERIMENTAL APPROACH TO RADIATION EFFECTS ON FE-CR MODEL ALLOYS

J. KWON, C. SHIN, H-H. JIN, Y. LEE
Nuclear Materials Research Division
Korean Atomic Energy Research Institute
Republic of Korea

Abstract

Microstructural evolution of Fe-Cr model alloys irradiated by various particles was studied using the electron microscope, the positron annihilation technique and the atom probe. Also, we measured the changes in the mechanical properties with the nano-indentation test. Additionally, we applied computer simulation in deriving the damage mechanism due to irradiation. The simulation techniques included molecular dynamics, Monte Carlo methods, dislocation dynamics (DD) and finite element methods (FEM). The methods developed in this work will enable us to predict the mechanical properties of alloys irradiated by any kind of radiation.

1. BACKGROUND

The swelling resistance of ferritic/martensitic (F/M) steels at elevated temperature has increased the interest in their use as structural materials for Generation IV and nuclear fusion reactors. It is well-known that the addition of Cr to pure Fe reduces radiation-induced swelling significantly. It would be interesting to investigate the role of Cr atoms in Fe-Cr model alloys, which are regarded as base binary ones for F/M steels. Binary Fe-xCr alloys with different Cr contents ($x = 5, 9, 15$ w/o) were used for this research. This research deals with two areas by combining computational and experimental methods. The first part is related to the observation of microstructural evolution of Fe-Cr model alloys irradiated by various particles using the electron microscope, the positron annihilation technique and the atom probe. Also, we measured the changes in the mechanical properties with the nano-indentation test.

In the second part, we applied computer simulation in deriving the damage mechanism due to irradiation. The simulation techniques included molecular dynamics, Monte Carlo methods, dislocation dynamics (DD) and finite element methods (FEM). The methods developed in this work will enable us to predict the mechanical properties of alloys irradiated by any kind of radiation.

2. ELECTRON IRRADIATION OF FE-CR MODEL ALLOYS

This section is aimed at qualitatively investigating the role of point defects during the microstructural evolution of Fe-Cr model. For Fe-Cu alloys irradiated by neutrons, irradiation-induced vacancies are stabilized by forming vacancy-Cu complexes, which was revealed by coincidence Doppler broadening (CDB) measurement of positron annihilation radiation [1, 2]. It is probable that these vacancy-Cu complexes provide the nucleation sites for full-fledged Cu precipitates. It would be of interest to establish whether the low swelling of Fe-Cr alloys under irradiation is related to the interactions between vacancies and Cr atoms. For this purpose, we irradiated by high-energy electrons Fe-Cr alloys with different Cr contents. Then, a positron annihilation (PA) measurement was made in order to verify the production of point defects and to investigate the resultant atomic configuration in the vicinity of vacancies. Positron annihilation techniques, including PA lifetime spectroscopy and CDB spectroscopy, were applied for the measurement. In parallel, we performed a Monte Carlo computer simulation to estimate the atomic arrangements of the evolved microstructure in the electron-irradiated Fe-Cr alloys.

2.1 Defect analysis by positron annihilation spectroscopy

The samples of Fe-Cr model alloys were irradiated with 2 MeV-electrons at a controlled temperature of $< 50^{\circ}\text{C}$. The total electron dose amounts to 1×10^{18} e/cm², which corresponds

to $\sim 7.5 \times 10^{-5}$ dpa. Most of the point defects produced by electron irradiation may exist in the form of isolated Frenkel pairs. Based on this assumption, the calculated concentration of vacancies was $\sim 6.5 \times 10^{18} / \text{cm}^3$ for the Fe-9Cr alloy [3].

The PA measurements for five samples (unirradiated Fe, irradiated Fe, Fe-5Cr, Fe-9Cr, Fe-15Cr) were performed at room temperature. We employed a ^{22}Na positron-source of about 1 MBq and collected about 2×10^6 counts over 12 hours. The PA lifetime data was analyzed by using the PALSFIT program [4]. CDB spectra were measured with two high-purity Ge-detectors in order to plot the ratio curve, which enabled us to examine the elemental information from the vicinity of the open-volume defects such as vacancies and voids. The results for positron annihilation lifetime data of each sample are listed in Table 1.

For the detailed analysis, the spectra for the irradiated samples were decomposed into two components, τ_1 and τ_2 . The τ_1 component corresponds to the annihilation of free positrons non-localized in the lattice. A relatively long lifetime component τ_2 reveals that the positrons are annihilated at vacancies which are formed after electron irradiation. The lifetimes of the vacancy are 170 ps for Fe and 180 ps for Cr [5]. The τ_2 components clearly indicate that a certain amount of vacancies are distributed in the irradiated samples.

Fig. 1 shows the CDB ratio spectra for the irradiated samples normalized to the momentum distribution of well-annealed pure Fe. The enhancement in the low-momentum region ($< 7 \times 10^{-3} m_0c$, where c is the speed of light and m_0 is the electron rest mass) represents that positron are trapped in open-volume defects induced by irradiation. A broad peak for all the samples could be clearly seen in the low-momentum region.

There is no significant difference in the high-momentum region of the CDB spectra between the irradiated pure Fe and Fe-Cr alloys. This result is expected in that the atomic configurations of pure Fe near the vacancies are similar to those of the Fe-Cr alloys. That is, vacancies do not form clusters with the neighbouring Cr atoms but exist in isolated form.

TABLE 1. POSITRON ANNIHILATION LIFETIMES AND THEIR INTENSITIES FOR FIVE SAMPLES (UNIRRADIATED / IRRADIATED PURE FE, FE-5CR, FE-9CR, FE-15CR)

Sample	Average PA lifetime, τ_{avg} (ps)	PA lifetime (ps)		Intensity (%)	
		τ_1	τ_2	I_1	I_2
pure Fe	106.0				
irr. pure Fe	120.0	99.5	169.8	78.6	21.4
irr. Fe-5Cr	120.6	97.6	178.2	76.1	23.9
irr. Fe-9Cr	121.0	104.6	217.5	92.1	7.9
irr. Fe-15Cr	120.4	95.6	166.4	68.8	31.2

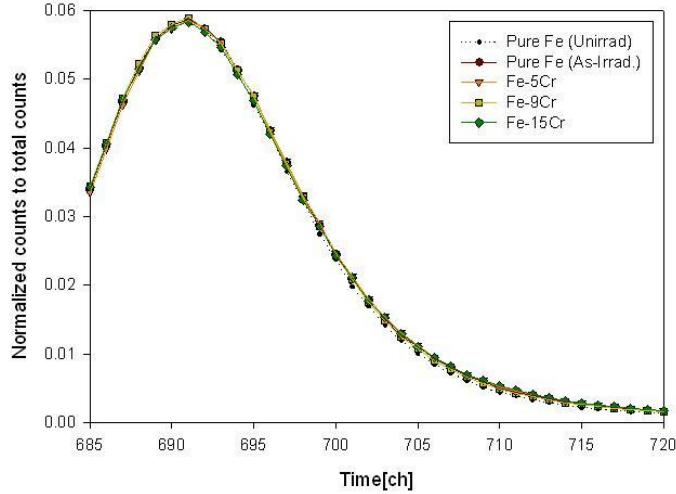


FIG. 1. Experimental positron annihilation lifetime spectra for all five samples.

2.2 Monte Carlo simulation

The point defects produced during the early stage of irradiation play a role in the development of microstructure through the interactions with surrounding atoms. For F/M steels containing Cr atoms, it might be important to understand the behaviour of solute atoms and point defects under irradiation. The Metropolis Monte Carlo (MMC) method provides a convenient tool to predict the atomic configuration of the microstructure by means of energy minimization techniques. The MMC algorithm is an importance random sampling method for obtaining the thermodynamic equilibrium states of a system. Here, this method is applied to the canonical (NVT) ensemble where the number of particles (N), the system volume (V) and temperature (T) are conserved. In this ensemble, the initial number of each element – Fe, Cr, and vacancy is maintained constant throughout the simulation. A periodic boundary condition is applied. The MMC simulation proceeds by randomly choosing a new trial state on the basis of the diffusion mechanisms. Atoms can exchange their position with neighbouring vacant lattice sites or two different atoms, Fe and Cr, may rotate together. Atoms are allowed to make first-neighbour jumps on a rigid lattice position, one out of eight first-neighbour sites in the bcc structure. This process is repeated until the given number of trials is reached.

We developed an MMC computer code to predict the minimum-energy configuration of the atomic structure for Fe-Cr alloys as a result of electron irradiation. The focal point in the MMC simulation is the role of the vacancies produced by electron irradiation in the formation of atomic clusters. We investigated the atomic configuration of the system through the MMC simulation by changing the initial Cr contents. Fig. 2 shows one example of Cr-atom distribution of the Fe-9Cr alloy before and after the MMC calculations. Although it is difficult to see the changes in Cr-atom distribution, the tendency to form the Cr agglomeration can be seen to some extent. Regardless of the Cr contents, we did not observe Cr-vacancy complexes but instead small-sized Cr clusters inside the block from visual inspection. It appears that the Cr atoms tend to gather together without any vacancy. Although the structure of a Cr cluster is not a complete precipitate, this cluster takes a transitional form which lies between molecules and bulk matter. The tendency to resist the formation of a Cr-vacancy complex is of significance in that binary Fe-Cr alloys experience relatively low swelling under irradiation. These results are in agreement with the *ab initio* calculations of Olsson et al. [6], where the interactions of Cr atoms and vacancies are explained in terms of the binding energy.

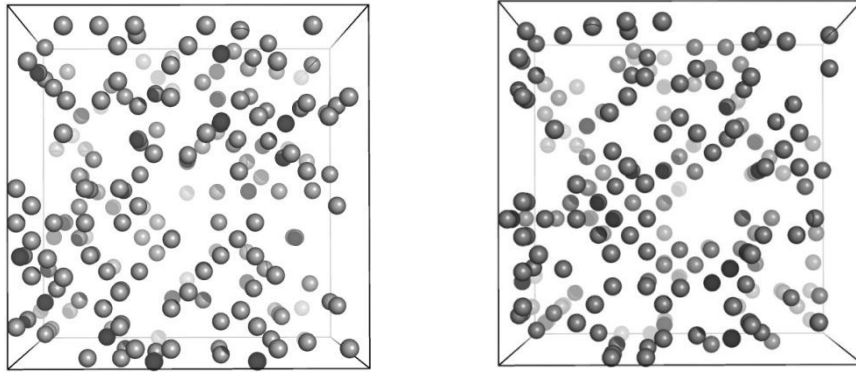


FIG. 2. Spatial distribution of Cr atoms for the Fe-9Cr alloy (a) before the simulation, and (b) after the simulation. The dimension of the cube is $20a_0 \times 20a_0 \times 20a_0$ (a_0 : lattice constant). The grey spheres represent Cr.

3. ION IRRADIATION OF FE-CR MODEL ALLOYS

This section is aimed at revealing the evolution of radiation induced defects in Fe-Cr alloys and elucidating the effect of Cr content on the hardening behaviour of ion irradiated Fe-Cr alloys. We performed transmission electron microscopy (TEM) observation, 3D atom probe tomography and nano-indentation tests. The Fe-Cr binary alloys are the base for low activated ferritic-martensitic steels which are now considered to be one of the candidate structural materials for fusion reactor steels because of their excellent resistance to material degradation modes such as swelling, helium embrittlement and irradiation creep [7, 8]. But these alloys have severe problems regarding irradiation-induced embrittlement at low temperature and irradiation hardening with increasing Cr content [9–11].

Extensive irradiation experiments by neutron, proton and an ion have shown that microstructural defects with nano scale features such as dislocation loops, voids and precipitates formed in a matrix have a significant influence on material degradation. However, the effect of the chromium content on the irradiation hardening behaviour of Fe-Cr alloys has not been elucidated clearly because of the resultant sometimes confusing and mixed microstructural defects formed under irradiation conditions. Therefore, it is one of the essential issues to analyze the evolution of radiation-induced defects, which is considered as a major factor to affect hardening of Fe-Cr alloys at room temperature.

For this purpose, we irradiated Fe-Cr alloys with different Cr contents by high-energy ions. Then, transmission electron microscopy (TEM) observation was performed in order to identify the structures. In addition, we investigate the elemental distribution of model alloys using the atom probe. In parallel, we conducted nano-indentation measurements to estimate irradiation induced hardening in the ion irradiated Fe-Cr alloys.

3.1 Microstructural analysis using transmission electron microscope

The Fe-Cr model alloys were irradiated with 8MeV Fe^{4+} ions accelerated with an ion accelerator in the Korea Institute of Geoscience & Mineral Resources (KIGAM). The beam current was $\sim 200\text{nA}$. The specimens were irradiated to fluence on the order of 6.16×10^{15} ion/cm² for Fe-5Cr alloy and 2.8×10^{15} ion/cm² for Fe-15Cr alloy, respectively. Fig. 3 shows a computation of the displacement damage profiles with a maximum range of 1.7 μm . There is no significant difference in the depth profiles between the Fe-5Cr and Fe-15Cr alloys.

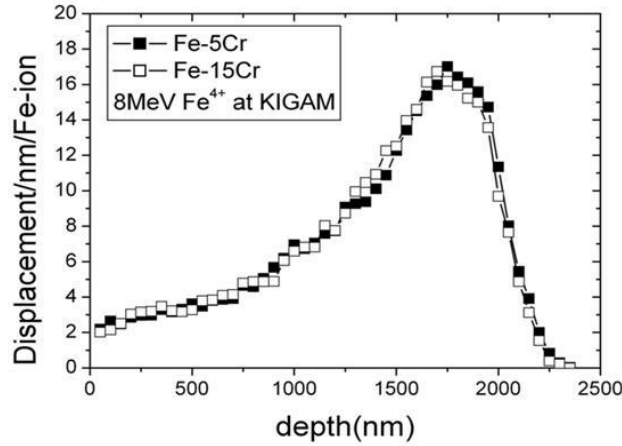


FIG. 3. Depth profile of displacement damage to ion-irradiated Fe-Cr model alloys.

Damage by ion irradiation was characterized using analytical TEM. A particular challenge for examining ion-irradiated samples is the preparation of a TEM sample because the depth of penetration of 8MeV Fe ions into Fe-Cr alloys is limited to about 2 μ m. Prior to examination of irradiated samples, a technique was developed for fabrication of TEM samples using FIB (focused ion beam) and low energy ion milling. The procedures for fabrication of TEM sample are displayed in Fig. 4, including (a) selection of interesting area by EBSD, (b) FIB milling, (c) fabrication of FIB lamella, and (d) low energy ion milling for removal of FIB-induced damage.

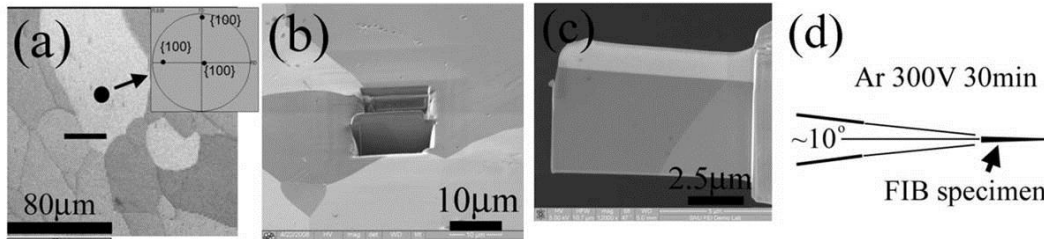


FIG. 4. Sample preparation for TEM observation of a specific site.

The characteristics of dislocation loops formed by ion irradiation were analyzed by transmission electron microscopy (TEM). The foils were examined by TEM (JEM-2100F) operated at 200 keV. Figs 5(a) and (b) show defect microstructures in Fe-5Cr alloy and Fe-15Cr alloy irradiated at room temperature. Very fine white dot contrasts were mainly observed in the Fe-5Cr alloy irradiated to 11 dpa at RT. On the other hand, we observed fine coffee bean contrasts at the reflection of $g=200$ in the Fe-15Cr alloy irradiated to 5 dpa at RT. To determine the Burger vector of dislocation loops in Fe-Cr alloys, we performed a Burgers vector analysis by imaging the same defect with different diffraction vectors and observing the contrast. In the Fe-5Cr alloy, the dislocation loops marked **A** in Fig. 5(c) were formed in the vicinity of the dislocation line. They are visible with reflections of $g=-110$ and $g=200$ and are invisible with a reflection of $g=110$. In the case of the Fe-15Cr alloy, the dislocation loops marked with arrows in Fig. 5(d) exhibited a coffee bean contrast with the reflections of $g=200$ and were visible with the reflections of $g=-110$ and $g=110$ as well.

Table 1 lists the possible values for $\mathbf{g}\cdot\mathbf{b}$ for dislocation loops with $\mathbf{b}=1/2\langle 111 \rangle$ and $\mathbf{b}=\langle 100 \rangle$. According to Table 2, the white spot contrast in the vicinity of dislocation in the Fe-5Cr alloy are identified as $1/2\langle 111 \rangle$ dislocation loops. These coffee bean contrasts in the Fe-15Cr alloy are identified as $\langle 100 \rangle$ dislocation loops.

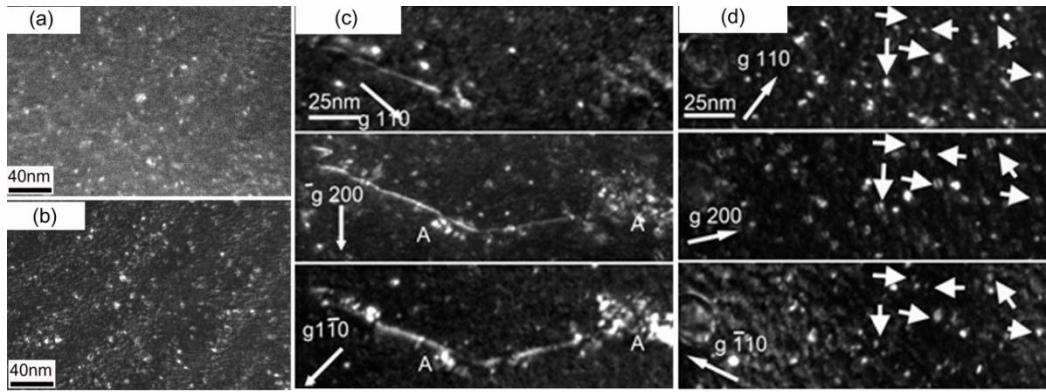


FIG. 5. Weak beam TEM micrographs of the irradiated Fe-5Cr (a) and Fe-15Cr alloys (b), irradiated at RT taken at a reflection of $[020]$ and the weak beam dark-field micrographs with the reflections of $g=110$, $g=200$ and $g=-110$ in the Fe-5Cr (c) and the Fe-15Cr alloys(d).

TABLE 2. POSSIBLE VALUES OF $\mathbf{G}\cdot\mathbf{b}$ FOR THE DISLOCATION LOOPS UNDER THREE REFLECTIONS

g	b							Contrast	
	[100]	[010]	[001]	$\frac{1}{2}$ [111]	$\frac{1}{2}$ [1-11]	$\frac{1}{2}$ [11-1]	$\frac{1}{2}$ [1-1-1]	(c)	(d)
110	1	1	0	1	0	1	0	invisible	visible
200	2	0	0	1	1	1	1	visible	visible
-110	1	1	0	0	1	0	1	visible	visible

Figs 6 (a) and (b) show defect microstructure in Fe-5Cr alloy and Fe-15Cr alloys irradiated to 1dpa at 400°C. Many white dot contrasts developed uniformly in the Fe-5Cr alloy. Some coffee bean contrasts had no contrast or weak contrast perpendicular to $[100]$ or $[010]$ direction. Therefore, they were expected to have Burgers vector of $\langle 100 \rangle$. Other white dots lay along specific directions of $\langle 110 \rangle$.

As the irradiation temperature increased from RT to 400°C, formation of $\langle 100 \rangle$ dislocation loop was frequently observed in the Fe-5Cr alloy. Large dislocation loops having various coffee bean contrasts formed in the ion-irradiated Fe-15Cr alloy. They are expected to be dislocation loops with $b=\langle 100 \rangle$ and $b=\frac{1}{2}\langle 111 \rangle$. Figs 6(c) and (d) show the defect microstructure in the Fe-5Cr alloy irradiated to 10dpa at 400°C. It was observed that line contrasts in the Fe-5Cr alloy existed along $\langle 100 \rangle$ directions in Fig. 6(c). These line contrasts are expected to be mostly composed of dislocation loops with $b=\langle 100 \rangle$ according to the $\mathbf{g}\cdot\mathbf{b}$ analysis. The high population of $\langle 100 \rangle$ dislocation loops in the Fe-5Cr alloys irradiated at 400°C is in keeping with TEM examination results of neutron irradiated Fe-Cr alloys which revealed that $\langle 100 \rangle$ loops predominated in low Cr containing Fe-Cr alloys irradiated at temperatures between 400°C and 450°C [12,13]. The Fe-15Cr alloy irradiated to 10dpa at 400°C contains complex dense defects as shown in Fig. 6(d). They were distributed intensively in the peak damage layer. Line contrasts observed in the Fe-5Cr alloy were not developed in the Fe-15Cr alloy. Unfortunately, quantitative analysis of the defects such as size, population and fraction of $\langle 100 \rangle$ loops could not be conducted because of the very high population of defects. We therefore must guess that the defect microstructure in the Fe-15Cr alloy under high dose and high temperature irradiation is composed of a mixture of $\langle 100 \rangle$ and $\frac{1}{2}\langle 111 \rangle$ dislocation loops.

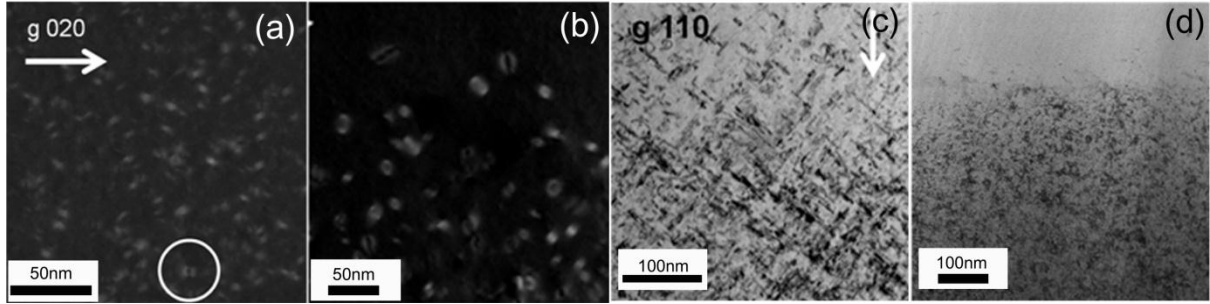


FIG. 6. Dark-field micrographs of defect images for the Fe-5Cr (a) and the Fe-15Cr alloy (b) irradiated to 1 dpa at 400°C taken at a reflection of [020], bright-field micrographs of defect images for the Fe-5Cr (c) and the Fe-15Cr alloys (d) irradiated to 10 dpa at 400°C taken at a reflection of [110].

3.2 Evaluation of yield strength changes due to irradiation by using finite element methods

The nano-indentation results were modeled using a two-dimensional axisymmetric model by using the commercial finite element program, ABAQUS (Hibbitt, Karlsson & Sorensen, Inc.). A Berkovich indenter was modeled as a rigid body by using a 2D analytic rigid shell with a tip radius to represent the blunting of the indenter, which is invariably present near a tip in real experiments. We found that the tip radius used in this study was 40 nm by comparing the modeled L-h curve with the calibration indentations of fused silica.

The Fe-9Cr specimen was modeled as being locally isotropic, and the plastic flow of a specimen was governed by a uniaxial stress-strain curve using the Mises yield criterion. The uniaxial stress-strain curve was represented by three parameters; Young's modulus, E , yield strength, σ_y , and strain hardening coefficient, n , i.e. $\sigma = \sigma_y (1 + E/\sigma_y \cdot \epsilon_p)^n$ after yielding, where ϵ_p represents a plastic strain. The vertical displacement was prescribed on the indenter and the load response of a specimen was monitored using a nonlinear static analysis. We used a contact friction value of 0.1 for the interaction between the indenter tip and the top surface of the specimen.

The parameters of the uniaxial stress-strain curve for the unirradiated Fe-9Cr specimen were evaluated by comparing the experimentally observed L-h curves with the computed curves. We limited the unknown parameters to E and σ_y . n was determined to be 0.29 from a separate uniaxial tensile test. Two unknown parameters (E , σ_y) were sought by the following procedure; i) by assuming a trial set of E and σ_y , a L-h curve was computed by using the FEM modeling, ii) the load at a depth of 465 nm and the stiffness of an unloading curve were compared to the experimentally measured values, iii) a new trial set of E and σ_y was generated and a new L-h curve computed with a new trial set was tested. We generated a new trial set by noting that an increasing E increases the stiffness and an increasing σ_y increases the load at a specific depth. Fig. 7 demonstrates the trial sets of E and σ_y , and the comparison between the computed and the experimentally measured load and stiffness data. The parameter set of $E=164$ GPa and $\sigma_y=265$ MPa was found to show a good match to the experimental data.

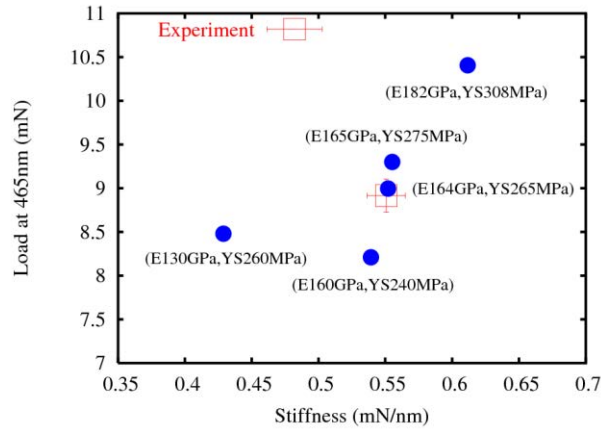


FIG. 7. Load and stiffness values (filled circles) computed by using the trial parameters of E and σ_y in brackets and the experimentally measured load and stiffness data (open square) with error bars.

The irradiated specimen had a damaged zone whose damage level is depth-dependent. The radiation damaged zone was discretized into ten different layers. Mechanical properties of each different layer were assumed as follows; i) E was assumed as invariable with the damage level, ii) n was assumed to be constant, iii) an increase in σ_y ($\Delta\sigma_y$) was assumed to be proportional to a power of the relative damage level. The unaffected region with a depth larger than $2.25 \mu\text{m}$ retained the mechanical properties of the unirradiated specimen.

A constant value of E appears to be reasonable, since the unloading curve of both the unirradiated and irradiated specimens showed an identical slope. Numerous studies have shown that σ_y increases with irradiation dose and saturates at higher doses at temperatures below 220°C . The dose-dependence of σ_y is often expressed in the form of the power-law expression, $\Delta\sigma_y = A\Phi^p$, where Φ represents the radiation fluence. We used the power-law expression without saturation in this study for simplicity, although any form of the expression can be used in the FE modeling. We assumed that the yield strength increment for i^{th} layer ($\Delta\sigma_y^i$) has a relation with the relative damage level (Φ^i) as $\Delta\sigma_y^i = A(\Phi^i)^p$, where A is the yield strength increment of the maximum damaged layer. The exponent p is chosen either 0.5 or 0.25, because various steels having an initial σ_y larger than 440 MPa showed $p \sim 0.5$, whereas low alloyed iron alloys having an initial σ_y lower than 220 MPa showed $p \sim 0.25$ for a low-dose regime.

Based on the damage profile and the relation for $\Delta\sigma_y$ as given above, the unknown parameter, A , was searched for by performing numerous trial simulations. We obtained an optimum value of $A=350 \text{ MPa}$ for the $\Delta\sigma_y^i = A(\Phi^i)^{0.25}$ relation, and $A=450 \text{ MPa}$ for the $\Delta\sigma_y^i = A(\Phi^i)^{0.5}$ relation. The overall computed L-h curves are compared to the experimental results in Fig. 8(a). The two relations for $\Delta\sigma_y$ were found to simulate very well the loading behaviour of the nano-indentation of the irradiated specimen. The distributions of $\Delta\sigma_y$ of each layer are presented in Fig. 8(b) for the two relations along with the depth-dependent yield strength distribution evaluated for the unirradiated specimen.

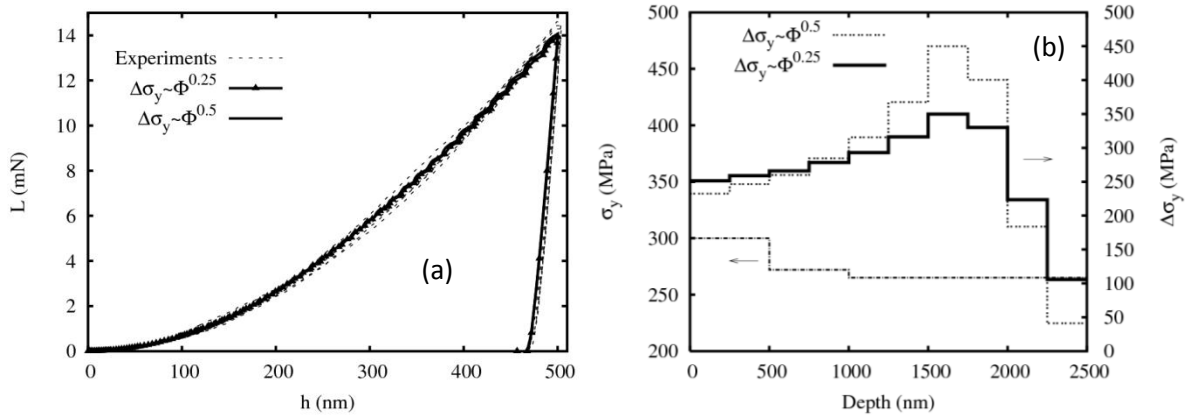


FIG. 8. (a) Comparison between the measured L - h curves (dashed lines) and the simulated curves by using the $\Delta\sigma_y$ - Φ relations; (b) Depth profile of σ_y for unirradiated Fe-9Cr (dash-dotted line) and depth profile of $\Delta\sigma_y$ for irradiated Fe-9Cr for each $\Delta\sigma_y$ - Φ relation.

3.3 Analysis of atomic distribution using the atom probe

To investigate the elemental distribution of the Fe-9Cr model alloy implanted by He-ions, the samples for the atom probe tomography (APT) analysis were manufactured by dual beam focused ion beam (FIB). The specimens were taken from three different damaged regions. The APT analysis was performed with a LaWaTAP (laser-assisted wide angle tomographic atom probe) using a UV Laser ($\lambda=343$ nm) at 60 K and 1.0×10^{-10} Torr. The analysis area in the sample was about 15nm in diameter by 300nm in height, which was obtained from the center of data measured by APT. We derived a part of the data from top, middle and bottom areas which were $\phi 15\text{nm} \times 15\text{nm}$ in height. In order to analyze the elemental distribution, we required the program to find the kNN (k-th nearest neighbour) and iso-concentration.

The distribution of the first nearest neighbour of Cr-Cr pair atoms was fitted to the Gaussian profile. While the profile of the bottom section had a bi-modal shape, profiles of the top and middle sections were expressed by only one profile. These distributions are shown in Fig. 9. The peak in the top and middle distribution corresponds to the (2,0,0) lattice point, whereas that in the bottom distribution is close to the (1,1,0) and (2,0,0) lattice points. The fraction of peak area corresponding to (1,1,0) and (2,0,0) in the bottom is approximately 7% and 93%, respectively. For the second nearest neighbour, the peak in both middle and top area corresponds to (3/2,3/2,3/2) or (5/2, 1/2, 1/2), but that in the bottom corresponds to (1,2,1). These distributions are shown in Fig. 10. In the region severely deformed by He-ion implantation, we found that a part of Cr atoms moved to the shorter inter-atomic distance. The Cr atoms tend to agglomerate readily in the severely deformed area. We calculated the iso-concentration of Cr atoms which are within 20 angstroms in diameter from the center atoms. The region where the Cr concentration is over 9 at% was investigated because the average Cr composition of model alloy is 9 at%, which was shown in Fig. 11. The iso-concentration in bottom area was higher than that in the other areas. This could be expected from the results of the nearest neighbour distribution. That is, Cr atoms tend to gather preferentially in severely distorted areas.

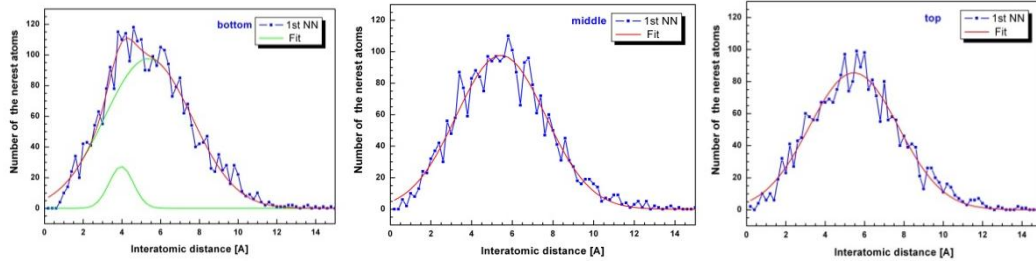


FIG. 9. The first nearest-neighbor distribution of the Cr-Cr pair atoms in the bottom, middle, and top areas.

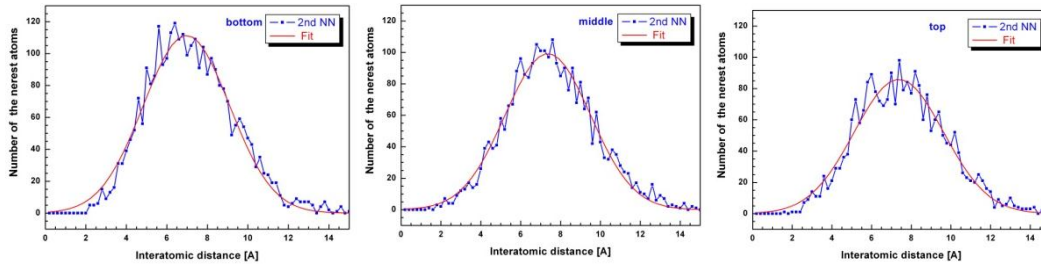


FIG. 10. The second-nearest neighbor distribution of the Cr-Cr pair atoms in the bottom, middle, and top areas.

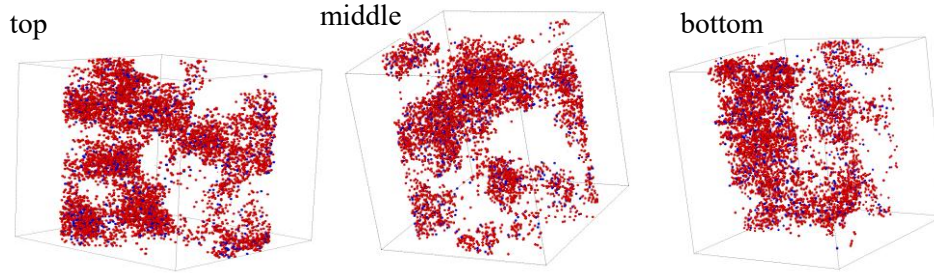


FIG. 11. Iso-concentration regions where Cr concentration is over 9% (Fe-red, Cr-blue).

4. CONCLUSIONS

This research was aimed at investigating the characteristics of ferritic/martensitic (F/M) steels after particle irradiation. Not only theoretical modeling, but also experimental work was carried out to understand the damage mechanism in detail. In the modeling part, we used computer simulation methods which include kinetic Monte Carlo, dislocation dynamics and finite element methods. In the experimental part, analytical methods were applied to investigate the microstructural evolution for Fe-Cr model alloys using electronic microscopy, atom probe, positron annihilation and nano-indentation techniques. The unique feature of this research was to combine the experimental and computational approaches.

This study demonstrates that the coupling of positron annihilation measurements and computer simulations helps us understand the microstructural evolution of binary Fe-Cr alloys. Measured data for the CDB spectra of the electron-irradiated samples revealed that vacancies existed in an isolated form without clustering with Cr atoms. Such a finding was supported by the MMC simulations. We did not observe an evolution of a Cr-vacancy complex but only clustering of Cr atoms. This finding suggests that the swelling resistance of F/M steels under irradiation is related to the absence of interactions between Cr atoms and vacancies.

A combination of two techniques was used to obtain the mechanical property changes for materials irradiated by ions due to the non-uniform distribution of radiation damage. Nano-indentation is a depth-sensing method, which measures the load with respect to the penetration depth of an indenter. From the hardness measurement data of irradiated Fe-9Cr alloy, we derived the magnitude of yield strength changes by applying the finite element (FE) numerical methods. We applied FE modeling in order to quantitatively evaluate the depth profile of yield strength and the intrinsic hardness of model alloys. Young's modulus and the yield strength were determined in several trial simulations by comparing with the experimentally measured load-depth curves. In the FE modeling of the irradiated samples, the ion-irradiated zone was divided into a certain number of discrete layers, and $\Delta\sigma_{ys}$ of each layer was expressed in terms of power-law behaviour such as $\Delta\sigma_{ys} \sim \Phi^p$. Our simulation showed that $\Delta\sigma_{ys}$ of the ion-irradiated Fe-9Cr alloy can be represented with $p=0.25$. The success of our simulation method suggests that the yield strength and intrinsic hardness of ion-irradiated region indeed vary with depth and can be evaluated by combining nano-indentation tests with FE modeling.

REFERENCES

- [1] Y. NAGAI, K. TAKADATA, Z. TANG, H. OHKUBO, H. SUNAGA, H. TAKIZAWA, M. HASEGAWA, "Positron annihilation study of vacancy-solute complex evolution in Fe-based alloys", *Physical review* **B 67** (2003) 224202–1 – 224202–6.
- [2] Y. NAGAI, Z. TANG, M. HASEGAWA, T. KANAI, M. SANEYASU, "Irradiation-induced Cu segregations in Fe: An origin of embrittlement of reactor pressure vessel steels", *Physical review* **B 63** (2001) 134110–1 – 134110–5.
- [3] O.S. OEN, "Cross sections for atomic displacements in solids by fast electrons", ORNL-4897, 1973.
- [4] J.V. OLSEN, P. KIRKEGAARD, N.J. PEDERSEN, M. ELDRUP, "PALSFIT: A computer program for analyzing positron lifetime data", Risø Nat. Lab., 2006.
- [5] M.J. PUSKA, R.M. NIEMINEN, "Defect spectroscopy with positrons: a general calculational method", *Journal of physics F: Metal physics* **13** (1983) 333–346.
- [6] P. OLSSON, C. DOMAIN, J. WALLENUS, "*Ab initio* study of Cr interactions with point defects in bcc Fe", *Physical Review* **B 75** (2007) 014110–1 – 014112–12.
- [7] D.S. GELLES, "Void swelling in binary Fe-Cr alloys at 200 dpa", *J. Nucl. Mater.* **225** (1995) 163–174.
- [8] Y. KATOH, A. KOHYAMA AND D.S. GELLES, "Swelling and dislocation evolution in simple ferritic alloys irradiated to high fluence in FFTF/MOTA", *J. Nucl. Mater.* **225** (1995) 154–162.
- [9] K. SUGANUMA, H. KAYANO AND S. YAJIMA, "Mechanical properties changes of Fe-Cr alloys by fast neutron irradiation", *J. Nucl. Mater.* **105** (1982) 23–35.
- [10] F.H. HAMMAD, M.K. MATTA AND K.E. MOHAMMED, "Effect of fast-neutron irradiation on mechanical properties of iron and some iron binary solid solutions", *J. Nucl. Mater.* **108&109** (1982) 428–435.
- [11] D.S. GELLES, "Microstructural examination of neutron irradiated simple ferritic alloys", *J. Nucl. Mater.* **108&109** (1982) 515–526.
- [12] D.S. GELLES, "Microstructural examination of neutron irradiated simple ferritic alloys", *J. Nucl. Mater.* **108&109** (1982) 515–526.
- [13] S.I. POROLLO, A.M. DVORIASHIN, A.N. VOROBYEV AND YU.V. KONOBEEV, "The microstructure and tensile properties of Fe-Cr alloys after neutron irradiation at 400°C to 5.5–7.1 dpa", *J. Nucl. Mater.* **256** (1998) 247–253.

NON-DESTRUCTIVE CHARACTERIZATION OF OXIDE DISPERSION STRENGTHENED STEELS

V. KRSJAK, Z. SZARAZ, P. HÄHNER

European Commission, Joint Research Centre – Institute for Energy,
PO BOX 2, 1755 ZG PETTEN,
The Netherlands

Abstract

This report discusses the application of various non-destructive testing methods on the microstructural characterization of the oxide dispersion strengthened steels with possible nuclear applications. Emphasis is put on a multi-technique approach and mutual correlation of results as well as on the validation and interpretation of the results obtained by destructive mechanical tests. The results of positron lifetime spectroscopy (PALS), Small angle neutron scattering (SANS) and thermoelectric power measurements (TEP) on the thermally aged ODS steels are discussed. Interpretation of the results was based on previously published papers on nuclear structural materials as well as on the preliminary TEM and XRD experiments performed in the collaboration with Nuclear Research Centre Negev, Israel.

1. INTRODUCTION

Next generation nuclear power installations require new nuclear structural materials. New types of coolants, elevated operating temperatures, different neutron spectra and considerably higher end-of-lifetime fluencies require high performance materials which are costly or, still have to be developed and qualified. Even for already existing materials, developed for particular applications and exhibiting promising irradiation performance under high neutron dose exposure (e.g. 9–12 %Cr ferritic/martensitic steel, 16–20 %Cr ODS steel [1]), microstructural properties may still not be sufficiently understood to reliably predict their long term behaviour in the above mentioned conditions.

More and more experimental techniques are being used in materials research in order to understand the effect of particular alloying elements, impurities and various nano-features on irradiation performance. Although many papers have been published on the application of (thermo) electric, magnetic, ultrasound or diffraction based techniques to radiation embrittlement studies [2–6], the connection between these techniques is missing. This can result in an underestimation of the potential contribution of the particular method or the lack of a link between the measured parameter and the actual microstructure state.

This report discusses the application of various non-destructive testing methods on the microstructural characterization of the oxide dispersion strengthened steels with possible nuclear applications. Emphasis is put on a multi-technique approach and mutual correlation of results as well as on the validation and interpretation of the results obtained by destructive mechanical tests.

Due to unavailability of the ion beam facilities for irradiation experiments, our research was not focused on the irradiation performance of the materials, but rather on other issues related to the material performance. One of the important phenomenon which significantly change the tensile, fracture and fatigue behaviour of the high Cr steels (>12 wt%) is so called 475°C embrittlement. This phenomenon is accompanied by decomposition of the ferritic phase to chromium-rich phase α' and iron-rich phase α in the temperature range of 280–500°C due to the presence of miscibility gap in iron–chromium binary alloy system [7]. In this report, the results of positron lifetime spectroscopy (PALS), Small angle neutron scattering (SANS) and thermoelectric power measurements (TEP) on the thermally aged materials are discussed. Interpretation of the results was based on the previously published papers on nuclear structural materials as well as on the preliminary TEM and XRD experiments performed in the collaboration with Nuclear Research Centre Negev, Israel.

2. MATERIALS

Oxide dispersion strengthened steels (ODS) have been developed for high temperature applications like heat exchangers in conventional power plants. In addition to superior creep properties at temperatures up to 1200°C these materials generally show excellent corrosion and swelling resistance when irradiated by neutrons [1], which suggests their application in future nuclear reactor systems. The combination of elevated temperatures, high pressures, new coolant environments and considerably higher displacement damage, together with general requirements for outstanding passive safety features, necessitates extensive R&D efforts including advanced microstructural characterization techniques.

The objects of our study were various oxide-dispersion strengthened (ODS) steels, namely PM2000, MA956, MA957 and ODM751 as well as ODS variant of Eurofer steel. Chemical compositions of the studied materials are listed in Table 1. These materials are strong candidates for structural materials used in Generation IV reactors which have to endure extreme service conditions. Service conditions that characterize these reactors include operating temperatures above 700°C; high neutron doses and highly corrosive environments.

Table 1 shows nominal compositions of commercially available ODS steels [8] investigated by PALS in this work. Ferritic PM2000 steel was supplied in both as-extruded and recrystallized conditions. MA957 and an ODS variant of ferritic-martensitic EUROFER steel were supplied in as-extruded condition and the ferritic alloys ODM751 and MA956 were available in recrystallized condition only. Non-ODS Eurofer 97 was included as a reference.

TABLE 1. NOMINAL CHEMICAL COMPOSITIONS [WT.%) OF THE MATERIALS STUDIED

Material	Form	Manufacturer	Cr	Al	Ti	Mo	W	Mn	V	Y ₂ O ₃
PM2000	1, 2	Plansee	20	5.5	0.5	-	-	-	-	0.5
MA956	2	INCO	20	4.5	0.5	-	-	-	-	0.5
ODM751	2	Dour Metal	16.5	4.5	0.6	1.5	-	-	-	0.5
MA957	1	INCO	14	-	0.9	0.3	-	-	-	0.25
ODS Eurofer	1	Plansee	8.9	-	-	-	1.1	0.4	0.2	0.3

Form: 1 - as extruded; 2 -recrystallized

The microstructures of the as-extruded materials can be described as fine grained with high dislocation densities and with complex microstructures [8]. Recrystallization annealing (typically at $\sim 0.9T_{\text{melt}}$) of the ODS steels leads to very coarse grain structures with exceptional creep resistance. In the process of recrystallization, very fine oxide particles in the diameter range 2 to 5 nm dissolve or coarsen while the number of larger dispersoids (15–40 nm) increases, thus resulting in larger mean diameters of the oxide nano-particle size distributions [8–12]. Basic characteristics of the mean particle size and concentration of the studied material, obtained from the literature, can be seen in Table 2.

To induce intermediate temperature embrittlement, all recrystallized samples as well as ODS Eurofer underwent isothermal annealing treatment at 475°C for 100, 500 and 1000h in a high temperature furnace, LECO HT 1600, under Ar atmosphere of 5 mBar overpressure.

TABLE 2. BASIC CHARACTERISTICS OF THE OXIDE NANOPARTICLES ADOPTED FROM LITERATURE

Material	Average particle size [nm]	Particle concentration [10^{22} m^{-3}]	Reference
	as extruded / recrystallized	as extruded / recrystallized	
PM2000	12 / 28	0.64 / 0.05	[8, 10]
MA956	- / 28	- / 0.05	[8, 10]
ODM751	- / 28	- / 0.05	[12]
MA957	3 / -	6.6 / -	[13]
ODS Eurofer	9 / -	1.1 / -	[14]

3. EXPERIMENTAL TECHNIQUES

Promising irradiation performance of the new generation of materials strengthened by the dispersions of oxide nanoparticles is offset by a material microstructure which is too complex to be captured by numerical simulations. Moreover these materials are typically strongly anisotropic, which complicates sampling of representative specimens for Transmission Electron Microscopy (TEM) and Atom Probe (AP) analysis. Therefore, the key motivation to our study was to overcome the material anisotropy by investigation of sufficiently large representative volumes with sufficiently sensitive methods in order to understand the role of individual nano-features in the material performance in operation and/or transition regimes.

In principle, the particular defects can act as trapping sites for positrons, scattering centres for neutrons, pinning sites for magnetic domain movement and significantly affect the material's electronic properties. Consequently, several experimental techniques based on different physical principles can be combined in an effort to obtain specific information. This part of the proposed research can be understood as a complex feasibility study to assess the application of individual NDT techniques for the characterization of radiation embrittlement of the nano-structured ferritic (or ferritic/martensitic) steels.

3.1 Positron annihilation lifetime spectroscopy

Positron annihilation lifetime spectroscopy (PALS) is a non-destructive testing method widely used in the solid state physics. This technique is extremely sensitive to atomic-scale defects in solids, like vacancies, their agglomerates or dislocations. In addition thermalized positrons are sensitive to (as they may be trapped in) precipitates of elements with higher (more negative) positron affinity (A^+) than the bulk material. For example this holds true for ODS steels, where yttrium (positron affinity $A^+ = -5.31$) oxides are being used as obstacles for dislocation motion in Fe-Cr matrix (A^+ of Fe and Cr = -3.84 and -2.62 respectively [2]). In this study, the PALS technique was used for the characterization of vacancy type defects in the studied ODS alloys, both in the as-extruded and the as-recrystallized state. Although the positron lifetime technique is not directly sensitive to the Cr-rich α' precipitates we use this technique in the study of thermally aged materials in order to obtain complementary information on the behaviour of vacancy type defects, which are mobile at this temperature and play a role in the material performance.

Schematic representation of the lifetime spectrometer in so-called fast-fast setup is shown in the Fig. 1. It is based on the universal NIM blocks of Canberra and Ortec suppliers and its resolution is < 220 ps. The BaF_2 scintillation detectors were fabricated and supplied by Scionix together with the HV (high voltage) dividers. The experimental facility is shown in Fig. 2 (left).

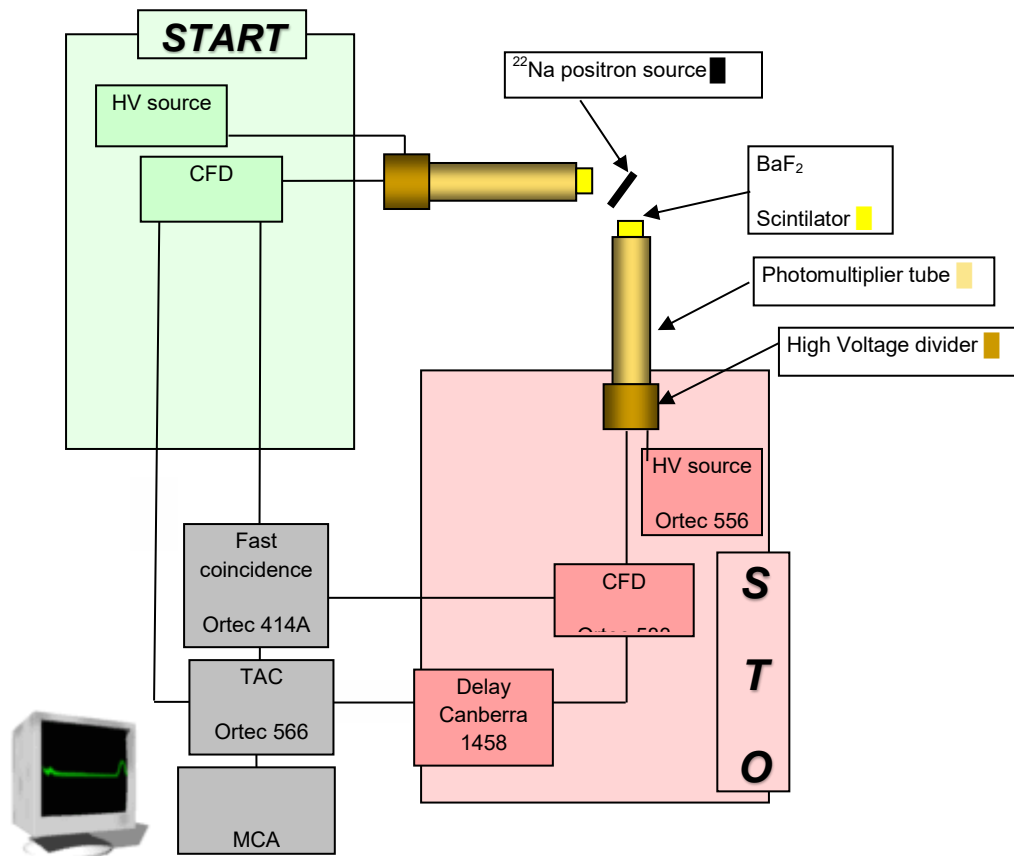


FIG. 1. Scheme of the setup for the measurement of positron lifetime at JRC-IET.

The positron source used for the experiments is shown in the Fig. 2(right). It was purchased from an external supplier and its activity $> 3\text{MBq}$ allowed us to obtain sufficient spectrum (10^6 counts) within few hours. Source contribution to the final lifetime spectra (17%) was described by two components and fixed during the data processing.

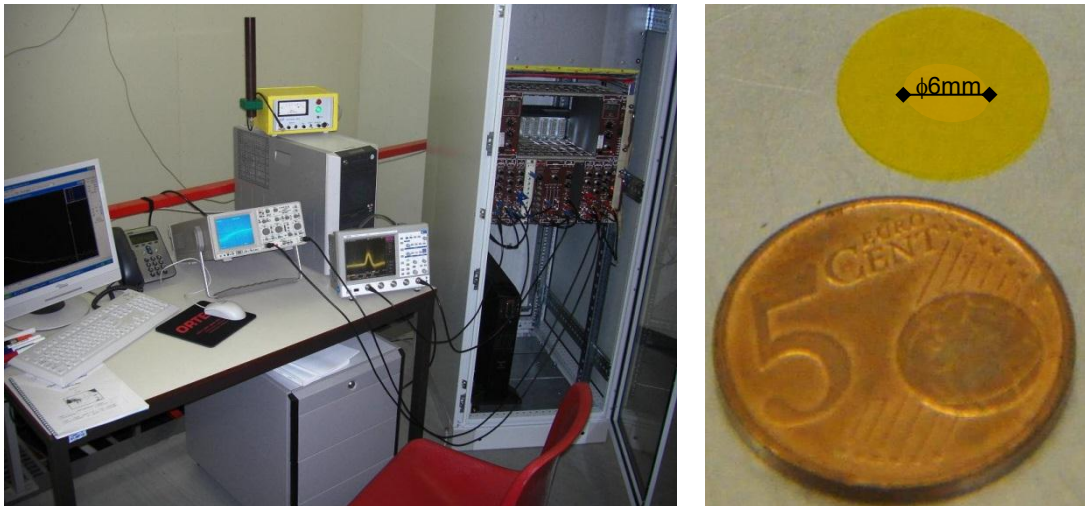


FIG. 2. Experimental facility (left) and the positron source used (right).

3.2 Small angle neutron scattering

Small-Angle Neutron Scattering (SANS) is a method for analyzing material inhomogeneities in the range of 1–100 nm. Neutrons, being neutral particles, interact weakly with matter which allows probing specimens of considerable thickness. In SANS experiments volumes up to 1 cm^3 are investigated. SANS determines the differential cross-section, which contains

information on the shape, size and interactions of the scattering bodies in the sample. This method can be used to study effects of thermal and/or irradiation ageing in ODS, duplex or Cr-rich ferritic steels.

The neutron scattering lengths vary with atomic number more or less randomly and are independent of momentum transfer q . Thus, isotopes and neighbouring elements can possess different scattering properties. SANS is particularly powerful in the case of study the α' phase separation because of the large difference between the neutron coherent scattering lengths of Fe (9.45×10^{-15} m) and Cr (3.635×10^{-15} m).

The measurements were made on the Yellow Submarine SANS diffractometer at the Budapest Neutron Centre. The diffractometer covers a q -range from 0.003 \AA^{-1} to 0.5 \AA^{-1} allowing investigation of inhomogeneities on a length scale from 5 \AA to 1400 \AA . The instrument is installed on the curved neutron guide No.2, of $4 \times 4 \text{ cm}^2$ cross-section, made from super-mirrors. The beam is monochromatized by a multidisk type velocity selector. The scattered neutrons are detected by a 64×64 pixels two-dimensional position sensitive detector filled with BF_3 gas. The pixel size is $1 \text{ cm} \times 1 \text{ cm}$. The samples can be placed into external magnetic field ($\sim 1.6 \text{ T}$) perpendicular to the incident neutron beam direction.

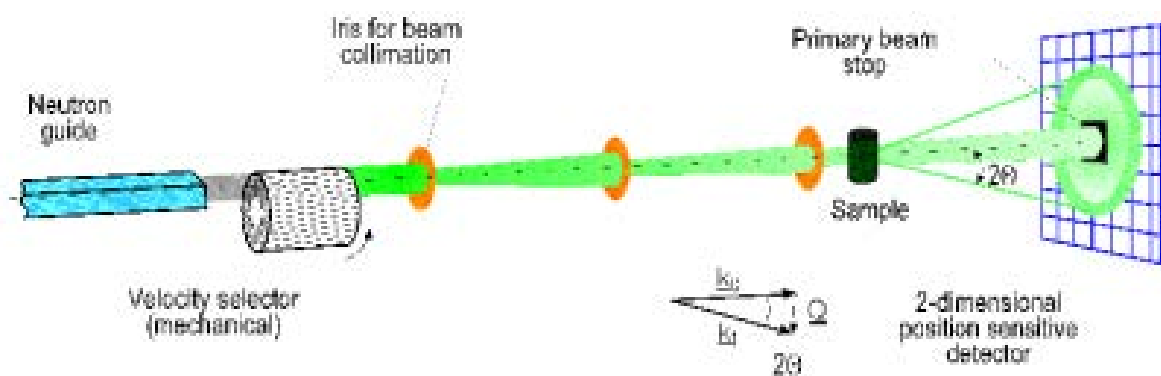


FIG. 3. Scheme of the SANS diffractometer at the Budapest neutron Centre.

3.3 Thermoelectric power measurements

In principle, all the processes involved in radiation embrittlement (precipitation, segregation, void swelling etc.) affect the electronic properties of materials and change their electrical and thermal conductivity. This phenomenon is utilized in electrical resistivity and thermo-electric power (TEP) measurements, which in the past have been successfully, applied to radiation embrittlement studies [15, 16]. The main advantage of these techniques is the simplicity of apparatus and excellent repeatability of results. However the results of these experiments must be interpreted very carefully and with respect to complementary information derived from other analytical techniques.

Experimental device for the TEP measurements (Fig. 4.) consists of two copper blocks, on top of which the specimen to be measured is placed. This makes an inhomogeneous circuit. Temperature gradients across the sample (when one of the blocks is heated) typically induces thermoelectric voltage between the sample's tips. During the measurements ($\sim 2 \text{ min}$) both the temperature difference and thermoelectric voltage (ΔE) are recorded and the thermoelectric power (also called the Seebeck coefficient) is obtained as the slope of the $\Delta E - \Delta T$ curve. Typical uncertainty of these measurements is 3%. Our experimental TEP device has been constructed for measurements of small samples where the dimensions can be in the range from $10 \times 10 \text{ mm}$ (here the maximum -diagonal distance is used) up to half Charpy samples. The device is portable and is suitable for measurements of irradiated samples in hot cells.

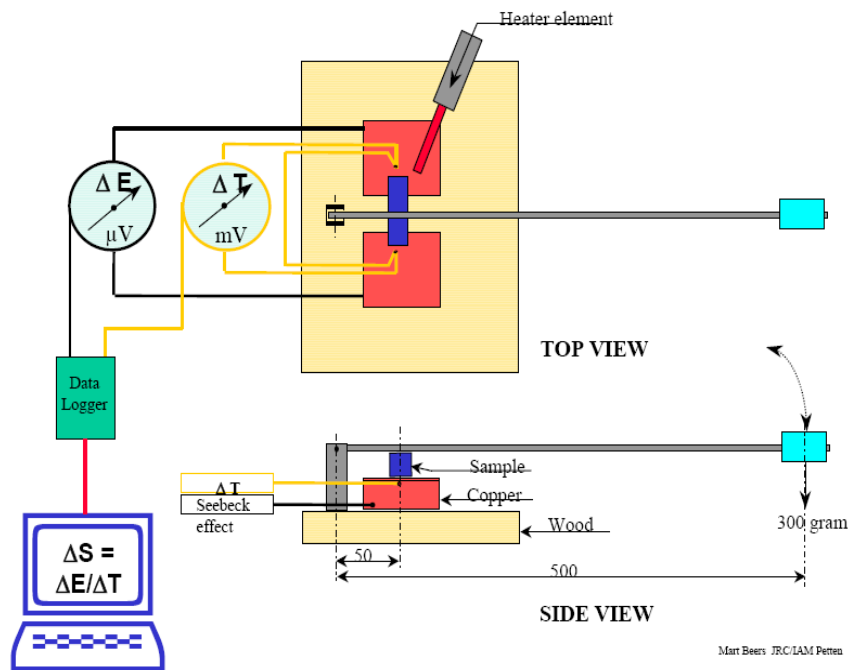


FIG. 4. Scheme of the TEP device for material characterization.

4. RESULTS

4.1 PALS

Analytical data processing was performed using the LT 9.0 program and two-component decomposition of the spectra. The lifetime spectra were fitted with a variance of fit (FV) ranging from 0.97–1.18 after source correction. As can be seen in Table 3, no presence of dislocations (or very small dislocation density respectively) has been observed in the recrystallized materials and the first lifetime component, which is then solely attributed to bulk annihilation, is reduced according to the standard trapping model [17]. On the other hand, the as-extruded ODS materials and reference Eurofer 97 show τ_1 values close to or higher than the bulk lifetime (108ps) and therefore τ_1 is considered to result from a combination of bulk annihilation and trapping in defects, preferably dislocations. Dislocation densities calculated according to the model described in the previous section are listed in Table 3. In all ODS steels investigated, the longer component of the lifetime spectra (~ 240 ps) can be well separated. Its value can be assigned to both yttria nanoparticles [18] and small clusters with the mean size of 4–5 vacancies¹ which are a result of mechanical alloying procedure [19, 20]. We assume that these defects are associated in particular with the yttrium and yttrium aluminium oxides where they have higher thermodynamic stability and a higher probability to “survive” the recrystallization. It is clear that positron trapping in small vacancy clusters and yttria particles in the ODS steels can hardly be distinguished experimentally. Reasonable estimates for the individual positron trapping processes can be made, however, using known characteristics of yttria nano-features (YNF) (see Table 2). The fractions of positrons trapped in four-vacancy clusters and positrons trapped in YNF calculated according to refs. 4–7 are compiled in Table 3. In particular, one can see a reduction of positrons trapped in YNF after recrystallization annealing of the materials. This is due to decreasing YNF concentrations, which accompany YNF coarsening at temperatures closely below the melting temperature.

¹ In case of the reference Eurofer 97 material, the second lifetime component can be attributed to di-vacancies in Fe [12].

TABLE 3. PALS RESULTS, CALCULATED DENSITIES OF VARIOUS DEFECTS AND INDIVIDUAL FRACTIONS OF POSITRONS ANNIHILATED IN THE MATERIAL BULK AND VARIOUS DEFECTS. MLT IS THE POSITRON MEAN LIFETIME GIVEN AS THE WEIGHTED AVERAGE OF TWO LIFETIME VALUES

Material	PALS results				FV	Defect concentration		Positron annihilation / trapping			
	\square_1 [ps]	\square_2 [ps]	I_2 [%]	MLT [ps]		$N_{\text{disl.}}$ [m ⁻²]	$N_{\text{VC (4V)}}$ [m ⁻³]	Bulk [%]	Disl. [%]	VC [%]	NF [%]
PM2000 ex.	129	253	54	196	1.09	1.4×10^{14}	1.9×10^{23}	19	27	34	20
MA957 ex.	152	256	57	211	1.00	4.5×10^{14}	5.5×10^{23}	7	36	39	18
ODS EU ex.	127	245	51	187	1.18	1.2×10^{14}	1.0×10^{23}	22	28	20	30
MA956 rec.	87	252	54	176	1.03	-	8.5×10^{22}	55	-	33	12
PM2000 rec.	83	241	54	168	1.05	-	8.2×10^{22}	57	-	31	12
ODM751 rec.	85	260	48	169	1.11	-	6.0×10^{22}	62	-	25	13
Eurofer 97	99	202	42	142	1.00	2.4×10^{13}	1.6×10^{23}	58	11	31 ²	-

As can be seen from Figs 5 and 6, the highest positron mean-lifetime caused by the highest fraction of positrons trapped in lattice imperfections was observed in MA957. Although this material has the lowest content of Y₂O₃, its oxide particles exhibit the finest dispersion structure, reducing the distance between particles and increasing the probability of positron trapping. Actually, in this material positron trapping is close to the saturation level (annihilation in bulk is only ~ 15%). On the other hand, the recrystallized materials with oxide particle sizes about 10 times higher show ~ 2–3 times lower positron trapping in YNF than the as-extruded materials. It is important to note that the vacancy type defects should be considered in conjunction with the YNF. In fact, the presence of vacancy type defects seems to stabilize the oxide particles [21, 22], a hypothesis which, in principle, can be explored by PALS experiments. This issue, however, requires further research in order to elucidate the role of vacancies in the structural stability of YNF.

Measurements of positron lifetimes in the ODS materials (three recrystallized ODS steels and the ODS Eurofer) aged at 475°C show the evolution of vacancy type defects with annealing time. The behaviour of the average positron lifetime $\tau_{AV} = \sum I_i \cdot \tau_i$ (Fig.7.), which constitutes the statistically most robust parameter, shows different trends for individual materials. Since the coarsening of oxide particles below ~1100°C is negligible, we can attribute these changes to the mobility and recovery of vacancy type defects. As can be seen in Fig.7, three different behaviours were observed. We assume that in the case of PM2000 and ODM751, dissociation of vacancy clusters, which saturates after 100h of 500h respectively, is taking place [23]. MA956 does not show this phenomenon and in fact no significant changes were observed during the thermal treatment. In contrast to this, the average positron lifetimes of ODS Eurofer increase after aging up to 500h. Similar behaviour was observed by Rajaraman et al. [23] for the Fe-Y₂O₃ steel thermally aged at intermediate temperatures.

² Calculated for di-vacancies.

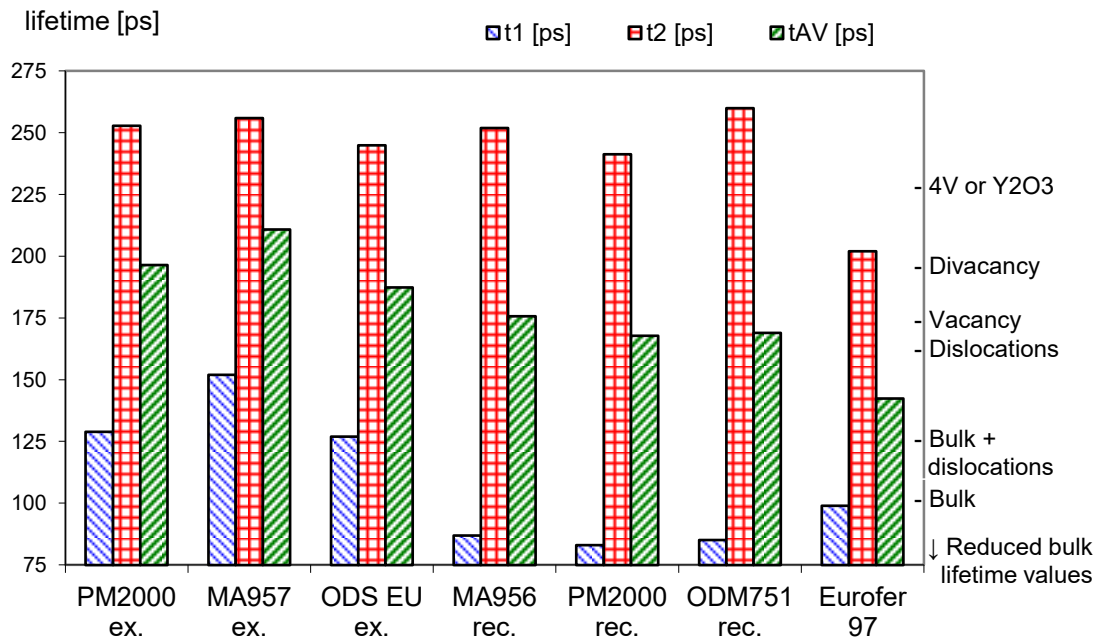


FIG. 5. Positron lifetimes in the investigated materials.

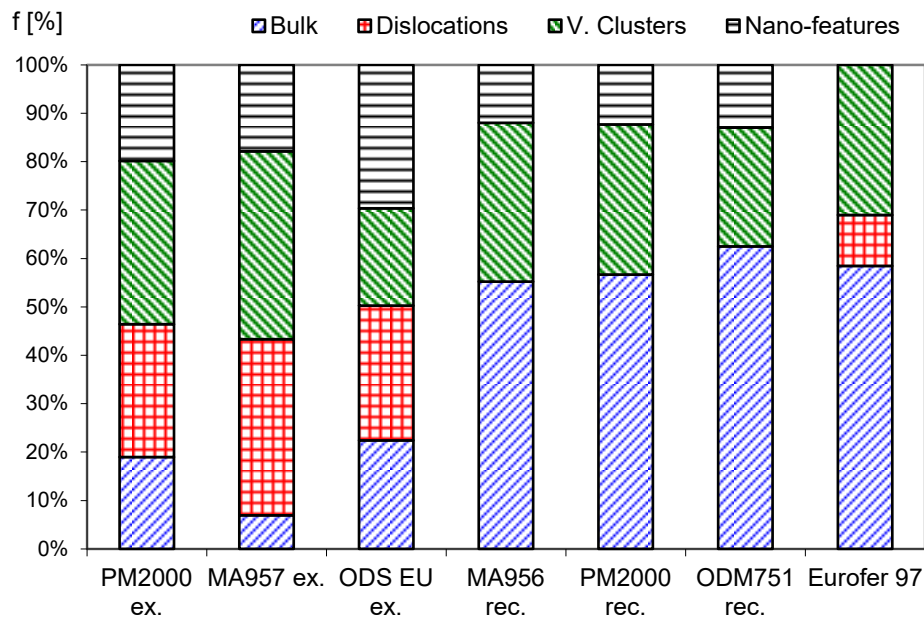


FIG. 6. Fractions of positron annihilation in bulk and individual trapping sites.

When only one type of trapping centre is considered to determine the large component of the positron lifetime spectrum, the calculated concentrations of these centres for individual materials are $1 - 3.5 \times 10^{23} \text{ [m}^{-3}\text{]}$. This would be in good agreement with the PALS experiments of Alinger et al. [19]. These trapping centres, however, cannot be considered neither as YNF nor as vacancy clusters, but rather as a combination of both. Since the information about the mean size and concentration of yttria nano-particles was available for the present materials, we have used the diffusion trapping model [24] to estimate fractions of positron trapping at these particles and consequently, to obtain more accurate results for the vacancy clusters concentrations (Table 3). For these calculations we have used the diffusion length (40nm) adopted from the literature, experimentally obtained for iron-based model alloys with similar concentrations of vacancy type defects. Our experiments show that the

value of 40nm is fairly close to the actual values of positron diffusion lengths for the materials investigated here, since the maximum possible value obtained from the experimentally measured trapping rate is $L_+ < 50\text{nm}$ for as-extruded materials and $L_+ < 65\text{nm}$ for recrystallized materials³. Higher values would lead to trapping rates higher than the actually measured ones. In other words, longer diffusion lengths would imply the positron trapping to occur exclusively in the YNF and the presence of vacancy type defects, if any, would be associated to those particles only. However, this is at variance with the observation that positron trapping at vacancy clusters was reported in mechanically alloyed materials without oxide nanoparticles as well [25]. So the presence of vacancy clusters seems to result from the fabrication process, rather than from the presence of nano-oxides.

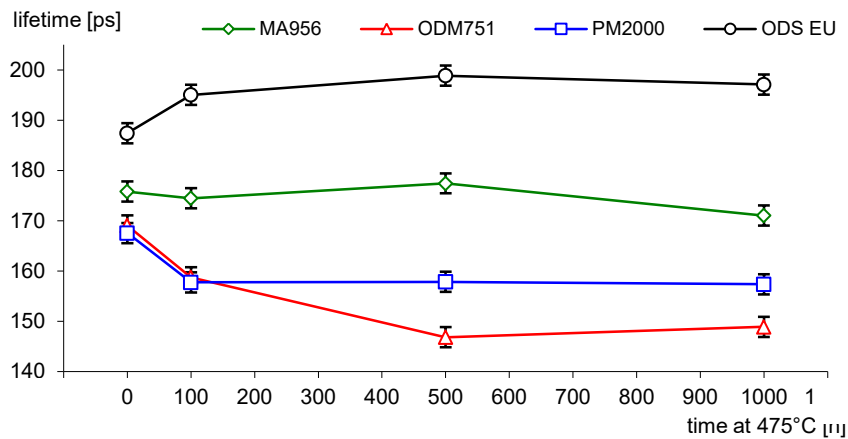


FIG. 7. Average positron lifetime in the isothermally aged materials.

The effect of α' precipitation, which is one of the key factors in the thermal (radiation) embrittlement of high Cr steels, cannot be observed in the Fe matrix by the positron lifetime technique directly. Positron lifetime of Cr bulk is very similar to Fe bulk, while the positron affinity of Cr is even lower than the one of Fe. This is the reason why the positron trapping at nano-sized Cr precipitates cannot be distinguished in the lifetime spectra. However, various studies published in the literature report effect of Cr rich zones on the mobility of vacancy clusters, which indicate a possibility of application of PALS technique on the study of the α' precipitation. In the paper by Kuramoto et al [26] the authors describe the effect of chromium precipitation on the formation of microvoids in the thermally annealed Fe-Cr alloys. This work concludes that the tendency to formation of microvoids is lower when Cr enriched zones are present in the matrix. The presence of such zones-precipitates was observed in our thermal aging experiments for high-Cr materials.

Direct evidence for α' precipitation was obtained from the small angle neutron scattering, where new ~ 5 nm scattering centres appeared after 100h hours of thermal aging and indirect confirmation was provided also by microhardness measurements, results of which are shown in Fig. 8. Consequently, the measurements of positron lifetime showed that an agglomeration of vacancies took place only in the ODS Eurofer material, where the Cr-rich α' precipitation was not observed (Fig. 7). Accordingly, the calculated fraction of positron trapping at vacancy clusters shows that this value increases with the time of the thermal aging for the ODS

³ For comparison, the positron diffusion lengths reported for defect-free metals is $\sim 100\text{nm}$ [22].

Eurofer in contrast with the PM2000 and ODM751 materials and early stages of the MA956 material (Fig. 9). We assume that this is due to the presence of Cr precipitates in the 16–20%Cr materials where the formation of vacancy agglomerates is hindered and consequently indirect PAS observation of this phenomenon is possible.

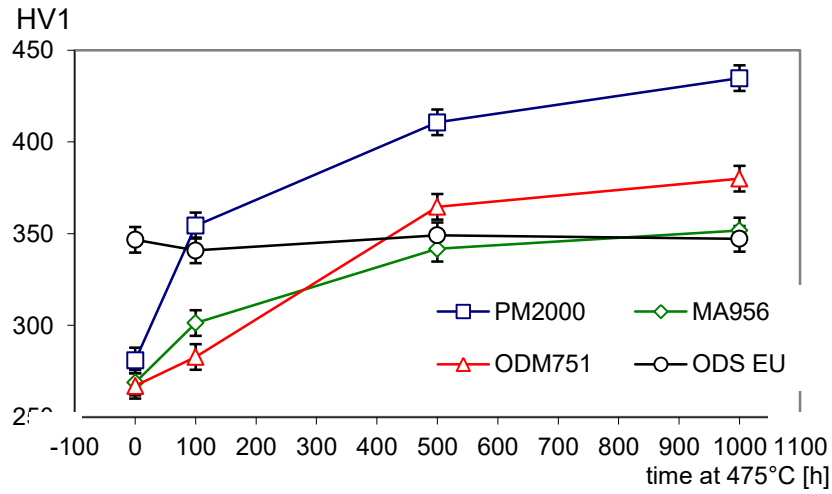


FIG. 8. HV1 results of the isothermally aged materials.

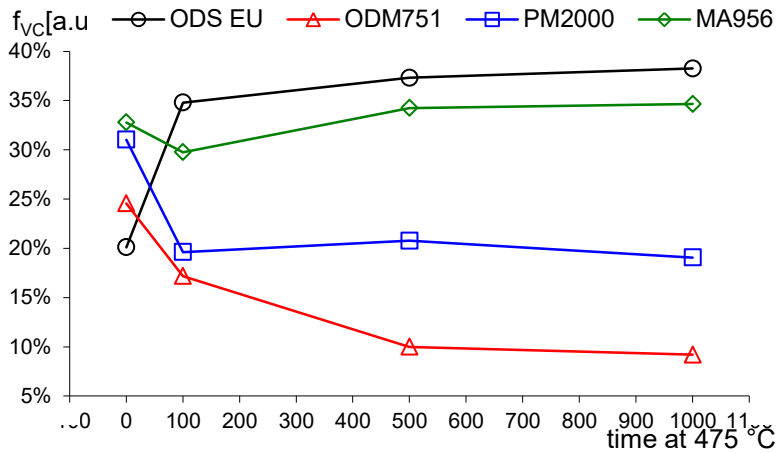


FIG. 9. Fraction of the positron trapping at vacancy clusters of the isothermally aged materials.

However, the work of Malerba et al. [27] concludes that although the presence of Cr in ferritic (ferritic/martensitic) alloys has an effect on radiation induced defect formation, the dependence on Cr concentration is non-monotonic and therefore difficult to rationalize. Yet it is not clear how the elevated temperature irradiation results can be extrapolated to the thermal-only degradation studies. Not only the role of chromium in material degradation, but also the effect of yttria nano-particles on the behaviour of the Fe-Cr systems needs further research to be carried out in conjunction with other techniques, providing complex information about all nano-sized features related to radiation embrittlement.

4.2 SANS

Samples in the shape of plates 1 mm in thickness were measured at two detector positions 1.3 and 5.5 m and at wavelengths of 6.09 Å and 15.96 Å in BNC Budapest. The corresponding q range was from $4 \times 10^{-2} \text{ nm}^{-1}$ to 2.5 nm^{-1} . The samples were placed into an external saturating

magnetic field (~ 1.6 T) perpendicular to the incident neutron beam direction. The measured data were corrected for sample transmission, detector response and background. Data calibration was done using a water standard.

All materials showed a strong SANS signal in both the as-recrystallised and aged states. The SANS measurements revealed that thermal treatments result in substantial changes in the microstructure at the nanometer scale. Figure 10 shows the magnetic and nuclear coherent scattering cross-sections of the as-received and the three aged states of PM2000 material. The curves for MA956 have the same character. A pronounced ageing-induced increase is found in the magnetic and nuclear scattering curves at scattering vectors $q > 0.40 \text{ nm}^{-1}$.

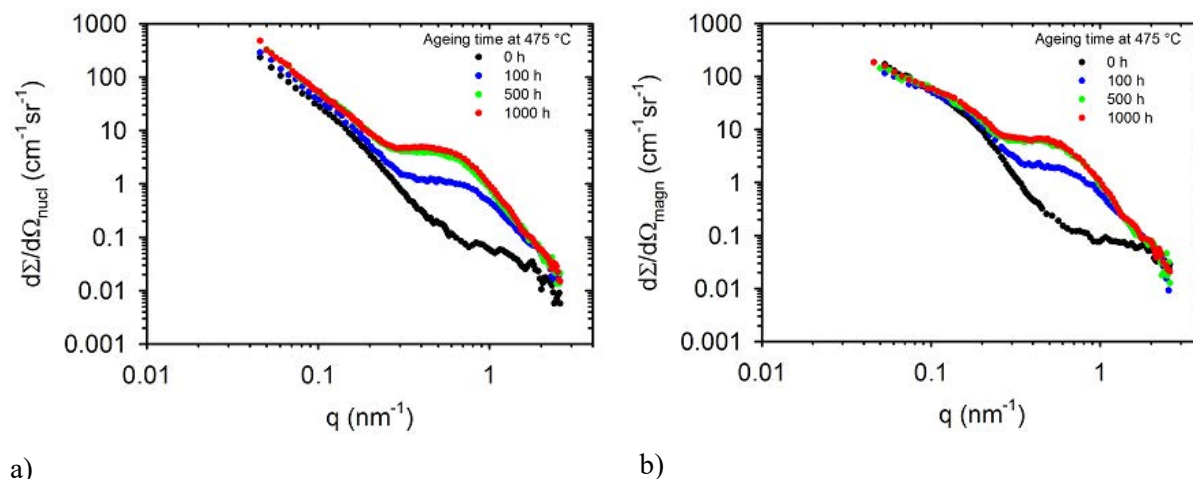
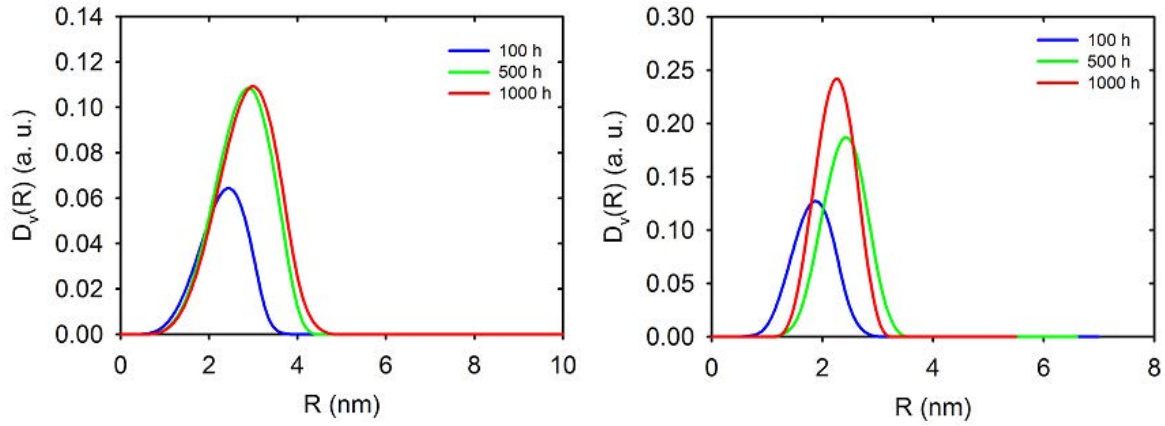


FIG. 10. Nuclear and magnetic SANS scattering cross-sections for PM2000 in as-received

The aged material states were compared to the as-received material. We focused on the pronounced effects at q -values larger than 0.4 nm^{-1} , on the formation of small precipitates during ageing. Analysis indicates formation of Cr-enriched precipitates (α' phase) at the nanometer scale during thermal ageing at 475°C . From the SANS data the volume distribution functions for the different material states were calculated using the indirect transformation method developed by O. Glatter. The corresponding size distributions are shown on Fig. 11. The A-ratio (defined as ratio of the scattering cross-sections perpendicular and parallel to the magnetic field direction) of the aged MA956 samples ($A=1.95\pm 0.15$) is in good agreement with $\alpha - \alpha'$ phase separation of the ferritic matrix. Higher A-ratio ($A=2.5\pm 0.2$) for PM2000 sample aged 100h indicates a mixture of α' particles and different type of scatter centres.



a) b)
 FIG. 11. Particle size distribution at three aged conditions in a) PM2000, b) MA956.

4.3 TEP

The Seebeck coefficient of iron-based solid solutions depends strongly on the alloying elements especially if the content is higher than 0.1wt%. Although the Seebeck coefficient of iron against platinum is $+19\mu\text{V/K}$ and the relative Seebeck coefficient of copper with the same reference material is $+6.5\mu\text{V/K}$ [28], measurements on steels with copper⁴ as the reference usually result in small, sometimes even negative values. This is also the case of ferritic ODS steels where, as can be seen in Table 4, the Seebeck coefficient values were found to be in the in the range $-1.1 - 2.2 \mu\text{V/K}$.

TABLE 4. RELATIVE SEEBECK COEFFICIENTS OF THE AS-RECEIVED ODS ALLOYS MEASURED WITH COPPER AS A REFERENCE MATERIAL

PM2000	MA956	ODM751
$-1.41 \mu\text{V/K}$	$-2.19 \mu\text{V/K}$	$-1.10 \mu\text{V/K}$

The relative Seebeck coefficient ($S=\Delta V/\Delta T$) can be expressed as: $S = \Delta S_{\text{SS}} + \Delta S_{\text{D}} + \Delta S_{\text{P}}$, where ΔS_{SS} , ΔS_{D} and ΔS_{P} are contributions from the elements in solid solution, dislocations and precipitates respectively. Since we have investigated only materials in the as-recrystallized state with low dislocation density, the effect of dislocations was not considered. Moreover, no indications of metallurgical changes other than decomposition of the ferritic phase to Cr-rich α' and Fe-rich α phase were observed by other techniques. This allowed us to reduce the expression for relative Seebeck coefficient to $S = \Delta S_{\text{SS}(\text{Cr})} + \Delta S_{\text{P}(\text{Cr})}$. Since chromium in solid solution increases the Seebeck coefficient value [29], the precipitations of this element from the matrix cause the opposite effect. In our case therefore, the first term in the expression above is negative. The effect of the precipitates (second term of the expression) depends strongly on the size and structure of the precipitates. As can be seen in the Fig. 12, the value of Seebeck coefficient increases with the precipitation of α' , which means that the second term of the expression above must be positive and the dominant one.

As can be seen in the Fig. 13, the behaviour of the Seebeck coefficient corresponds very well to the evolution of the hardness of the heat treated materials. We assume that this is primarily due to the precipitation of Cr-rich phases which increase both hardness and thermoelectric power. Since the precipitation of α' is typical for the intermediate temperatures, in our future

⁴ Hereinafter the thermoelectric power coefficient is always given as a relative Seebeck coefficient or ΔS measured against copper, unless stated otherwise.

experiments we propose higher temperature (650°C) in order to thermally age the materials without introduction of α' . At the time of submission of this report, the experiments are running. Evaluation of the experiments is planned for 2012.

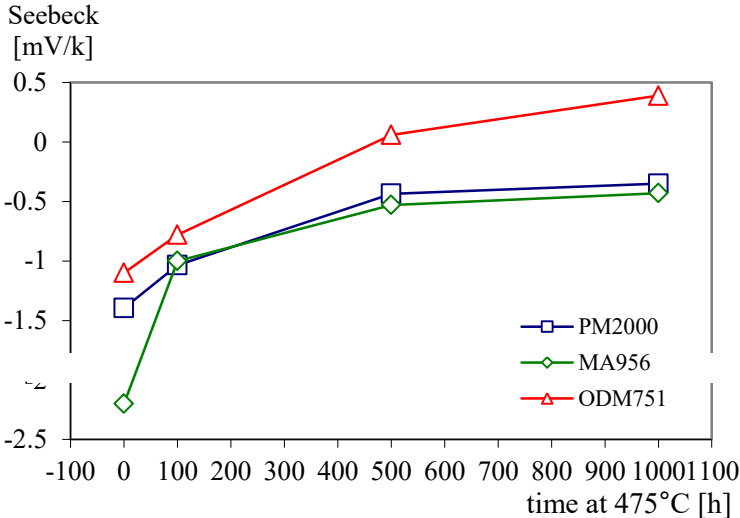


FIG. 12. Seebeck coefficient of the thermally aged materials. Measurements with copper as a reference.

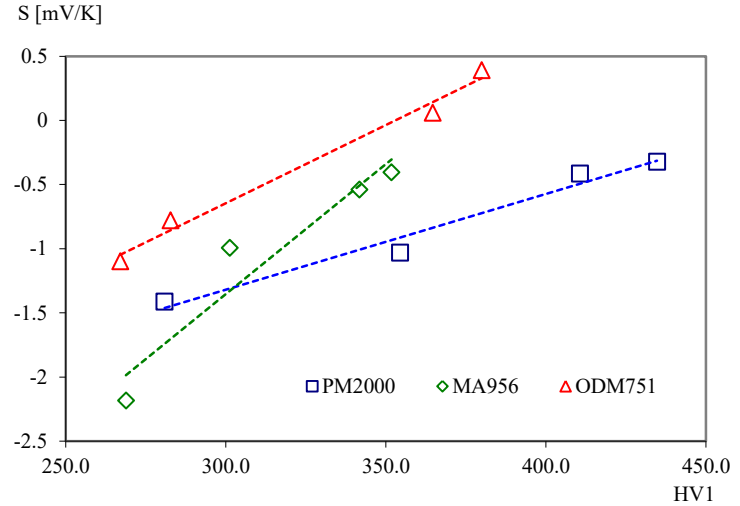


FIG. 13. Correlation of the TEP results with the hardness measurements on the materials aged at 475°C for 0 - 1000h.

5. CONCLUSIONS

This study describes the behaviour of the microstructure of oxide dispersion strengthened steels at intermediate temperatures. Three different techniques were used for the characterization of the microstructure of the oxide dispersion strengthened steels thermally aged at 475°C. All techniques, namely positron annihilation lifetime spectroscopy, small angle neutron spectroscopy and thermoelectric power measurements are very sensitive to metallurgical modifications and presence of nano-sized imperfections in the crystal lattice. As can be seen in the results, precipitation of the nano-sized α' phases, directly observed by SANS, affects the mobility of vacancy type defects and change the thermoelectric Seebeck coefficient of the high-Cr materials (PM2000, MA956 and ODM751). Since complementary TEM and XRD investigations did not confirm other metallurgical changes in the materials,

we assumed that the observed changes were mostly due to α' precipitation. The main conclusions obtained from the experiments are summarized below:

- Although the positron lifetime technique is not directly sensitive to the Cr-rich α' phase in the Fe lattice, the experiments showed that these precipitates affect the mobility of point defects and consequently change the annihilation characteristics.
- Presence of chromium rich zones in the ferritic materials with high Cr content (>15 wt%) plays a role in the mobility of point defects at 475°C. While in high-Cr alloys thermal aging leads to annealing of vacancy type defects, Fe-9%Cr ODS Eurofer showed notable coarsening of the vacancy clusters. This may lead to a significantly different radiation performance of the low and high chromium alloys at intermediate temperatures.
- SANS analysis indicated formation of Cr-enriched precipitates (α' phase) at the nanometer scale during thermal ageing at 475°C.
- The A-ratio of the aged MA956 samples is in good agreement with $\alpha - \alpha'$ phase separation of the ferritic matrix. Higher A-ratio for PM2000 sample aged 100h indicates a mixture of α' particles and different type of scatter centres.
- TEP experiments showed that the precipitation of chromium from the matrix has a more pronounced effect in the changes of Seebeck coefficient than the chromium depletion of the matrix.
- The course of the Seebeck coefficient with the aging time corresponds very well to the results of hardness measurements in all studied materials.

In conclusion, we have demonstrated the successful feasibility of the applied techniques on the complementary characterization of the ODS steels performance. We believe that the understanding of the irradiation performance cannot be separated from the studies of thermal-induced degradation processes. In particular, irradiation experiments on ferritic ODS alloys at intermediate temperatures must be interpreted carefully and with respect to the chromium behaviour. NDT complementary techniques therefore must be thoroughly considered for the irradiation experiments in order to obtain complex information about the behaviour of material microstructure.

REFERENCES

- [1] R. L. KLUEH, D. R. HARRIES, High-Chromium Ferritic and Martensitic Steels for Nuclear Applications, West Conshohocken, American Society for Testing and Materials, ISBN: 0-8031-2090-7 (2001).
- [2] V. SLUGEN et al., Journal of Nuclear Materials **302** (2002) 89–95.
- [3] V. KRSJAK et al., Applied Surface Science, **255** (1) (2008) 153–156.
- [4] B. ACOSTA et al., Nuclear Engineering and Design **235** (2005) 1951–1959.
- [5] J. KOCIK et al., Journal of Nuclear Materials **303** (2002) 52–64.
- [6] F. BERGNER et al., Journal of Nuclear Materials **373** (2008) 199–205.
- [7] J.K. SAHU et al., Materials Science and Engineering A 508 (2009) 1–14.
- [8] H. K. D. H. BHADSHIA, Mater. Sci. Eng. **A223** (1997) 64–77.
- [9] P. KRAUTWASSER, A. CZYRSKA-FILEMONOWICZ, M. WIDERA, F. CARSUGHI, Mater. Sci. Eng. **A177** (1994) 199–208.
- [10] J. CHEN, W. HOFFELNER, Journal of Nuclear Materials **392** (2009) 360–363.
- [11] H. K. D. H. BHADSHIA, Materials Science and Engineering **A223** (1997) 64–77.
- [12] H. CAMA, T. A. HUGHES, Materials for Advanced Power Engineering (monograph), D. Coutsouradis et al (eds.), Kluwer Academic Publishers, Netherlands, 1994, pp. 1497 – 1506.

- [13] J. GOULD, J. BERNATH, R. MILLER, M. ALINGER, C. ZANIS, *Journal of Nuclear Materials* **367–370** (2007) 1197–1202.
- [14] C. HEINTZE, F. BERGNER, A. ULBRICHT, M. HERNÁNDEZ-MAYORAL, U. KEIDERLING, R. LINDAU, T. WEISSGÄRBER, *Journal of Nuclear Materials* **416** (2011) 35–39.
- [15] M. NIFFENEGGER, H.J. LEBER, *Journal of Nuclear Materials* **389** (2009) 62–67.
- [16] G. R. ODETTE and C. COWAN, “Use of Combined Electrical Resistivity and Seebeck Coefficient Measurements to Characterize Solute Redistribution Under Irradiation and Thermal Aging,” *Proceedings of the 10th International Symposium on Environmental Degradation of Materials in Light Water Reactors* (Houston, TX: National Association of Corrosion Engineers, 2001).
- [17] A. VEHANEN, P. HAUTOJARVI, J. JOHANSSON, J. YLI-KAUPPILA, P. Moser, *Phys. Rev.* **B 25** (1982) 762.
- [18] L. C. DAMONTE, M. A. TAYLOR, J. DESIMONI AND J. RUNCO, *Rad. Phys. Chem.* **76** (2007) 248.
- [19] M. J. ALINGER, S.C. GLADE, B.D. WIRTH, G.R. ODETTE, T. TOYAMA, Y. NAGAI, M. HASEGAWA, *Mater. Sci. Eng.* **A 518** (2009) 150–157.
- [20] J. H. SCHNEIBEL, Z. P. LU AND S. H. SHIM, “Nanoprecipitates in Steels, in ”*Proceedings of the Twenty First Annual Conference on Fossil Energy Materials*, April 30-May 2, 2007, published December 2007, R. R. Judkins, ed., url <http://www.ms.ornl.gov/fossil/proceedings.shtml>, pp. 212–219.
- [21] C. L. FU, M. MILLER, M. KRCCMAR, D. HOELZER and C. T. LIU, TMS2007 136th Annual Meeting & Exhibition, February 25-March 1, 2007, Orlando, FL, USA, Abstract in Final Program, p. 27.
- [22] M. MILLER, C. L. FU, M. KRCCMAR, D. HOELZER, C. T. LIU, *Frontiers of Materials Science in China*, Vol. 3, Issue 1, 2009.
- [23] R. RAJARAMAN, G. AMARENDRA, C. S. SUNDAR, *Phys. Stat. Sol. (c)* **6** (2009) 2237–2603.
- [24] O. MELIKHOVA, J. CIZEK, J. KURIPLACH, I. PROCHAZKA, M. CIESLAR, W. ANWAND, G. BRAUER, *Intermetallics* **18** (2010) 592–598.
- [25] ORTEGA et al., *Journal of Nuclear Materials* **376** (2008) 222–228.
- [26] E. KURAMOTO, S. NAGANO, K. NISHI, K. MAKII, Y. AONO and M. TAKENAKA, *Mater. Sci. Forum* **105–110** (1992), p. 1125.
- [27] L. MALERBA, A. CARO, J. WALLENIUS, *Journal of Nuclear Materials* **382** (2008) 112–125.
- [28] ZEKI BERK, *Food Process Engineering and Technology*, 2008, p.143.
- [29] V. MASSARDIER et al., *Materials Science and Engineering* **A355** (2003) 299–310.

INFLUENCE OF IRRADIATION EFFECTS ON MECHANICAL PROPERTIES OF AUSTENITIC STAINLESS STEEL

W. SZTEKE, J. WASIAK, W. BŁOVS, E. HAJEWSKA, T. WAGNER

Material Research Laboratory
National Centre for Nuclear Research
Otwock,
Poland

Abstract

The influence of irradiation with heavy ions and electrons on mechanical properties of stainless steel was studied. The small punch method was used in the experiments. It was found that the small punch method is not useful for specimens with thickness of only 0.05mm. Good results were obtained for specimens with thickness 0.25mm. Whereas swift heavy ions were sufficient for penetration of 0.05mm foils, the use of 0.25mm foils required the use of high energy electrons to conduct studies on radiation embrittlement. It was determined that the small punch method can be successfully applied for determination of crack toughness of metals, but the technique is not very precise for evaluation of tensile and yield strengths.

1. INTRODUCTION

Stainless steel is the main structural material used in the construction of some types of nuclear reactors. Each power reactor has a surveillance program, which involves the necessity of investigating changes of material properties during the time of its exploitation. Evaluation of the influence of radiation on the properties of materials therefore needs long time irradiation of specimens in research reactors. In the absence of such reactors and sufficient time, the use of heavy ion irradiation in an accelerator facilitates the investigation of radiation-induced changes in material properties and involves much lower costs than in the case of reactor neutron irradiation.

Radiation defects, introduced by either heavy ions or by neutron radiation, produce point defect complexes and longitudinal defects in metals that can cause changes of structural phase state. As a result, other properties of metals can change, especially the mechanical properties. In the frame of this project the dependence of tensile strength and impact strength of stainless steel on swift heavy ion and electron irradiation was studied.

As a result of the work performed in the scope of this project we expected to evaluate the influence of both specimen size and effect of heavy ion radiation on the mechanical properties of stainless steel. During the project we also found it necessary to use electron irradiation rather than swift heavy ions.

Small punch test specimens of thin stainless steel foils have been investigated and the results have been compared with the tensile strength obtained with normal tensile specimens. After evaluation of this dependence experiments involving specimens irradiated by swift heavy ions were investigated. The irradiation was performed in the heavy ion accelerator in JINR in Dubna, using swift heavy ions of ^{40}Ar , ^{84}Kr or ^{129}Xe .

The other part of the investigation was the evaluation of impact strength also using thin stainless steel plates. The tests were conducted on the micro-specimens made from the steel plates and the results have been compared with these obtained with thin foils. After evaluation of the dependence of specimen size and the impact strength, the specimens from thin plates were irradiated in the accelerator in Dubna. Further examination of the irradiated specimens was conducted in Materials Research Laboratory in Świerk.

2. SMALL PUNCH TEST

The small punch test involves specimen deformation by pushing a ball into a free-standing section of plate. The specimens have a form of thin plate with a circular or rectangular cross section. The schema of the assembly used in these tests is given in Fig. 1.

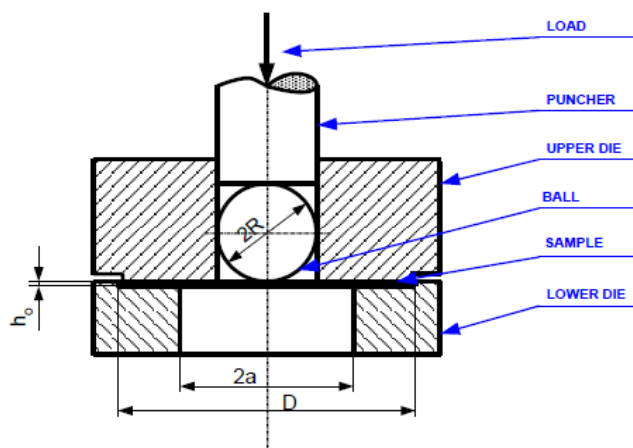


FIG. 1. The schema of the assembly used in the small punch tests.

During the time of measurement the force – deflection curve of the specimen was recorded. An example of a typical curve is presented in Fig. 2. The curve incorporates information about the elastic – plastic properties and strength properties of the material. The curve may be divided into several zones and for each zone the phenomenon determining its shape can be ascribed.

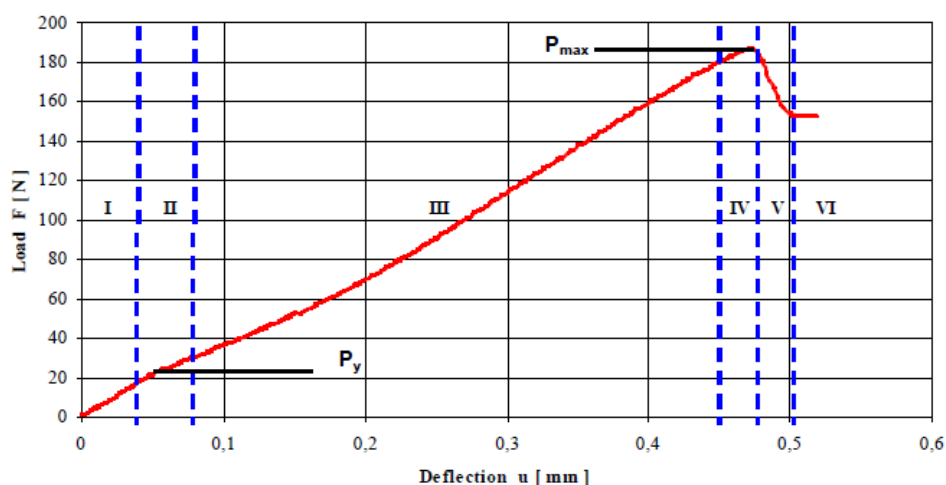


FIG. 2. Example of the force – specimen deflection diagram.

In zone I the elastic properties dominate. Zone II shows the transient zone between elastic and plastic properties of material. Zone III shows the strengthening of material up to zone IV where the plastic deformation and flow of specimen occurs. At the beginning of zone V crack initiation commences, where cracks progressively develop and join. This is coincident with a rapid decrease of the force loading the specimen. Zone VI determines the force necessary for forcing the ball through the specimen notwithstanding the crack.

As will be shown, the dependence between curves obtained in the small punch test and the mechanical properties of the material are rather complicated, such that it is impossible to describe it with one generalized formula. Of necessity the small punch method requires many different empirical formulas to be elaborated.

On the basis of phenomenological dependencies some correlations between the results of measurements with small punch method and obtained using standard mechanical tests can be determined. In this:

P_y - usually determined from the yield point,

P_{max} - can be determined from the tensile strength,

W_u - surface under P-u diagram, related to the impact strength or the crack resistance.

3. MATERIALS USED IN THE INVESTIGATION

Different structural materials were used for the investigation. They were selected for diversification of mechanical properties to obtain calibration curves with a very large range. Analyses of the chemical composition of the steels were performed using the spectrometer method. The measurements of alloying components and impurities are presented in Table 1. It was found that the compositions of all materials are compatible with their individual standard specifications.

TABLE 1. CHEMICAL COMPOSITION OF THE STEELS USING FOR DETERMINATION OF CALIBRATION CURVES

Material	contents in weight %									
	C	Si	Mn	P	S	Cr	Ni	Cu	Mo	V
0H18N10T (tape ≠0,4mm)	0,038	0,557	1,570	0,257	0,003	17,92	9,463	0,140	0,349	0,107
H10N7K10M5Pr (≠0,1mm)	0,026	0,072	0,081	0,006	0,004	9,851	7,126	-	5,610	-
R260 (1) (segment of rail)	0,745	0,290	1,090	0,025	0,011	0,052	0,030	0,053	0,010	-
R260 (2) (segment of rail)	0,721	0,365	0,876	0,014	0,012	0,037	0,037	0,020	0,002	-
R260 (3) (segment of rail)	0,750	0,271	1,170	0,033	0,009	0,010	0,021	0,010	0,010	0,010
L480 (pipe Ø1420x22mm)	0,099	0,241	1,490	0,011	0,001	0,017	0,014	0,012	0,002	0,056
13HMF (pipe Ø420x20mm)	0,153	0,289	0,501	0,018	0,013	0,438	0,119	0,052	-	0,288
30HGSNA (rod 50x25mm)	0,284	0,341	1,300	0,025	0,020	1,458	1,186	-	0,017	-
Steel under investigation 0H18N9 (rod Ø18)	0,290	0,463	1,627	0,040	0,020	18,32	8,302	0,504	0,282	-

All small punch tests were performed on specimens made from stainless steel 0H18N9 with austenitic structure, without precipitation of secondary phases.

4. DETERMINATION OF CALIBRATION CURVES

The parameters obtained in the small punch tests for specimens with 0.05mm thickness for determination of yield point and tensile are presented in Table 2.

TABLE 2. THE PARAMETERS OF CALIBRATION CURVES FOR DETERMINATION OF THE YIELD POINT AND TENSILE STRENGTH IN THE SMALL PUNCH TESTS

Material	R_m MPa	$R_{0,2}$ MPa	A_5 %	Z %	K_{mat} MPa m ^{1/2}
0H18N10T (tape ≠0,4mm)	1510	1090	-	-	-
H10N7K10M5Pr (tape≠0,1mm)	1280	840	-	-	-
R260 (1) (segment of rail)	950	540	13,2	26,7	34
R260 (2) (segment of rail)	940	490	11,8	28,8	30
R260 (3) (segment of rail)	980	570	11,6	26,7	29
L480 (pipe Ø1420x22mm)	577	480	29,7	78,2	180
13HMF (pipe Ø420x20mm)	600	440	24,0	66,1	130
30HGSNA (rod 50x25mm)	1090	940	12,9	31,7	100
Steel under investigation 0H18N9 (rod Ø18)	750	550	49	78	170

The equations of calibration curves were calculated using linear regression method.

TABLE 3. CALIBRATION CURVE PARAMETERS USED FOR DETERMINATION OF YIELD STRENGTH ON THE BASIS OF SMALL PUNCH TESTS (SPECIMENS WITH THICKNESS 0.05MM)

Material	P_y/h_0^2 kN/mm ²	P_{max}/h_0^2 kN/mm ²
0H18N10T (tape ≠0,4mm)	1,51	30,78
H10N7K10M5Pr (tape≠0,1mm)	1,33	49,17
R260 (2) (segment of rail)	0,63	13,92
13HMF (pipe Ø420x20mm)	1,13	14,50
Steel under investigation 0H18N9 (rod ø18)	1,51	31,0

The equation describing the dependence of the yield point from coefficient P_e and the initial thickness of the specimen h_0 is:

$$R_e = 585 \cdot \frac{P_y}{h_0^2}$$

The coefficient of correlation $R=0.7005$.

The equation describing the dependence of the tensile strength from coefficient P_{max} and the initial thickness of the specimen h_0 is:

$$R_m = 19,73 \cdot \frac{P_{max}}{h_0^2} + 497$$

The coefficient of correlation $R=0.687$.

The calibration curves as well as the results of measurements of P_y and P_{max} parameters determined by the small punch method using specimens of stainless steel 0H18N9 with thickness 0.05mm are presented in Figs 3 and 4. On these diagrams the index of mechanical properties obtained using standard specimens, as well as using small punch method are presented. A large enough difference between the values of mechanical parameters obtained by the two different methods indicates the small accuracy of the measurements obtained by the small punch method. Also, the scatter of results of measurements of P_y and P_{max} coefficients (standard deviation about 30% of the measured value) indicate the low precision of the small punch method.

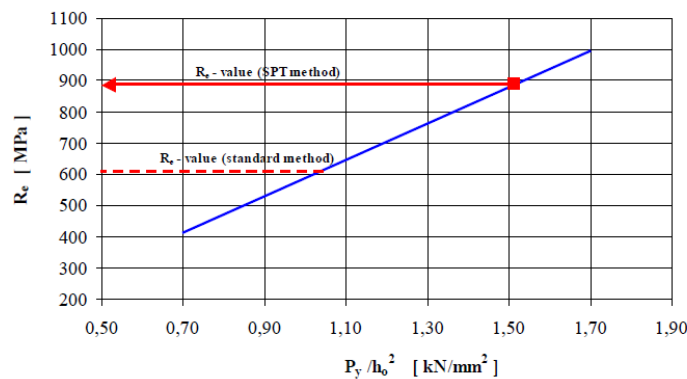


FIG. 3. Measurements of yield point with small punch method using 0H18N9 with thickness 0.05mm.

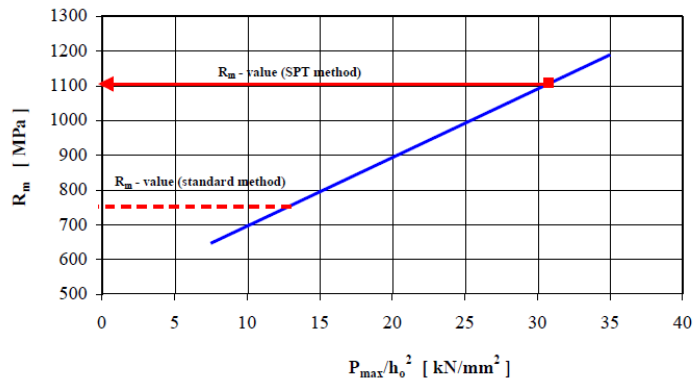


FIG .4. Measurements of tensile strength with small punch method using 0H18N9 with thickness 0.05mm.

On the first phase of loading specimens with thickness 0.05mm the diagrams had linear courses, without a distinct point of change from elastic strains to plastic strains. In this situation it was impossible to precisely determine the P_y value. A similar character of the loading – deflection diagrams (Fig. 5) was seen for specimens with thickness 0.10mm, where the calibration curves have correlation coefficients near to the values obtained for specimens with thickness 0.05mm.

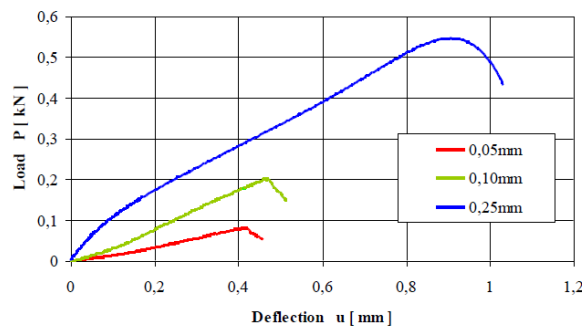


FIG. 5. Loading – deflection diagram of specimens studied using small punch method at thicknesses of: 0.05, 0.10 and 0.25mm.

As shown in Fig. 5, use of specimens with thickness 0.25mm allows a more precise determination of the P_y value. In connection with this observation, it was decided to perform further studies using specimens of thickness 0.25mm. Estimated parameters for calculation of calibration curves equations used for determination of yield point and tensile strength on the basis of small punch measurements for specimens with thickness 0.25mm are presented in Table 4.

TABLE 4. CALIBRATION CURVE PARAMETERS USING FOR DETERMINATION OF YIELD POINT AND TENSILE STRENGTH ON THE BASIS OF SMALL PUNCH TESTS (SPECIMENS WITH THICKNESS 0.25MM)

Material	P_y/h_0^2 kN/mm ²	P_{max}/h_0^2 kN/mm ²
30HGSNA (rod 50x25mm)	1,920	6,896
R260 (1) (segment of rail)	1,544	5,756
R260 (2) (segment of rail)	1,447	5,708
R260 (3) (segment of rail)	1,482	5,762
L480 (pipe Ø1420x22mm)	1,116	5,358
13HMF (pipe Ø420x20mm)	1,162	5,270
Steel under investigation 0H18N9 (pret Ø18)	1,705	8,147

The equation of calibration curve describing the dependence between yield point from P_y and the initial thickness of the specimen h_0 is:

$$R_e = 393 \cdot \frac{P_y}{h_0^2}$$

The coefficient of correlation $R=0.832$.

The equation of calibration curve describing dependence between tensile strength from P_{max} and the initial thickness of the specimen h_0 is:

$$R_m = 195 \cdot \frac{P_{max}}{h_0^2} - 378$$

The coefficient of correlation $R=0.808$.

The calibration curves and the results of measurements of parameters, as well as the results of the measurements with small punch method, using specimens with thickness 0.25mm from the 0H18N9 steel are presented in Figs 6 and 7. Plotted are the coefficients of mechanical properties determined from standard size specimens and the values determined from the small punch tests.

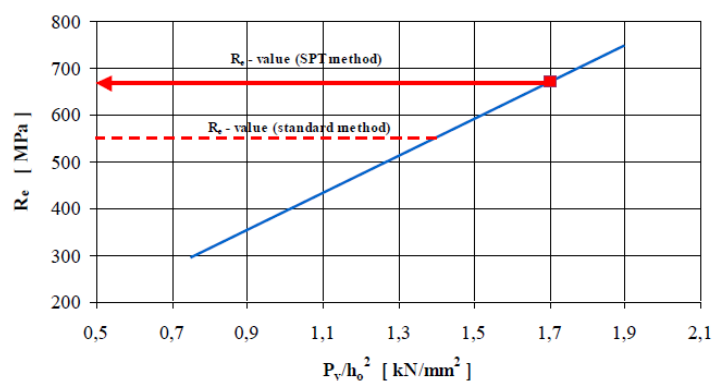


FIG. 6. Yield point measurements by small punch method using 0H18N9 specimens with thickness 0.25mm.

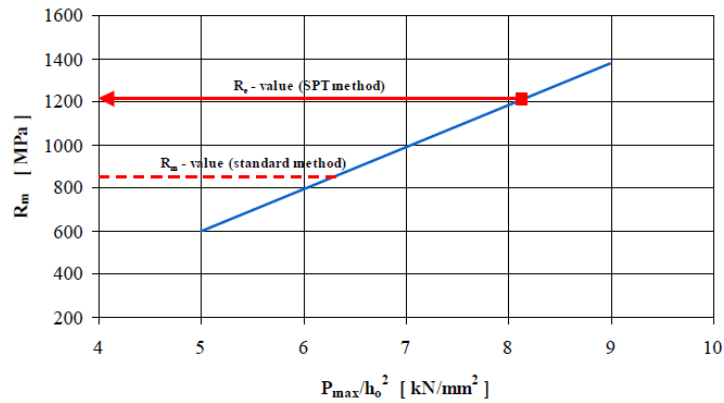


FIG. 7. Tensile strength measurements by small punch method using 0H18N9 specimens of thickness 0.25mm.

Similarly, as in the case of measurements of specimens with thickness 0.05 mm, the index of mechanical properties determined from standard, as well as small punch tests, are presented on the diagram. In the case of specimens with thickness 0.25 mm the differences between the measurements values determined with both standard and small punch methods were significantly smaller. Also the scatter of results of measurements, P_y and P_{max} coefficients (standard deviation range 10% of measurement values) confirm the better accuracy of small punch measurements for specimens with thickness of 0.25 mm.

The determined parameters for crack resistance evaluation on the basis of small punch tests for the specimens with thickness 0.25 mm are presented in Table 5.

TABLE 5. CALIBRATION CURVE PARAMETERS FOR EVALUATION OF CRACK RESISTANCE ON THE BASIS OF MEASUREMENTS WITH SMALL PUNCH METHOD (SPECIMENS WITH THICKNESS 0.25MM)

Material	$W_u/(P_y + P_{max})$ mm
30HGSNA (rod 50x25mm)	0,234
R260 (1) (segment of rail)	0,255
R260 (2) (segment of rail)	0,248
R260 (3) (segment of rail)	0,274
L480 (pipe Ø1420x22mm)	0,515
13HMF (pipe Ø420x20mm)	0,357
Steel under investigation 0H18N9 (pret Ø18)	0,474

On the basis of the coefficient of mechanical properties and energy of specimen cracking, the calibration curve was elaborated in the coordinated system: crack resistance – energy of specimen cracking. The formula of this calibration curve describing dependence of the crack resistance on P_y and P_{max} , as well as on the energy of the destroyed specimen is:

$$J_{mat} = 0,5886 \cdot \frac{W_u}{P_y + P_{max}} - 0,1288$$

The coefficient of correlation $R=0.928$.

The calibration curve used for crack resistance on the basis of measurements by small punch method for specimens with thickness 0.25 mm is shown in Fig. 8.

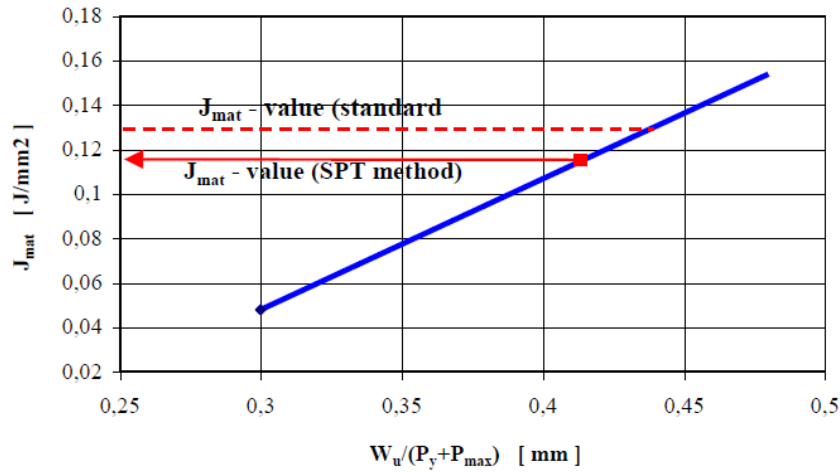


FIG. 8. Results of the crack resistance measurements by small punch method for 0H18N9 specimens with thickness 0.25mm.

The differences between the values of crack resistance determined by both methods (small punch tests and standard tensile tests) indicate that small punch tests can be used for determination of the materials properties after irradiation.

5. RESULTS OF MEASUREMENTS AFTER IRRADIATION

The results obtained in the tests performed using specimens with thickness 0.05mm do not permit the credible evaluation of the coefficients R_e and R_m . Therefore, it was decided that only specimens with thickness 0.25mm will be used in further investigations. This thickness is recognized by the investigators to be the minimum required to perform comparative tests. As a consequence, the increased thickness forced a change in the procedure of radiation damage simulation. Because the swift heavy ion energy was insufficient to penetrate a specimen of thickness 0.25mm and therefore produced only surface damage, it was decided to perform irradiation by electrons to study changes of fluence. The measured parameters for developed crack resistance on the basis of small punch tests using specimens with thickness 0.25mm are presented in Table 6.

TABLE 6. MEASURED PARAMETERS FOR CRACK RESISTANCE ON BASIS OF SMALL PUNCH TESTS AFTER ELECTRON IRRADIATION OF SPECIMENS WITH THICKNESS 0.25MM

Fluence electron/cm ²	P_y/h_0^2 kN/mm ²	P_{max}/h_0^2 kN/mm ²	$W_u/(P_y + P_{max})$ mm
0	1,705	8,147	0,474
$2,80 \cdot 10^{18}$	1,356	7,229	0,355
$5,50 \cdot 10^{18}$	1,594	7,728	0,345
$7,20 \cdot 10^{18}$	1,702	7,965	0,347
$1,12 \cdot 10^{19}$	1,498	7,048	0,332

In Table 7 and Fig. 9 the evaluated values of crack resistance of 0H18N9 steel using small punch method are presented. The measurements of crack resistance indicate that as a result of irradiation significant hardening of the material has occurred.

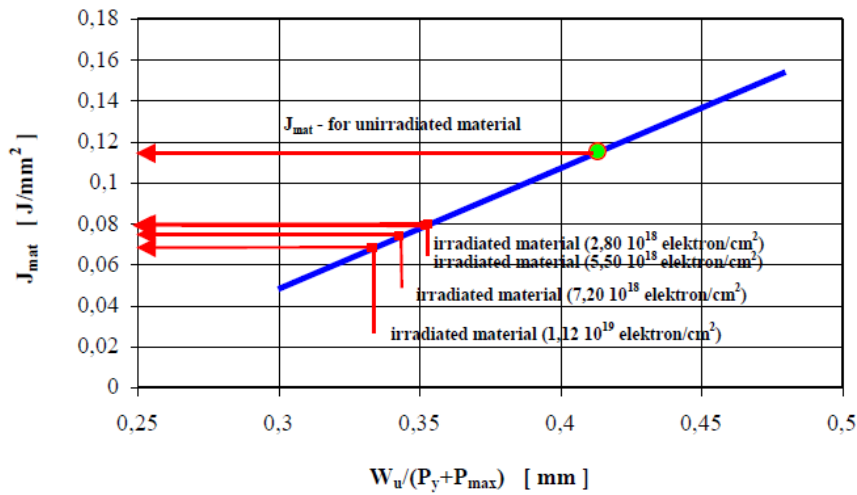


FIG. 9. Results of measurements of crack resistance using small punch method of 0H18N9 steel with thickness of 0.25mm.

6. SCANNING ELECTRON MICROSCOPE OBSERVATIONS

After small punch tests some of the specimens were observed in the scanning electron microscope. Figs10 and 11 present examples of these observations.

TABLE 7. CRACK RESISTANCE EVALUATED ON THE SMALL PUNCH TESTS AFTER ELECTRON IRRADIATION (SPECIMENS WITH THICKNESS 0.25MM)

Fluence electron/cm ²	J _{mat} J/mm ²	K _{mat} mm
0	0,150	173
2,80 10 ¹⁸	0,080	127
5,50 10 ¹⁸	0,074	122
7,20 10 ¹⁸	0,076	123
1,12 10 ¹⁹	0,066	115

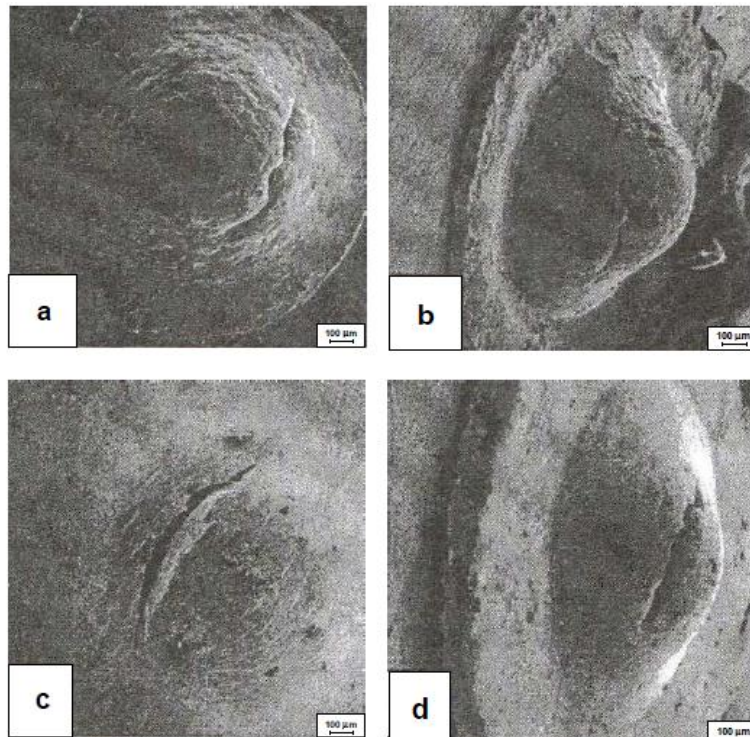


FIG. 10. Samples of 0H18N9 steel: a and b - specimens irradiated with krypton ions (energy 240MeV, fluences up to 10^{14} cm^{-2}), c and d - specimens before irradiation.

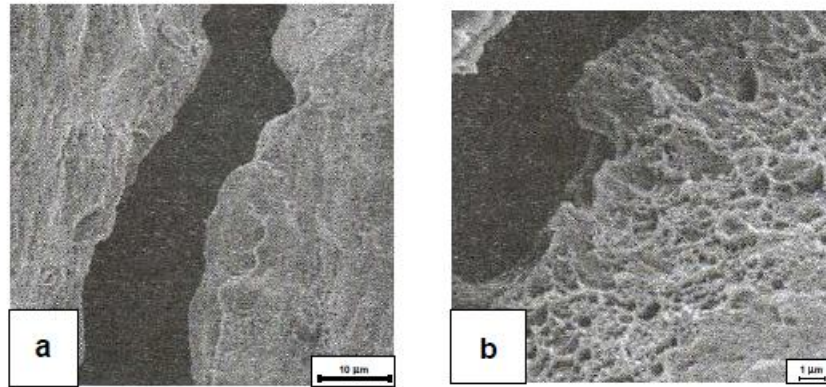


FIG. 11. The surface of samples of 0H18N9 steel: a - specimen irradiated with krypton ions (energy 240MeV, fluences up to 10^{14}cm^{-2}), b - specimen before irradiation.

7. SUMMARY

Our investigations using 0H18N9 stainless steel lead us to conclude that:

- (1) The small punch test method is useful to investigate changes of mechanical properties. The results obtained demonstrated rather good repeatability, as visualized in load – deflection diagrams. This dependence was observed for each of the investigated materials.
- (2) Information on small punch test method published in the literature advise the use of some empirical formulas descriptive of the dependencies between $R_{0.2}$ as a function P_y/h_0^2 and R_m as a function P_{\max}/h_0^2 , where h_0 is the thickness of the specimen. In the case of our steel 0H18N9, however, this empirical dependence for R_m was not verified because of the very high plasticity of this alloy, especially for very thin foils. This was the reason the value of R_m was determined on the basis of specimens with thickness 0.25mm. According to the literature, this is the thickness recommended by some investigators as a minimum in the small punch test method.
- (3) Increasing of the specimen thickness forced a change in irradiation sources, since fast heavy ions could not penetrate 0.25 mm. Specimens with thickness 0.25mm were therefore irradiated by electrons up to fluences from 2.8×10^{18} up to 1.12×10^{19} electrons/cm².
- (4) The results of our investigation after irradiation show significant differences in comparison with the results before irradiation, and therefore testify that the small punch test is a very sensitive method to assess radiation-induced changes in mechanical properties.
- (5) The scatter of results observed in the measurements of strength coefficients arise primarily from the small dimensions of the specimens compared to that taken from a larger volume of material.

Some results obtained during our investigation were presented:

1. W.Szteke, J.Wasiak, A.Hofman, T.Kochański, E.Hajewska, T.Wagner: *The investigation of radiation damages in the structural materials as the effect of accelerator irradiation*, Materials Investigation for Power Industry. XVI. Seminar, Zakopane, 22–24 June 2009, Raport IAE-139/A (in Polish)

2. Jan Wasiak, Waldemar Biłous, Witold Szteke, Ewa Hajewska, Andrzej Hofman, Tadeusz Wagner: *Investigations of the mechanical properties using small-punch method*, XVII. Seminar, Zakopane, 23–25 June 2010, Raport IAE-145/A (in Polish)
3. W.Szteke, J.Wasiak, W.Biłous, E.Hajewska, T.Wagner, A.Ju.Didyk, V.Semina: *The investigation of the stainless steel 0H10N9 before and after irradiation using small-punch method*, Materials Investigation for Power Industry. XVIII. Seminar, Zakopane, 28–30 June 2011, Raport IAE-148/A (in Polish)
4. A.Ju.Didyk, V.K.Semina, W.Szteke, A.Hofman, E.Hajewska, J.Wasiak, W.Biłous: *Investigation of stainless steel 0H18N10T irradiated with heavy ions with high energy*, XXI, International Conference on: “Radiation Physics of Solids”, Sevastopol, 22–27 August 2011 (in Russian)
5. I.V.Borovickaja, A.Ju.Didyk, V.K.Semina, W.Szteke, A.Hofman, E.Hajewska, J.Wasiak, W.Biłous: *Investigations of the mechanical characteristics of the stainless steel irradiated with the electrons with energy 2,2MeV*, XXI. International Conference on: “Radiation Physics of Solids”, Sevastopol, 22–27 August 2011 (in Russian)

REFERENCES

- [1] M. ABENDROTH, M. KUNA, “Determination of deformation and failure properties of ductile materials by means of the small punch test and neural networks,” *Computational Materials Science* **28** (2003) 633–644.
- [2] M. ABENDROTH, M. KUNA, “Identification of ductile damage and fracture parameters from the small punch test using neural networks,” *Engineering Fracture Mechanics* **73** (2006) 710–725.
- [3] J.-M. BAIK, J. KAMEDA, O. BUCK, “Small punch test evaluation of intergranular embrittlement of an alloy steel”, *Scripta Metallurgica* **17** (1983) 1443–1447.
- [4] J.S. CHEON, I.S. KIM, “Initial deformation during small punch testing,” *Journal of Testing and Evaluation* **24** (1996) 255–262.
- [5] D. FINARELLI, F. CARSUGHI, P. JUNG, “The small ball punch test at PZJ,” *Journal of Nuclear Materials* **377** (2008) 65–71.
- [6] D. FINARELLI, M. ROEDIG, F. CARSUGHI, “Small punch tests on austenitic and martensitic steels irradiated in a spallation environment with 530MeV protons,” *Journal of Nuclear Materials* **328** (2004) 146–150.
- [7] A. HOFMAN, “Raport IEA – 49/A,” Instytut Energii Atomowej (1999) pp. 1–365.
- [8] P. JUNG, A. HISHINUMA, G.E LUCAS, H. ULLMAIER, “Recommendation of miniaturized techniques for mechanical testing of fusion materials in an intense neutron source” *Journal of Nuclear Materials* **232** (1996) 186–205.
- [9] G. E. LUCAS, A. OKADA, M. KIRITANI, "Parametric analysis of the disc bend test", *Journal of Nuclear Materials* **141–143** (1986) 532–535.
- [10] LUCAS G.E., SHECKHERD J.W., ODETTE G.R., PANCHANADEESWARAN, S.; “Shear punch tests for mechanical property measurements in TEM disc-sized specimens,” *Journal of Nuclear Materials*, **122** (1984) 429–434.
- [11] LUCAS G.E.; “Review of small specimen test techniques for irradiation testing,” *Metallurgical Transactions A* **21A** (1990) 1105–1119
- [12] MANAHAN M., ARGON A., HARLING O.; “The development of a miniaturized disc bend test for the determination postirradiation mechanical properties”, *Journal of Nuclear Materials*, **103–104** (1981) 1545–1550.
- [13] MAO X., SAITO H., TAKAHASHI H.; “Small punch test to predict ductile fracture

- toughness JIC and brittle fracture toughness KIC,” *Scripta Metallurgica*, **25** (1991) 2481–2485.
- [14] MAO X., SHOJI T., TAKAHASHI H.; “Characterization of fracture behavior in small punch test by combined recrystallization-etchmethod and rigid plastic analysis,” *Journal of Testing Evaluation*, **15** (1987) 30–37.
- [15] MAO, X., TAKAHASHI, H.; “Development of a further-miniaturized specimen of mm diameter for TEM disk small punch tests,” *Journal of Nuclear Materials*, **150** (1987) 42–52.
- [16] ZHAO-XIWANG, HUI-JI SHI, JIAN LU, PAN SHI, XIAN-FENG MA; “Small punch testing for assessing the fracture properties of the reactor vessel steel with different thicknesses;” *Nuclear Engineering and Design*, **238** (2008) 3186-3193.
- [17] E. ALTSTADT, M. HOUSKA, M. ABENDROTH: Determination of deformation and failure properties of radiated ductile materials by means of small punch test and neuralnetworks.//www.fzd.de.
- [18] A.B.CEPELIEV: Primienienije mietoda uzgiba diskovych mikroobrazcov dla ocenki mechaniczieskich swojstw obłucziennych fierritnych staliej. *Fizyka i chemia obrabotki materiałov*, 2001, No 1, 31–38.
- [19] A.B. CEPELIEV, S.I.O. SADYHOV, I.W. BOROVIKKAJA: Miechaniczieskije swojstwa oblycziennoego splava V-Ga-Cr, *Fizyka i chemia obrabotki materiałov*, 2009, No 6, 12–15.

IRRADIATION OF STRUCTURAL MATERIALS BY HEAVY IONS AND THEORETICAL MODELLING OF SWELLING AND RADIATION-INDUCED SEGREGATION PHENOMENA

V. PECHENKIN*, YU. KONOBEV, V. ROMANOV, G. LYSOVA, A. CHERNOVA, A. DVORIASHIN, G. EPOV, S. OBRAZTSOV, K. CHERNOV, V. MOLODTSOV, V. RYABOV
Institute of Physics and Power Engineering
Obninsk, Russia – 248033
Email: vap@ippe.ru

Abstract

Modelling of RIS in alloy samples along the projected range of metal ions was performed accounting for the non-uniformity of the PD generation rate. It is shown that RIS induces significant changes in alloy composition not only near the sample surface, but also in a wide region near the maximum in PD generation rate. The sample regions with minimum changes in composition of austenitic and ferritic-martensitic steels are recommended for TEM investigation of microstructural evolution at high damage doses under 7 MeV Ni⁺² and 1.8 MeV Cr⁺³ ion irradiations. Molecular dynamic calculations of self-interstitial atom diffusion coefficients as well as of Fe and Cr atoms self-diffusion coefficients in Fe – (5 – 25) Cr alloys at temperatures from 600 to 1000 K were performed. The interatomic potentials used indicate the possibility of the matrix enrichment in Cr near point defect sinks via an interstitial mechanism in Fe-Cr alloys at Cr contents up to 15%.

1. INTRODUCTION

High-chromium ferritic-martensitic (F/M) steels (~9-12 at.% Cr), especially oxide dispersion strengthened alloys, are proposed as structural materials for advanced nuclear reactors. In particular, EP-823 (0.16C–10.85Cr–0.71Ni–0.7Mn–1.29Si–0.8Mo–0.69W–0.32V–0.31Nb, in wt%) F/M steel is now considered as the most attractive cladding material for new designs of nuclear power reactors and accelerator-driven systems with either lead-bismuth or lead coolants.

The main attention in our experimental investigations in the framework of SMORE CRP was devoted to this steel including irradiation with Ni ions, He ions and fast neutrons, measurements of RIS (radiation-induced segregation), hardening and microstructure [1–3]. Theoretical investigations were performed on a wide subject range including damage doses under irradiation in reactors, neural network modeling of radiation effects, models of void nucleation and growth, modeling of RIS, MD modeling of Fe-Cr alloys.

Because of space limitations in this document several works are not included in this report: measurements of radiation-induced segregation in EP-823 near the sample surface after irradiation with 30 and 70 keV He ions; characteristics of dose in metals under irradiation in the cores of power reactors; neural network modeling (interrelationship between irradiation embrittlement and irradiation hardening in low-Cr alloys like RPVs, investigation of the effect of silicon and titanium on void swelling in austenitic stainless steels); models of void nucleation and void growth in fcc and bcc metals accounting for the mobility of small vacancy clusters (MD calculation of the migration energy and diffusion characteristics of smallest vacancy clusters in Fe and Ni, a generalization of the void nucleation theory, influence of divacancy mobility on swelling of metals); modelling of helium-vacancy clusters evolution in metals under fast reactor irradiation.

This report comprises the following experimental works: irradiation of F/M steel EP-823 with 7 MeV nickel ions, measurements of irradiation hardening and RIS in EP-823 near sample surface after irradiation with 7 MeV nickel ions, investigation of the microstructure of EP-823 irradiated in the fast reactor BR-10. Theoretical investigations include modelling of radiation-induced segregation near the surface in EP-823 irradiated with 7 MeV nickel ions, modelling of radiation-induced segregation near point defect sinks in ternary substitution alloys (Fe-Cr-Ni and Fe-Cr-Si alloys), modelling of RIS in the samples of austenitic and ferritic-martensitic

steels along the projected range of metal ions (7 MeV nickel and 1.8 MeV chromium ions), MD studies of Fe and Cr diffusion by self - interstitials in Fe-Cr alloys.

2. EXPERIMENTAL INVESTIGATIONS

Ferritic/martensitic steels are known for their high resistance to swelling and relatively low irradiation creep rate, and therefore are attractive as possible fission and fusion candidate structural materials. The steel EP-450 is used most widely in Russia and CIS states, especially as the reference structural material of hexagonal wrappers and safety control tubes of the BN-600 sodium fast reactor. The compositions of the steel fall within the limits of the EP-450 specification (0.1–0.15C, <0.8Mn, <0.5Si, 0.015S, <0.025P, 11.0–13.5Cr, 0.05–0.30Ni, 1.2–1.8Mo, 0.1–0.3V, 0.3–0.6Nb, wt %). The EP-823 (0.16C–10.85Cr–0.71Ni–0.7Mn–1.29Si–0.8Mo–0.69W–0.32V–0.31Nb, in wt%) F/M steel is now considered as the most attractive cladding material for new designs of nuclear power reactors and accelerator-driven systems with either lead-bismuth or lead coolants. EP-823 was developed to have high corrosion resistance in lead-bismuth coolants by increasing the silicon content (~1.1 wt%) relative to ~0.2 wt% of EP-450.

2.1 Irradiation of ferritic-martensitic steel EP-823 with 7 MeV nickel ions and measurements of irradiation hardening

Mechanically polished and annealed specimens of EP-823 were irradiated with 7 MeV Ni⁺⁺ ions to fluencies from 5×10^{18} to 5.4×10^{19} ion/m² at 500°C in the ion accelerator EGP-15. During irradiation the base vacuum in the target chamber was not worse than 1×10^{-6} Pa. The ion flux density $j = 1.6 \times 10^{16}$ ion/m²s. Fig. 1 (left) presents the depth profiles of radiation damage and implanted ions in EP-823 steel after irradiation with 7 MeV Ni⁺⁺ ions in the ion accelerator EGP-15 calculated using TRIM-98 code with the Kinchin-Pease option. The dose rate is maximal at the depth of $\approx 1.4 \mu\text{m}$ and is equal to $\approx 3.4 \times 10^{-3}$ dpa/s.

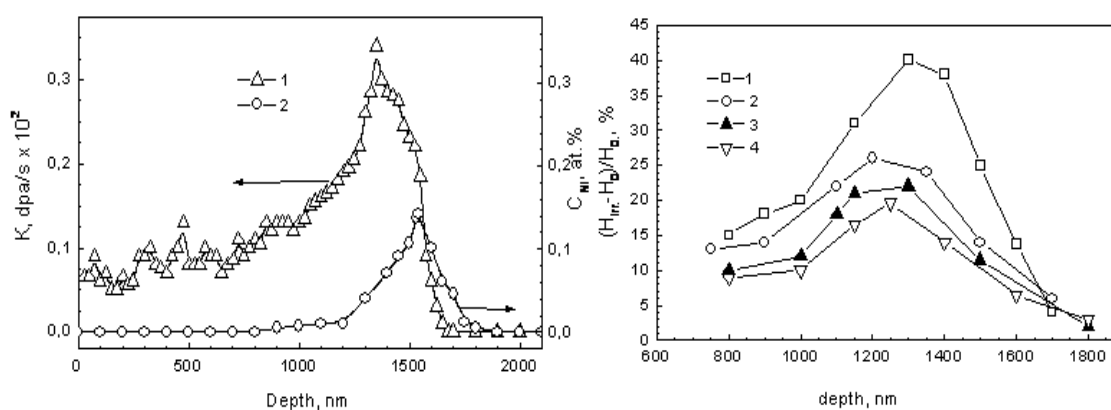


FIG. 1. Depth profiles of damage rate and implanted ions in EP-823 steel after irradiation with 7 MeV Ni⁺⁺ ions in the ion accelerator EGP-15: 1 – dose rate K ; 2 – C_{Ni} (Dose = 10 dpa) (left). Indent-depth dependence of relative changes in Vickers microhardness under similar irradiation conditions at different temperatures 1 – 380, 2 – 450, 3 – 550, 4 – 600 °C (right).

Usually there is a correlation between Vickers microhardness H values and yield strengths σ_y in both ferritic and austenitic steels ($\Delta\sigma_y = 3,06\Delta H$ in ferritic steels [1]). So the measurements of microhardness allow studying of the radiation-induced hardening in materials after ion irradiation. Fig. 1 (right) presents the relative changes in Vickers

microhardness near the sample surface of EP-823 steel after irradiation with 7 MeV Ni^{++} ions at different temperatures. The maximal fluence of Ni^{++} ions at the profile's peak corresponds to the damage dose of ≈ 114 dpa.

An increase in microhardness is observed in entire temperature range. Relative changes in Vickers microhardness profiles correlate with those of the radiation damage. The highest hardening was achieved at 380°C. The radiation hardening decreases with the increase in irradiation temperature.

2.2 Measurements of radiation-induced segregation in EP-823 near sample surface after irradiation with 7 MeV nickel ions

The depth distribution of elements near the surface of the samples was determined on an XSAM-800 facility using X-ray photoelectron spectroscopy (XPS) in combination with 3 keV Ar^+ ion surface sputtering. The estimated surface sputtering coefficient of the steel in this case using the TRIM-98 code is equal ≈ 3 at./ion, yielding a surface sputtering rate $\approx 0,03$ nm/s.

Fig. 2 presents experimental and calculated relative depth profiles of chromium and silicon concentrations measured in EP-823 steel after Ni^{++} irradiation to 0.2 dpa.

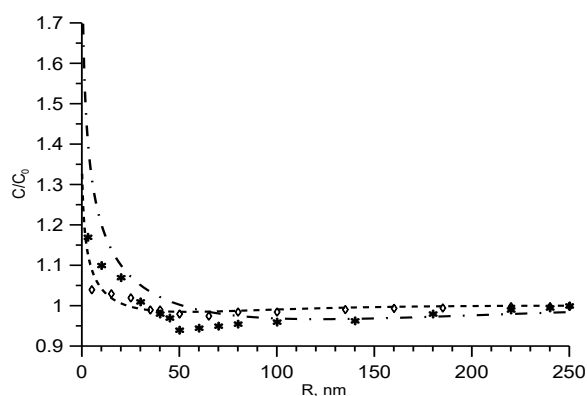


FIG. 2. Experimental (figures) and calculated (curves) profiles of relative silicon and chromium concentrations near the surface of EP-823 after irradiation with Ni^{++} ions (o, - - - - - Cr; *, — - — Si); see text for the input parameters in calculations.

It is seen that an enrichment of both chromium and silicon near the sample surface is revealed in EP-823 steel after irradiation with 7 MeV Ni^{++} ions.

2.3 Investigation of the microstructure of EP-823 irradiated in BR-10

Plate samples of EP-823 were normalized at 1050°C for 20 min with subsequent tempering at 760 °C for 1.5 h. They were irradiated at temperatures of 350 and 400°C in the BR-10 fast reactor to doses of 25 and 27 dpa. The microstructure was observed with a JEM-100CX electron microscope operating at 100 kV. The initial structure of EP-823 was a mixture of polyhedral grains of ferrite ($\sim 10\%$) and tempered martensite ($\sim 90\%$) with grain sizes of 5–10 microns.

The martensite grains consisted of sub-grains having the shape of equally-oriented thin plates 0.5–1.0 μm in width. Equiaxed MC particles of 0.3–0.5 μm diameter at $\sim 5 \times 10^{11} \text{ cm}^{-3}$ were observed inside the grains. The grain boundaries of ferrite and martensite, as well as sub-boundaries in the martensite, were partially filled with blocky M_{23}C_6 carbides. The dislocation density was $\sim (1-2) \times 10^{10} \text{ cm}^{-2}$ in ferrite grains and $\sim 1 \times 10^{11} \text{ cm}^{-2}$ in martensite sub-grains.

Irradiation at 350°C to 25 dpa results in formation of dislocation loops, most with Burgers vector $\langle 100 \rangle$. In ferrite grains both the mean loop diameter (13 nm) and loop concentration ($1.2 \times 10^{16} \text{ cm}^{-3}$) are slightly larger than in grains of tempered martensite (11 nm and $1 \times 10^{16} \text{ cm}^{-3}$). Also, a high concentration ($\sim 3 \times 10^{16} \text{ cm}^{-3}$) of uniformly distributed fine precipitates (6 nm) is observed in both the ferrite and tempered martensite grains. Analyses of diffraction patterns have revealed the fcc structure of these precipitates with lattice parameter 1.14 nm, equal to 4-fold that of the ferrite matrix. Comparison with literature data [2–5] leads to the conclusion that these precipitates are G-phase.

Irradiation of EP-823 in BR-10 at 400°C to 27 dpa resulted in some decrease in dislocation density to a level of $\sim (0.5-1) \times 10^{10} \text{ cm}^{-2}$ in ferrite grains only. No formation of dislocation loops was revealed. The distribution of G-phase precipitates was not uniform but exhibited preferential decoration on dislocations.

When EP-823 is compared to the alloy EP-450 often used in Russia it is observed that the primary microstructural difference is the formation of G-phase in EP-823 instead of α' precipitates observed in EP-450 [6] and other steels of this type [7–9] during neutron irradiation at relatively low temperatures. The reason for this difference is thought to arise from the higher content of Ni and Si in EP-823 [4, 10].

3. THEORETICAL MODELLING

3.1 Modelling of RIS near the surface in EP-823 irradiated with 7 MeV nickel ions

As one can see in Fig. 1, the displacement generation rate profile along the projected range of 7 MeV nickel ions is nearly constant up to the depth of ≈ 500 nm. The damage rate near the surface was therefore taken as uniform and equal to 0.65×10^{-3} dpa/s (see Fig. 1). So our models of non-steady-state RIS in ternary alloys under uniform PD generation [11, 12] are applicable in the near-surface region of the irradiated sample. Modelling of RIS in Fe–12Cr–1Si alloy (the base of EP-823 steel) near the surface of irradiated sample was performed as applied to match experimental RIS data in EP-823 steel under irradiation with 7 MeV Ni^{++} ions.

The main difficulty here is the lack of reliable data on point defect (PD) and component diffusivities in Fe–Cr and Fe–Cr–Si alloys. A typical example is the origin of the controversy about the vacancy migration energy in Fe [13]. Schaefer et al. [14], on the one hand, measured a value of 1.28 eV, while Vehanen et al. [15] and Takaki et al. [16], on the other hand, obtained a vacancy migration energy of 0.55 eV. This data scattering very likely results from the difficulty of obtaining very pure Fe crystals. Impurity atoms, even in very small amounts, trap the vacancies and thus decrease the vacancy diffusion coefficient. Carbon and nitrogen atoms are the most frequent foreign interstitial atoms in the Fe matrix along with hydrogen atoms. Above their solubility limit, these elements are responsible for the formation of carbides or nitrides, which are very useful in improving the strength and hardness of steels.

Below their solubility limit, the presence of even a very little amount of these impurities in interstitial positions (a few tens ppm) can have a drastic influence on the vacancy diffusion coefficient [13]. So, averaged vacancy migration energy of 0.9 eV was used in our calculations. Molecular dynamics (MD) simulations result in the SIA migration energy of 0.2 eV both in Fe [17] at temperatures $\geq 500^\circ\text{C}$ and in Fe–15Cr alloys over a wide temperature range [18]. This value was used in calculations.

Alloy component redistribution near PD sinks due to RIS (enrichment or depletion of the element and its extent) is governed by the ratios of component diffusivities via vacancy and also via interstitial mechanisms (see e.g. [19]). For undersized alloying atoms, like Si in both Fe–Cr and Fe–Cr–Ni alloys, a binding energy in mixed dumbbells is important [11].

Considering the data on self-diffusion in binary Fe alloys [20] we have used the following relations of diffusivities of Cr and Si to that of Fe via vacancy mechanism: 1.28 and 10, respectively. Applying the model [11, 12] to Fe–Cr–Si alloys we have two fitting parameters: the binding energy of undersized Si atoms in mixed dumbbells E_b , and the migration energy of Cr atoms via interstitial mechanism E_i^{Cr} ($E_i^{Fe} = 0.2$ eV). Results of modelling with $E_b = 0.175$ eV and $E_i^{Cr} = 0.17$ eV are shown in Fig. 2. Note that earlier modelling [11] of Si RIS in Fe–Cr–Ni alloys resulted in $E_b = 0.15$ eV. There is in qualitative agreement with experimental data at depths beyond ≈ 10 nm. For a more correct fitting, reliable data on PD and component diffusivities in Fe–Cr and Fe–Cr–Si alloys are needed, as well as experimental profiles of relative silicon and chromium concentrations near the surface of EP-823 after ion irradiation at various temperatures.

3.2 Modelling of radiation-induced segregation near point defect sinks in ternary substitution alloys

Earlier in [11, 12, 21] a model of RIS near motionless and moving plane point defect sinks in ternary substitution alloys was developed and applied to grain boundaries (GB) in Fe–Cr–Ni alloys. In the present work the model is generalized for cylindrical (dislocations) and spherical (precipitates and voids) point defect sinks. Calculations of component concentration profiles induced by RIS near these sinks are performed for Fe–Cr–Ni and Fe–Cr–Si alloys in dependence of point defect generation rate, temperature and damage dose.

As a first approximation, the influence of an elastic interaction between an alloy component and a dislocation on the segregation is neglected. The dislocation is considered as an absorbing cylinder of radius R_d (the dislocation core radius), and the precipitate or void as a sphere of radius R_p . For convenience, the regular spatial distribution of the sinks is considered. Then each sink absorbs point defects from a Wigner – Seitz cell, the radius of which (the width of a calculation cell) is determined by the density of the sinks as follows: $R_{WS} = (1/(\pi\rho_d))^{1/2}$, $R_{WS} = (3/(4\pi N_p))^{1/3}$, where ρ_d and N_p are the dislocation density and the concentration of spherical sinks, respectively.

A system of diffusion equations for concentrations of vacancies and interstitials C_n ($n = v, i$) and components C_m (A, B, C) in a ternary substitution alloy under irradiation accounting for a binding energy of mixed dumbbells with A atom was developed in [11,12,21]. This system of equations in one-dimensional Cartesian, cylindrical or spherical geometry with appropriate boundary conditions was approximated using the integral-interpolation method and the implicit scheme and was solved numerically.

3.2.1 Fe–Cr–Ni alloys

Calculations were performed in Fe–Cr–Ni alloys with the parameters adopted in [11, 21]. Fig. 3 presents the results of RIS numerical calculations and the data by Sethi and Okamoto [23] on component segregation near the sample surface of Fe-20Cr-12Ni alloy irradiated with 3 MeV Ni ions to 6 dpa at 600°C. One can see that a satisfactory agreement is achieved using the parameters fitted earlier in [12] to the data on RIS near both motionless and moving GB in Fe–Cr–Ni alloys under electron irradiation.

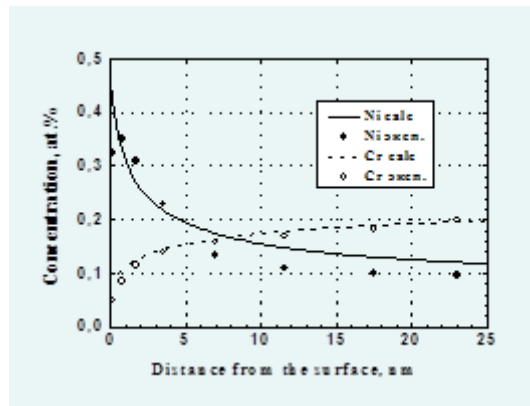


FIG. 3. Results of RIS numerical calculations along with experimental data by Sethi and Okamoto [22] on component segregation near a sample surface of Fe-20Cr-12Ni alloy irradiated with 3 MeV Ni ions to 6 dpa.

Calculations of RIS near the sinks with various geometries were performed for the Fe-20Cr-12Ni alloy in dependence of point defect generation rate, temperature and damage dose. As an example, Figs 4 and 5 present the temperature dependence of calculated Ni concentrations near the surfaces of voids with radius of 50 and 5 nm in this alloy at 6 dpa and different dose rates: 10^{-3} dpa/s (typical for irradiation with MeV energy ions in accelerators and with electrons in HVEM), 10^{-6} dpa/s (typical for neutron irradiation in the core of fast reactors), 10^{-9} dpa/s (typical for neutron irradiation of austenitic internals in thermal reactors of PWR and VVER type).

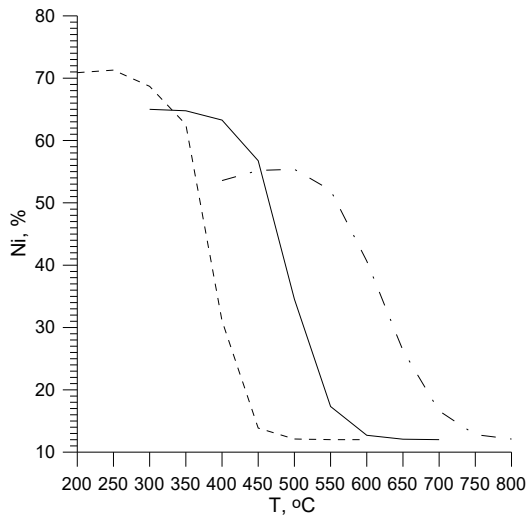


FIG. 4. The temperature dependence of calculated Ni concentrations near the surface of a void with 50 nm radius.

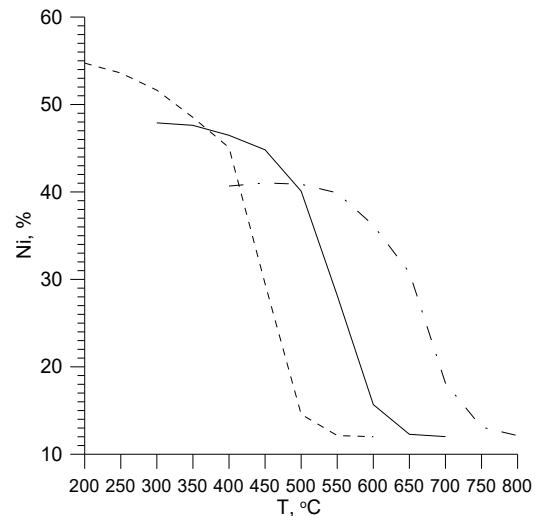


FIG. 5. The temperature dependence of calculated Ni concentrations near the surface of void with 5 nm radius.

- - - - $K = 10^{-3}$ dpa/s
 ——— $K = 10^{-6}$ dpa/s
 - · - · $K = 10^{-9}$ dpa/s

- - - - $K = 10^{-3}$ dpa/s
 ——— $K = 10^{-6}$ dpa/s
 - · - · $K = 10^{-9}$ dpa/s

From the calculations it follows that RIS near a void surface is increased with increasing void radius (see Figs 4 and 5) and tends to approach that near a flat sink (sample surfaces or grain boundaries). Note that the temperature dependences in the figures above are similar and

shifted by approximately 100°C with increasing dose rate by three orders of value (dose rate effect).

The models developed in this effort allow us to predict RIS in alloys near various microstructural features under neutron irradiation using RIS modelling to match RIS near the sample surface under ion irradiation.

3.2.2 Fe-Cr-Si alloys

Modelling of RIS in EP-823 steel near spherical precipitates was performed as applied to irradiation-induced α' or G-phase precipitates observed in ferritic-martensitic steels under neutron irradiation [3, 23]. Two populations of precipitates were considered: the first one is with concentration of 10^{16}cm^{-3} and average radius of 5 nm and the second is with concentration of 10^{15}cm^{-3} and average radius of 20 nm. The system of diffusion equations was solved in one-dimensional spherical geometry (Wigner – Seitz cell) with the outer boundary radius determined by the concentration of precipitates. Irradiation conditions and input parameters are the same as used in Fig. 2. Results of modelling for precipitates with radius of 5 nm are shown in Fig. 6 and results for the radius of 20 nm in Fig. 7.

Enrichment of silicon and chromium is stronger near the surface of larger precipitates. Component profiles are more monotonic near the spherical precipitates than near the plane surface because of the difference in geometry of computational cells. So the enrichment of silicon and chromium near PD sinks in ferritic-martensitic steels creates a prerequisite for a formation and growth of radiation-induced Si and Cr enriched precipitates [3].

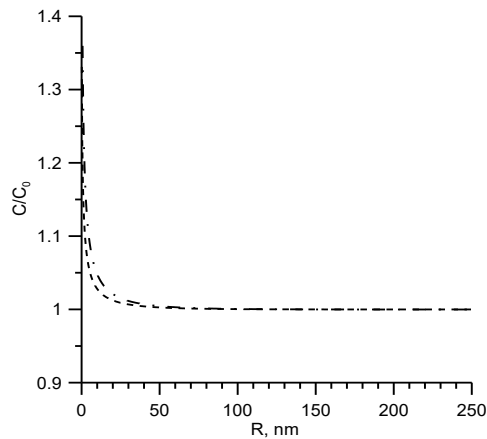


FIG. 6. Calculated profiles of relative silicon and chromium concentrations near a spherical precipitate with average radius of 5 nm in EP-823 after irradiation with Ni^{++} ions (-----Cr; — — — Si); see text for the input parameters in calculations.

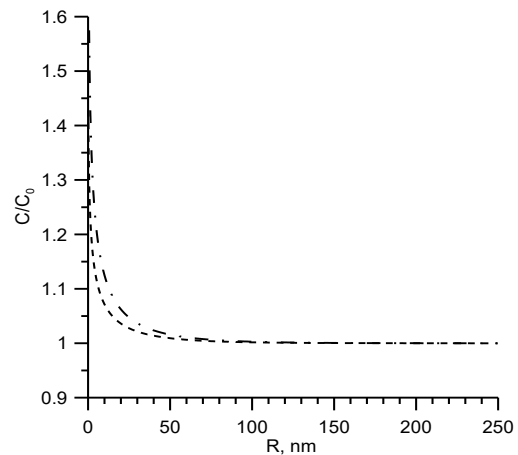


FIG. 7. The same as in FIG. 6 for average radius of 20 nm.

3.3 Modelling of radiation-induced segregation in samples of austenitic and ferritic-martensitic steels along the projected range of metal ions

Radiation-induced segregation during uniform (e. g. neutron) irradiation leads to significant changes in alloy composition near point defect sinks. An additional RIS effect should be revealed in the matrix, apart of sinks in regions of high non-uniformity of PD generation rate such as regions of maximum PD generation rate under ion irradiation (see Fig. 1). For

modelling of this kind of RIS we have advanced our model of non-steady-state radiation-induced segregation under uniform PD generation developed earlier (see above), accounting for the profile of PD generation rate along the projected range under ion irradiation.

Two types of ion irradiations were considered: 7 MeV Ni^{+2} ions typical for the EGP-15 accelerator at IPPE and 1.8 MeV Cr^{+3} ions typical for the ESUVI accelerator at KIPT. Modelling of RIS was performed for Fe–19Ni–16Cr alloy (the base of austenitic stainless steel EK164) at 650°C as well as for Fe-12Cr-2Si alloy representing the base of EP-823 ferritic-martensitic steel at 500°C.

3.3.1 7 MeV nickel ions

Since PD generation rate profiles calculated using the TRIM-98 code are similar for Fe–Ni–Cr and Fe–Cr alloys, the approximation of the profile in Fig. 1 was used. Component concentration redistribution due to RIS in Fe–19Ni–16Cr alloy at various irradiation times are presented below in Fig. 8.

PD generation rates estimated with the TRIM code do not account for some specific features of cascade-producing irradiation such as possible low cascade efficiency in producing PDs and intracascade correlative recombination [24]. These factors can result in reduction of PD generation rates up to one order of magnitude. So we have performed the calculations with PD generation rates divided by ten. The results indicate that these reduction factors delay the profile evolution.

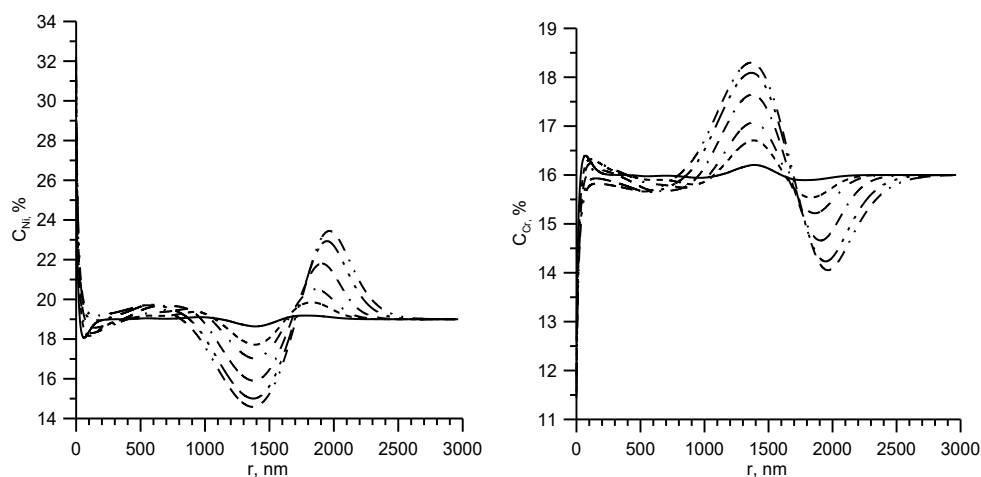


FIG. 8. Component profiles along the projected range in Fe–19Ni–16Cr alloy under irradiation with Ni^{++} ions at different times: — 1000 s, - - - 5000 s, - · - · 10 000 s, - - - 25 000 s, - - - 50 000 s, - · - · 70 000 s.

One can see that RIS induces significant changes in alloy composition not only near the sample surface, but also in a wide region near the maximum in PD generation rate under ion irradiation. It should be noted that only the sample surface acting as a PD sink and mutual vacancy and interstitial recombination are responsible for annihilation of generated PD in these calculations. Growing PD sinks can compete with PD recombination and delay the evolution of alloy composition at high damage doses. For more reliable estimates data on PD sink strength evolution along the projected range of ions during irradiation are needed.

Similar modelling was performed for EP-823 ferritic-martensitic steel. The results are presented in Fig. 9.

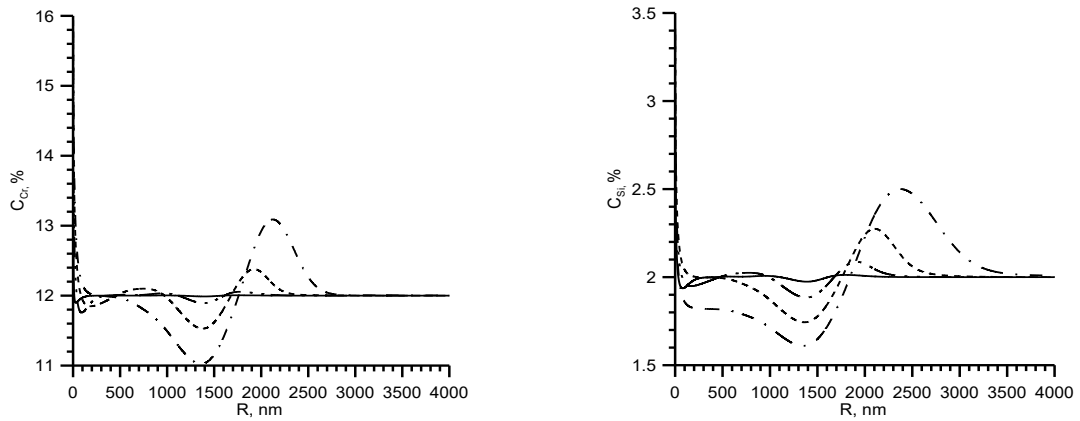


FIG. 9. Component profiles along the projected range in EP-823 ferritic-martensitic steel under irradiation with Ni^{++} ions at different times: ———— 10^2 s, - - - - 10^3 s, - · - · 10^4 s, · · · · 10^5 s.

Note that RIS in ferritic-martensitic steel is less pronounced than in the austenitic alloy.

3.3.2 MeV chromium ions

The approximation of PD generation rate profile calculated with TRIM-98 for 1.8 MeV chromium ions was used in calculations done in the framework of the SMore CRP. Component concentration redistribution profiles due to RIS in Fe-19Ni-16Cr and Fe-12Cr-2Si alloys at various irradiation times are presented below in Fig. 10 and Fig. 11. In both cases of Ni and Cr ions RIS in ferritic-martensitic steel is less pronounced than in austenitic steel.

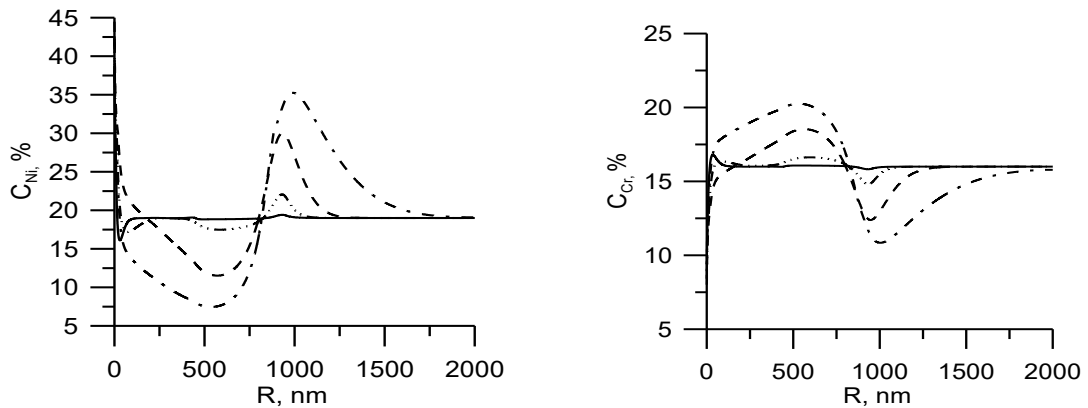


FIG. 10. Component profiles along the projected range in Fe-19Ni-16Cr alloy under irradiation with Cr^{+3} ions at different moments: ———— 10^2 s, - - - - 10^3 s, - · - · 10^4 s, · · · · 10^5 s.

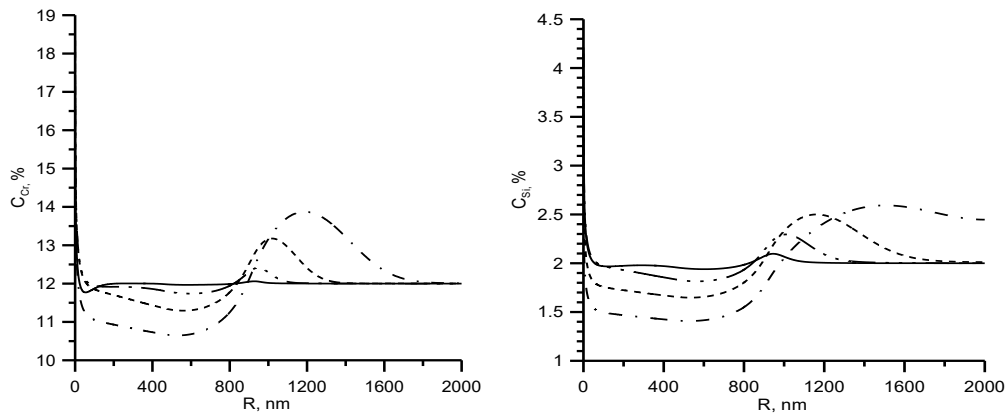


FIG. 11. Component profiles along the projected range in EP-823 ferritic-martensitic steel under irradiation with Cr^{+3} ions at different times ———— 10^2 s, - - - - 10^3 s
- . - . - 10^4 s, 10^5 s.

From the figures above, one can see that minimal changes in the alloy composition due to RIS are revealed in the region of the depths from 200 to 700 nm for 7 MeV Ni^{+2} ions and from 100 to 200 nm for 1.8 MeV Cr^{+3} ions for both austenitic and ferritic-martensitic steels. These regions can be recommended for TEM investigations of microstructure evolution at high damage doses.

3.4 MD studies of Fe and Cr diffusion by self - interstitials in Fe-Cr alloys

Molecular dynamics calculations of self - interstitial atom (SIA) and component diffusivities in Fe-Cr alloys were performed using the code DYMOKA [25]. Interatomic potentials were taken from [18]. MD simulations were carried out in a box of $N \approx 2000$ atoms with randomly distributed Cr atoms. Alloys with different Cr contents were considered: Fe-5, 10, 15, 20, 25%Cr in the interval of temperatures from 600–1000 K.

The diffusivity of any species (defects or atoms of alloy components) can be computed using Einstein's random-walk law [26, 27]. The calculated temperature dependence of SIA diffusion coefficients, as well as of Fe and Cr atoms self-diffusion coefficients via interstitial mechanism in Fe-Cr alloys, is presented in Fig. 12. For SIAs the trajectory time decomposition technique [17] was used with different isochronal segments. Fig. 13 presents ratios of Cr to Fe self-diffusion coefficients versus Cr content in dependence on temperature.

Fig. 13 indicates, with interatomic potentials used, the possibility of the matrix enrichment in Cr near point defect sinks via the interstitial mechanism in Fe-Cr alloys at Cr contents below ~15%, where the ratio $D_{\text{Cr}}/D_{\text{Fe}} > 1$. Experimental data [20] and MD calculations (see e.g. [18] and references therein) point to higher diffusivity of Cr atoms via vacancy mechanism in Fe-Cr alloys. This means that Cr should deplete the matrix near sinks via vacancy mechanism.

As a result of both mechanisms the behaviour of Cr in the matrix near sinks should depend on the relation of vacancy and SIA fluxes to the sink, as well as on the content of alloying and impurity elements effecting PD diffusion. Real behaviour of Cr near grain boundaries (GB) in ferritic-martensitic steels under irradiation is rather complex, revealing both enrichment and depletion (see e.g. [28] and references therein). From Fig. 13 it follows that the ability of Cr to enrich the matrix near GB via the interstitial mechanism is stronger for low Cr content and low temperatures. This fully agrees with the conclusions in [28].

4. CONCLUSIONS

Accelerators are widely used to simulate high dose microstructural damage in metals and alloys resulting from fission or fusion neutrons. As shown in this report it is useful to also conduct in parallel studies of radiation-induced segregation near the sample surface in these materials. Physical models and numerical methods were developed for modelling of RIS in ternary substitutional alloys near point defect sinks of various geometry such as grain boundaries and sample surfaces, dislocations, precipitates and voids. The data on RIS in alloys near the sample surface obtained under heavy ion irradiation can be used in modelling of RIS in these alloys near other PD sinks under both ion and neutron irradiations.

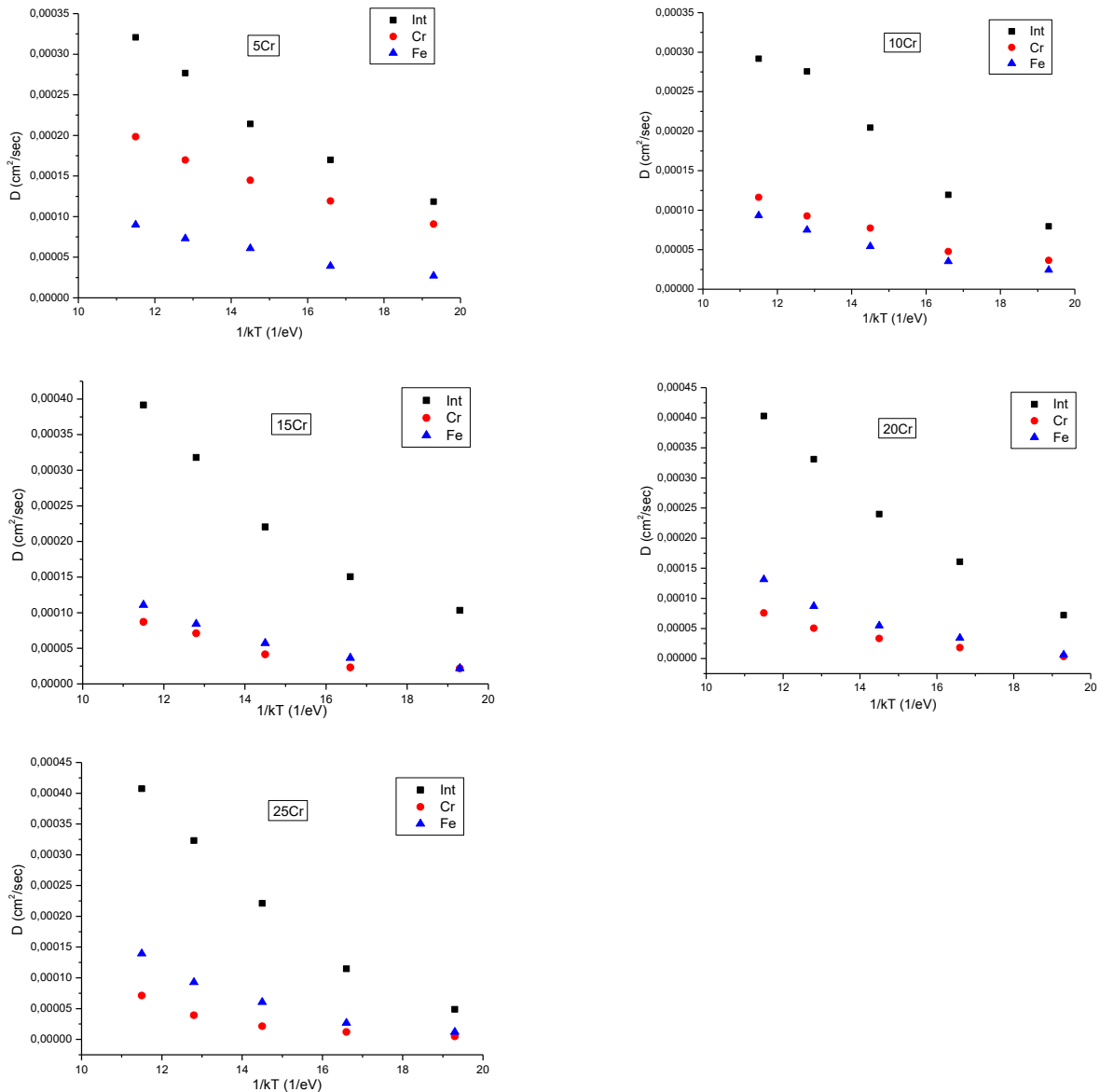


FIG. 12. Temperature dependence of SIA diffusion coefficients as well as of Fe and Cr atom self-diffusion coefficients in Fe-Cr alloys.

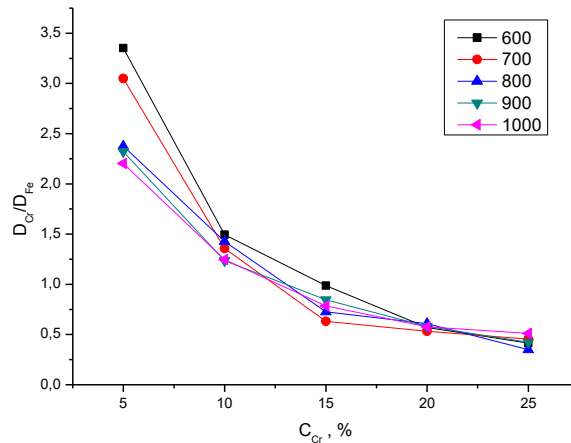


FIG. 13. Ratio of Cr to Fe self-diffusion coefficients versus Cr content at different temperatures.

Modelling of RIS in alloy samples along the projected range of metal ions was performed accounting for the non-uniformity of the PD generation rate. It is shown that RIS induces significant changes in alloy composition not only near the sample surface, but also in a wide region near the maximum in PD generation rate. The sample regions with minimum changes in composition of austenitic and ferritic-martensitic steels are recommended for TEM investigation of microstructural evolution at high damage doses under 7 MeV Ni⁺² and 1.8 MeV Cr⁺³ ion irradiations.

Molecular dynamic calculations of self-interstitial atom diffusion coefficients as well as of Fe and Cr atoms self-diffusion coefficients in Fe-(5–25) Cr alloys at temperatures from 600–1000 K were performed. The interatomic potentials used indicate the possibility of the matrix enrichment in Cr near point defect sinks via an interstitial mechanism in Fe-Cr alloys at Cr contents up to 15%.

REFERENCES

- [1] BUSBY J.T., HASH M.C., WAS G. S., J. Nucl. Mater. **336** (2005) 267.
- [2] WILLIAMS, T.M., TICMARSH, J.M., "The occurrence of a silicon rich phase of the M₆C type in neutron-irradiated FV-548 steel", J. Nucl. Mater. **87** (1979) 398–400.
- [3] LITTLE, E.A., and STOTER, L.P., "Microstructural stability of 10–12% Cr ferritic-martensitic steels irradiated in a fast reactor", (Proc. Effect of Irradiation on Materials, 11th Conference, 1982), ASTM STP782, H.R. Brager and J.S. Perrin Eds. (American Society for Testing and Materials, Philadelphia) (1982) 207–219.
- [4] MAZIASZ, P.J., "Formation and stability of radiation induced phases in neutron-irradiated austenitic and perlite steels", J. Nucl. Mater. **169** (1989) 95–115.
- [5] MORGAN, T.S., LITTLE, E.A. and FAULKNER, R.G., "Microstructural studies in fast reactor irradiated FV448 ferritic-martensitic alloy plate and weldment", (Proc. Effect of Radiation on Materials: 16th International Symposium, 1993), ASTM STP 1175 A.S. Kumar, D.S. Gelles, R.K. Nanstad and E.A. Little, Eds., ASTM, Philadelphia (1993) 607–621.
- [6] DVORIASHIN, A.M., POROLLO, S.I., KONOBEEV, YU. V. and GARNER, F.A., "Influence of high dose neutron irradiation on microstructure of EP-450 ferritic-martensitic steel irradiated in three Russian fast reactors", J. Nucl. Mater. **329–333** (2004) 319–323.
- [7] GELLES, D. S., J. Nucl. Mater., **103–104** (1981) 975–980.
- [8] GELLES, D. S., J. Nucl. Mater., **148** (1987) 136–144.

- [9] GELLES, D. S., and THOMAS, L. E., "Effects of neutron irradiation on microstructure in experimental and commercial ferritic alloys", (Proc. of Topical Conference on Ferritic Alloys for Use in Nuclear Technologies), J. W. Davis and D. J. Michel, Eds., Metal Society of AIME New York (1984) 559–568.
- [10] MAZIASZ, P.J., KLUEH, R.L., and VITEK, J.V., "Helium effects on void formation in 9Cr–1MoVNb and 12Cr–1MoVW steels irradiated in HFIR", *J. Nucl. Mater.* **141–143** (1986) 929–937.
- [11] PECHENKIN, V.A., STEPANOV, I.A., "Modeling the radiation-induced segregation of undersized solutes near grain boundaries", *Mater. Science Forum*, **294–296** (1999) 771–774.
- [12] STEPANOV, I.A., PECHENKIN, V.A., KONOBEV, Yu.V., "Modeling of radiation-induced segregation at grain boundaries in Fe-Cr-Ni alloys", *J. Nucl. Mater.*, **329–333** (2004) 1214–1218.
- [13] DOMAIN, C., BECQUART, C. S., and FOCT, J. "*Ab initio* study of foreign interstitial atom (C, N) interactions with intrinsic point defects in Fe", *Phys. Rev. B* **69** (2004) 144112.
- [14] SCHAEFER, H.E., MAIER, K., WELLER, M., HERLACH, D., SEEGER, A., and DIEHL, J., *Scr. Metall.* **11** (1977) 803.
- [15] VEHANEN, A., HAUTOJARVI, P., JOHANSSON, J., YLI-KAUPPILA, J., and MOSER, P., *Phys. Rev. B* **25** (1982) 762.
- [16] TAKAKI, S., FUSS, J., KUGLER, H., DEDEK, U. and SCHULTZ, H., "The resistivity recovery of high purity and carbon doped iron following low temperature electron irradiation", *Radiation Effects*, **79** (1983) 87–122.
- [17] ANENTO, N., SERRA, A., OSETSKY, Yu. N., "Atomistic study of multimechanism diffusion by self-interstitial defects in α -Fe", *Modelling Simul. Mater. Sci. Eng.* **18** (2010) 1–18.
- [18] TERYTYEV, D., OLSSON, P., KLAVER, T. V. S., MALERBA, L., "On the migration and trapping of single self-interstitial atoms in dilute and concentrated Fe-Cr alloys: Atomistic study and comparison with resistivity recovery experiments", *Computational Materials Science*, **43** (2008) 1183–1192.
- [19] PECHENKIN, V.A., and EPOV, G.A., "Analytical expressions for steady-state component profiles of irradiated substitution alloys near point defect sinks", *J. Nucl. Mater.* **186** 3 (1992) 269–276.
- [20] MURCH, G. E., BRUFF, C. M., "[Chemical Diffusion in Inhomogeneous Binary Alloys](#)", Landolt-Bornstein, New Series, Group III, vol. 26, Springer-Verlag, Berlin (1990).
- [21] STEPANOV, I.A., PECHENKIN, V.A., "Calculation of radiation-induced segregation near moving grain boundaries in Fe-Cr-Ni alloys", *Mater. Science Forum*, **294–296** (1999) 775–778.
- [22] SETHI, V.K. and OKAMOTO, P.R., "Radiation-induced segregation in complex alloys", (Proc. Conf. on Phase Stability during Irradiation, Metallurgical Society AIME), 1981, p. 109.
- [23] SENCER, B.H., KENNEDY, J.R., COLE, J.I., MALOY, S.A., GARNER, F.A., "Microstructural stability of an HT-9 fuel assembly duct irradiated in FFTF", *J. Nucl. Mater.* **414** (2011) 237–242.
- [24] ZINKLE, S.J., SINGH, B.N., *J. Nucl. Mater.*, **199** (1993) 173.
- [25] BECQUART, C.S., DECKER, K.M., DOMAIN, C., RUSTE, J., SOUFFEZ, Y., TURBATTE, J.C., VAN DUYSSEN, J.C., *Radiat. Eff. Defect Solids* **142** (1997) 9.
- [26] MANNING, J. R., *Diffusion Kinetics for Atoms in Crystals*, Van Nostrand, London, (1968) 88.

- [27] OSETSKY, Yu. N., and SERRA, A., Defect Diffus. Forum, **188–190** (2001) 71–92.
- [28] WAS, G.S., WHARRY, J.P., FRISBIE, B. et al., J. Nucl. Mater. **411** (2011) 41–50.

INVESTIGATION OF PHYSICAL MECHANISMS OF RADIATION-INDUCED PROCESSES IN STRUCTURAL MATERIALS FOR FISSION AND FUSION REACTORS USING ACCELERATORS OF CHARGED PARTICLES AND THEORETICAL MODELING

*A.I. RYAZANOV, *O.K. CHUGUNOV, *V.S. KOIDAN, *B.I. KHRIPUNOV, *S.T. LATUSHKIN, **R. LINDAU, **A. MÖSLANG, *M.A. PETUKHOV, *K.E. PRIKHODKO, *E.V. SEMENOV, *M.V. SOROKIN, *V.N. UNEZHEV, **P. VLADIMIROV *

* National Research Centre “Kurchatov Institute”. 123182, Moscow, Kurchatov Sq.1, Russia

**Karlsruhe Institute of Technology, Institute for Applied Materials, 76021 Karlsruhe, Germany

E-mail: ryazanoff@comail.ru

Abstract

This report overviews the work performed at NRC “Kurchatov Institute” as a contribution to the SMORE CRP of the IAEA during a three year project. The main aim of the project is the joint theoretical and experimental investigations of some physical mechanisms of radiation-induced processes in graphite materials, W and ODS materials for fission and fusion reactors using fast charge particle irradiation in the cyclotron of NRC KI. Similar to fast neutron irradiation in atomic reactors, fast particle irradiation of materials in accelerators results in considerable changes of their physical and mechanical properties. Fast particles can be used for fast tests of new radiation resistance materials in the cyclotron at NRC KI. This report consists of three parts: 1) Investigation of the changes in physical-mechanical properties of tungsten and carbon materials after fast particle irradiation on cyclotron at NRC KI, including irradiation by helium and carbon ions and investigation of the effect of high levels of radiation damage produced in these materials following interaction of them with deuterium plasma; 2) Determination of the effects of irradiation and high concentrations of helium atoms (up to 1000 appm) on microstructure and mechanical property changes of ODS materials after uniform helium implantation in the NRC KI cyclotron in the energy interval up to 30 MeV; 3) Theoretical investigation of stability and growth of precipitates in irradiated materials (Y-Ti-O particles) under neutron or charged particle irradiation at high irradiation doses, taking into account the generation rates of atomic collision cascades; development of di-atomic models for investigations of helium atom effects on helium bubbles and interstitial dislocation loop formation at low temperatures and high helium generation under irradiation and development also the theoretical models of helium bubble growth in irradiated materials, taking into account the growth kinetics of helium bubbles in the volume and on Y-Ti-O precipitates in ODS materials under high doses of neutron or charged particle irradiation.

1. INTRODUCTION

This report presents a review of the main experimental and theoretical results obtained during the work performed at NRC KI as a contribution to the SMORE CRP of the IAEA. This activity includes the experimental investigations of radiation-induced processes in structural materials (graphite, tungsten and ODS materials) for fission and fusion reactors after irradiation of them by fast charged particles in the NRC KI cyclotron, and theoretical modeling of the effects of irradiation on materials.

The experimental work in this report consists of two parts: investigations of plasma interaction with radiation damaged (irradiated) and non-irradiated plasma-facing materials (tungsten and graphite materials) for fusion reactors. These main results presented in the topic 2.1.

Plasma-facing materials (PFMs) of a fusion reactor will be exposed to high heat flux, fast particle emission from the plasma and 14 MeV-neutron irradiation. All of these factors determine the lifetime of the reactor first wall and diverter, which is mainly limited by erosion of PFMs. The radiation damage in PFMs produced by fast neutrons may play an important role as an additional limiting factor for the PFM lifetime. Estimations of radiation damage for power fusion reactor fall in the range from a few tens to hundred dpa. Therefore experimental investigation of plasma impact on the materials at high level of radiation damage is extremely required.

This part of report describes a new experimental approach to the study of plasma erosion [1] aiming to account for the radiation damage effect, and presents the first experimental results

on surface erosion of high-level, radiation-damaged materials. Preparation of material samples with high level of accumulated radiation damage is a difficult experimental task [2]. The fast charged particles from accelerators (protons as well as heavy ions) are well suited for experimental modeling of radiation damage produced in fusion materials and was developed on the basis of using the cyclotron at NRC KI (see papers [1–7]).

Investigations of helium effects at different irradiation temperatures on ODS materials suggested for fusion and fast breeder atomic reactors are described in topic 2.2. Oxide dispersion strengthened (ODS) ferritic/martensitic steels produced in many countries appear to be promising candidates for structural materials for future fusion and fast breeder atomic reactors, because of their high temperature mechanical properties and their potential radiation resistance [8–17].

The results presented here are joint scientific investigations of NRC KI and KIT (Karlsruhe, Germany with Dr. A. Moslang). Investigations of effects of neutron irradiation up to 15 dpa at 250–450°C on tensile specimens showed in [9] the typical strengthening of this steel between 250 and 350°C. Performed microstructural examinations of ODS alloy in [11] indicates that oxides undergo dissolution under neutron irradiation. Irradiation with electrons [11] leads to a significant dissolution of oxides with a radius decrease proportional to the dose. The results in [14] show that in irradiated ODS steel by heavy ions over a temperature range of 500–700°C up to 150 dpa the average oxide size decreased, but the oxide density increased. The effects of interaction of helium bubbles formed under α -particle irradiation in ODS steel under applied external stress were considered in paper [15].

It is well known that helium atoms accumulated in matrix of ODS materials under neutron irradiation in fusion reactors due to (n, α) nuclear reactions can considerably contribute to low temperature irradiation hardening and embrittlement (below $\sim 400^\circ\text{C}$) [16]. On the other hand, ODS ferritic-martensitic steels have shown recently very favourable tensile properties with significant work hardening capability even after substantial neutron irradiation (up to 30 dpa). In addition, it is expected that another favourable behaviour of ODS ferritic-martensitic steels is the capability of ODS particles to act as very effective sinks and trapping centers for migrating helium atoms, thus suppressing substantially helium bubble formation at lath and grain boundaries or the surface of larger M23C6 precipitates. As a consequence, nano-dispersed ODS particles should greatly retard helium embrittlement.

ODS samples were irradiated in these tests by fast helium ions in the cyclotron at NRC KI with the energy up to 35 MeV, with the irradiation temperature in the temperature interval from 300°C up to 500°C. The post irradiation analysis included tensile tests and detailed microstructure analyses with TEMs to analyze the accumulation of helium and defect morphology and their interaction of helium atoms with ODS particles.

Theoretical modeling of the effect of atomic collision cascades that are formed under neutron or charged particle irradiations on the process of coalescence of precipitates in irradiated materials is considered in the topic 3.1. The forecast of the dynamics of the precipitate growth is important for the estimation of stability of mechanical properties of different types of materials of pressure vessel steels in atomic reactors and Y-Ti-O precipitates in ODS materials, including such mechanical properties as yield stress or stress (strain) to rupture. Experimental investigations of influences of different types of fast neutron and charged particle irradiations on the stability of precipitates in different materials have been published in papers [18–21].

In this part of our investigations the general theoretical model of the precipitate-cascade interaction under fast particle irradiation is proposed. Expressions describing concentration and size of precipitates are developed based on the theoretical model, and the contribution of

high doses of fast particle irradiation due to atomic collision cascades in these expressions is comparable to the contribution of diffusion or even exceeds it. The obtained theoretical results are verified by experimental data on pressure vessel steels for atomic VVER-400 reactor being irradiated by fast neutrons [21] and some general theoretical consideration for the behaviors of Y-Ti-O precipitates in irradiated ODS materials. Coalescence is the process that can be realized at high irradiation doses by which big precipitates grow while small precipitates dissolve. In the absence of irradiation the coalescence is driven by only diffusion of impurity atoms [22]. The suggested model and calculations are based on paper [22] taking into account some results in [23].

Accumulation of helium atoms in materials under α -implantation or nuclear (n, α) reactions during neutron irradiation can induce drastic changes in mechanical properties (radiation hardening, swelling and embrittlement) of structural fusion reactor materials [24]. These phenomena are associated with defect cluster formation (voids, bubbles, dislocation loops and precipitates) under irradiation. Experimental results [25–32] show that high concentrations of helium atoms affect strongly not only helium bubble formation, but also dislocation loop nucleation. So the density of dislocation loops is increased with increasing helium atom concentration. Up to now, theoretical models for the description of this process do not exist. The experimental investigations of the nucleation stage of small defect clusters with average sizes of helium-vacancy clusters and dislocation loops up to one nm by TEM is very difficult.

At small concentrations of helium atoms and point defects, when the critical radius of defect clusters is high, this phenomenon can be described as a phase transition of first order with energy barrier at some critical radius [33]. For high concentrations of helium atoms (high production rate of helium) and for low temperatures ($T < 0,3 T^*$, where T^* is the melting temperature) bubble nucleation is controlled by atomistically small critical cluster sizes when a few and (in the extreme case only two) helium atoms form a stable nucleus. In this case the kinetics of nucleation of small defect clusters can be described by the di-atomic (spontaneous) nucleation model [34, 35].

In topic 3.2 a general theoretical model based on the di-atomic approximation is suggested which can describe defect cluster formation including both helium bubbles and dislocation loops at high concentrations of helium. On the basis of the suggested model, the main aspects will be studied of the kinetics of helium-vacancy cluster formation, small dislocation loop formation, both separately and in conjunction with helium bubble formation. The obtained theoretical results are compared with experimental data for density and mean size of defect clusters obtained by TEM after α -implantation in dependence of helium concentration.

One of the main problems of precipitation-hardened ferritic-martensitic steels is the precipitation effect on radiation swelling under high doses of irradiation. The peculiarity of precipitation-hardened alloys is void creation on the precipitates [36, 37]. Kinetics of these voids, associated with precipitates, significantly differs from that of free voids [8], and therefore can drastically change the rate of swelling. A very important problem for fusion structural materials (including ODS steels) is the effect of helium atoms that can be accumulated in these materials under 14 MeV neutron irradiation due to (n, α) nuclear reaction on their radiation resistance. Radiation swelling is one very important phenomenon that determines radiation resistance. As shown in topic 2.2, when the effect of irradiation and high concentration of helium atoms (up to 1000 appm) on microstructure and mechanical property changes of ODS materials after uniform helium implantation on the NRC KI cyclotron has been considered that helium bubbles are formed and attached to ODS precipitates. The kinetic model of the precipitate effect on radiation swelling at high irradiation doses, based on the evolution of size distribution function of voids and helium bubbles attached to precipitates, is developed in topic 3.3.

2. EXPERIMENTAL RESULTS

2.1 Investigation of the changes in physical-mechanical properties of tungsten and carbon materials after fast particle irradiation in the cyclotron at NRC KI, including irradiation by helium and by carbon ions and investigation of the effect of high levels of radiation damage produced in these materials following interaction with deuterium plasma

Integrated experiments have been performed to study the plasma erosion effect of radiation-damaged materials. The first stage of the experiments consisted of production of high levels of radiation damage in test materials. In the second stage, these irradiated materials were subjected to plasma exposure. Radiation damage resulting from neutron irradiation effect was simulated by fast ions accelerated in the cyclotron at NRC KI (similar to [3]). The NRC KI cyclotron provides acceleration of different ion species H⁺, He⁺, Li⁺, C⁺ etc. in the energy interval 1–60 MeV. By this method we can produce a high level of radiation damage and obtain in a few days an effect equivalent to fast neutron irradiation to the dose of 1022 neutron/cm².

The linear plasma machine LENTA [1] was used in the second stage of these experiments to process the irradiated materials in deuterium plasma and to study their surface erosion under conditions relevant to SOL of a tokamak reactor. The plasma simulator LENTA generates plasmas in a steady state discharge powered by electron beam, thus providing an ion current on the surface of materials at $j_{\text{ion}}=1017\text{-}1018$ ion/cm²s ($n_e=1012\text{-}1013$ cm⁻³, $T_e=1\text{-}20$ eV). Plasma exposures were performed step-by-step in order to reach in each of them deuterium ion fluence on the surface about 1021 ion/cm². The erosion effect was measured by a weight loss method and analysis of the sample surface microstructure was made with SEM after each plasma test.

2.1.1 Carbon materials

Irradiation by high-energy carbon ions. Carbon ions ¹²C⁺ accelerated to 5 MeV were taken to produce radiation damage in three types of graphite samples: SEP NB-31, MPG-8 and pyrographite [4]. Three high levels of radiation damage (1 dpa, 5 dpa and 10 dpa in average) over the damaged layer were obtained in samples of each graphite material. The numerical calculations of the distribution of the primary radiation defects D (dpa) produced in graphites by 5 MeV ¹²C⁺ ions were performed using the SRIM program [5] at a dose of $5 \cdot 10^{17}$ ion/cm² yielded the damage level $D_{\text{max}}=65$ dpa at ~ 5 μm depth, and an average value $\langle D \rangle = 9.7$ dpa.

Considerable linear deformations of the irradiated graphites were detected by a profilometer. The MPG-8 was found as the most radiation-resistant in our case, while the composite SEP NB-31 has shown large values of deformation: $\Delta H = 20$ μm on 10 dpa sample (10^{18} cm⁻²) compared with the 5 μm ion range.

Plasma experiments. The irradiated graphite samples were then exposed to steady-state deuterium plasma on the LENTA plasma simulator. The deuterium ion current density was about 10 mA/cm², ion energy 100 eV, with the sample temperature during plasma operation at ≤ 40 C. A layer of about 2–3 μm was eroded during the first step, and the layer of the maximal radiation damage was eroded in the second plasma exposure ($\sim 3\text{--}7$ μm) [6]. Weight losses and surface microstructure were analyzed after each plasma run.

Weight loss due to the plasma bombardment and erosion rate G was measured. Figure 1(c) shows the erosion rate of the SEP NB-31 composite in the plasma as a function of plasma current to the irradiated material sample and for comparison to the non-irradiated one. The results give evidence that the erosion rate is higher for irradiated (damaged) material. The enhancement factor of the erosion yield given by appropriate ratio of Y values for irradiated

to non-irradiated materials was $Y_{\text{SEP irradiated}}/Y_{\text{SEP}} = 2.6 \pm 0.6$ for SEP NB-31, and even larger $Y_{\text{pyroirradiated}}/Y_{\text{pyro}} = 4.8 \pm 0.4$ for pyrographite, while the lower value $Y_{\text{MPG irradiated}}/Y_{\text{MPG}} = 1.6 \pm 0.4$ was found for MPG-8.

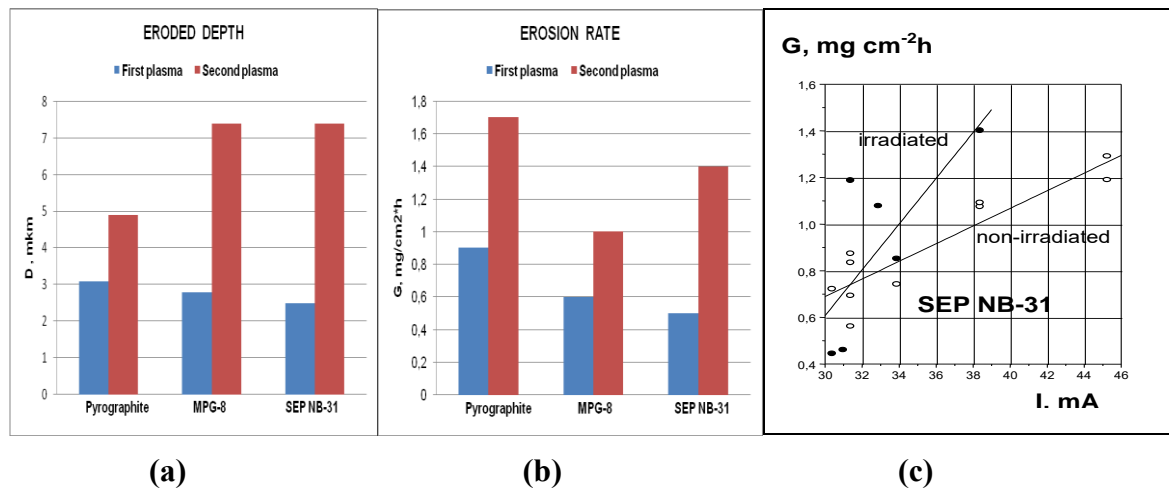


FIG. 1. Erosion depth (above left), erosion rate (above right) in double plasma experiment for 1 dpa samples of SEP NB-31, MPG-8 and pyrographite (b) and erosion rate (below) of SEP NB-31 graphite vs. plasma ion flux.

The results of double successive plasma exposure of carbon materials are illustrated in Fig. 1(a) and Fig. 1(b), showing erosion depth and erosion rate of three types of graphite after the first and second plasma exposures. All materials exhibit an increase of erosion rate in the second plasma exposure, corresponding to the layer of maximal defect density involved in the erosion.

2.1.2 Tungsten

Irradiation by $^4\text{He}^{+2}$ ions. Tungsten samples (99.95% wt W) of size $10 \times 12 \times 1$ mm have been irradiated by $^4\text{He}^{+2}$ ions accelerated to 4 MeV. Three series of irradiations have been performed to reach high levels of radiation damage. The α -particle fluences collected on the samples were $5 \cdot 10^{17}$ ion/ cm^2 , 10^{18} ion/ cm^2 [7] and $3 \cdot 10^{18}$ ion/ cm^2 , that correspond to different levels of induced defects. The distribution of the radiation defects in irradiated tungsten by helium ions at energy of 4 MeV has maximum of ~ 5 dpa for 10^{17} ion/ cm^2 at about $6.2 \mu\text{m}$ characterizing the range of the high-energy α -particles in tungsten.

Plasma effect on radiation damaged tungsten. The successive plasma experiments were pursued till the depth of maximal defect concentration was reached. We have made 5 successive exposure tests of the sample having taken the $^4\text{He}^{+2}$ fluence of $5 \cdot 10^{17}$ ion/ cm^2 . Total deuterium ion fluence on the surface from the plasma accumulated during this series was $2 \cdot 10^{22}$ D $^+$ / cm^2 ; and the surface layer eroded after 5 experiments was $7 \mu\text{m}$ thick. Considerable changes in the structure were observed when the sputtering process came to the layer of maximal defect concentration. Three parts of this sample are shown in Fig. 2: a) the no-damage zone subjected only to 5 plasma exposures, b) the border of irradiated zone (to the right), c) damage (irradiated) area. The defect structure is distinctly seen on the irradiated side.

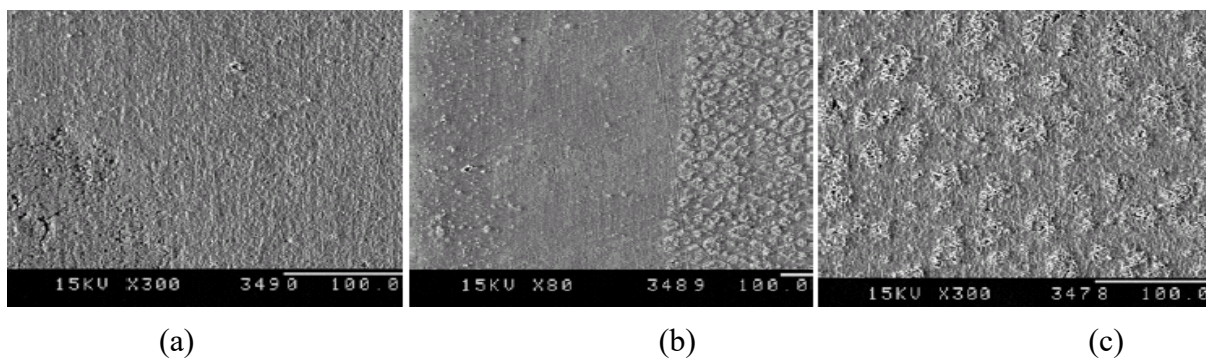


FIG. 2. Tungsten surface after plasma exposure to $2 \cdot 10^{22} D^+ / \text{cm}^2$: a) area subjected only to plasma; b) the border between the irradiated (${}^4\text{He}^{+2}$ fluence of $5 \cdot 10^{17}$, to the right) and non-irradiated zone; c) damage (irradiated) zone (scale bar at 100 microns).

Weight losses were measured in these tests and the erosion rate was evaluated. It was found to fall in the range $Y = (1-2.5) \cdot 10^{-3}$ at/ion, as estimated for the sample having received $5 \cdot 10^{17} {}^4\text{He}^{+2} / \text{cm}^2$.

2.2 Determination of the effects of irradiation and high concentrations of helium atoms (up to 1000 appm) on microstructure and mechanical property changes of ODS materials after uniform helium implantation at the NRC KI cyclotron in the energy interval up to 30 MeV

To study the impact of high concentrations of helium atoms on the changes of physical-mechanical properties and radiation resistance of irradiated EUROFER-ODS materials, the optimal regimes for helium ion implantation were selected for the production of degradation system on NRC KI cyclotron for obtaining a uniform distribution of helium atoms in the irradiated ODS samples.

The microstructure changes of EUROFER ODS samples were investigated before and after helium irradiation (saturation) using usual transmission electron microscopy (TEM) techniques (see Fig. 3). There are no dramatic changes in the structure of the EUROFER ODS steel after irradiation by α -particles and saturation with helium atoms of matrix of EUROFER ODS at irradiation temperatures $T = 300^\circ\text{C}$ (Fig. 3a). The sizes and distribution of carbides Me_{23}C_6 (Fig. 3b) and yttrium oxide remain practically without changes. At this irradiation temperature helium bubbles was observed in the EUROFER ODS matrix with average size 1–2 nm.

The microstructure investigations of irradiated EUROFER ODS samples at a higher temperature of 500°C demonstrate stronger effect of helium atoms on microstructure changes. TEM results at this temperature show that there are a much larger number of helium bubbles in comparison with the above conditions during investigation of the microstructure of EUROFER ODS steel after irradiation and helium implantation at 500°C . The size of the bubbles is near 5 nm in this case and the concentration of large bubbles in some areas is higher (Fig. 3a). It should be noted that under the given irradiation conditions, helium bubbles are usually present (decorated) around the excessive constituent and precipitates in the form of M_{23}C_3 carbides and can be attached to Y_2O_3 precipitates in EUROFER ODS steel (Fig. 3b).

Thus, it can be assumed that the excessive constituent (precipitates) in the ferritic-martensitic type steels (including ODS particles) are good sinks for helium atoms and small bubbles under irradiation by fast α -particles and saturation with helium atoms of matrix of EUROFER ODS, which may result in the changes of mechanical properties of steels of this type e.g. including the formation of helium embrittlement effect.

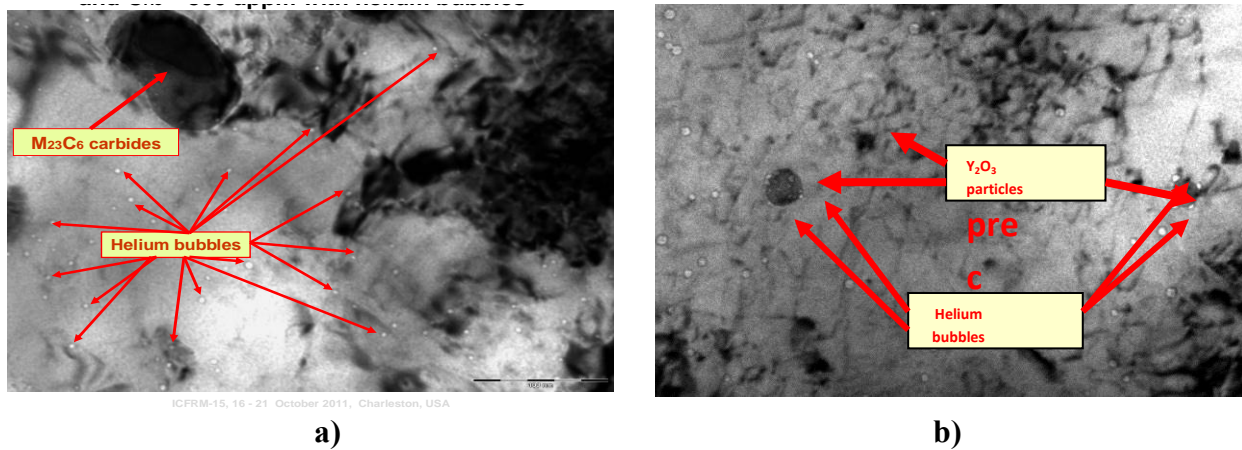


FIG. 3. Microstructure of irradiated EUROFER-ODS material at 500°C with different location of helium bubbles in matrix: a) free helium bubbles and near $M_{23}C_6$ carbide, b) free helium bubbles and helium bubbles attached to Y_2O_3 precipitates.

Tensile tests of un-irradiated and irradiated EUROFER ODS samples with tensile recording in coordinates “stress tension - relative strain” have been performed on the universal mechanical testing machine “Inspekt 50”. The typical rates of straining deformation curves by axial tensions for un-irradiated and irradiated EUROFER ODS samples are shown in Fig. 4b. These samples have been irradiated at 300°C with total helium concentration in the matrix $C_{He} = 1000$ appm.

From this picture we can see that the ultimate tensile stress (σ_u) and yield stress (σ_y) after irradiation by α -particles with dpa level $D = 0.23$ dpa and helium concentration $C_{He} = 1000$ appm were increased compared with un-irradiated values by ~ 1.4 times. These results confirmed the radiation hardening effect of EUROFER ODS material at low irradiation temperature ($T = 300^\circ C$). In these experimental tests the saturation of EUROFER ODS samples by helium atoms was up to $C_{He} = 1000$ appm. From the obtained data we can see that the total elongation to rupture in irradiated EUROFER ODS samples at the two irradiated temperatures (300°C and 500°C) decreased from practically $\varepsilon_{non} \approx 20\%$ (for the un-irradiated samples) up to $\varepsilon_{irr} \approx 10\%$ (for the irradiated samples). This means that at these two irradiation temperatures the embrittlement process of these samples with high helium concentration ($C_{He} = 1000$ appm) was clearly observed, producing helium embrittlement.

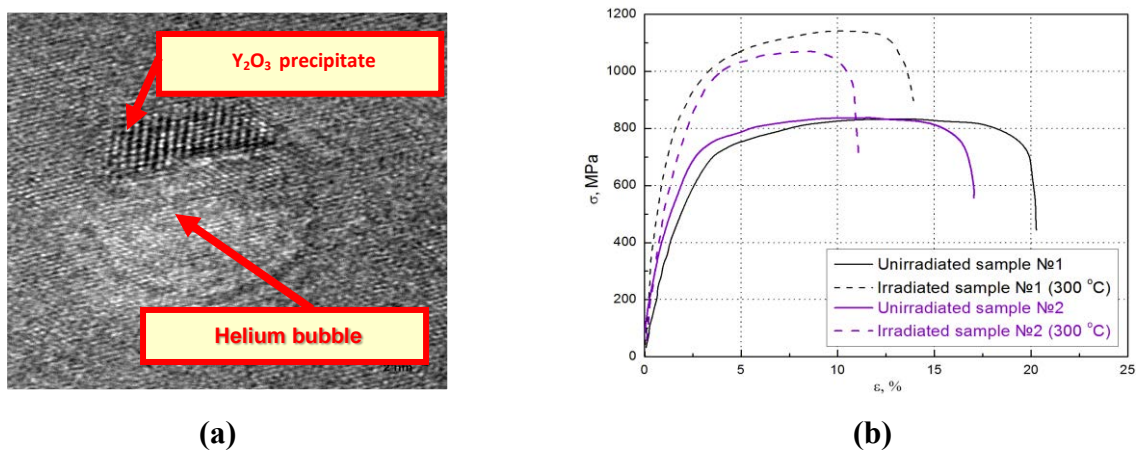


FIG. 4. HRTEM picture of helium bubble attached to Y_2O_3 precipitate (a) and deformation curves after mechanical tests for two different un-irradiated and irradiated EUROFER ODS samples N21, N22 at $T = 300^\circ C$ and $C_{He} = 1000$ appm (b).

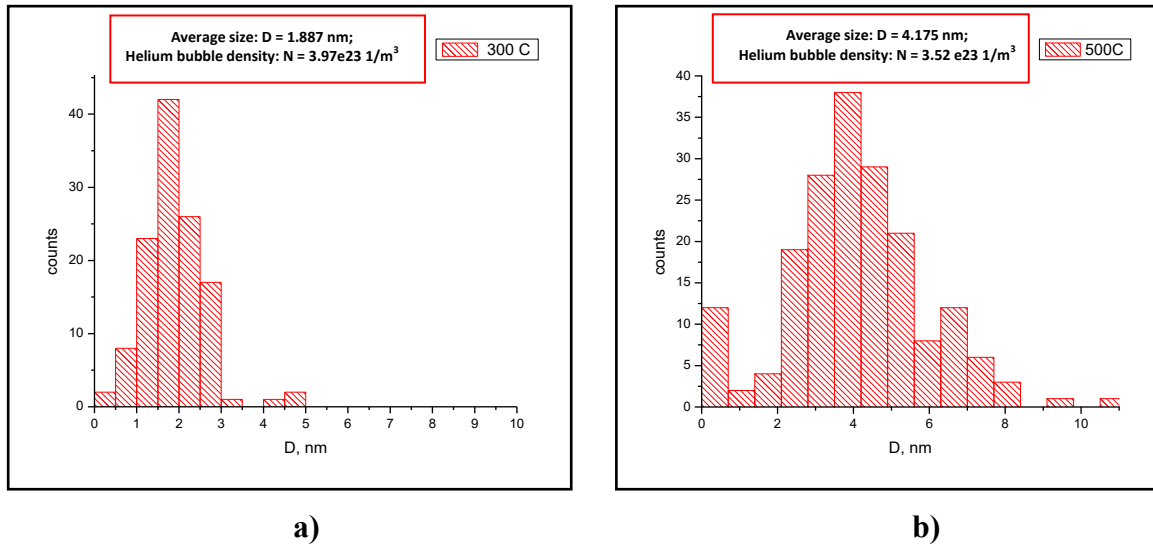


FIG. 5. Size distributions of helium bubbles in EUROFER ODS at helium concentration $C_{HE} = 1000$ appm and two irradiation temperatures: a) at 300°C and b) 500°C.

Joint analysis of three images of HRTEM: under-focusing, focus and over-focusing allows us to distinguish between free bubbles and bubbles attached to precipitates. Based on these tests, a very detailed analysis of the fractions of free and precipitate-attached bubbles and size distribution functions for two irradiation temperatures: 300°C and 500°C at $C_{HE} = 1000$ appm were received (see Fig.5).

3. THEORETICAL MODELLING

3.1 Theoretical investigation of stability and growth of precipitates (Cu precipitates, Y-Ti-O particles) under neutron or charged particle irradiation at high irradiation doses, taking into account the generation rates of atomic collision cascades

In this topic the effect of atomic collision cascades produced by fast particles (fast neutrons and charged particles) on the coalescence process of precipitates in irradiated materials is analyzed. Atomic cascades can partially destroy precipitates under interaction with overlapping cascades. This interaction increases the effective concentration of the impurity atoms in the matrix due to displacement from precipitates and decreases the density of small precipitates. This leads to the adjustment of concentration and average size of precipitates. Both precipitates and atomic collision cascades are considered in this model to have spherical forms.

In this work we calculated the volume of the intersection of spherical precipitate and spherical atomic cascade. The dependence of V/L^3 (where V is the intersection volume of cascade and precipitate, L is the cascade size) as a function of R/L (where R is the precipitate size) and it is presented in Fig. 6(a). The suggested theoretical model based on the developed method [22] allows determination of the asymptotic behaviour of average radius ($\langle R \rangle$) and density of precipitates (N) that at high irradiation doses and low temperatures is equal to $N = 3Q/L^3 I_C t$, (where Q is the initial concentration of impurity atoms in the matrix, I_C is the generation rate of cascades under irradiation, t is the irradiation time). We made the comparison of obtained theoretical results with the experimental data for microstructure investigations and concentration changes of spherical copper precipitates under neutron irradiation of pressure-vessel steel of VVER-440 reactor, obtained in [21] by virtue of experimental investigation of surveillance samples of this pressure-vessel steel.

For comparison of theoretical with experimental data we have used the following values: $D \sim 10^{-14}$ cm²/s, $L \sim 5 \cdot 10^{-8}$ cm, $I_C \sim 10^{-6}$ 1/s, $Q \sim 3 \cdot 10^{-4}$, $T = 550$ K. The comparison of experimental data for time dependence of the precipitate density with the theoretical curve is shown in Fig. 6(b). We can see that that diffusion processes do not determine the decreasing density of precipitates in irradiated pressure-vessel steel of VVER-440 reactor at high irradiation doses relatively low temperature ($T < 300^\circ\text{C}$). Instead, this process is determined by destruction of precipitates by atomic collision cascades.

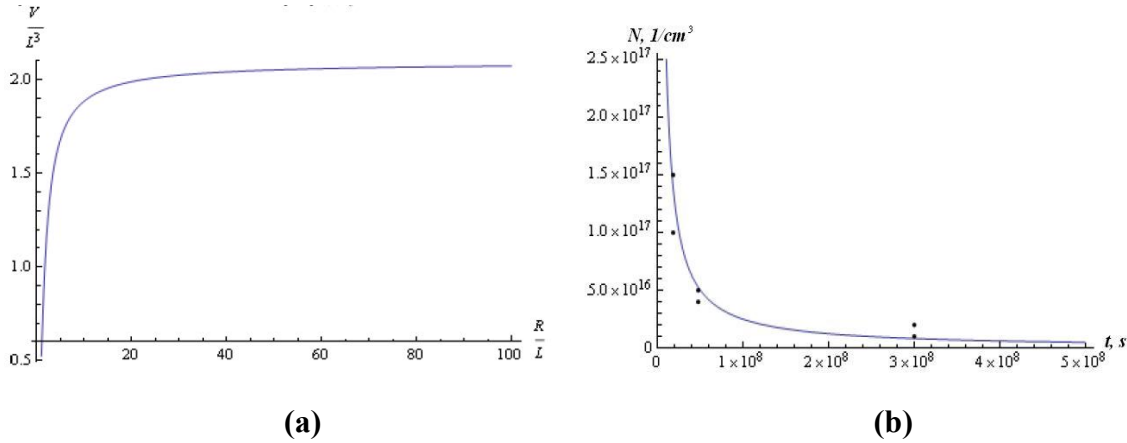


FIG. 6. Dependence of V/L^3 as a function of R/L (a) and comparison of experimental data (dots) for time dependence of the precipitate density with the theoretical curve (b).

3.2 Formation of small defect clusters: dislocation loops and bubbles in irradiated materials at high concentration of helium atoms and low temperatures

3.2.1 Helium-vacancy cluster nucleation

At high helium generation rates and low temperatures for investigations of helium-vacancy cluster formation, we will use the di-atomic nucleation model of helium bubbles where the critical size of bubbles is small, and in the extreme case, only two helium atoms and two interstitials needed to form a stable helium bubble and dislocation loop nucleus. Solving the suggested system of kinetic equations we can find the asymptotic behavior for the bubble density (C_b), the number of helium atoms in bubble nucleus (m), the helium concentration and mean bubble radius (R_b) in the nucleation and growth stages.

In the nucleation stage, taking into account the stationary conditions for helium atoms the bubble density and the number of helium atoms in the bubble, the nucleus is characterized by

the following relationships: $C_b = \frac{3^{1/3} G_h^{2/3}}{(4\pi r_o D_h)^{1/3}} t^{1/3}$, $m = \frac{3 (4\pi G_h r_o D_h)^{1/3}}{2 \cdot 3^{1/3}} t^{2/3}$,

For thermal equilibrium, helium bubbles where the gas pressure (p) is determined by the surface tension of the bubble ($p = 2\gamma/R_b$, where γ is the surface free energy) the mean bubble radius and helium concentration in matrix have the following dependencies:

$$R_b = \frac{3}{4} \left(\frac{T}{\pi\gamma} \right)^{1/2} \frac{(12\pi G_h r_o D_h)^{1/6}}{3^{1/3}} t^{1/3}, \quad C_h = \frac{3^{1/3} G_h^{1/3}}{(4\pi r_o D_h)^{1/3}} t^{-1/3},$$

During the growth stage the combined solution of system of kinetic equations gives the following relations for the main physical values, so for overpressurized bubbles: $C_b \sim t^{1/7}$, $R_b \sim t^{2/7}$, $C_h \sim t^{-3/7}$, and for the equilibrium helium bubbles: $C_b \sim t^{-1/5}$, $R_b \sim t^{2/5}$, $C_h \sim t^{-3/5}$.

3.2.2 Dislocation loop formation into cascades

Dislocation loops inside cascades are formed at the ballistic stage of penetrating cascades during very short time (up to 100 ps). So we can neglect the diffusivity of point defects (interstitial atoms) at low temperature after penetrating of cascades. So using the main assumptions in this theoretical consideration: $G_L \gg \beta_v D_i C_i^2, G_L \gg \beta_v (D_h + D_i) C_i C_h$ we can get the following relations for the dislocation loop density and loop size on the nucleation stage, that are described by the following relations: $N_L = G_L t, \quad R_L = a(G_i / \pi G_L)^{1/2} \ln^{1/2} t, \quad G_i/G_L \approx 10 \div 10^2$

3.2.3 Dislocation loop formation at low irradiation temperatures

Interstitial dislocation loops play a very important role in such phenomena as radiation hardening and swelling. Here we will show some results for description of the kinetics of dislocation loop nucleation at low temperature using a di-atomic model. At low temperature we can neglect the diffusivity of vacancies below stage II, and we assume here also, that the di-interstitials form the stable nuclei of dislocation loops.

Solving the suggested system of kinetic equations we get the time dependence for the mean radius and loop density on the nucleation stage that are equal:

$$R_L = 2\left(\frac{z_i D_i}{2b}\right)^{1/2} \left(\frac{G_i \omega_s}{\pi \beta D_i}\right)^{1/4} t^{1/2}, \quad N_L = \frac{b}{2z_i} \left(\frac{G_i \omega_s \beta_i}{\pi D_i}\right)^{1/2} \ln t,$$

where R_L, N_L are the mean radius and density of dislocation loops, D_i, C_i are the diffusivity and concentration of interstitials in matrix, Z_i is the bias for interstitials, β_i is the recombination coefficient for interstitials, G_i is the generation rate for interstitials.

These relations can be used for the determination of dose and temperature dependencies for radiation hardening of irradiated materials due to nucleation of interstitial dislocation loops.

3.2.4 Effect of helium atoms on the dislocation loop formation under α -particle irradiation

The effect of helium on dislocation loop formation has been analysed in papers [28, 30–32]. In our model we assume that helium atoms affect dislocation loop nucleation due to the formation of dislocation loop nuclei on the basis of small helium/self-interstitial clusters.

The solution of the suggested system of kinetic equations allows us to find the asymptotic behavior for mean radius, density of dislocation loops and concentration of helium clusters in the nucleation stage of this process. So the mean radius and density of dislocation loops and small bubbles can be written in the following form:

$$R_L = A_r (4\pi a r_b^2)^{1/9} \left[\frac{\omega_s z_i G_i D_i}{\pi b (D_i + D_h)} \right]^{1/3} \frac{D_h^{1/6}}{G_h^{1/9}} t^{5/9}, \quad N_L = A_n \left[\frac{b(D_i + D_h)}{a^{1/3} z_i D_i} \right]^{2/3} \frac{G_h^{2/9} D_h^{1/9}}{(4\pi r_b D_h)^{4/9}} t^{7/18}.$$

According to the experimental data the dose (time dependence for the dislocation loop density has the following form $N_L \sim t^n$, with the slope $n_{\text{exp}} = 0.4$. The suggested theoretical model gives us $n_{\text{th}} = 0.38$ and the temperature dependence is described by $N_L \sim \left(\frac{D_i + D_h}{D_i}\right)^{2/3} \frac{1}{D_h^{1/3}} t^{7/18}$,

3.2.5 Simultaneous formation of helium bubbles and dislocation loops at low irradiation temperature

The self-consistent solution of the system of kinetic equations based on di-atomic models for simultaneous formation of helium bubbles and interstitial dislocation loops in the matrix allows us to obtain the main parameters for this process. The dose and temperature dependencies for

the density and mean radius of helium bubbles are determined by the following relationships: for equilibrium bubbles $R_b \sim D_h^{1/6} t^{1/3}$ and for overpressurized bubbles $R_b \sim D_h^{1/9} t^{2/9}$ with bubble density $C_b \sim D_h^{-1/3} t^{1/3}$. The mean radius and concentration of dislocation loops can be written in the following form:

$$R_L = \frac{3}{2} \left[\frac{z_i \omega_s \omega r_b^2 D_i D_b^2 G_i}{b r_i (D_i + D_h) G_h} \right]^{1/3} t^{4/9}, \quad N_L = 3 \left(\frac{32 \pi G_i}{3} \right)^{1/3} \left[\frac{b r_i (D_i + D_h)}{z_i \omega D_i} \right]^{2/3} t^{1/9},$$

Comparison of experimental data for density of interstitial dislocation loops in Cu irradiated at low temperature $T = 30^\circ\text{C}$ with 30 keV He^+ ions as a function of He^+ dose (black dots) [31] and theoretical curves: for loop formation in cascades ($N_L \sim t$), di-atomic model for helium effect on dislocation loop formation with accompanying equilibrium helium bubbles ($N_L \sim \ln^{1/2} t$) and incompressible bubbles ($N_L \sim t^{1/21}$) presents in Fig. 7(a). The comparison of experimental data for density of interstitial dislocation loops in Ni irradiated at 200°C with 25 keV He^+ ions as a function of He^+ dose (black dots) [28] and theoretical curves: for loop formation into cascades ($N_L \sim t$), di-atomic model for helium effect on dislocation loop formation with accompanying equilibrium ($N_L \sim \ln^{1/2} t$) and incompressible bubbles ($N_L \sim t^{1/21}$) is shown in Fig. 7(b).

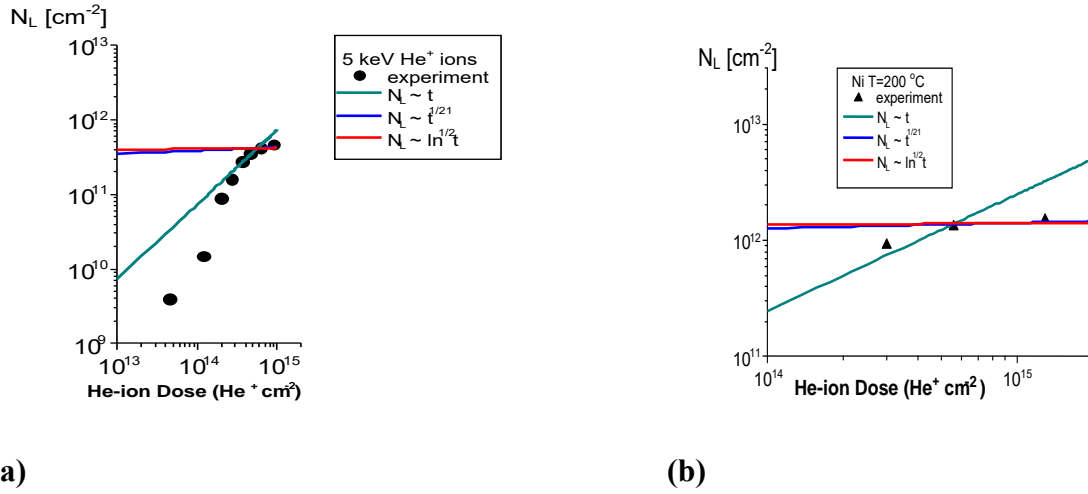


FIG. 7. Comparison of theoretical results with experimental data for density of interstitial dislocation loops formed in Cu irradiated at 30°C (a-left) and at 200°C (b-right) with 30 keV He⁺ ion energies as a function of He⁺ dose.

3.3 Effect of helium bubbles (big voids) attached to precipitates (Y₂O₃) on radiation swelling of ODS materials irradiated at high doses

It was shown by Mansur et al. in [39] that the growth rate kinetics of big bubbles with low helium gas pressure and vacancy voids are similar at $R_C > R > R_C$, (where R_C is the critical radius of void). So in this topic we will find as a first step the asymptotic behaviour of kinetics of voids (or big helium bubbles with low helium gas pressure inside) that are attached to precipitates.

In this theoretical model we will assume that all point radiation defects, absorbed by the precipitate with the radius R_p , are moving due to fast surface diffusivity of point defects on the precipitate surface to the attached void or to helium bubble of radius R . In this case we can find the growth rate of voids that is determined by the diffusion currents of point defects from the matrix toward the surface of the precipitate j_α , $\alpha = i, v$ [40–43] and follow by surface diffusivity of point defects to the void.

In the coalescence stage of void kinetics, when the void nucleation process is negligible, the size distribution function of voids on precipitates $f(R, t)$ satisfies the continuity equation, which includes growth rate for voids (or bubbles) dR/dt in the size space [40]. Long-term irradiation leads to steady-state concentrations of the point defects. The values of these concentrations (super saturations) are determined by the balance equations including generation rate of point defects under irradiation (G), absorption of them on precipitates and dislocations with density (ρ_d).

After some calculations we can get the following relations for the average radius of void $\langle R_V \rangle$ (big helium bubbles), density of voids $N_V(t)$ and dose dependence of radiation swelling ΔS that are determined by the following values

$$\langle R_V \rangle = f_1(T)t^{1/3}, \quad N_V(t) = f_2(T)G^{1/2}t^{-1/6}, \quad \Delta S = f_3(T)G^{1/2}t^{5/6}$$

Here $f_1(T)$, $f_2(T)$ and $f_3(T)$ are the temperature dependant functions, that are determined and depend on the thermal diffusivity of point defects and impurity atoms.

Finally, the dose dependencies of radiation swelling determined by voids attached to precipitates in irradiated ODS materials are plotted in the Fig. 8 for high doses of fast neutron and charged particle irradiations using the numerical parameters ($E_{mv} = 0.56$ eV, $\sigma = 200 \text{ erg/cm}^2$, $\rho_d = 10^{10} \text{ cm}^{-2}$, E_{mv} is the energy migration for vacancy, σ is the surface tension of voids).

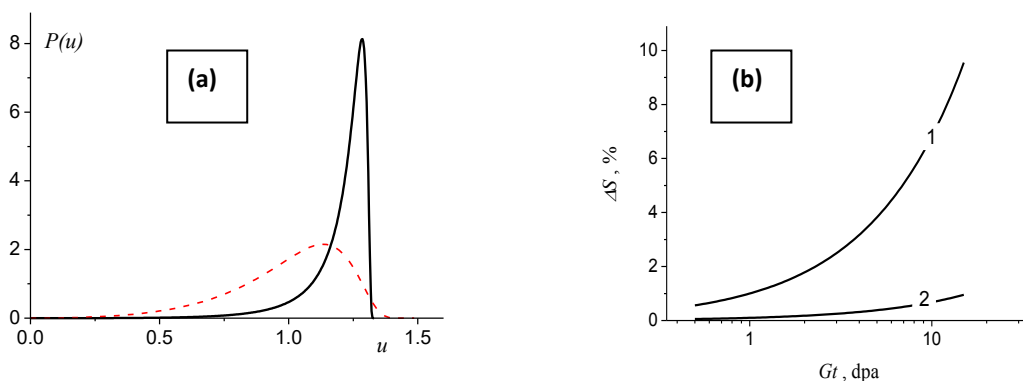


FIG. 8. Non-dimensional size distribution function $P(u)$ ($u = R/R_c$, R_c is the critical radius of voids) for voids attached to precipitates. Dashed curve corresponds to the distribution function for free voids [6] (a) and the dose dependence of radiation swelling (ΔS) in irradiated ODS materials at 500°C and at high doses under different point defect generation rates. (1) – $G = 1 \times 10^{-6} \text{ dpa/s}$ (fast neutron irradiation); (2) – $1 \times 10^{-3} \text{ dpa/s}$ (irradiation with fast charged particles on accelerators) (b).

4. CONCLUSION, REMARKS AND SUMMARY

The experiments presented here for investigations of behaviour of fusion-facing plasma materials allow use and development of new experimental tests for research of plasma facing materials for fusion reactors, accounting for neutron radiation damage effect simulated on graphite materials and tungsten with high-energy ions accelerated at the NRC KI cyclotron. Irradiations of three different graphites, CFC SEP NB-31, MPG-8 and pyrographite were performed with 5 MeV $^{12}\text{C}^+$ ions while 4 MeV helium ions $^4\text{He}^{+2}$ were used to produce radiation damage in tungsten. Damage levels of 1–10 dpa were reached on these materials. A swelling effect was registered on the irradiated samples and it was important on graphite.

The irradiated materials with radiation damage were subjected to deuterium plasma exposure in conditions simulating tokamak SOL in steady state at 100 eV of plasma ions on graphite and 250 eV on tungsten. Evidence of radiation damage influence on the erosion process was found by analysis of deformation, surface modification and erosion data. Surface modification was detected on the radiation-damaged materials. The study of erosion characteristics in plasma has shown enhancement of erosion yield on graphite's and structure damage on tungsten.

The new experimental approach developed in this work to explore the plasma-facing materials for accounting of neutron irradiation and the results obtained appear to be promising for further studies of the combined plasma and neutron effect on fusion PFM's.

The developed degradation system of accelerated fast helium ions at the NRC KI cyclotron for the production of uniform distribution profile of high concentration of helium atoms (up to 1000 appm) in irradiated bulk EUROFER ODS materials with the initial helium ion energy 30 MeV allow us to investigate the effects of irradiation (dpa level) and helium atom

accumulation in the matrix of ODS materials on microstructure change and mechanical properties in the temperature interval 300-500°C. Based on the produced degrader system for the stopping of fast helium ions on the NRC KI cyclotron and the uniform saturations of EUROFER ODS materials by high concentration of helium atoms (up to 1000 appm) at 300°C and 500°C, the investigations of mechanical tests and microstructure were performed. Mechanical tests of irradiated and non-irradiated EUROFER ODS material have shown that helium embrittlement (decreasing of the elongation to rupture) in irradiated EUROFER ODS material occurs at 300°C and 500°C.

It was shown that after α -particle irradiation to 0.23 dpa with the uniform helium concentration up to $C_{\text{He}} = 1000$ appm the ultimate tensile stress (σ_u) and yield stress (σ_y) were increased comparing with unirradiated values by about 1.4 times. These results confirmed the radiation hardening effect of EUROFER ODS material at low irradiation temperature ($T = 300^\circ\text{C}$).

The detailed microstructure investigations including TEM and high resolution TEM (HRTEM) of EUROFER ODS materials before and after irradiation at 300°C and 500°C have been performed. Helium bubble formation was observed, including helium bubbles attached to precipitates and free bubbles in the volume. Higher bubble density with smaller average size ($N = 3.97 \times 10^{23} \text{ 1/m}^3$, $D = 1.887 \text{ nm}$) were observed at 300°C and bigger bubbles ($D = 4.175 \text{ nm}$) with smaller density ($N = 3.52 \times 10^{23} \text{ 1/m}^3$) were observed at 500°C. The fractions of free helium bubbles and bubbles attached to precipitates have been measured at $C_{\text{HE}} = 1000$ appm. The fraction of free helium bubbles in the EUROFER ODS matrix is smaller (near 33%) comparing with the fraction of bubbles attached to precipitates (near 67%) at 300°C and 500°C.

A theoretical model was suggested for the effect of atomic collision cascades produced by fast particles (fast neutrons and charged particles) on the coalescence process of precipitates in irradiated materials. The critical radius of precipitates in irradiated materials taking into account the interaction of atomic collision cascades with precipitates is higher than in unirradiated materials. The average size of precipitates is increased at high doses under charged fast particle and neutron irradiation, and their concentration is decreased. In the frame of this model the irradiation term at $\sim 270^\circ\text{C}$ dominates the obtained theoretical expression that describes the decreasing density of precipitates in irradiated pressure-vessel steel of VVER-440 atomic reactor. Experimental data for the size distribution function of precipitates in pressure-vessel steel of VVER-440 atomic reactor provides a good correlation with the theoretical model suggested here.

According to experimental data, dislocation loops in Ni and Cu at low temperatures ($< 400^\circ\text{C}$) are formed early compared with visible helium bubbles at high helium production levels. Helium atoms can promote the process of dislocation loop formation at low PKA energies ($E_{\text{PKA}} < 3\text{--}5 \text{ KeV}$). At high PKA energies ($E_{\text{PKA}} > 3\text{--}5 \text{ KeV}$) the dislocation loops are formed mostly in cascades and helium atoms with concentrations ($> 10\ 000$ appm) can affect the stabilization of dislocation loops.

A di-atomic model has been suggested to describe the effect of high concentration of helium atoms on the nucleation of helium bubbles and dislocation loops at low temperatures in irradiated materials. The suggested model allows estimating the dose and temperature dependencies for defect cluster formation taking into account the effect of helium atoms on this process. The suggested di-atomic model for dislocation loop formation with helium atoms overestimates the effect of helium on this process. However, the obtained dose dependence of dislocation loop density is very slow and has a much smaller slope compared with the experimental data. This means that the main effect of helium is related with dislocation loop

formation into cascades under helium implantation, and helium atoms can increase the growth of dislocation loops due to decreasing interstitial recombination with vacancies trapped in helium vacancy clusters.

The dose dependence of radiation hardening is mostly determined by the growth stage of dislocation loops and helium bubbles. Theoretical results obtained here for the description of defect cluster formation based in the di-atomic model can be used to estimate dose and temperature dependencies of radiation hardening in irradiated materials at low temperatures and high production of helium atoms.

Without straightforward relations between diffusion currents toward a void and its surface area, the asymptotical size distribution function of voids attached to precipitates has been obtained and it has a specific shape. The size distribution function of voids $P(u)$ attached to precipitates is narrower comparing with the size distribution function of free voids in the matrix. Different dependencies of radiation swelling behaviour on time and point defect generation rates (G) lead to different swelling effects for the same total dose $\Phi = Gt$ (dpa) but for the different point defect generation rates: for fast neutron irradiation ($G = 1 \times 10^{-6}$ dpa/s) and for irradiation with fast charged particles on accelerators ($G=1 \times 10^{-3}$ dpa/s). The obtained theoretical relations give the following dependence of radiation swelling as $\Delta S \sim \Phi^{5/6} / G^{1/3}$.

REFERENCES

- [1] B.I. KHRIPUNOV, et al., "Erosion of Fusion Materials under High-Power Steady-State Plasma Stream on the LENTA Facility", Fusion Energy 2006, Proc. 21st IAEA Conf., IAEA-CN-149. Rep. EX/P4-3, (CD-ROM).
- [2] N. BALUC, et al., Nucl. Fusion, 47 (2007) 696-717.
- [3] A.I. RYAZANOV, et al., J. Nucl. Mat. **307-311** (2002), 1107-1111.
- [4] B.I. KHRIPUNOV, et al., "Effect of radiation damage on material erosion in plasma", Proc. 34th EPS-2007 Conf. on Plasma Phys. Warsaw, Rep. O2.003 (CD-ROM).
- [5] J.F. ZIEGLER, et al, Stopping and Range of Ions in Solids. NY: Pergamon Press, 1985.
- [6] V.S. KOIDAN, et al., "Influence of radiation damage on plasma-facing material erosion", Rep.00035 ICFRM-13, Nice 2007, J. Nucl. Mat. **386-388**, (2009), 261-263.
- [7] B.I. KHRIPUNOV, et al., "Evidence of radiation damage impact on material erosion in plasma environment", PSI-18, Toledo, Spain, 2008, Rep. 0-35.
- [8] S. UKAI et al., J. Nucl. Sci. Technol. **34** (1997) 256.
- [9] S. UKAI et al., J. Nucl. Mat. **258-263** (1998) 1745.
- [10] R. LINDAU, A. MOSLANG, M. SCHIRRA, and M. KLIMENKOV, J. Nucl. Mat., **307-311** (2002) 769.
- [11] I. MONNET, P. DUBUISSON, Y. SERRUYS, M.O. RUAULT, O. KAITASOV, J. Nucl. Mat. 335 (2004) 311-321.
- [12] S. OHTSUKA, S. UKAI, M. FUJIWARA, J. Nucl. Mat. **323** (2006) 56-70.
- [13] A. KIMURA, R. KASADA, A. KOHYAMA, et al., J. Nucl. Mat. **367-370** (2007) 60-67.
- [14] T.R. ALLEN et. al., J. Nucl. Mat. **375** (2008) 26-37.
- [15] J. CHEN, P. JUNG, W. HOFFELNER, H. ULLMAIER, Acta Mat., **56** (2008) 250-258.

- [16] E. MATERNA-MORRIS, A. MÖSLANG, R. ROLLI, *J. Nucl. Mat.* **386–388** (2009) 422–425.
- [17] R. LINDAU, M. KLIMENKOV, U. JÄNTSCH, A. MÖSLANG, *J. Nucl. Mat.*, **416** (2011) 22–29.
- [18] I. MONNET, P. DUBUISSON, Y. SERRRUYS, M.O. RUAULT, *J. Nucl. Mat.*, **335** (2004) 311–321.
- [19] H. TANIGAWA et al., *J. Nucl. Mat.* **367–370** (2007) 132–136.
- [20] T.R. ALLEN et al., *J. Nucl. Mat.* **375** (2008) 26–37.
- [21] E.A. KULESHOVA, B.A. GUROVICH, YA.I. STROMBAKH, YU.A. NIKOLAEV, V.A. PECHENKIN, *J. Nucl. Mat.* **142** (2005) 77–89.
- [22] I.M. LIFSHITZ, V.V. SLEZOV, *J.E.T.P.*, **35** (1958) 2.
- [23] I.M. KIRUKHIN, V.V. SAGALOVICH, V.V. SLEZOV, Preprint Kh.Ph.T.IKhar'kov, 1987.
- [24] H. ULLMAIER, H. TRINKAUS, *Materials Science Forum* **97–99** (1992) 451.
- [25] W.J. CHOYKE, et al., *J. Nucl. Mat.* **85–86** (1979) 647.
- [26] D.F. PEDRAZA, P.J. MAZIASZ, R.N. KLUEH, *Rad. Eff.* **113** (1990) 213.
- [27] K.Q. CHEN, S.H. YANG, Z.G. WANG, J.G. SUN, J.M. YUAN, *J. Nucl. Mat.* **191–194** (1992) 737.
- [28] K. NIWASE, T. EZAWA, T. TANABE, M. KIRITANI and F.E. FUJITA, *J. Nucl. Mat.* **203**(1993) 56.
- [29] C.H. ZHANG, K.Q. CHEN, Y.S. WANG, J.G. SUN, D.Y. SHEN, *J. Nucl. Mat.* **245** (1997) 210.
- [30] J. SHIMIZU, K. YASUDA, C. KINOSHITA, *J. Nucl. Mat.* **212–215** (1994) 207.
- [31] K. YASUDA, C. KINOSHITA, M. KUTSUWADA, T. HIRAI, *J. Nucl. Mat.* **233–237** (1996) 1051.
- [32] H. IWAKIRI, H. WAKIMOTO, H. WATANABE, N. YOSHIDA, *J. Nucl. Mat.* **258–263**(1998) 873.
- [33] A.E. VOLKOV, A.I. RYAZANOV, *J. Nucl. Mat.* **273**(1999) 155.
- [34] H. TRINKAUS, *J. Nucl. Mat.* **133–134** (1985) 105.
- [35] H. TRINKAUS, *Rad. Effects* **101** (1986) 91.
- [36] A. F. ROWCLIFFE and E. H. LEE, *J. Nucl. Mat.* **108–109** (1982) 306.
- [37] P. J. MAZIASZ, *J. Nucl. Mat.* **122–123** (1984) 472.
- [38] L. K. MANSUR, *Phil. Mag. A* **44**, 867 (1981).
- [39] L. K. MANSUR, W.A. COGHLAN, *J. Nucl. Mat.* **119**(1983) 1–25.
- [40] J. M. LIFSHITZ and V. V. SLEZOV, *J. Phys. Chem. Solids* **10**, 35 (1961).
- [41] V. V. SLEZOV, *Kinetics of First-order Phase Transitions* (Wiley-VCH, Weinheim, 2009).
- [42] Yu. V. MIKHAILOVA and L. A. MAKSIMOV, *Sov. Phys. JETP* **32**, (1971) 747.
- [43] V.A. PECHENKIN, G. A. EPOV, *J. Nucl. Mat.* **233–237** (1996) 1009.

EXAMINATION OF FE-CR BINARY AND ODS ALLOYS BY POSITRON ANNIHILATION SPECTROSCOPY AND OTHER TECHNIQUES

VLADIMÍR SLUGEN

Institute of Nuclear and Physical Engineering
FEI Slovak University of Technology Bratislava,
Slovakia

Results of two studies conducted in this SMoRE CRP are presented in this report.

PAPER 1. DIFFERENT CHROMIUM CONTENT AND THERMAL ANNEALING INFLUENCE ON ION IMPLANTED FE-CR MODEL ALLOYS

S. SOJAK, V. SLUGEŇ, V. KRŠJAK, W. EGGER, L. RAVELLI, M. PETRISKA, S. STANČEK, M. SKARBA, P. PRIPUTEN, K. VITÁZEK, M. STACHO, J. VETERNÍKOVÁ, V. SABELOVÁ

Abstract 1

Reduced activation ferritic/martensitic steels (RAFM) represented by binary Fe-Cr alloys, with different chromium content, were studied in as-received state, as well as after helium ion implantation. In order to study changes in dependence on the temperature, thermal annealing of He ion implanted Fe-11.62%Cr specimens was performed. Measurements by Pulsed Low Energy Positron System (PLEPS) were performed afterwards in Garching, Germany. Annealing out of defects at lower temperatures was not significant, as was expected, and some uncertainties are present. Extensive decrease of the positron lifetime of defects was observed in specimens annealed at a temperature of 600°C.

1. INTRODUCTION

Current nuclear power plants (NPPs) require radiation, heat and mechanical resistance of their structural materials with ability to stay operational during NPP planned lifetime. Radiation damage, much higher than in current NPPs, is expected in new generation of nuclear power plants, such as Generation IV and fusion reactors. Investigation of structural materials is among others focused on study of reduced activation ferritic/martensitic (RAFM) steels with good characteristics as reduced activation, good resistance to volume swelling, good radiation, and heat resistance. From this point of view, these steels are considered for application in future fission and fusion reactors.

Our work focused on study of radiation damage and thermal treatment evaluation of RAFM steels represented by binary Fe-Cr alloys, and partially on chromium influence on the increase of radiation damage resistance. For definite expression of chromium influence, model binary Fe-Cr alloys with varied chromium content and different damage levels were studied. Irradiation of structural materials is the main source of changes/damage in microstructure.

Therefore, an approach for restoration of initial physical and mechanical characteristics was applied in form of thermal annealing, with the goal to eliminate the size and amount of accumulated defects. Experimental analysis of material damage at the microstructural level was performed by a non-destructive technique, positron annihilation spectroscopy (PAS), by pulsed low energy positron system (PLEPS) and conventional positron annihilation lifetime spectroscopy (PALS).

Application of PLEPS [1] at the high intensity positron source NEPOMUC [2, 3] at the Munich research reactor FRM-II gives us, in comparison with PALS, the opportunity to investigate specific depths due to energy of positron which can be set to specific levels (0.5 eV–20 keV) and allows investigation of near surface regions, and provides information about defect structure, namely, their size and distribution.

Difficulties connected with experiments in real reactor conditions led us to simulation of radiation damage by ion beams (He^+ ions) at different levels, reaching high fluences expected in new reactor concepts. Implantation was performed using the linear accelerator at the Department of Nuclear Physics and Technology, and the resulting vacancy type defects produced by helium ions were studied in detail.

2. MATERIALS TREATMENT

The detailed chemical composition of studied Fe-Cr alloys with different chromium content can be seen in Table 1.1. More information about fabrication processes and heat treatment of measured reduced activation ferritic/martensitic steels can be found in [4]. “As-received” materials were cut to desired dimensions, ground and polished to mirror-like surfaces before

exposure to helium implantation. Subsequently, non-implanted reference specimens and the implanted specimens were investigated with positron annihilation techniques.

TABLE 1.1 – CHEMICAL COMPOSITION OF STUDIED FE-CR ALLOYS [4]

Alloy	Cr*	O*	N*	C*	Mn	P	Ni	Cu	V
L251	2.36	0.035	0.012	0.008	0.009	0.013	0.044	0.005	0.001
L259	4.62	0.066	0.013	0.02	0.02	0.011	0.06	0.01	0.001
L252	8.39	0.067	0.015	0.021	0.03	0.012	0.07	0.01	0.002
L253	11.62	0.031	0.024	0.028	0.03	0.05	0.09	0.01	0.002

*measured after heat treatment

Accelerated helium ions were used to obtain cascade collisions in the microstructure of the studied materials without neutron activation. Helium implantation was performed in two steps, with ion energy 250 keV and 100 keV, respectively. Implantation at different dose levels (Table 1.2) was performed at the linear accelerator of the Slovak University of Technology in Bratislava [5]. The ion energies were chosen to ensure the possibility of application of non-destructive techniques, sensitive in near-surface areas (PAS, SEM, etc.). Applicability of these energies was also simulated using the SRIM code (Stopping and Range of Ions in Matter).

Specimens were thermally treated after PLEPS measurement at different implantation doses with the aim to understand the influence of annealing on structure formation and defect behaviour. Thermal treatment was performed at Universität des Bundeswehr in Neubiberg (Munich, Germany). Specimens were annealed in an argon atmosphere (10 kPa) at temperatures of 400, 475, 525 and 600°C for 2 hours, then gradually cooled down, and repeatedly measured after each temperature by the PLEPS technique.

TABLE 1.2 – IMPLANTATION DOSES OF STUDIED FE-CR ALLOYS.

Cr content [%]	2.36		4.62		8.39		11.62			
Specimen	L25100	L25101	L25900	L25901	L25200	L25201	L25300	L25301	L25303	L25305
Dose Ions/cm ²	0	6.24x10 ¹⁷	1.87x10 ¹⁸	3.12x10 ¹⁸						
Dose C/cm ²	0	0.1	0	0.1	0	0.1	0	0.1	0.3	0.5

3. RESULTS

Depth profiling of vacancy type defects was performed by PLEPS on the “as-received” Fe-11.62%Cr specimen and three Fe-11.62%Cr specimens with different damage levels (Table 1.2) using positron implantation energies between 2 keV and 18 keV, corresponding to depths of 15 – 525 nm. The specific depth profiles of defect distributions were obtained by helium implantation at two energies, 100 keV and 250 keV.

Evaluation of Fe-11.62%Cr measured spectra was performed by the PosWin code [6, 7] and the spectra were decomposed into three components assigned as, τ_1 - positron annihilation in bulk, τ_2 - positron annihilation in defects (vacancies, vacancy clusters), and τ_3 - positron annihilation in large defects (e.g., voids).

Data achieved by PLEPS technique were significantly influenced by the Scanning Electron Microscopy (SEM) results performed at Institute of Materials Science (Faculty of Materials Science and Technology, STU). A diagonal cut was performed at a 12° angle for the SEM

technique in a specimen of Fe-11.62%Cr implanted at 0.3 C/cm^2 and annealed at $475 \text{ }^\circ\text{C}$ (Fig. 1.1).

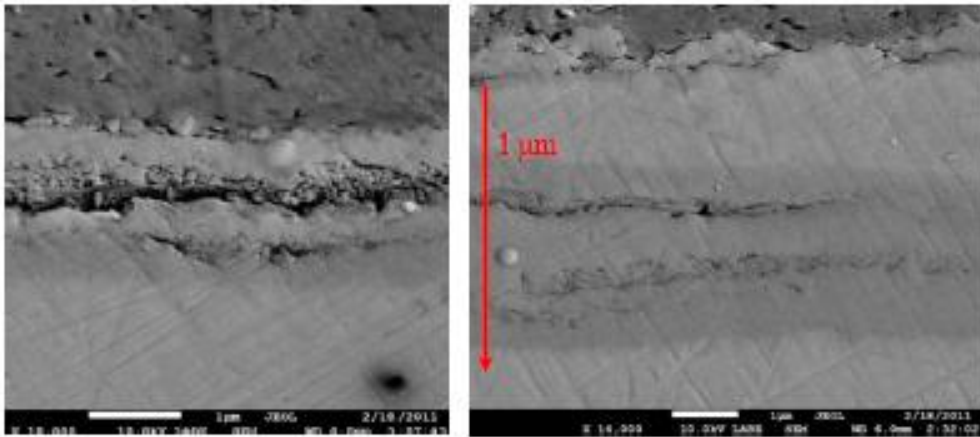


FIG. 1.1. – Alloy Fe-11.62%Cr annealed at $475 \text{ }^\circ\text{C}$ and implanted at 0.3 C/cm^3 .

This figure shows major damage in two regions. If we consider results achieved from the Stopping and Range of Ions in Matter (SRIM) simulation (Fig. 1.2), these two regions could be assigned to the maximum damage caused by He ion implantation. The first peak at $\sim 300 \text{ nm}$ is very significant and implies damage from 100 keV and partially also from 250 keV helium ions.

This can be recognized also from the SEM figures where the area closer to the surface has more significant damage (100 keV He) than the one further from the surface, which was influenced mainly by 250 keV He ions. Some uncertainties are introduced into the SRIM software and SEM technique results due to the SEM deviations of about $50\text{--}100 \text{ nm}$ from the expected maximum damage calculated in SRIM. This could be influenced by undulation on the surface of the diagonal cut of the specimen. According to reference [8] annealing at temperatures between $0.3T_m\text{--}0.4T_m$ (melting temperature) can cause void and dislocation structure formation (the dislocation loops are unstable and grow into a dislocation networks), and diffusion is sufficient for the formation of precipitates. This corresponds well with an annealing temperature of $475 \text{ }^\circ\text{C}$ and partially of $525 \text{ }^\circ\text{C}$ (this was not verified by SEM), as ion damaged area was multiplied and voids reached a width of tens of nanometers.

Specimens implanted at level 0.3 and 0.5 C/cm^2 registered a significant decrease of mean positron lifetime (MLT) at 600°C (Fig. 1.3). Analysis based on the MLT at this temperature could be interpreted as an extensive decrease of defect size. Specimens irradiated at 0.3 and 0.5 C/cm^2 show a growing MLT from the depth of $\sim 170 \text{ nm}$ to the surface. This growth of MLT could be assigned to the oxide layer on the surface. The minimum of the trend line is close to the area (depth) of large voids which are unrecognizable by positron techniques at annealing temperature of 475°C . Then the increase of MLT trend line from depth of $\sim 300 \text{ nm}$ is recognized, and implanted 250 keV helium ions could participate in its increase. If we take into account such a complicated system as Fe-Cr alloys after all treatments, then these mean lifetimes can be in some way misleading. Therefore, the components of the measured spectra also have to be analyzed for better understanding.

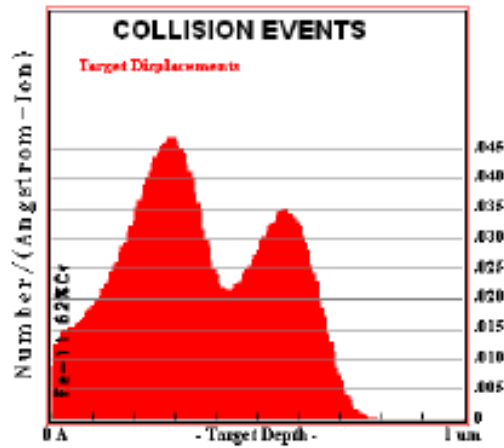


FIG. 1.2. – Simulation of damage by 100keV (left peak) and 250 keV (right peak) He ions.

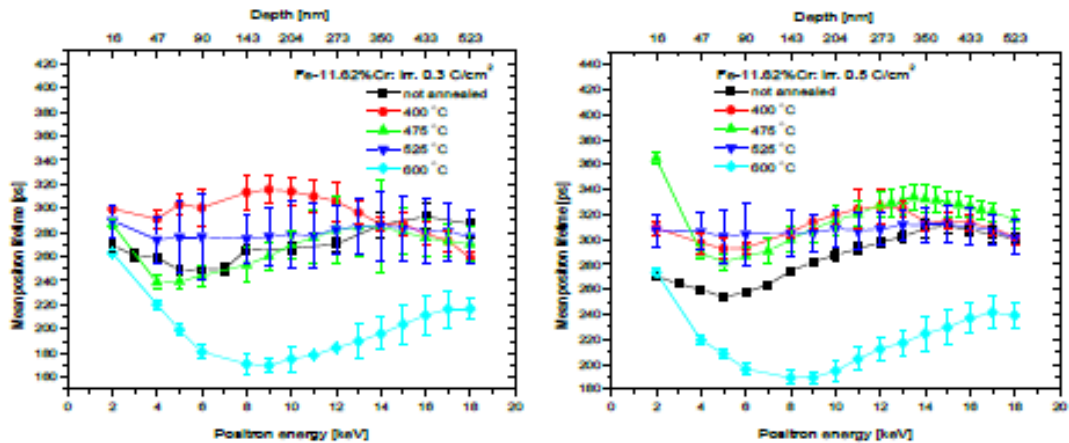


FIG.1.3. – Mean positron lifetime of Fe-11.62%Cr alloys.

Considering the theoretical statements from [8] for RAFM steels, that above $0.4T_m$ there occurs a continuous annealing out of displacement damage, resulting in little change in strength (at these temperatures strength sometimes decreases because irradiation-enhanced diffusion accelerates the normal thermal aging process), we could say that such large voids in the affected area were annealed out at temperature of 600°C, or at least their size decreased to rather small vacancy clusters.

Specimens with different chromium content according to the Table 1.2 were evaluated after 250 keV and 100 keV He ion implantation energies, respectively. This measurement was performed only on “as-received” specimens and at 0.1 C/cm^2 implantation dose. According to Fig. 1.4 showing the results achieved by PALS (Positron annihilation lifetime spectroscopy), there are a mean positron lifetime (MLT) of $\sim 148 \text{ ps}$ for “as-received” specimens, and for a dose of 0.1 C/cm^2 are an MLT of about 154 ps. According to [9] such mean lifetimes are characteristic of bulk material with dislocations. Major changes in MLT values are not observed to be dependent on different chromium content.

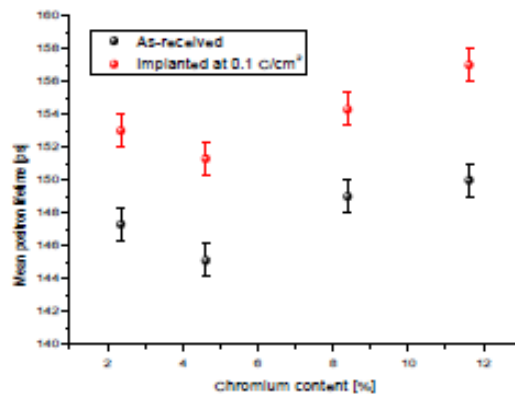


FIG. 1.4. – MLT of specimens with different chromium content by PALS.

This is in comparison to results achieved by the PLEPS (Fig. 1.5) technique, allowing depth profiling of materials, showing an extensive decrease of mean positron lifetime. MLT measured by PLEPS in 0.1 C/cm² implanted specimens with different chromium content reaches its lowest value of ~ 230 ps and then goes higher. Difference between PALS and PLEPS results of MLT is from 60–130 ps. Such enormous growth of MLT cannot be explained by technique deviations, and it has to be assigned to the ability of PLEPS technique to see an increased amount of defects. According to reference [9] results achieved by PLEPS should be interpreted as showing a significant presence of vacancy clusters. The MLT increase in case of “as-received” specimens did not reach such variations as seen in implanted specimens, probably due to the uninfluenced structure by ion implantation. Some defects are present from the fabrication of alloys. With increasing content of chromium, the mean lifetime slightly decreases, and except for the Fe-2.36%Cr alloy the MLT is about 190 ps. This is a difference of about 20–40 ps in comparison to the PALS results. Mean lifetimes of implanted specimens were quite similar with respect to deviations, but the lowest values were registered in the Fe-11.62%Cr specimen. Interference of bulk structure to the final PALS results could also be indirectly influenced by blistering because of the exposed undamaged structure.

4. CONCLUSIONS

Investigation of Fe-Cr alloys with different chromium content and thermal annealing of chosen specimens was performed in this work. Evaluation of the measured data of annealed (475°C) Fe-11.62%Cr alloy by PLEPS technique was significantly influenced by Scanning Electron Microscopy (SEM) results which showed major damage in two helium-influenced regions.

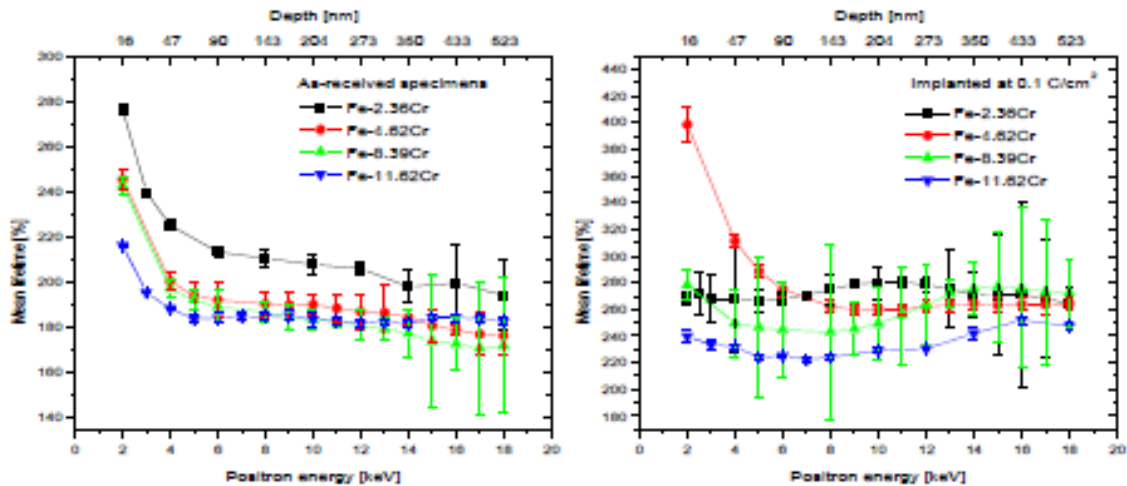


FIG. 1.5. – MLT of specimens with different chromium content by PLEPS.

Expected damage in form of increased positron lifetimes was not observed in case of using a 600°C annealing temperature, and a significant decrease of defect positron lifetimes from large voids to smaller vacancy clusters was well recognized. Considering the literature [8] about temperature influence on reduced activation ferritic/martensitic steels above $0.4T_m$, we could say that such large voids in the affected area ($<1 \mu\text{m}$) were continuously annealed out or at least their size was decreased to small vacancy clusters.

The influence of different chromium content in the case of “as-received” and 0.1 C/cm^2 implanted specimens was not so significant, even though the MLT of ion implanted specimens increased. A difference of about 10 ps was recognized in PALS technique, and also the PLEPS had small deviations between particular implantation doses. A significant chromium influence was well recognized in our former experiments at higher implantation doses [10].

Ion implantation damage occurred in our specimens, and was at very high level. Considering the influence of thermal annealing and surface oxide layer introduces many variables and therefore creates a complicated system for final evaluation of the measured data. Therefore, although the positron annihilation spectroscopy is a very applicable technique for study of vacancy type defects, some limitations were recognized in our inability to study specific depths (PALS) or defining too large defects (PLEPS). Therefore, other destructive or non-destructive techniques have to be used to give us other points of view on the examined materials.

ACKNOWLEDGMENTS

Financial contributions from the IAEA grant to project SMoRE are acknowledged. The authors gratefully acknowledge the assistance of the staff of the high-intensity positron source (NEPOMUC), PLEPS at the Munich research Reactor FRM II and for the support of OP VaV (ITMS: 26220120014) and ERDF.

REFERENCES

- [1] SPERR, P., EGGER, W., KÖGEL, G., DOLLINGER, G., HUGENSCHMIDT, CH., REPPER, R., PIOCHACZ, C., Applied Surface Science **255** (2008) 35–38.
- [2] HUGENSCHMIDT, C., DOLLINGER, G., EGGER, W., KÖGEL, G., LÖWE, B., MAYER, J., PIKART, P., PIOCHACZ, C., REPPER, R., SCHRECKENBACH, K.,

- SPERR, P., STADLBAUER, M., Applied Surface Science, **255** Issue 1 (2008) 29–32.
- [3] <http://e21.frm2.tum.de/index.php?id=207> .
- [4] MATIJASEVIC, M., ALMAZOUZI, A., Journal of Nuclear Materials **377** (2008)147–154.
- [5] KOVAC, P., PAVLOVIC, M., DOBROVODSKY J., NIM **B 85** (1994) 749–751.
- [6] KIRKEGAARD, P., ELDRUP, M., Comput. Phys. Commun. **3** (1972) 240.
- [7] BOCHERT, D., Diploma Thesis, Universität der Bundeswehr Muenchen (2004).
- [8] KLUEH, R.L., HARRIES, D.R., High-Chromium Ferritic and Martensitic Steels for Nuclear Applications, ASTM USA (2001).
- [9] KRŠJAK, V., Positron annihilation study of advanced nuclear reactor materials, Doctoral thesis, Slovak University of Technology, Slovakia, 2008.
- [10] SLUGENŤ, V., KRŠJAK, V., EGGER, W., PETRISKA, M., SOJAK, S., VETERNÍKOVÁ, J., Fe-Cr alloys behavior after helium implantation, Journal of Nuclear Materials **409** (2011) 163–166.

PAPER 2. STUDY OF RESIDUAL STRESS AND VACANCY DEFECTS IN OXIDE DISPERSION STRENGTHENED STEELS

V. SLUGEŇ, J. VETERNÍKOVÁ, S. KILPELÄINEN, F. TUOMISTO

Abstract 2

This study focused on commercial oxide-dispersion strengthened (ODS) steels - MA 956 (20%Cr), ODM 751 (16%Cr) and ODS Eurofer (9%Cr), developed for fuel cladding of GEN IV reactors. The ODS steels are described in order to compare their microstructure features. Vacancy defects were observed by Doppler Broadening Spectroscopy (DBS) and Positron Annihilation Lifetime Spectroscopy (PALS). Residual stress proportional to all types of defects was investigated by Magnetic Barkhausen Noise (MBN) measurement. From the DBS results, the highest defect presence was found for ODS Eurofer. This steel is followed by MA 956. ODM 751 demonstrates the lowest presence of defects. PALS measurements confirmed the DBS results. The lowest defect density belongs to ODM 751; although these defects are the largest ones (three or four vacancy clusters). MA 956 has di- or three-vacancies and ODS Eurofer has the highest defect density with di-vacancies. MBN results are in a good accordance with positron techniques. The highest residual stress is found for ODS Eurofer, followed by MA 956, and finally, the lowest residual stress proportional to hardness is found for ODM 751.

1. INTRODUCTION

Design and introduction of future nuclear reactor systems are strongly dependent on the choice of structural materials. These materials must withstand more exacting operating conditions typical for the reactors within the international program Generation IV (Gen IV). In comparison to current commercial reactors, all construction materials (particularly for internal components) of the GEN IV reactors will be operated at elevated temperatures (up to 900–950°C, in the case of High Temperature Reactors). They will be also loaded by higher radiation damage (up to tens of dpa for internal structures) due to the high fast neutron flux [1].

Current knowledge about ageing-induced changes of microstructure of construction materials [2, 3] is not sufficient for Gen IV reactors. Therefore, structural materials (new materials of Gen IV included) have to be tested, and the results of these tests are needed to provide the microstructural interpretation.

This paper is focused on a group of Oxide-Dispersion Strengthened (ODS) materials which have been considered as candidate materials in most Gen IV concepts. Our experiments provide the microstructural characterization of chosen ODS steels by use of non-destructive techniques including Positron Doppler Broadening Spectroscopy (DBS), Positron Annihilation Lifetime Spectroscopy (PALS) and Magnetic Barkhausen Noise (MBN).

2. EXPERIMENT

Commercial high chromium ODS steels are investigated in this paper. Although these ODS steels were primarily designed for application in space and for heat exchangers in thermal power plants, their derivatives have been developed for nuclear applications. ODS materials are appropriate for applications requiring a higher temperature limit than do classical ferritic steels. ODS steels are able to resist high thermal strain up to a temperature of ~ 900°C [4, 5].

Three following commercial materials, all candidates for Gen IV fuel cladding, were measured:

- i) MA 956 (20% Cr, product of Incoloy);
- ii) ODM 751 (16% Cr, product of Plansee);
- iii) ODS Eurofer (9% Cr, product of Plansee).

The chemical composition of investigated steels is listed in Table 1.

TABLE 1. CHEMICAL COMPOSITION OF STEELS (IN % WT.).

	C	Mn	Ni	Cr	Mo	Ti	Al	Si	W	Y ₂ O ₃
MA 956	0.07	0.12	0.07	20	0.1	0.3	3.4	0.04	-	0.5
ODM 751	0.07	0.07	0.02	16	1.74	0.7	3.8	0.06	-	0.5
ODS Eurofer	0.1	0.44	-	9	0.01	-	-	0.01	1.1	0.3

The investigated ODS alloys were produced by mechanical alloying, i.e. matrix materials were milled and mixed together with yttrium particles to form solid solutions with a uniform dispersion of oxide nano-particles. The mixtures were then consolidated using Hot Extrusion (ODS Eurofer) or Hot Isostatic Pressing (MA 956 and ODM 751). The MA 956, ODM 751 and Eurofer ODS alloys were supplied as rods in the recrystallized condition for improved creep strength. The recrystallization heat treatment resulted in a coarse columnar grain structure.

Samples of investigated steels were prepared from as-received material by cutting the steel sheets into suitable pieces. After cutting, the sample surfaces were polished in order to remove surface impurities (up to $\sim 0.3\mu\text{m}$).

The applied technique of Doppler Broadening Spectroscopy (DBS) [6] with conventional method of measurement utilizes the principles of momentum conservation during positron annihilation [7]. The momentum of annihilating positron-electron pairs is detected as a broadening of the 511 keV annihilation peaks [8], which is recorded by two HPGe detectors in conventional mode. The DBS technique expresses its results in S and W parameters. The W parameter (the area under the tail of the spectra) describes the positron annihilation with high momentum core electron. The S parameter from the peak area is typical for positron annihilation with low momentum electrons (mostly valence ones).

The S and W parameters are sensitive to annihilation surroundings. The S parameter grows for the lattice with an increase of defect concentration. The W parameter decreases at the same time but with a smaller gradient [6, 8]. If the sample contains only bulk and one type of defects, the S and W parameters should exist on a line between these two states [8].

The DBS was associated with a slow positron beam [9 –11] accelerating positrons up to 36 keV. The defect depth profile can be observed in surface and subsurface layers of the samples by application of this equipment. The maximal investigated depth slightly exceeds $1.6\ \mu\text{m}$ according to calculations published in [12].

The Magnetic Barkhausen Noise (MBN) technique is useful for determination of residual stress in materials, which relates to the presence of all kinds of defects, such as precipitates, grain boundaries and lattice defects. MBN is based on an electromagnetic field going through ferromagnetic material. During the measurement, the structure composed of domains starts to reorganize according to the external field. This phenomenon requires movement of the domains which is made by discontinuous jumps recorded as MBN signal [13]. Defects located in the samples act as pinning sites for magnetic domains and hinder the movement of magnetic domains. This tends to reduce the noise signal; therefore specific types of defects or residual stress can be observed by applying this technique.

Results acquired by this experimental technique can be given as follows [14]:

i) Barkhausen Noise Amplitude (BNA), which characterizes a maximum value of the voltage in the MBN signal.

ii) Corresponding magnetic field (H_{peak}), describing the position of BNA in the applied field.

iii) Signal envelope; the envelope is plotted as a function of the applied magnetic field (current).

BNA and the trend of the envelope are decreasing with growth of defect concentrations, residual stress or hardness [13]. The position of the BNA peak - H_{peak} can establish the grain size as described in [15]. The MBN measurement was performed using the commercial system Stresstech AST μ Scan 500 [16] at a magnetizing frequency up to 50 Hz and a magnetizing voltage of 3 V_{pp} (Volts peak-to-peak). The sampling frequency was set to 1 MHz. The signal of the pick-up coil was filtered from 5 to 500 kHz and amplified with a gain of 10.

The Positron Annihilation Lifetime Spectrum (PALS) [17, 18] can determine the concentration and size of vacancy-type defects in a sample with very low concentrations (from 0.1 to 500 ppm) [18]; therefore it can describe the area where transmission electron microscopy (TEM) is not so sensitive. Positron lifetime is proportional to defect size. A percentage of positrons (intensity) trapped and annihilated in the defects, can give information about the defect concentration

The measuring equipment used in this work consists of two BaF2 scintillation detectors and two discriminators [20]. The measured spectra were evaluated by program LifeTime9 [21] according to the three-state positron trapping model [22]. The value of FWHM parameter, which describes the sensitivity of measuring equipment, was close to 240 ps. Fit Variant (reduction of chi-square) achieved value in range (1; 1.1), which means that the goodness of the fit was sufficient, and the aberration of the fit was below 0.1%.

3. RESULTS

DBS results are acquired from annihilation spectra via S and W parameters. Fig. 1 shows results on a S-W diagram. The behaviour of S-W parameters differs significantly for individual samples. The curves are intersecting at one point. The lowest gradient is for ODS Eurofer, followed by MA 956. The highest gradient was found for ODM 751. ODM 751 is probably described by the lowest defect presence due to its DBS results. This sample should have values closest to bulk values (defect-free structure).

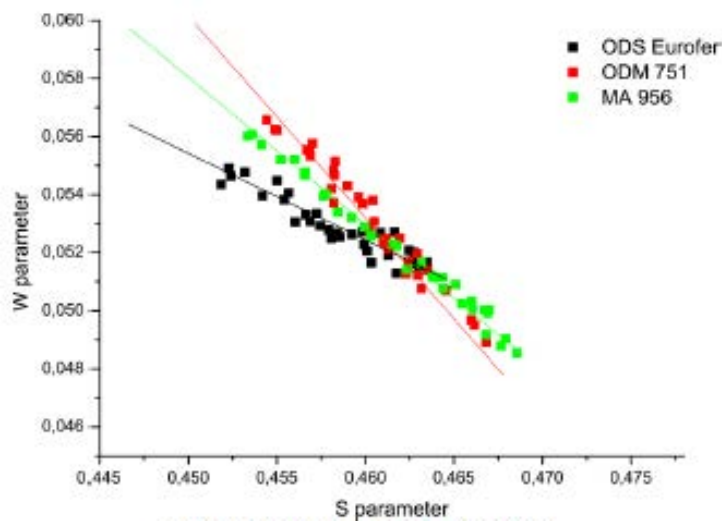


FIG.1. Behavior of S- W parameters.

The MBN data are presented by BNA values, according to which the presence of defects, residual stress or hardness for each material, respectively, can be compared. The MBN results are graphically illustrated by the signal envelope. Moreover, the shift of H_{peak} for individual samples is shown for the purpose of grain size comparison.

The BNA parameters are listed in Table 2. The highest signal amplitude - BNA was observed for ODM751, which demonstrates the lowest concentration of all structural defects (vacancies, precipitates, grain boundaries) than in ODS Eurofer and MA 957. It can also denote a lower hardness or a lower level of residual stress in ODM 751. The highest residual stress belongs to ODS Eurofer (Table 2). The smallest grains were found in MA 956. The highest H_{peak} as well as the coarsest grains were detected for ODM 751.

TABLE 2. RESULTS OF MAGNETIC BARKHOUSEN NOISE MEASUREMENTS – BARKHAUSEN NOISE AMPLITUDE (BNA) AND BNA POSITION (H_{peak}).

Sapmle	BNA (V)	H_{peak} (%)
MA 956	5,9	-25
ODM 751	14,8	16
ODS Eurofer	3,1	-3

Fig. 2 also demonstrates visible higher envelope of ODM 751, followed by for MA 956 and the smallest envelope is for ODS Eurofer.

PALS measurement was applied to three different pieces of all samples. Each spectrum was treated to yield three composite lifetimes (LT) and the average values are further presented.

The shortest lifetime-achieved values, up to 100 ps, which describes positron annihilation in defect-free structure, small defects as well as in impurities of the sample according to the Standard trapping model [22]. The second positron lifetime (LT2), within the range 200 and 250 ps, characterizes vacancy type defects and is proportional to defect size. The last lifetime (>500 ps) expresses annihilation in the air, which was not fully removed during process of source calibration.

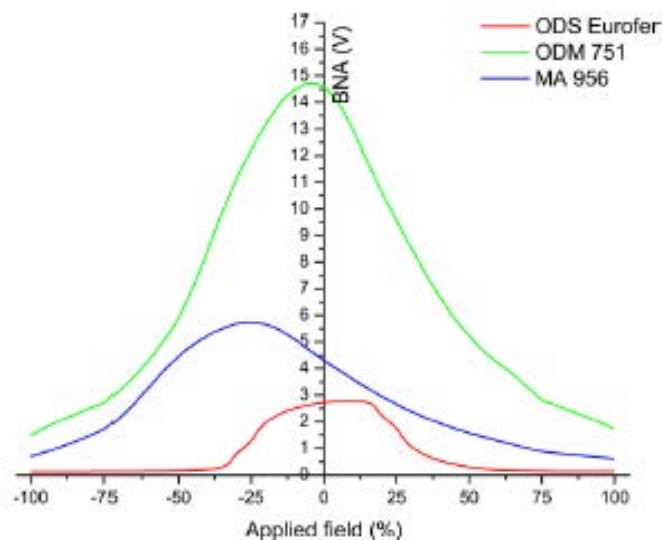


FIG. 2. The signal envelope of Magnetic Barkhausen noise for frequency up to 50 Hz (depth~1 mm).

LT2 for steel MA 956 and ODS Eurofer are almost the same. MA 956 achieved 210 ps and ODS Eurofer achieved 218 ps (see Fig. 3). ODM 751 had visible higher values of 250 ps. This signifies that MA 956 and ODS Eurofer contain defects probably with similar size of di-vacancies, although the lifetime of MA 956 has a much higher deviation. According to Δ LT2, MA 956 can also contain tri-vacancies. ODM 751 has tri- and four-vacancy clusters.

The intensities (percentages) of positron annihilation in the defects (I2) differ significantly for the investigated steels, i.e. for MA 956 ~ 60%, ODM 751 - 51% and ODS Eurofer at over 70%. The observed defects are categorical and they are formed during manufacture.

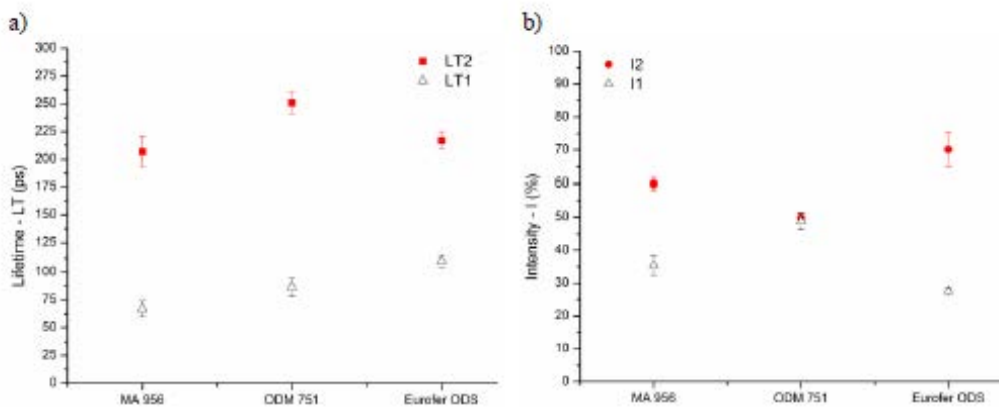


FIG. 3. Results of Positron Annihilation Lifetime Spectroscopy: Lifetimes (a); Intensities (b).

The mean lifetime (MLT) calculated as an average value from all lifetimes, referring to appertaining intensities, was the highest for ODS Eurofer (205 ps), followed by ODM 751 (180 ps). Steel MA 956 contains the smallest defects and its MLT is also the smallest at 173 ps.

4. DISCUSSION AND CONCLUSION

Positron annihilation lifetime spectroscopy, Doppler broadening spectroscopy and Magnetic Barkhausen Noise measurements were applied in the microstructural study of three commercial Oxide Dispersion Strengthened steels, MA 956, ODM 751 and ODS Eurofer. Differences in microstructure of the studied materials were found, which resulted from small variations of chemical composition, manufacturing, and probably post-manufacturing thermal treatment.

From the DBS results, the lowest defect presence was found for ODM 751. This technique studies defects up to 1,6 μ m. PALS measurements, describing defects in much deeper layers (120 μ m), also demonstrate the lowest defect density; although the defects were the largest. ODM 751 showed the presence of tri- or four-vacancies, while MA 956 contains di- or tri-vacancies while ODS Eurofer di-vacancies were in predominance.

Magnetic Barkhausen noise measurements measure the presence of all kind of defects, grain boundaries and precipitates included. The MBN results identify ODM 751 as the steel with the smallest residual stress, and show that ODS Eurofer has the highest residual stress, also proportional to hardness.

Results from all experimental techniques demonstrated that the smallest defect presence and smallest residual stress is for material with the largest defect size, namely ODM 751 (16% Cr), which was prepared by Hot Isostatic Pressing.

The differences in microstructure of the samples were caused primarily due to differences of chemical composition. The chromium content is variable in these samples, but it is not the only elemental effect on microstructure. The observed behaviour for positrons as well as magnetic measurements did not identify a dependency on chromium content. There are other influences, i.e. different processing of mechanical alloying, with ODS Eurofer (Hot Extrusion) versus Hot Isostatic Pressing of MA 956 and ODM 751. Also, the thermal treatment and post-treatment annealing can affect microstructure. It is not currently possible to isolate individual influences in microstructure from each other and describe them. In future work, a comparison of the contributions of various microstructural features to mechanical properties will be studied.

ACKNOWLEDGEMENT

Financial contributions from the IAEA (SMoRE) and VEGA 1/0129/09 are acknowledged.

REFERENCES

- [1] S. J. ZINKLE, Fusion Materials Science: "Overview of challenges and recent progress", APS Division of Plasma Physics 46 Annual Meeting, Savannah, GA, USA (2004).
- [2] C. W. HUNTER, G. D. JOHNSON, "Mechanical properties of fast reactor fuel cladding for transient analysis", ASTM STP 611 (1976) 101. ISSN 0066-0558.
- [3] R. L. KLUEH et al., J. Nuc. Mat. 341 (2005) 103.
- [4] B. A. PINT et al. J. Nuc. Mat. 307-311 (2002) 763.
- [5] R. et al., 'ODS-Eurofer – A reduced activation ferritic martensitic ODS-steel for application in advanced blanket concepts", Proc. of EUROMAT congress LINDAU, A. MÖSLANG, M. RIETH, Prague (2005). Retrieved from <http://www.extremat.org/ib/site/publication/downloads/Paper%20Lindau1.pdf>
- [6] S. EICHLER, R. KRAUSE-REHBERG, Appl. Surf. Sci. **149** (1999) 227.
- [7] R. KRAUSE-REHBERG et al., Appl. Phys. A 66 (1998) 599.
- [8] J. Slotte et. al., Phys. Rev. B 78 (2008) 085202.
- [9] K. Saarinen et al., Semiconduct. Semimet. **A 51** (1998) 210.
- [10] J. OILA et. al., Appl. Surf. Sci. **194** (2002) 38.
- [11] J. LAHTINEN et. al., Nucl. Instr. Meth. Phys. Res. **B 17** (1986) 73.
- [12] M. J. PUSKA, P. SANKU, R. M. NIEMINEN, J. Phys. Condens. Matter. **1** (1989) 608.
- [13] X. KLEBER, A. HUG-AMALRIC, J. Merlin, Metalurg. & Mater. Trans. **A 39** (2008) 1308.
- [14] M. WILLCOX, T. MYSAK, An introduction to Barkhausen noise and its applications. [online] Insight NDT. Available from: www.insight-ndt.com/papers/technical/t013.pdf [cited 22 Sept. 2010].
- [15] R. BALDEV, T. JAYAKUMAR, V. MOORTHY, S. VAIDYANATHAN, Russian Journal of Nondestructive Testing **37** (2001) 789.
- [16] Informational website of StressTech Group, [online] StressTech group. Available from: <http://www.stresstech.fi> [cited 2010 5 Sept].
- [17] V. SLUGENŇ, V. KRŠJAK, M. PETRISKA, A. ZEMAN, M. MIKLOŠ, Physica Status Solidi C 4 (2007) 3481.
- [18] V. SLUGENŇ, What kind of information we can obtain from positron annihilation spectroscopy, Report, DG JRC, Institute for Energy, European Commission, Netherlands, 2006. EUR 22468.
- [19] M. PETRISKA, A. ZEMAN, V. SLUGENŇ, V. KRŠJAK, S. SOJAK, Phys. Stat.Solidi. **C 60** (2009) 2465.

- [20] J. KANSY, Nucl. Instr. Meth. Phys. Res. A **374** (1996) 235.
- [21] P. HAUTOJÄRVI, C. CORBEL, Positron spectroscopy of solids, Amsterdam, IOS Press, 491, 1995. ISBN 90 5199 203 3.
- [22] M. J. ALINGER et al., Mat. Sci. Eng. A 518 (2009) 150.
- [23] D.T. HOELZER, J. BENTLEY, M. K. MILLER, M. K. SOKOLOV, T. S. BYUN, "Development of the advanced ODS 14YWT ferritic alloy for nuclear energy applications", In Proc. DIANA I: 1st International workshop on dispersion strengthened steels for advanced nuclear applications, Centre CNRS Paul Langevin, Aussois, France, 4 – 8 April 2011. SCK·CEN-BA-36.

DEFECT FORMATION AND BINDING ENERGIES IN FECR ALLOYS AS A FUNCTION OF CR CONCENTRATION: A SIMULATION STUDY

E. DEL RIO, J.M. PERLADO
Instituto de Fusión Nuclear
Universidad Politécnica de Madrid, Madrid
Spain

Abstract

Significant progress has been made in modelling the formation and stability of defects and clusters in Fe-Cr alloys as a function of chromium content. A new version of the CDM potential can be used in the study of defects in Fe-Cr alloys. Vacancy formation energy shows a linear dependence with the concentration for concentrations above 6% between the vacancy formation energy in iron and the vacancy formation energy in chromium, while it is almost constant for smaller concentrations. Formation energies for $\langle 100 \rangle$, $\langle 110 \rangle$ and $\langle 111 \rangle$ self- and mixed-interstitials converge to a unique value with Cr concentration independently of the starting geometry. $\langle 100 \rangle$ geometry is the more stable. A change in the stability of $\langle 110 \rangle$ interstitials is observed: Fe-Cr interstitial is more stable for concentrations below 5% Cr while Fe-Fe is the most stable for concentrations above 10% Cr. The $\langle 110 \rangle$ Fe-Fe interstitial formation energy shows a very weakly dependence on the Cr position. A strong dependency of the formation energy with the Cr position for the case of $\langle 110 \rangle$ Fe-Cr interstitials is observed and could be explained by the strong repulsion between the two Cr atoms at short distances. This is the same for the vacancy. The stability of vacancy clusters increases with the cluster size for the studied sizes (up to 5 units) and it slightly differs between both potentials for higher Cr concentrations. However binding energies are shown to be not dependent on the Cr concentration for both potentials.

1. BACKGROUND

The selection of suitable materials to be used in the future fusion and fission reactors is one of the key points in the development of these technologies [1]. Due to their high resistance to corrosion and radiation damage high-Cr ferritic/martensitic steels head the list of structural materials [2–6]. However, they present a problem of embrittlement. The addition of Cr improves the behavior of these steels under irradiation [7, 8], but not in a monotonic way. Also, these materials should be able to withstand high irradiation doses and temperatures which will change the microstructure with time. Therefore a better knowledge of the radiation induced changes in their microstructure will result in a better choice of materials in order to have the best possible safety and longer lifetime in future nuclear plants. The lack and cost, in terms of time and resources, of experimental devices able to reproduce the conditions in future fusion and fission applications makes the development and use of computational techniques very helpful and desirable to study the response to irradiation of ferritic steels [9].

Multi-scale modeling approach has been used very successfully in calculations of the defect migration energies and a satisfactorily reproduction of the resistivity recovery in pure Fe [10–12] as well as other metals [12–14] has been obtained. A similar problem has to be solved in Fe-Cr alloys as a first approximation to describe high-Cr ferritic/martensitic steels in a modeling framework. Understanding fundamental questions such as the dependence of defect formation energies on Cr concentration could help in the development of object kinetic Monte Carlo models for alloys under irradiation.

In the present work we afford the study of the effect of Cr concentration on the stability of a variety of defects in FeCr alloys at an atomistic level. Firstly, we test the feasibility of a new interatomic potential for the radiation damage study of FeCr alloys as a comparative study between two empirical interatomic potentials and DFT values reported in the literature for a variety of point defect configurations. Next, we afford the study of the effect of Cr concentration on defects stability in FeCr alloys in a wide range of concentrations. Interstitial and vacancy formation energies and vacancy cluster formation and binding energies have been studied. Finally, some calculations of the vacancy and $\langle 110 \rangle$ self- and mixed-interstitial formation energy as a function of Cr local position with respect to the defect have been performed in order to reach a better understanding of the results previously obtained.

Two different empirical potentials specially developed to describe the atomic interactions in Fe–Cr alloys have been managed in this work. One is an empirical potential based on a two band model formalism (2BM) [15] and the other one is a new version of a potential that has been created by introducing an explicit dependence on concentration (CDM) [16] and modified to better describe the relative energy of the mixed interstitials [17]. When possible, results are compared with those obtained for DFT calculations by Olsson et al. [18].

All the calculations have been performed at constant volume, relaxing the atomic positions with a conjugate gradient algorithm [19]. Periodic boundary conditions were set for all the calculations. The size of the cell used for the calculation of the formation energies is 2000 atoms, if not otherwise mentioned. The equilibrium lattice parameter employed in the calculation of defects in Fe and Cr bcc cells is the obtained by both the CDM and 2BM potentials which is 2.855 Å for bcc Fe and 2.878 Å for bcc Cr (experimental values 2.86 Å and 2.88 Å, respectively, from Ref. [20]). This lattice parameter is adequately modified when performing the calculations with different Cr concentrations.

2. RESULTS

2.1 Testing a new Fe-Cr potential

In order to benchmark the performance of the newly developed potential against values obtained with other available methodologies, we have calculated the formation energies of a variety of point defect configurations. (For further information see refs. 17 and 21). The definition of defect formation and binding energies used in this work are the same as those in Ref. [18] in order to compare with those DFT results. Positive binding energy means attraction between the objects and reciprocally. The substitution energy of Cr in bcc Fe obtained is -0.29 eV for the 2BM potential and -0.14 eV for the modified CDM potential. DFT value is -0.12 eV. Energies for Fe–Fe interstitials and vacancy formation energy in pure bcc Fe are the same for the two potentials. The vacancy formation energy is 1.71 eV with the new version of the CDM potential and 1.72 eV with the 2BM one. Fig. 1 shows, the formation energies for Fe–Fe, Fe–Cr and Cr–Cr interstitials in pure bcc Fe for the CDM potential (Fig. 1a), the 2BM potential (Fig. 1b). Defects in bcc Cr have also been studied. Results are presented in Table 1 (Calculations were performed with cell size of 1024 atoms, except for the Cr-Cr interstitials, performed with 2000 atoms). Interactions between Cr atoms and vacancies have also been calculated. The vacancy–Cr formation energy is about 0.1 eV smaller in 2BM with respect to CDM and about 0.5 eV than in DFT. The calculations of point defects with the CDM potential have been extended to include multiple defects: we have evaluated the interactions of one and two substitutional Cr atoms with <100>, <110> and <111> interstitials and compare results with Olsson et al. DFT calculations [18].

2.2 Effect of Cr concentration

The good reliability had shown for the CDM potential in the above section permit us to apply it in the study of the effect of Cr concentration on defect formation energy.

2.2.1 Vacancy and interstitial formation energy

Vacancy and interstitial formation energies for <100>, <110> and <111> geometries for both self- and mixed-interstitials have been calculated with the new version of the CDM potential for Cr concentrations ranging from 0 to 17% Cr. Due to the influence on the formation energy not only of the number of Cr atoms but also of the distance between these Cr atoms to the defect, a large enough number of calculations for the same concentration and different Cr distribution have been performed. (For further information see ref. 17).

In the case of the vacancy all possible locations of the vacancy for a given sample of 1024 atoms have been analyzed for each concentration. The vacancy is added taken care only Fe

atoms were removed. A histogram of energies was produced for each set of samples containing the same number of Cr atoms and a Gaussian distribution function was fitted to it, providing mean energy and standard deviation. Each mean value for total enthalpy of a sample including a vacancy was then used in conjunction with the respective value of total enthalpy of the same sample without the vacancy to provide the formation energy of the vacancy and its dispersion at the given Cr concentration, as shown in Fig. 2.

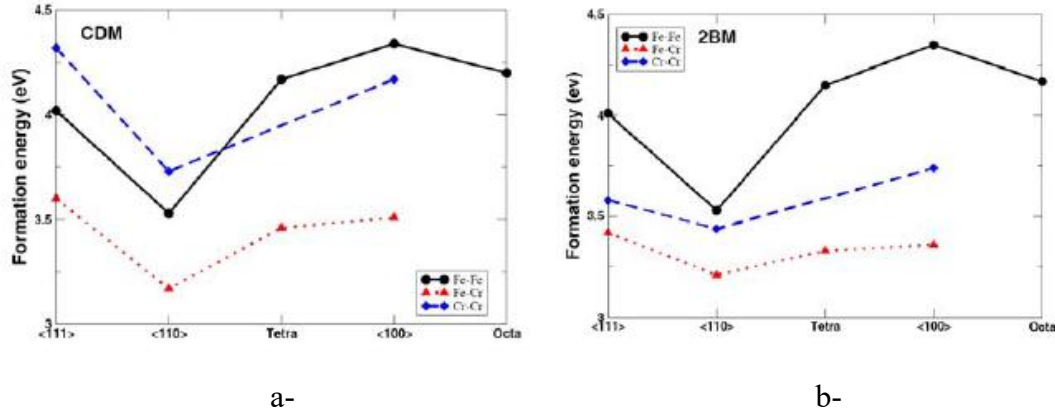


FIG. 1. Formation energies of Fe-Fe, Fe-Cr and Cr-Cr interstitials in bcc Fe for different geometries obtained with (a) the CDM potential, (b) the 2BM potential.

TABLE 1. POINT DEFECT FORMATION ENERGIES (EV) IN PURE BCC CR

Defect	E_f (eV)	E_f (eV)	PAW ^[18] NM (128 atoms)	PAW ^[18] AF (128atoms)
	CDM	2BM		
<100> _{Fe-Cr}	3.73			
<110> _{Fe-Cr}	3.72			
<111> _{Fe-Cr}	4.14			
<100> _{Fe-Fe}	3.83			
<110> _{Fe-Fe}	3.54			
<111> _{Fe-Fe}	4.10			
<100> _{Cr-Cr}	6.84	6.84	6.75	6.71
<110> _{Cr-Cr}	5.60	5.61	5.62	5.66
<111> _{Cr-Cr}	5.62	5.62	5.63	5.70
Octahedral	7.07	7.07	6.78	6.73
Tetrahedral	6.50	6.50	6.35	6.31
Vacancy	2.56	2.56	2.61	2.71

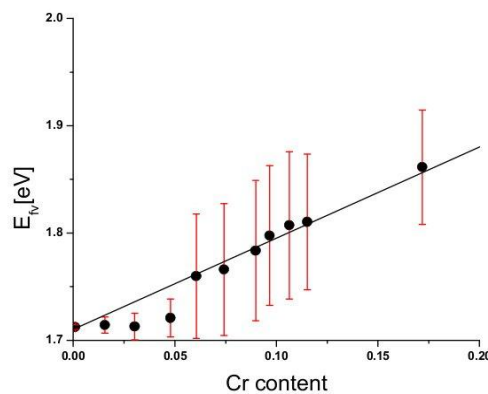


FIG. 2. Vacancy formation energy as a function of Cr content calculated with the CDM potential. Bars represent the dispersion for each concentration.

In the case of the interstitials we have performed calculations for 2000 different and randomly created samples for each concentration and different defect. In order to have the reference value of the energy to calculate the formation energy for the different defects as a function of the Cr concentration, calculations for each randomly created samples without the defect and for all the concentrations have also been carried out. $\langle 100 \rangle$ Fe-Fe, $\langle 110 \rangle$ Fe-Fe, $\langle 111 \rangle$ Fe-Fe, $\langle 100 \rangle$ Fe-Cr, $\langle 110 \rangle$ Fe-Cr and $\langle 111 \rangle$ Fe-Cr have been studied. The interstitial formation energy for each concentration is calculated as the average value of these calculations. These calculations show that with increasing Cr concentration the interstitial formation energy tends to a unique value, regardless of the interstitial. In many cases the optimized configuration did not match the start one. A program to compare the initial and optimized configurations was developed and those samples where they did not coincide were removed from the values taken into account in the average formation energy calculation. The new results show different values of the average formation energy as a function of the Cr content and for each different interstitial type. The percentage of samples used in the calculation of the average formation energy has been calculated and only $\langle 110 \rangle$ presents a large percentage of useful configurations.

2.2.2 Cr local concentration effect on the vacancy and $\langle 110 \rangle$ interstitials formation energy

We have also studied the influence of the distance between the solute Cr atoms and the vacancy and interstitial defects. In the case of the vacancy, we have firstly calculated the formation energy for four different and random Cr distributions. Minima and maxima values as a function of Cr content are represented in Fig. 3. Next, we have calculated the formation energy for Fe samples with only two substitutional Cr atoms to try to reach a better understanding of the correlation between the Cr atoms and the vacant site. For these calculations we have first fixed one of the Cr atoms in a 1st nearest neighbor (1nn) position with respect to the vacancy and move the other one to all possible positions from 1st nn to 5th nn to the vacancy, and then repeating these calculations fixing the 1st Cr atom at 2nn, 3nn, 4nn and 5nn positions with respect to the vacancy. To confirm the results observed, we have calculated the vacancy formation energy in a bcc Fe lattice with Cr atoms placed at 1st or 2nd nn positions performing calculations over the complete set of possible configurations from 1 Cr atom up to 14 Cr. In this case maxima and minima values increase almost linearly with the number of Cr atoms at 1nn or 2nn positions.

In the case of the interstitials, calculations have only been performed for the self- and mixed-interstitials with the $\langle 110 \rangle$ geometry, which has been shown as the more stable. We have calculated the interstitial formation energy in a bcc Fe lattice with one Cr atom placed at 1st or 2nd nn positions taking into account all the complete set of possible configurations. The different positions studied are shown in Fig. 4. The formation energy has been analyzed as a function of the distance between the substitutional Cr atom and the nearest interstitial atom.

Results are shown in Table 2.

2.2.3 Vacancy clusters formation and binding energies

Vacancy cluster calculations have been performed for the 2BM and the new version of the CDM empirical potentials, in order to compare the results and study the possible dependence of these results in the potential employed. Initial calculations to determine the more stable cluster geometry for each cluster size (up to a size of 5 vacancy defects), have been carried out. Only 1nn sites with respect to the vacancy in the cluster of lower size were taken into account to build the new clusters, except in the case of the divacancy where the 2nn vacancy cluster is more stable than the 1nn vacancy cluster. These calculations were performed in pure iron and four different Cr concentrations: 1, 5, 10 and 15% Cr and for 4 different Cr

distributions due to a possible effect of the local position of the Cr atoms on the defect formation energy. Once the geometry more stable for each cluster size has been determined, we have performed calculations on the effect of Cr concentration for the more stable geometries of each cluster size. Since the local position of the defect could influence the formation energy value obtained, we have explored all the possibilities of the cluster position for these geometries. Due to the large number of possibilities, these calculations were performed over smaller cell sizes of 250 atoms.

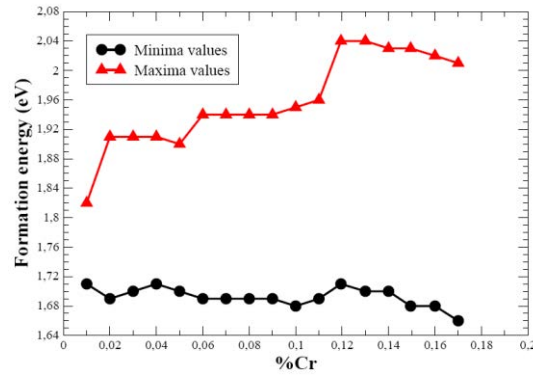


FIG. 3. Minimum and maximum values of the vacancy formation energy as a function of Cr content for random FeCr solutions.

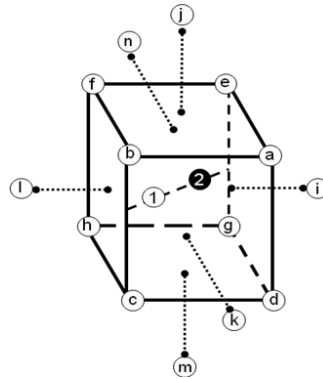


FIG. 4. One bcc Fe cell with a $\langle 110 \rangle$ interstitial. 1 and 2 are the interstitial atoms. Atom 2 can be Fe (Fe-Fe interstitial) or Cr (Fe-Cr interstitial) $1nn$ (a, b, c, d, e, f, g, h) and $2nn$ (i, j, k, l, m, n) positions are labeled with letters.

TABLE 2. FORMATION ENERGY FOR $\langle 110 \rangle$ FE-FE AND $\langle 110 \rangle$ FE-CR INTERSTITIALS FOR DIFFERENT LOCATIONS OF THE SUBSTITUTIONAL CR ATOM. D_{1-2} : DISTANCE BETWEEN INTERSTITIAL ATOMS. $D_{\text{CR SUBST-FE}}$, $D_{\text{CR SUBST-CR}}$: DISTANCE BETWEEN THE CR IN THE SUBSTITUTIONAL POSITION AND THE INTERSTITIAL ATOM LABELED AS 2, FE OR CR RESPECTIVELY

Cr_{subst}	E_f	D_{1-2}	$D_{\text{Cr subst-Fe}}$	E_f	D_{1-2}	$D_{\text{Cr subst-Cr}}$
a, e	3.47	0.740	0.721	3.85	0.709	0.799
c, h	3.47	0.740	1.302	3.16	0.714	1.301
d, g	3.42	0.737	0.927	3.29	0.712	0.958
b, f	3.42	0.737	0.927	3.29	0.712	0.958

Cr_{subst}	E_f	D_{1-2}	$D_{\text{Cr subst-Fe}}$	E_f	D_{1-2}	$D_{\text{Cr subst-Cr}}$
i, j	3.49	0.738	0.765	3.44	0.711	0.862
l, m	3.49	0.739	1.328	3.18	0.714	1.338
k, n	3.52	0.733	1.040	3.32	0.711	1.029

3. DISCUSSION

3.1 Testing a new FeCr potential

Both empirical potentials present a good agreement with the PAW value for the substitution energy of Cr in bcc Fe, although the CDM value is closer to it. Fe–Fe interstitials and vacancy formation energy in pure bcc Fe are the same for the two potentials. This is due to both empirical potentials use a very similar Fe-Fe potential [22 for the CDM potential, 23 for the 2BM potential]. Vacancy formation energy also presents a good agreement with the values obtained for the Fe-Fe potentials previously reported [22, 23] and about 0.4 eV lower than the values reported with the DFT methodology [18, 24]. It is interesting to note that DFT is a different method and its value can only be accurately reproduced if it is used in the fitting procedure in the construction of empirical potentials.

Fe-Cr mixed-interstitials are more stable than the Fe-Fe and Cr-Cr interstitials for all the studied configurations for both potentials and $\langle 110 \rangle$ geometry is the most stable for all the interstitials, in good agreement with DFT results [18] and with values reported with the 2BM potential for Fe-Cr interstitials [15]. One of the main effects of the two empirical potentials is to reduce the energy differences between the configurations in Fe-Cr interstitials (Fig. 1a and 1b) when compared with DFT values. Despite these agreements, we can also appreciate important differences between the two empirical potentials as is the case of the energy difference between the $\langle 110 \rangle$ and $\langle 111 \rangle$ Fe-Cr configurations, which is perfectly reproduced by the CDM potential (0.43 eV) and significantly decreased in the 2BM potential (0.21 eV) when compared with DFT values (0.41 eV).

Cr–Cr interstitials in bcc Fe also show important differences between the two empirical potentials under study. One of these important differences is the order of stability predicted by the two empirical potentials. In all cases, empirical potentials and DFT, the most stable configuration is the $\langle 110 \rangle$, but the $\langle 110 \rangle$ Cr–Cr is higher in energy than the $\langle 110 \rangle$ Fe–Fe with the CDM potential, in agreement with DFT results and in contrast with the 2BM value. However, the difference between the $\langle 110 \rangle$ Cr–Cr and $\langle 111 \rangle$ Cr–Cr configurations for the CDM potential is larger than in DFT, and therefore the $\langle 111 \rangle$ Cr–Cr interstitial is higher in energy than the $\langle 111 \rangle$ Fe–Fe. This also makes the $\langle 100 \rangle$ configuration more stable than the $\langle 111 \rangle$ in contrast with DFT results. 2BM values predict the same order of stability as DFT but all the three configurations are more stable than Fe–Fe self-interstitials.

Both potentials use a very similar form and parametrization for Cr–Cr interactions [25]. Therefore, the energy values obtained for the vacancy and Cr-Cr interstitials in bcc Cr are the same (Table 1). These values agree with those published by Olsson et al. [15]. The most stable geometry for all cases is the $\langle 110 \rangle$ dumbbell, as in the case of a bcc Fe matrix. However, in the case of the Fe–Cr mixed-interstitials the energy difference between the $\langle 110 \rangle$ dumbbell and the $\langle 100 \rangle$ configuration is almost negligible. This is also the case between the $\langle 110 \rangle$ and $\langle 111 \rangle$ Cr–Cr self-interstitials in agreement with DFT results and reproducing the same order of stability. It is interesting to note that the Fe–Cr and Fe–Fe interstitial formation energies in chromium are more than 1 eV smaller than Cr–Cr self-interstitial formation energies and have the same order of magnitude than these interstitials in iron.

Interactions between Cr atoms and vacancies show that there is no effect on the vacancy formation energy if the Cr is at first nearest neighbors (1nn) or second nearest neighbors (2nn) as DFT predicts. Cr atoms at third (3nn) or fifth nearest neighbors (5nn) neither show any effect on the vacancy formation energy. Interactions between Cr atoms in substitutional positions in DFT studies show that formation energies increase with the number of Cr–Cr pairs formed. This is completely reproduced by the CDM potential while the 2BM potential predicts an almost constant value. Nevertheless, the Cr–Cr pair repulsion is well captured by the two interatomic potentials [26].

The calculations of point defects with the CDM potential to evaluate the interactions of one and two substitutional Cr atoms with $\langle 100 \rangle$, $\langle 110 \rangle$ and $\langle 111 \rangle$ interstitials show that there are significant qualitative, and in some cases, quantitative agreements with the DFT results in terms of binding energies and relative stabilities of defects although the interatomic potential has not been fitted explicitly to any of these configurations.

3.2 Effect of Cr concentration

3.2.1 Vacancy and interstitial formation energy

These studies have been performed for concentrations from 0.1 to 17 at.% Cr. Although the solid solution is thermodynamically unstable for concentrations above $\sim 10\%$, the conditions used in the calculations, static or low temperature calculations, do not allow for precipitation to occur.

We should expect that in an ideal solution the vacancy formation energy would follow a direct interpolation between the pure element values. However, the formation energy in Fig. 2 deviates from the linear interpolation in the region below 6% Cr concentration, similar to the behavior of the heat of formation of the alloy. Additionally, an increase in the Cr concentration translates into an increase in the number of different possible configurations and consequently in the spread of values. This can also be translated in the larger dispersion bars at higher Cr concentrations. Furthermore, this result suggests a strong dependence of the formation energy on the relative positions of Cr atoms each other.

As it has been mentioned above, interstitial formation energy calculations show that all the values converge to a unique one regardless of the starting interstitial when all the samples are taken into account. However, if only those samples where geometry is maintained are used in the average formation energy, six different values are found. The lowest formation energy values are both for the $\langle 110 \rangle$ geometry, self- and mixed interstitials. A change in the stability of these $\langle 110 \rangle$ interstitials is observed with increasing Cr concentration: mixed Fe-Cr interstitial is the most stable for concentrations below 5% Cr, while self-interstitial presents lower energy for Cr concentration values above 10%. The percentage of samples used in the calculation of the average formation energy supports the idea of only one interstitial formation energy value with increasing Cr concentration as other geometries seem not to be stable.

3.2.2 Cr local concentration effect on the vacancy and $\langle 110 \rangle$ interstitials formation energy

It would be expected, in the calculations of the formation energy for different and random Cr distributions, the maxima and minima values will increase linearly with the concentration. In contrast, Fig. 3 shows that minima values are almost constant with the increasing Cr concentration and almost equal to the value of the vacancy formation energy in pure iron, whereas maxima values increase with the Cr concentration in steps.

DFT calculations have shown [18] that the presence of a single Cr atom does not influence the vacancy formation energy and this is not influenced by the distance between the Cr atom and

the vacancy. However, we can observe three different value ranges for the vacancy formation energies when two substitutional Cr atoms are introduced in a bcc Fe cell. The first one is obtained when two Cr atoms are further away than the 2nn position with respect to the vacancy and the value is almost equal to that of the vacancy formation energy in iron (1.7 eV). There is another set of values slightly higher than the first set and that is obtained when only one of the two Cr atoms is at 1nn or 2nn position. And finally a third set of values with the highest vacancy formation energy when the two Cr atoms are in 1nn or 2nn positions with respect to the vacancy. These results imply that at least two Cr atoms must be closer than 2nn position in order to observe a significant difference in the vacancy formation energy. This could explain the behavior of the average vacancy formation energy as a function of Cr content shown in Fig. 2, where for concentrations less than 6% the vacancy formation energy is almost constant, since the probability of having two Cr atoms close to the vacancy at these concentrations is quite low. Calculations on the vacancy formation energy as a function of the number of Cr atoms at 1nn or 2nn positions show that maxima and minima values increase almost linearly with the number of Cr atoms at 1nn or 2nn positions. We can also observe that the vacancy formation energy increases from 1.7 eV when there is no Cr atom at 1nn or 2nn positions to 2.25 eV when all the 14 Cr atoms are at 1nn and 2nn (the vacancy formation energy in Cr is 2.56 eV [21]). In general, these results show a dependence of the vacancy formation energy on the Cr local concentration increasing with Cr atoms at 1nn or 2nn positions, but not being affected when the Cr atoms are further away from these positions. We conclude that the influence of the chemical nature of neighbors beyond the second coordination shell contributes with only ~10% to the total vacancy formation energy.

All of these findings are in good agreement with some experimental and DFT calculations performed by Froideval et al. [27] where they find that the alloy composition strongly influences the Cr local structure. They have also observed changes in the magnetic and structural properties of FeCr alloys with the Cr content with a distance contraction in the two first shells around the Cr atom.

Formation energy values for the $\langle 110 \rangle$ Fe-Fe interstitial are very similar for all the cases studied (between 3.42 eV and 3.52 eV) and very close to that of the formation energy in a bcc iron matrix without any Cr in substitutional position (3.53 eV). Nevertheless, the formation energy in the case of the mixed-interstitial shows a strong dependence in the position of the substitutional Cr atom. The values range between 3.85 eV and 3.16 eV, the larger value corresponding to the smaller distance between Cr atoms and the lower to the larger distance. The $\langle 110 \rangle$ mixed-interstitial formation energy is 3.15 eV. These results are in good agreement with the results for the vacancy formation energy and the change of stability in $\langle 110 \rangle$ interstitials with increasing Cr concentration.

3.2.4 *Vacancy clusters formation and binding energies*

These differences in the energies increase for larger vacancy clusters. Similar values for the 2BM and CDM potentials are found and it can be observed a greater dispersion in the values of the formation energy with increasing Cr concentration. A similar behavior is shown with the size of the cluster: the dispersion increases with the size of the cluster. This can be explained in terms of possibilities of having Cr atoms in the nearby. A large range of energy values is shown for the CDM potential, indicating a greater sensitivity to local Cr distribution for this potential. Formation energy increases with the cluster size and Cr concentration. CDM potential predicts higher formation energies than the 2BM potential and these differences are greater for higher Cr concentrations. Also, the change in the formation energy with Cr concentration is smaller with the 2BM potential than with the CDM potential.

Very similar results are obtained for the binding energy with both potentials. The binding energy increases with the cluster size. Small increases in the binding energy are observed for 3 and 5 vacancy clusters with respect to the 2 and 4 vacancy clusters respectively. On the other hand, whereas a little increase in the formation energy with Cr concentration is observed, the binding energy shows no dependency on the Cr concentration.

4. CONCLUSIONS

Main conclusions that can be outlined from the work described above are:

- The new version of the CDM potential can be used in the study of defects in FeCr alloys.
- Vacancy formation energy shows a linear dependence with the concentration for concentrations above 6% between the vacancy formation energy in iron and the vacancy formation energy in Chromium, while it is almost constant for smaller concentrations.
- Formation energies for $\langle 100 \rangle$, $\langle 110 \rangle$ and $\langle 111 \rangle$ self- and mixed-interstitials converge to a unique value with Cr concentration independently of the starting geometry. $\langle 100 \rangle$ geometry is the more stable. A change in the stability of $\langle 110 \rangle$ interstitials is observed: Fe-Cr interstitial is more stable for concentrations below 5% Cr while Fe-Fe is the most stable for concentrations above 10% Cr.
- Cr concentration has to be high enough in order to have a high probability of finding a Cr atom at 1nn or 2nn positions to show any effect in the energy.
- The $\langle 110 \rangle$ FeFe interstitial formation energy shows a very weakly dependence on the Cr position. A strong dependency of the formation energy with the Cr position for the case of $\langle 110 \rangle$ FeCr interstitials is observed and could be explained by the strong repulsion between the two Cr atoms at short distances. This is the same for the vacancy.
- Cluster vacancy formation energy studies show similar results for both CDM and 2BM potentials. However CDM potential seems to be more sensitive to the Cr local concentration and differences in the formation energy values are more appreciable with the Cr concentration and the cluster size.
- The stability of the vacancy clusters increases with the cluster size for the studied sizes (up to 5 units) and it slightly differs between both potentials for higher Cr concentrations. However binding energies are shown to be not dependent on the Cr concentration for both potentials.
- Experimental studies have pointed out the magnetism as a key issue to take into account when trying to explain the FeCr alloys behavior. The particular empirical potential used in this work does not contain any explicit degree of freedom of magnetic origin. However, it can provide a qualitative description of this type of behavior in FeCr systems as the strong repulsion showed by two or more Cr atoms when they are nearby.

REFERENCES

- [1] ZINKLE, S.J., Fusion materials science: Overview of challenges and recent progress, Phys. Plasmas **12** (2005) 058101.

- [2] JENKINS, M.L., ENGLISH, C.A., EYRE, B.L., Heavy-ion irradiation of α -iron, *Philos. Mag. A* **38** 1 (1978) 97.
- [3] LITTLE, E.A., STOW, D.A., Void-swelling in irons and ferritic steels: II. An experimental survey of materials irradiated in a fast reactor, *J. Nucl. Mater.* **87** (1979) 25.
- [4] LITTLE, E.A., BULLOUGH, R., WOOD, M.H., On the swelling resistance of ferritic steel, *Proc. R. Soc. Lond. A* 372 (1980) 565.
- [5] GARNER, F.A., TOLOCZKO, M.B., SENCER, B.H., Comparison of swelling and irradiation creep behavior of fcc-austenitic and bcc-ferritic/martensitic alloys at high neutron exposure, *J. Nucl. Mater.* **276** (2000) 123.
- [6] FRY, A., OSGERBY, S., WRIGHT, M., Oxidation of alloys in steam environment – A review, *National Physics Laboratory Report NPL MATC(A)* **90**, September 2002.
- [7] MAURY, F. et al., A study of irradiated FeCr alloys: deviations from Matthiessen's rule and interstitial migration, *J. Phys.: met. Phys.* **17** (1987) 1143
- [8] NIKOLAEV, A. L., Stage I of recovery in 5 MeV electron-irradiated iron and iron-chromium alloys: the effect of small cascades, migration of di-interstitials and mixed dumbbells, *J. Phys.: Condens. Mat.* **11** (1999) 8633
- [9] DUDAREV, S.L., DERLET, P. M., BULLOUGH, R., The magnetic origin of anomalous high-temperature stability of dislocation loops in iron and iron-based alloys, *J. Nucl. Mater.* **386–388** (2009) 45
- [10] FU, C.C. et al., Multiscale modelling of defect kinetics in irradiated iron, *Nature Mater.* **4** (2005) 68.
- [11] SONEDA, N., ISHINO, S., TAKAHASHI, A., DOHI, K., Modeling the microstructural evolution in bcc-Fe during irradiation using kinetic Monte Carlo computer simulation, *J. Nucl. Mater.* **323** (2003) 169.
- [12] DOMAIN, C., BECQUART, C. S., MALERBA, L., Simulation of radiation damage in Fe alloys: an object kinetic Monte Carlo approach, *J. Nucl. Mater.* **335** (2004) 121.
- [13] TERYTYEV, D. A., MALERBA, L., CHAKAROVA, R., et al., Displacement cascades in Fe–Cr: A molecular dynamics study, *J. Nucl. Mater.* **349** (2006) 119
- [14] KISSAVOS, A. E. et al., Total energy calculations for systems with magnetic and chemical disorder, *Comp. Mater. Sci.* **35** (2006) 1
- [15] OLSSON, P. et al., Two-band modeling of α -prime phase formation in Fe-Cr, *Phys. Rev. B* **72** (2005) 214119.
- [16] CARO, A., CROWSON, D.A., CARO, M., Classical Many-Body Potential for Concentrated Alloys and the Inversion of Order in Iron-Chromium Alloys, *Phys. Rev. Lett.* **95** (2005) 075702
- [17] DEL RIO, E. et al., Formation energy of vacancies in FeCr alloys: Dependence on Cr concentration, *J. Nucl. Mater.* **408** (2011) 18–24.
- [18] OLSSON, P., DOMAIN, C., WALLENUS, J., *Ab initio* study of Cr interactions with point defects in bcc Fe, *Phys. Rev. B* **75** (2007) 014110.
- [19] PRESS, W.H., TEUKOLSKY, S. A., VETTERLING, W. T., FLANNERY, B. P., *Numerical Recipes in Fortran 77: the Art of Scientific Computing*, 2nd ed., Cambridge University Press, 1992.
- [20] KITTEL, C., *Introduction to Solid State Physics*, 7th ed., Wiley, New York, 1996.
- [21] SAMPEDRO, J. M. et al., Defect energetics in Fe–Cr alloys from empirical interatomic potentials, *J. Nucl. Mater.* **417** (2011) 1050–1053.
- [22] MENDELEV, M.I. et al., Development of new interatomic potentials appropriate for crystalline and liquid iron, *Philos. Mag.* **83** 35 (2003) 3977.
- [23] ACKLAND, G. et al. Development of an interatomic potential for phosphorus impurities in α -iron, *J. Phys.: Condens. Matter* **16** (2004) S2629.

- [24] FU, C.C., WILLAIME, F., ORDEJON, P., Stability and Mobility of Mono- and Di-Interstitials in α -Fe, Phys. Rev. Lett. **92** (2004) 175503.
- [25] WALLENIUS, J. et al., Modeling of chromium precipitation in Fe-Cr alloys, Phys. Rev. B **69** (2004) 094103.
- [26] BONNY, G. et al., Numerical prediction of thermodynamic properties of iron–chromium alloys using semi-empirical cohesive models: The state of the art, J. Nucl. Mater. **385** (2009) 268.
- [27] FROIDEVAL, A. et al., Magnetic and structural properties of Fe-Cr alloys, Phys. Rev. Lett. **99** (2007) 237201

EXPERIMENTAL STUDIES OF FUNDAMENTAL MATERIALS PROPERTIES AND IRRADIATION BEHAVIOR USING SUB-SIZED SAMPLES AND MICRO-TESTING

MANUEL A. POUCHON

Paul Scherrer Institute, CH-5232 Villigen PSI

Abstract

Micromechanical testing is a powerful method to address local features within a large sample, or to test sub-sized samples. Here two major aspects are elaborated: on one hand, the change in mechanical property of an ion beam irradiated surface layer, and on the other hand, the extraction of single grains within a polycrystalline material with adjacent mechanical testing. In order to address the surface layer modification, existing data from single ion beam irradiated samples are treated in a new way. A new calculation method is envisaged in order to achieve a better understanding of the indenter response within shallow surface layers, as they appear in ion irradiations. This new analysis is performed in collaboration with KAERI, who is developing models for finite element calculations treating exactly this question. The data of two oxide dispersion strengthened (ODS) ferritic steels have been treated in a way that KAERI can validate the models. The validation is still ongoing. The single grain mechanical characterization is performed on technical austenitic steels. Knowing the grain orientation relative to the load, the relative slip plane angles are known and the corresponding Schmid factor can be determined. Therefore, the critical resolved shear stress can be experimentally determined and compared to modeling results. The experimental technique applied for the single grain testing is the fabrication of micro-pillars, followed by mechanical testing using a nano-indenter with a flat punch. Two austenitic steels were tested this way, and the corresponding data delivered to EDF, where the validation of the corresponding dislocation dynamics models is being undertaken.

1. INTRODUCTION

The two following sections shortly describe two major aspects being treated in this work, one deals with modified shallow regions within samples and the other with micro-samples extracted from samples. Both demonstrate applications of micromechanical testing. One material modifications being relevant to nuclear applications, and the other studying fundamental properties of nuclear materials.

1.1 Characterization of modified regions within a material

Advanced nano-indentation is an evolving tool which can be applied for nuclear material research. The conducted work helps to better understand the potential of this new measurement technique and to develop nuclear materials related measurements. Here especially, the mechanical characterization of an irradiated surface layer is studied, which allows a determination of the materials degradation (or enhancement) as a function of the irradiation dose. As the region being modified by radiation is very shallow (typically in the range from 500 nm to 3 μm), a direct interpretation of the mechanical response from a nano-indenter is not possible, but it has to be analyzed with a finite element based model. The method can be extended to the characterization of any thin feature, being parallel to the surface (with property gradients perpendicular to the surface), such as coatings and corrosion layers. The modeling could probably also be extend to a better characterization of features with property gradients being parallel to the surface, such as welds.

1.2 Single grain characterization for basic understanding and model validation

The second study being conducted within the SMORE program is the mechanical testing of single grains in a polycrystalline material. The motivation here is to obtain a basic understanding of the mechanical behavior within the monocrystal, without the influence of grain boundaries and with the information of the resolved shear stress for the different slip systems. This, on the other hand, helps to validate computational models treating these questions.

2. EXPERIMENTAL

2.1 Depth dependent hardness analysis of irradiated ODS steel

2.1.1 Materials

For this study two ODS materials were used. The commercial alloy PM2000 from Plansee [5,6,7] and a severely plastic deformed (SPD) version of it [8], fabricated by G. Korb. PM2000 is a Fe-based Oxide Dispersion Strengthened (ODS) steel formed by Mechanical Alloying (MA). This ODS alloy is in a class of advanced materials offering both creep-and oxidation-resistance and is used for tubing in a combined-cycle gas turbine (CCGT) heat exchanger in biomass power plants. PM2000 is a Fe – 20 at. % Cr – 5 at.% Al Cr – 0.5 at.% Ti alloy to which 0.5 at% yttria particles (about 20 nm in diameter) have been added to enhance creep performance. In order to justify a possible nuclear application, its radiation behavior is being studied in several programs. Meanwhile, the production of this alloy has been discontinued. Whereas the annealed version of PM2000 has grains in the mm to cm range, the SPD version offers grain sizes below the μm scale.

2.1.2 Irradiation of the samples

The irradiation was performed with the Tandem accelerator of the Swiss Federal Institute of Technology in Zurich[1]. In order to achieve an irradiated surface layer rather than a very thin irradiated layer below the surface where the stopping power is maximal, the irradiation was performed under different incident angles. The resulting irradiation profile is depicted in Fig. 2, as a result of a SRIM simulation and of a low resolution TEM analysis. The irradiation parameters are summarized in Table 1.

TABLE 1: IRRADIATION PARAMETERS

Ion	He	He	He	He
Energy [keV]	1500	1500	1500	1500
angle of incidence [deg]	0	37	54	66
Fluence [cm^{-2}]	$2 \cdot 10^{16}$	$2 \cdot 10^{16}$	$2 \cdot 10^{16}$	$2 \cdot 10^{16}$

2.1.3 Mechanical testing of samples by nano-indentation

Irradiation creates point defects and leads to the formation of point-defect clusters and/or dislocation loops. These additional obstacles for dislocation movement increase the yield strength and decrease the ductility of the material. Ion implantation is a convenient way for introducing irradiation damage into a material. Damage depth is only in the micrometer range as already indicated in the introduction. The depth profile of this type of damage distribution depends on the irradiation conditions and is not homogeneous. Fig. 3 shows the measured hardness for PM2000 annealed and for PM2000 SPD as a function of indentation depth. The measurements were performed with a G200 nano-indenter from MTS (today Agilent Nano Indenter G200), using the continuous stiffness mode [3] and a Vickers-tip. The continuous stiffness was measured with a superimposed sinusoidal signal of 45 Hz and 2 nm amplitude. The targeted indentation depth was $2.5 \mu\text{m}$ with a strain rate of 0.05 s^{-1} .

2.1.4 Pillar study of the austenitic steels AISI 304 and AISI 316

Micromechanical testing offers the possibility to investigate single grains, which allows us to characterize the monocrystal properties within a polycrystal. This is especially interesting to achieve a basic understanding, but also to validate computational models. In this study micro-pillars are extracted from within single grains of austenitic steels. The typical grain size is 30–50 μm , so that pillar diameters between 5–15 seem reasonable. The grains were selected from

an EBSD surface picture and each extracted pillar was assigned with its grain orientation. Therefore, with the known slip systems and the relative load to grain orientation, the resolved shear stress could easily be assigned. In the following is presented a description of the analyzed materials and a description of the experimental procedure. And finally examples of results are given.

2.1.5 Materials

2.1.5.1 SS304

This material was characterized and delivered by EDF.

2.1.5.2 AISI 316L

The material was delivered by SAARSCHMIEDE GmbH (heat no. 000735) and its composition can be found in Table 2 [9, 10].

TABLE 2: CHEMICAL COMPOSITIONS OF MATERIALS (WT%)

	Ni	Cr	Mn	Cu	Mo	Co	W	Ta	C	Si	P	B	S	N	Fe
AISI 316L	12.24	17.17	1.75	0.07	2.31	0.077	–	0.002	0.019	0.35	0.02	0.0009	0.0007	0.073	Bal.

2.1.5.3 Pillar extraction by a focused ion beam

For both materials a focused ion beam (FIB) device from Zeiss (Nano Vision) was used to extract the pillars.

2.1.5.4 Experimental procedure for AISI 304 samples from EDF

For the AISI 304 samples, it was decided that many pillars should be extracted and that the placement within the grain, plus the grain orientation should be characterized for the existing pillars. First, a lot of effort was done to find the right milling procedures and to minimize the re-deposition of material. It turned out, that the austenitic steels showed a very different behavior compared to the ferritic ODS materials, which were normally treated. Therefore, only pillars of a square $2 \times 2 \mu\text{m}^2$ cross section were first extracted to minimize the effort for the optimization cycles.

Fig. 4c shows such a pillar. In order to better control the milling deposits, for these first pillars a rather large outer trench ($22 \times 22 \mu\text{m}^2$) was excavated with a remaining inner tower. From this inner tower the final pillar was extracted, standing on a platform (remaining portion of the initial middle tower, not visible in Fig. 4c). This way the sputtered material from the ion beam could deposit in a large volume without interacting with the structure of interest, the final pillar. About 20 pillars were extracted this way.

Unfortunately, the pillar orientation and the orientation of the containing grain could not be analyzed in the electron backscatter diffraction (EBSD, also known as backscatter Kikuchi diffraction (BKD)) anymore. It turned out that the gallium ion beam used in the FIB partially modified a very shallow layer at the surface, covering the original structure underneath, thereby making it invisible to the EBSD. Fig. 4a) and b) show the top view of a triple pillar group. The green area in Fig. 4a), including the pillar surface, represents a modified ferritic structure. Fig. 4b) shows the corresponding orientation. At the time of these analyses a paper appeared, where K.E. Knippling is describing exactly this effect [4]. For these examples the approach of pillar extraction with a post-EBSD characterization turned out to be the wrong approach. The pillars were tested with the nano-indenter, but no correlation with the grain orientation was possible.

As a possible solution, a pre-characterization of the grain orientation by EBSD was conducted. In order to help assigning the right pillar positions to the corresponding grains, a grate can be introduced on the surface, or the grain structure can be etched as a guide to orientation.

For investigating the more relevant AISI 316L sample, the latter procedure was decided, described in the next section.

2.1.5.5 Experimental procedure for AISI 316L sample

As a consequence from the experience with the AISI 304 sample (section 0), it was decided to etch the sample after electro-polishing. This way the grain structure became visible in the microscope, retaining a surface quality still allowing an EBSD analysis. Fig. 5 shows the EBSD grain pattern of a selected region with the color legend indicating the grain orientations.

From Fig. 5 the best grains were selected for the study, and pillars were extracted correspondingly. Fig. 6 shows an overview of all 19 pillars with 17 of these being small pillars with a diameter of 5 μm and a height of 10 μm . Two are large pillars with a diameter of 15 μm and a height of 30 μm . The important size ratio of the two kinds of pillars allows addressing the question of size effects. Fig. 6 also indicates the grain structure which reflects the results from the EBSD study in Fig. 5.

In contrast to the study of the AISI 304 samples, it was decided (together with EDF) to fabricate cylindrical pillars and not rectangular prisms. A new method could be used with the FIB, which allowed direct annular milling and not a raster mode, where the annular shape is realized by scanning the corresponding annular cavity line-wise. The circle-wise scanning offers a better re-depositing behavior. In contrast to the rectangular prism no load concentrations are to be expected in the cylinder. With the parameters learned from the AISI 304 study, it was also decided that no special platform was to be produced, but the pillars were designed to directly reach the trench base. This way less material had to be excavated.

For mechanical testing the same nano-indenter was used, as described in 0. Instead of a Vickers or Berkovich tip, a flat diamond punch with 10 or 20 μm diameter was used for the pillars with a diameter of 5 μm and 15 μm diameter, respectively. The compression speed was 2 $\text{nm}\cdot\text{s}^{-1}$.

3. RESULTS

3.1 Depth dependent hardness analysis of irradiated ODS steel

Fig. 3 shows the hardness value ratios sensed by the nano-indenter used in this study using the mentioned CSM mode. The hardness values leading to this graph of course do not represent the effective hardness in the corresponding depth, but the hardness in the region being sensed by the indenter, addressing roughly a depth 7 times more important than the actual indenter depth. In order to find the effective hardness, a sophisticated finite element calculation is required. KAERI provided this kind of expertise by developing the corresponding models.

3.2 Pillar study of the austenitic steels AISI 304 and AISI 316L

Fig. 7 shows an example of a small pillar compression. In this case a total strain of about 14% was reached. The slip-planes are nicely visible.

Fig. 8 shows an example of a large pillar before and after compression. Also here the slip-planes are nicely visible. Here a total strain of about 7% was reached.

Fig. 9 contains the stress strain curve of a small pillar test. Obvious is the step character of the curve, indicating the critical stress for the different slip systems. Fig. 10 shows the corresponding result for one of the two large pillar tests. Also here the stepwise increase of the stress is obvious. With the known relative grain to load angle, the Schmid factor can be calculated, and the resolved critical shear stress can be expressed and compared to modeling results. This work will soon be performed in collaboration with EDF. The data of totally 19 pillars will be matched and further evaluated. The one set of un-loading and reloading cycles in Fig. 9 and the two corresponding cycles in Fig. 10 were performed intentionally to check the elasticity response of the material.

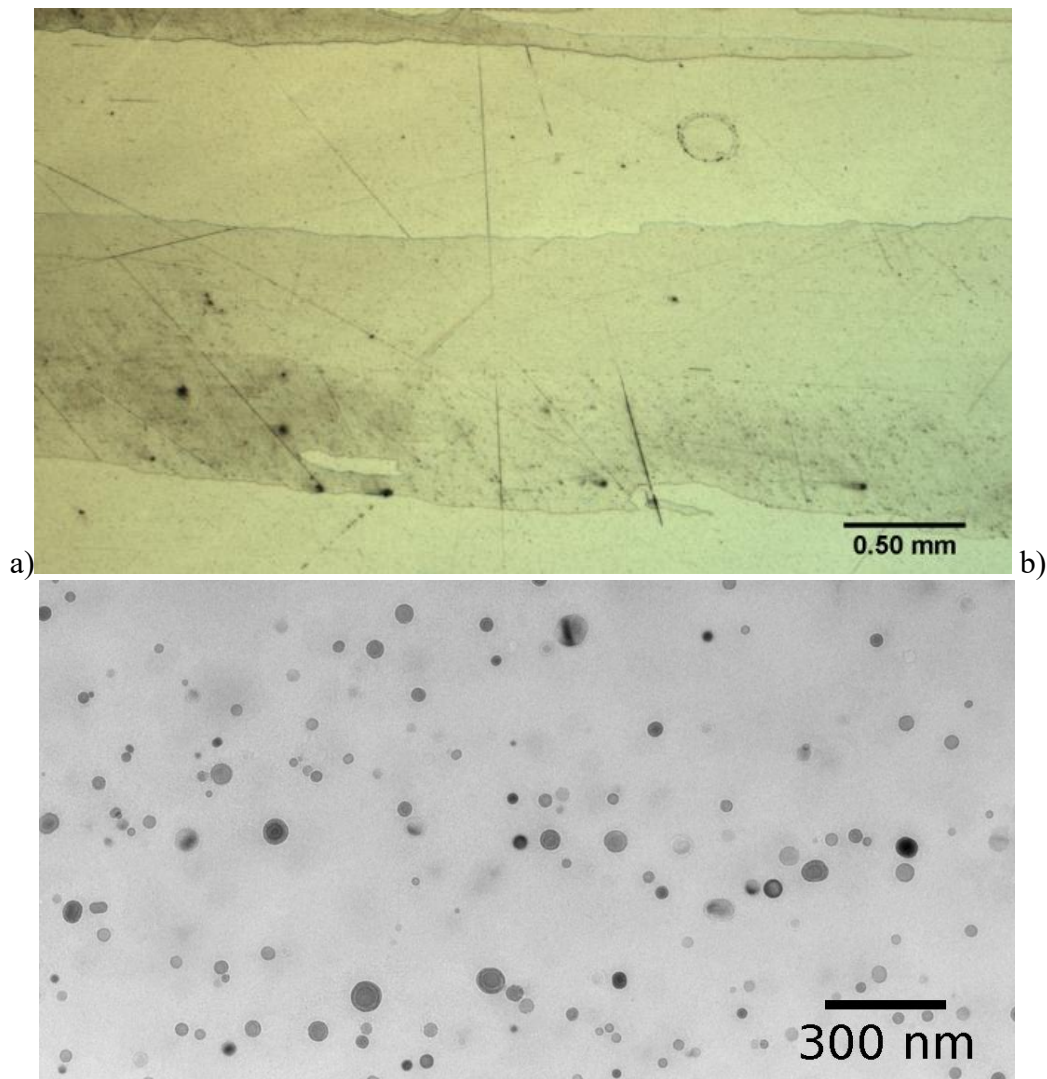


FIG. 1. PM2000 micrographs. a) grain size of annealed PM2000 b) oxide dispersions.

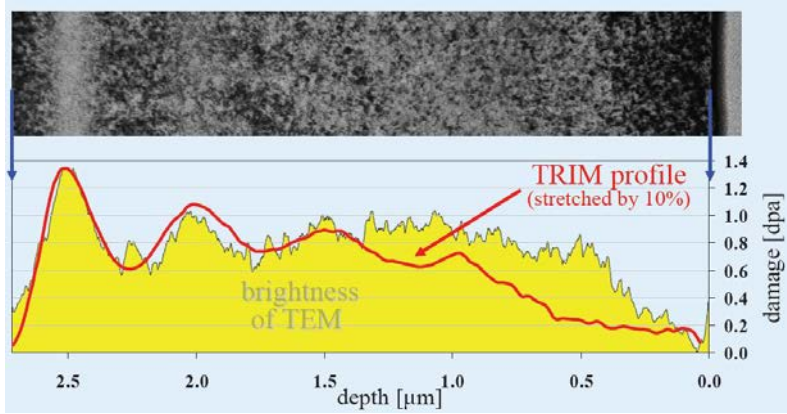


FIG. 2. Simulated irradiation profile, plus profile extracted from low resolution TEM picture.

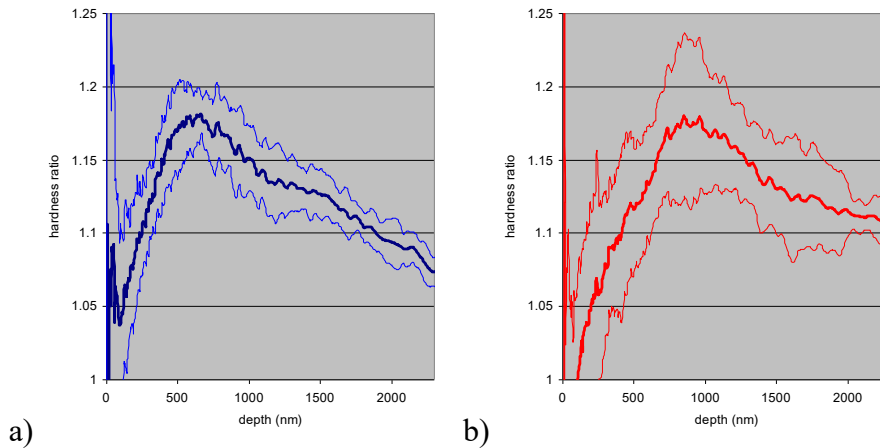


FIG. 3. Ratio of the depth-dependent hardness values of irradiated to non-irradiated samples [2] sensed by a nano-indenter using the continuous stiffness method (CSM) [3]. The depth-dependent radiation damage introduced by ion irradiation can be found in Fig. 2. a) represents the ratio for annealed PM2000 and b) for the SPD version with its micro/nanoscale grains.

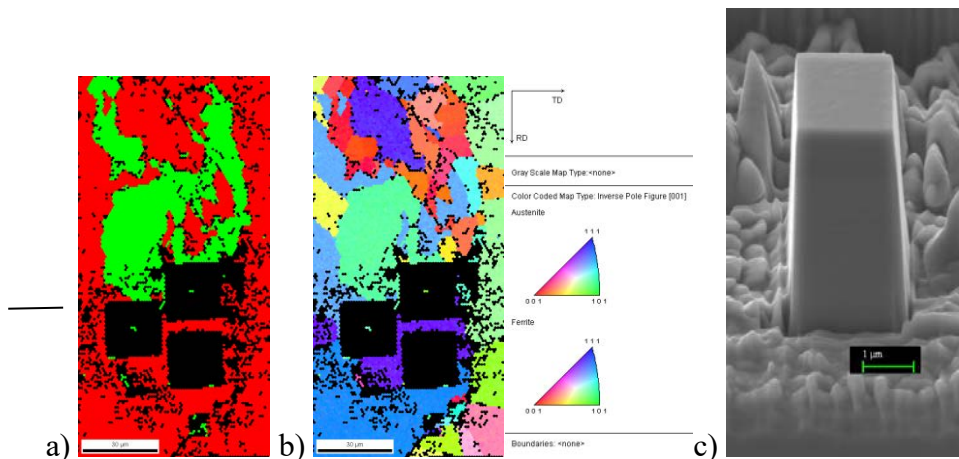


FIG. 4. EBSD of SS304L sample. The EBSD analysis with pre-cut pillars was not successful. a) shows the phase transformation into ferrite for large regions (green), whereas red represents the original austenite structure. This effect is also reported in [4] b) shows the corresponding grain orientations. c) example for a pillar.

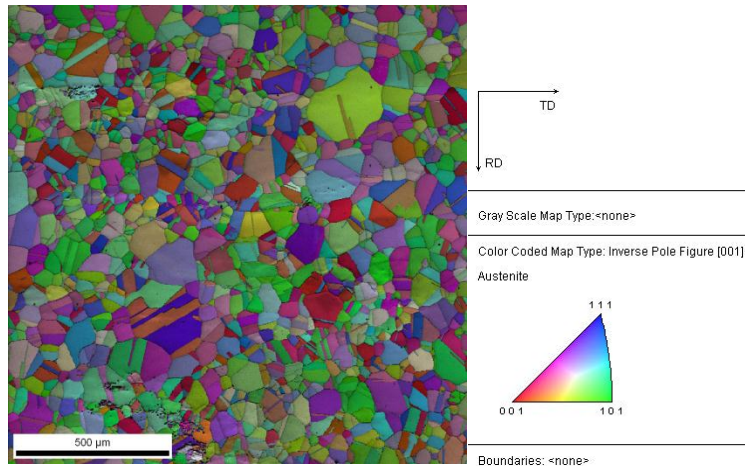


FIG. 5. EBSD pattern of SS316L sample.

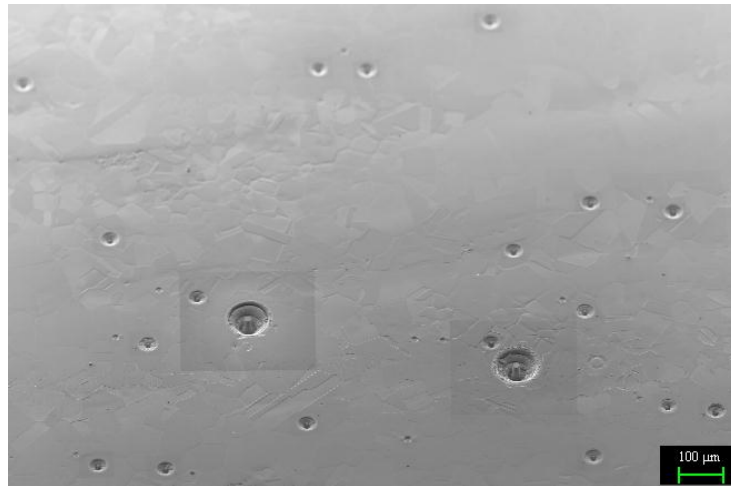


FIG. 6. Overview of pillars on SS316L sample. Clearly visible the two large pillars with $15\ \mu\text{m}$ diameter. The small pillars have a diameter of $5\ \mu\text{m}$. In all cases the aspect ratio is about 1/2 resulting in a pillar height of $30\ \mu\text{m}$ and $10\ \mu\text{m}$ respectively.

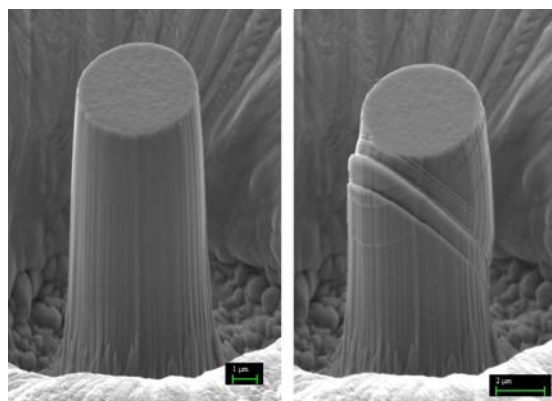


FIG. 7. Example for a small pillar (diameter $5\ \mu\text{m}$) as fabricated on the left and compressed on the right. Slip planes are easily visible. The corresponding grain orientation determined by EBSD (see FIG. 5) resulted in the following Euler angles of the surface:

$\phi_1=5.53264$, $\Phi=0.4983$ and $\phi_2=1.17641$. The compression corresponds to the stress-strain curve shown in Fig. 9.

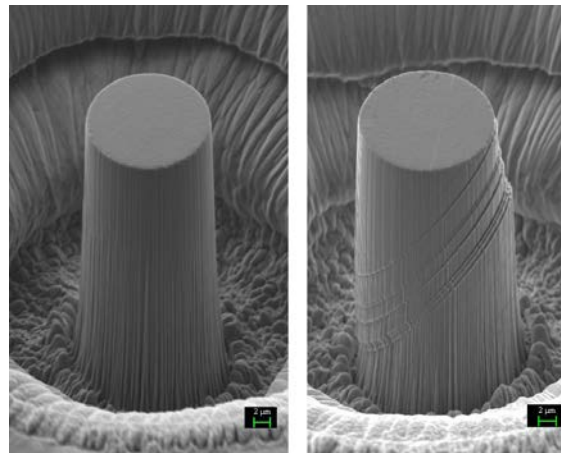


FIG. 8. Example for a large pillar (diameter 15 μm) as fabricated on the left and compressed on the right. Slip planes are easily visible. The corresponding grain orientation determined by EBSD (see FIG. 5) resulted in the following Euler angles: $\phi_1=1.40188$, $\Phi=0.43016$ and $\phi_2=4.94994$. The compression corresponds to the stress-strain curve shown in Fig. 10.

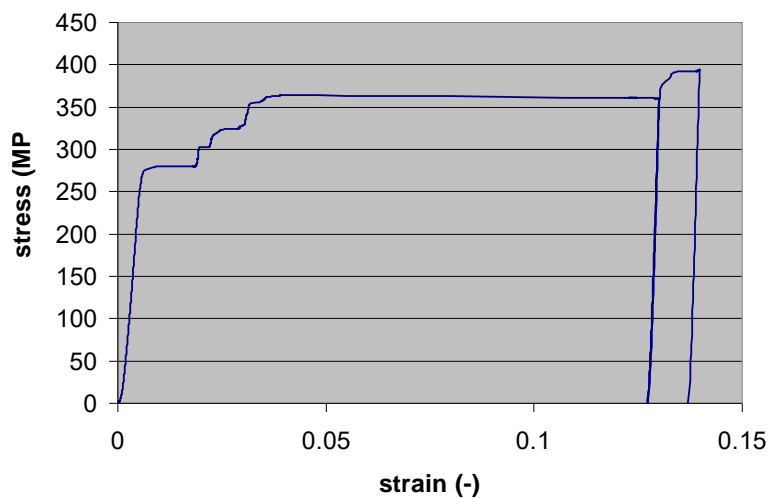


FIG. 9. Stress-strain curve for the small pillar depicted in FIG. 7.

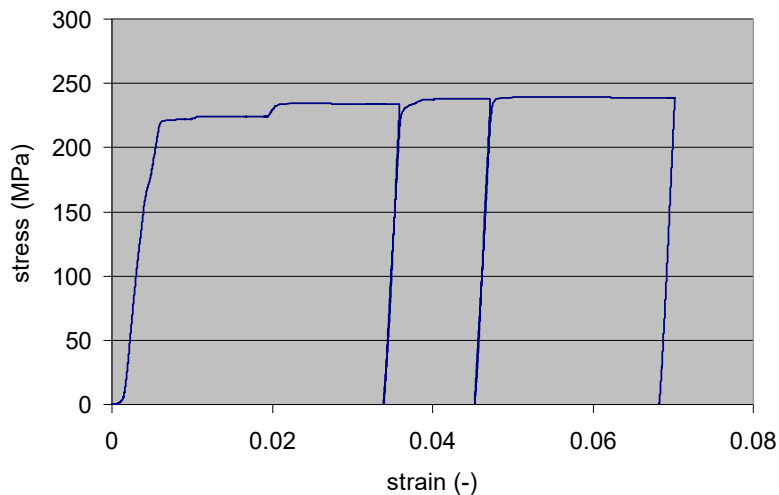


FIG. 10. Stress strain curve for the large pillar depicted in Fig. 8.

4. CONCLUSIONS

Both of the conducted studies promise interesting results. The continuous hardness analysis will open a new application of the nano-indentation technique, making it possible to characterize thin layers within a surrounding matrix. It is recommended to pursue this kind of study. In case of the single grain analysis, the comparison with modeling will show the potential of this method. With the possibility to resolve the stress levels of different slip systems in the stress-strain curve, the results look promising, and this kind of studies should also be pursued.

REFERENCES

- [1] <http://www.ams.ethz.ch/about/facilities/tandem>
- [2] M.A. POUCHON, J. CHEN, R. GHISLENI, J. MICHLER, W. HOFFELNER, Characterization of Irradiation Damage of Ferritic ODS Alloys with Advanced Micro-Sample Methods, *Experimental Mechanics*, 50[1] (2010) 79–84. (DOI:10.1007/s11340-008-9214-5)
- [3] Li X, Bhushan B (2002) A review of nanoindentation continuous stiffness measurement technique and its applications. *Mater Charact* 48:11–36
- [4] K.E. KNIPLING, D.J. ROWENHORST, R.W. FONDA, G. SPANOS, Effects of focused ion beam milling on austenite stability in ferrous alloys, *Materials Characterization*, 61, Issue 1, January 2010, Pages 1–6, DOI: 10.1016/j.matchar.2009.09.013.
- [5] G. KORB, D. SPORER, Recrystallization behaviour of PM2000 Oxide Dispersion Strengthened Iron-Base Superalloy, *High temperature materials for power engineering, 1990: proceedings of a conference held in Liège, Belgium, 24–27 September 1990, Part 2*, p. 1417–1442
- [6] Dispersion-Strengthened High-Temperature Materials /Material properties and applications, Prospectus from Plansee. 2003, 706 DE.04.03(1000)RWF.
- [7] A. CZYRSKA-FILEMONOWICZ and B. DUBIEL, Mechanically alloyed, ferritic oxide dispersion strengthened alloys: Structure and properties, *Journal of Materials Processing Technology*. 1997, v. 64 (1-3), p. 53–64.
- [8] A G. KORB, EU FW6 Project EXTREMAT, samples received (2006).

- [9] J. CHEN, M. RÖDIG, F. CARSUGHI, Y. DAI, G.S. BAUER, H. ULLMAIER, The tensile properties of AISI 316L and OPTIFER in various conditions irradiated in a spallation environment, *Journal of Nuclear Materials*, **343**, Issues 1–3, 1 August 2005, Pages 236–240, ISSN 0022-3115, 10.1016/j.jnucmat.2004.10.168.
- [10] HERBERT SCHROEDER, WANPEI LIU, Dependence of the tensile properties of 316 L parent material and welds on implanted hydrogen and/or helium, *Journal of Nuclear Materials*, **191–194**, Part B, September 1992, Pages 776–780, ISSN 0022-3115, 10.1016/0022-3115(92)90577-8.

SIMULATION AND STUDIES OF HIGH DOSE RADIATION DAMAGE IN CORE STRUCTURAL MATERIAL WITH THE USE OF CHARGE PARTICLE ACCELERATORS AND HIGH-TECH INSTRUMENTATION

V. VOYEVODIN, V. BRYK, O. BORODIN, A. TURKIN, N. LAZAREV, G. TOLSTOLUTSKAYA
National Science Center “Kharkov Institute of Physics and Technology”
1, Academicheskaya Str, 61108 Kharkov, Ukraine
Email: voyev@kipt.kharkov.ua

Abstract

Problems of life extension for working nuclear reactors and development of new-type reactors require that a lot of data be obtained about behavior of fuel and core structural materials under irradiation. Now, as part of several basic material science programs such data are being generated using charged particles accelerators. This report overviews the work performed at NSC KIPT as its contribution to the SMoRE CRP of the IAEA, to carry out a comprehensive program of simultaneous irradiation by self-ions and by helium and/or hydrogen ions of ferritic, ferritic-martensitic and austenitic steels. These alloys are attractive for use in advanced reactors, with our work focusing on high doses, high temperatures and both low-gas producing concepts and moderate to high-gas producing concepts. In this report we focus on three of our accomplishments, the first involving the development and use of triple ion irradiation to study the simultaneous introduction of displacement damage, helium and hydrogen on void swelling of austenitic steel, and the application of the results to provide a predictive swelling equation for application to VVER internals. Second, we focus on demonstrating that even in the absence of helium and hydrogen, ferritic-martensitic steel EP-450 and an ODS variant of the steel will swell significantly when irradiations are conducted to hundreds of dpa, but that ferrite grains begin to swell earlier than do tempered martensite grains. Third, we present results of some of our fundamental studies directed toward interaction and trapping of helium and hydrogen by radiation-induced microstructural sinks.

1. INTRODUCTION

The development of materials for operation in unique conditions of irradiation and the evaluation of their radiation resistance consist in the use of existing irradiation facilities for determination of mechanisms of radiation damage and selection of materials with high radiation resistance. These experiments may be carried out either under neutron irradiation in existing nuclear reactors or by irradiation with charged particles that generate radiation damage similar to that expected in a reactor of modern or next generation design.

NSC “Kharkov Institute of Physics and Technology (KIPT) is involved in the field of simulation and investigation of radiation damage using accelerators of charged particles. Such charged particle irradiations provide a low-cost method for conducting valuable radiation effects research in absence of, or as a precursor to, verification experiments conducted in reactors.

2. RESULTS

2.1 Modernization of laboratory equipment and facilities, development of improved methods of irradiation and experimental examination

H/dpa ratios are completely variable, with the two gases coming to rest in the specimen volume selected for microscopy extraction of swelling data, as shown in Fig. 1. A hollow guide source introduces 40 keV He and 40 keV H₂ ions into the 1.8 MeV Cr ion beam at a point just upstream of the specimen holder. The 40 keV H₂ ions break into two separate 20 keV H ions as they impinge on the specimen surface. The “ESUVI” electrostatic accelerator with external injector of 1.8 MeV chromium ions is used to produce hundreds of dpa at a depth of 100 nm from the ion-incident surface. The depth characteristics of ion deposition and damage are shown in Fig. 2. The near-surface region was chosen for analysis to avoid the well-known effect of the injected interstitial deeper in the foil. Additionally, at very high dpa levels the deposited Cr ions can significantly change the composition, providing another reason for avoiding the deeper portions of the ion range.

The irradiations are conducted on one TEM specimen at a time with a very stable non-rastered beam. The region under examination experiences a dpa rate of 1×10^{-2} dpa/sec. The

temperature of the specimen is maintained in balance between beam heating and electrical heating, controlled to $\pm 1^\circ\text{C}$ by a thermocouple.

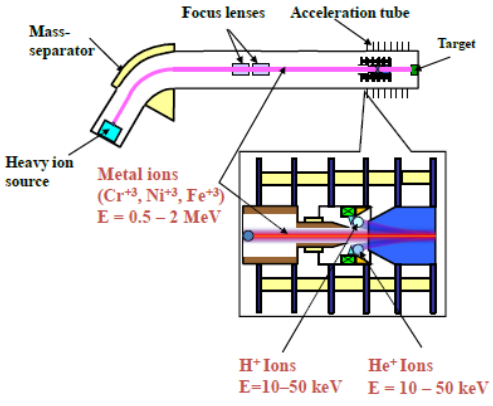
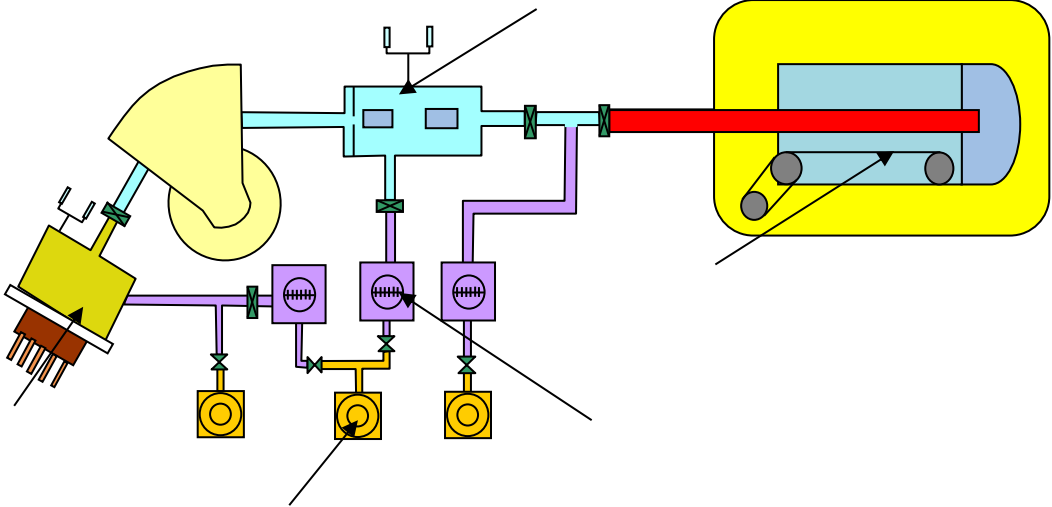


FIG. 1. ESUV-1 accelerator and the hollow ion guide source of helium and hydrogen ions.

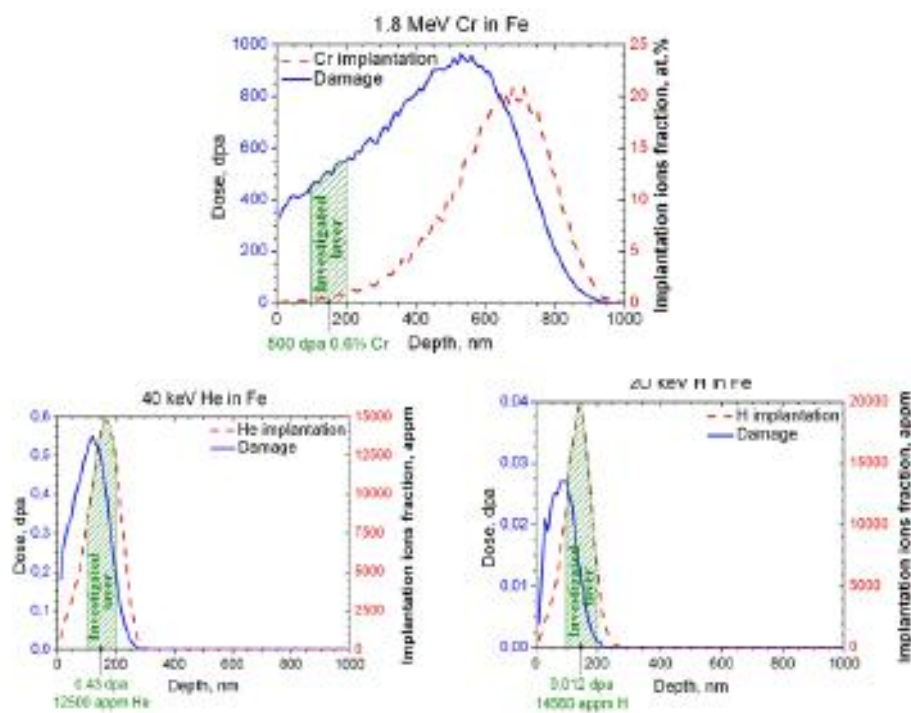


FIG. 2. Dose-deposition characteristics of Cr, He and H ions, showing region chosen for examination to avoid any strong effect of the injected interstitial on void nucleation. The interstitial also alters the local composition at high dpa levels. In the figure above 20% Cr has been added at the location of peak deposition.

In support of ion irradiation studies, a thermal desorption mass-spectrometry technique for simultaneous measurement of helium and hydrogen evolution was developed using the “ANT” facility. Graduation of mass-spectrometers by the method of calibrated leakage allows us to obtain absolute values of gas release rates with accuracy $\pm 15\%$. The sensitivity on partial gas pressure is $\sim 4 \cdot 10^{-8}$ Pa or 10^{10} atom of analyzed gas. Also, the measuring system “ESU-2” allows the use of various ion beam analysis techniques, including Rutherford backscattering spectroscopy (RBS) and nuclear reaction analysis (NRA). Other high-tech instrumentation used are electron microscopes JEM-100CX and JEM-2100 for transmission and scanning microstructure investigations; X-ray micro-analyzer Link systems 860 for microchemical investigations; ion slicer for cross section production.

2.2 Study of porosity development on damage formation and simultaneous implantation of helium and hydrogen into austenitic stainless steel 18Cr10NiTi

18Cr10NiTi steel in the solution annealed state with composition 0.08C, 18.2Cr, 10.4Ni, 0.2Ti, 1.2Mn, 0.3Si, wt. % was used in this study. This steel has been used to construct the baffle-ring in Ukrainian VVER nuclear power plants.

Specimens in the form of 3 mm diameter disks of 0.2 mm thickness were irradiated with 1.8 MeV Cr^{3+} ions in the accelerator ESUVI. The specimens for electron microscopy studies were thinned on both sides, choosing the layer at a depth of 100–200 nm from the incident surface for analysis. The choice of this layer was specified first by the necessity of minimizing the effect of the surface, and second to avoid the influence of a high concentration of implanted chromium atoms which exert a chemical effect, and also act as injected interstitials which tend to strong reduction in void nucleation [1–3].

Mechanisms of porosity development during simultaneous implantation of helium and hydrogen into 18Cr10NiTi were investigated over a wide range of temperature. Conditions chosen were 1000 appm He and 2000 appm H introduced during irradiation to 50 dpa. At 600°C under irradiation only by chromium ions porosity develops with mean size 33 nm and density $\rho = 1 \times 10^{15} \text{ cm}^{-3}$ as shown in Fig. 3.

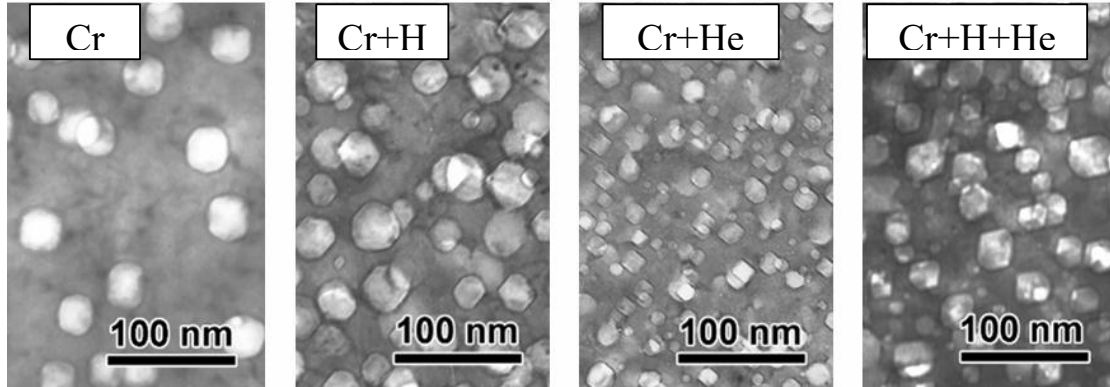


FIG. 3. Microstructures of 18Cr10NiTi after ion irradiation at 600°C with simultaneous implantation of helium and hydrogen (50 dpa Cr^{3+} , 1000 appm He, 2000 appm H) [4]

Irradiation of specimens with co-implantation of helium causes a higher void concentration and decreases the size of voids (mean size of 27 nm and density $\rho = 7 \times 10^{15} \text{ cm}^{-3}$). Hydrogen coinjection also increases the void density and swelling at this temperature, but addition of both He and H together at 600°C does not have a synergistically larger effect on swelling, as shown in Fig. 4 The greater refinement of void concentration by helium compared to that by hydrogen is thought to reflect the relative immobility of helium relative to the larger mobility of hydrogen.

The most important effect of either gas is observed at irradiation temperatures below 600°C, where voids cannot be nucleated without gas. It is known that the injected interstitial effect exerts its greatest influence on void nucleation at lower temperatures, especially at very high rates. It is thought that the two gases help to overcome the suppressive effects of both the surface and the interjected interstitial in the region examined by microscopy.

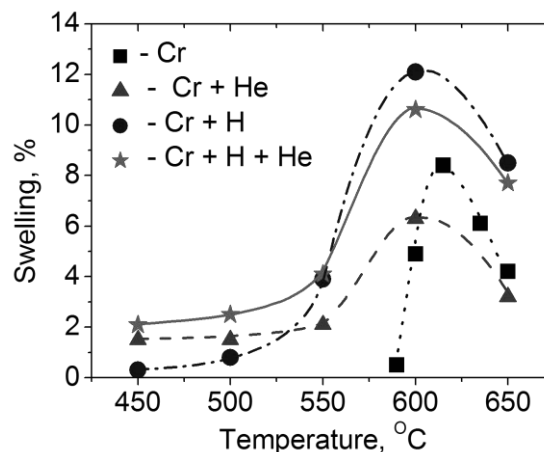


FIG. 4. Swelling versus temperature for various irradiation conditions, showing that the greatest effect of either gas lies at temperatures below ~600°C [4].

2.3 Prediction of swelling of 18Cr10NiTi austenitic steel over a wide range of displacement rates

Using heavy-ion irradiation at very high dpa rates (10^{-2} and 10^{-3} dpa/s) and doses (5-100 dpa) and coupling the results to available neutron data, a swelling equation within the framework of a single empirical model has been developed that specifically incorporates the effect of dpa rate on void swelling [5].

Swelling maps constructed from this model permit forecasting of the behavior of the steel in the baffle-former assembly of VVERs under the required irradiation conditions, not only at already attained exposure doses, but more importantly to higher dose levels that will be reached following plant life extension. We have recently completed such a forecast [6].

We obtain the following mathematical relationship for swelling of the 18Cr10NiTi steel:

$$S = (0.25 - 0.022 \ln k) \cdot \varphi(D - 103 + 0.1T - 2.6 \ln k) \cdot \exp \left\{ -\frac{(T - 690 - 15.5 \ln k)^2}{2 \cdot (12.3 - 1.9 \ln k)^2} \right\} \quad (1)$$

where S is swelling in %, D is the damaging dose in dpa; T is the irradiation temperature in °C; k is the dose rate in dpa/s; and the function $\varphi(x)$ is defined by expression: $\varphi(x) = x \cdot \theta(x)$

$$\text{where } \theta(x) = \begin{cases} 1, & x > 0 \\ 0, & x \leq 0 \end{cases}$$

Fig. 5 shows predicted dose-temperature maps of 18Cr10NiTi swelling that were calculated using expression (1) at different dose rates typical of accelerator irradiation ($k = 10^{-3}$ dpa/s), fast reactor ($k = 10^{-6}$ dpa/s) and low-flux thermal reactor ($k = 10^{-8}$ dpa/s) environments.

The swelling becomes progressively larger at lower dpa rates. The generality of this phenomenon is supported by other studies on a variety of austenitic steels, such as that of Budylkin and coworkers [7] and Seran and Dupouy [8]. In every case the shortened incubation period at lower dpa rates leads to earlier, and therefore more, swelling at the lower dpa rates. In one exceptional study the 18Cr10NiTi steel when irradiated in the BR-10 fast reactor at a very low dpa rate (1.9×10^{-9} dpa/sec) was observed at 350°C to be clearly swelling after accumulating only 0.6 dpa [9].

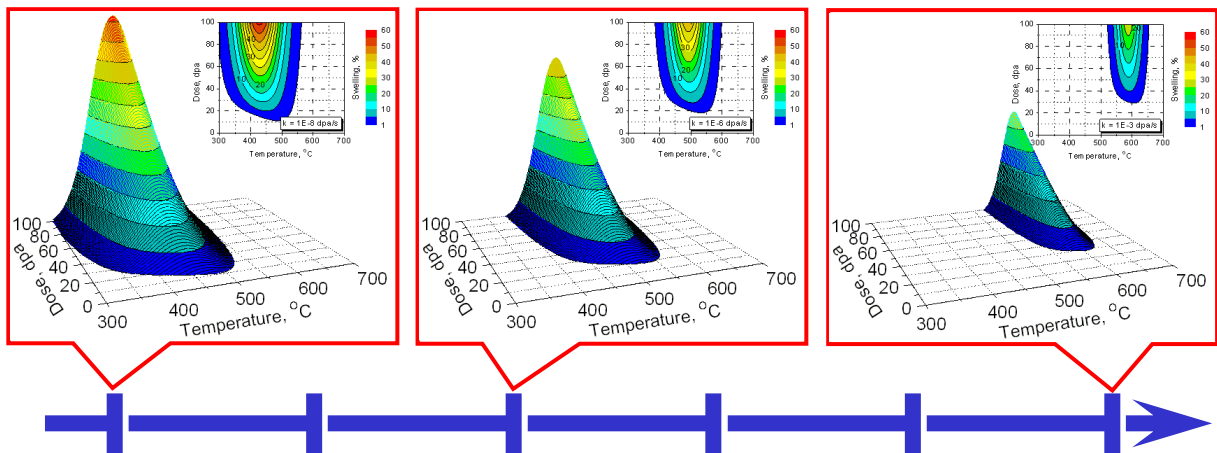


FIG. 5. Temperature-dose maps of 18Cr10NiTi steel swelling for different dose rates, calculated by a fitting function [5].

As seen in Fig. 5, with increasing dose rate at a given dose the temperature corresponding to the swelling peak shifts towards higher temperatures. This "temperature shift" is known to be due to the necessity of keeping constant the relationship between the rates of point defect formation and disappearance at sinks, so that the vacancy supersaturation level characteristic of charged particle irradiation conditions should be maintained at reactor-relevant levels [11].

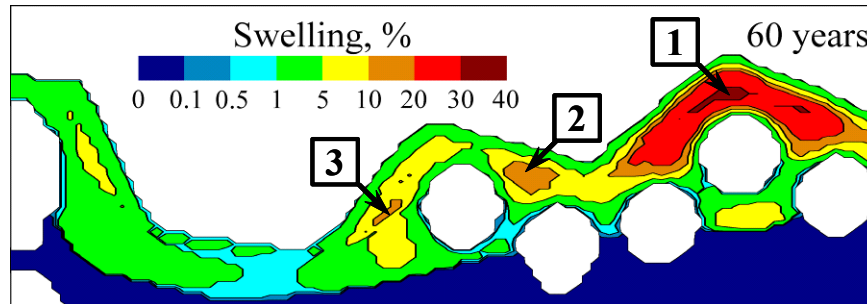


FIG. 6. Predicted swelling map of one-sixth section of VVER-1000 baffle ring after 60 years of service calculated using the derived equation [6]. Areas 1 to 3 exceed 10% swelling and are likely to be very brittle.

As shown in Fig. 6 an empirical equation incorporating both ion bombardment and fast reactor data on annealed 18Cr10NiTi steel was used to provide prediction of the spatial dependence of void swelling anticipated in the austenitic core internal components of WWER reactors, especially under conditions expected due to plant life extension [6]. This equation explicitly contains dependence not only on the dpa level and irradiation temperature, but also on the dpa rate, an approach that was not taken in earlier studies that produced equations containing no dose rate dependence.

2.4 Investigation of the effect of high dose ion irradiation on swelling in ferritic structural steels EP-450 and EP-450 ODS

EP-450 is the most studied ferritic-martensitic steel with respect to its radiation performance. It is routinely used for wrappers in both the BOR-60 and BN-600 fast reactors and was also tested in BN-350. It is duplex steel with ~50% of its grains being ferrite and the other 50% being tempered martensite. Large globular $M_{23}C_6$ carbides existed on boundaries of grains between both ferrite-ferrite and ferrite-tempered martensite, and finer carbides were observed on internal boundaries of martensitic grains. Voids have been observed in this steel under neutron irradiation at rather low levels, but data above ~80 dpa are not available [10].

In this study irradiation by Cr ions up to 300 dpa but without gas coinjection, was used for investigation of swelling resistance of EP-450. Discs with diameter 3 mm and thickness 300 μm were electropolished in an electrolyte consisting of 10% of perchloric acid and 90% ethyl alcohol to prepare an undamaged surface for irradiation. The samples were irradiated in accelerator ESUVI by Cr^{+3} ions with energy 1.8 MeV. The rate dose during irradiation was $1 \cdot 10^{-2}$ dpa/sec in the area where data would be extracted. The irradiation was carried out in the temperature range of 430 to 550°C and to doses from 50 to 300 dpa.

Increase of irradiation temperature at 100 dpa caused an increase of void size from 10 to 20 nm and a decrease of their concentration from $2 \cdot 10^{14}$ to $8 \cdot 10^{13} \text{cm}^{-3}$. Formation of porosity is observed only in ferrite at 100 dpa. Evolution of void microstructure in ferrite grains of EP-450 with increasing dose at the temperature of maximal swelling (480°C) is shown on Figs 7 and 8. Note that after 150 dpa there is an abrupt increase in swelling rate to ~0.2%/dpa.

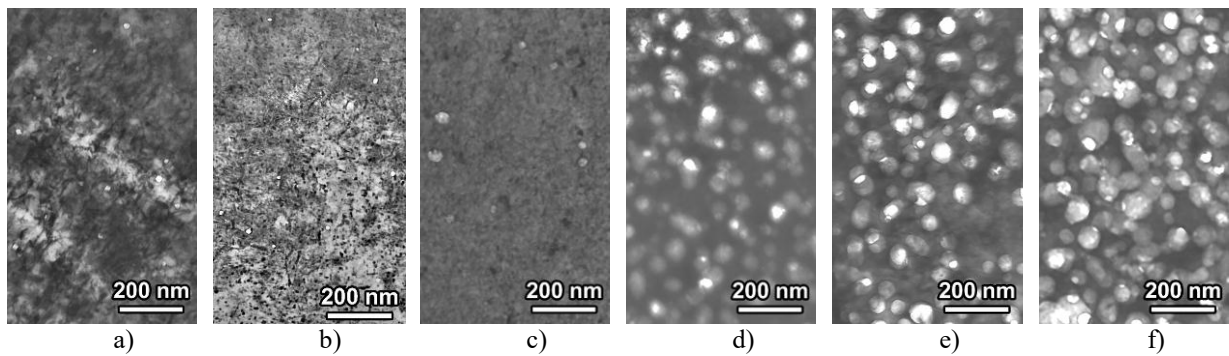


FIG.7. Microstructure of steel EP-450 irradiated at 480°C to doses of 50 (a); 100 (b); 150 (c); 200 (d); 250 (e) and 300 dpa (f).

How do we relate the results above to neutron irradiation results? It is well known that BCC-iron and ferritic alloys, at least to neutron doses of ~ 100 dpa, have an apparent “immunity” to the high rate of swelling observed in iron-base alloys with FCC-lattice ($\sim 1\%/dpa$) [12,13]. Nevertheless, the question arises if α -alloys will always have a very low rate of swelling and could the swelling of these alloys reach swelling at tens of percent under irradiation dose above 100 dpa. It was shown in papers [14, 15] that under certain conditions, such as low dose rate and cold-work, pure iron has a considerably higher rate of swelling than was considered earlier. It was established for binary alloy Fe-12Cr that the steady-state swelling rate in FFTF was $\sim 0.2\%/dpa$ [16]. It was also shown that for American steel HT-9 and for alloy Fe-9Cr-1Mo the rate of swelling in FFTF was comparable with the rate of swelling observed in pure Fe-12Cr alloy, but after a longer incubation period [16]. As to the maximum observed value of ferritic steel swelling of HT-9 at 208 dpa and 400°C the swelling increases from 1% to 2.5% for stress levels of 0 to 200MPa [17]. Therefore from neutron data alone we have no evidence that ferritic steels can reach swelling levels, $>10\%$.

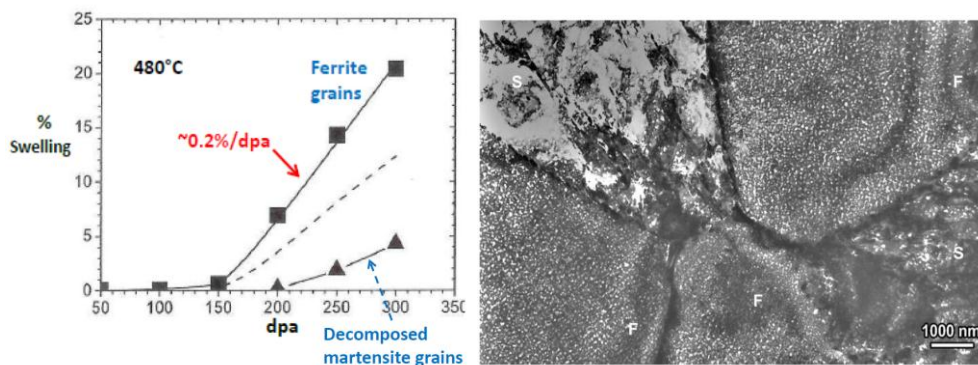


FIG. 8. Swelling vs. dose for EP-450 at 480°C without gas injection, showing swelling starts first in ferrite grains (F), with tempered martensite grains (S) swelling later, as shown at 300 dpa on the right side figure.

We are encouraged, however, that 0.2% per dpa was observed in the above-cited FFTF results but also in our ion irradiation of EP-450. Additionally, the same swelling rate was recently observed in HT9 following irradiation in our facility [18]. Therefore, we are confident that we can examine other ferritic steels to assess their swelling resistance relative to that of EP-450. The most significant finding of our study is that even a swelling rate of $\sim 0.2\%/dpa$ can lead to several tens of percent swelling at high enough dpa rates.

Ion bombardment was used successfully to explore the swelling of EP-450 ferritic-martensitic alloy and one of its ODS variants. The EP-450 ODS steel was prepared by mechanical

alloying of EP-450 powder for 30 hours with yttrium oxide powder. Unlike EP-450, all grains had only a ferritic structure with grains elongated in the direction of extrusion. Grains were of two classes; large (~30–50 μm) and fine (~0.5–2.0 μm). Yttrium oxides of size ~5–200 nm were located on boundaries and also within the grains. The oxide size inside the grains was ~5–10 nm. Grains with an increased concentration of yttrium oxides were almost always the fine grains, indicating that the dispersion was not very uniform. Fig. 9 shows comparison of ion-induced swelling at 100 dpa of EP-450 and ODS variant of EP-450, both without gas implantation. Surprisingly, the ODS variant swelled more than the non-ODS variant.

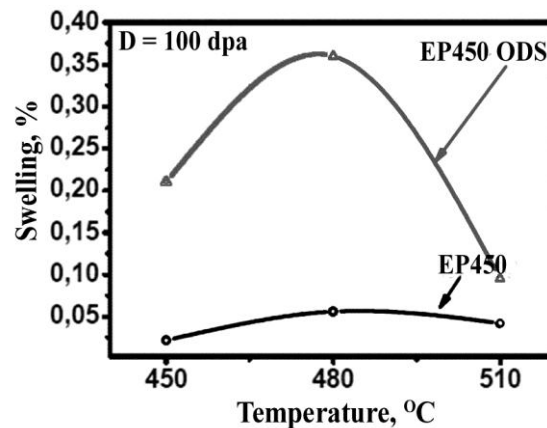


FIG. 9. Ion-induced swelling at 100 dpa of EP-450 and ODS variant of EP-450.

EP-450 is a duplex alloy, with ~1:1 ratio of ferrite to tempered martensite grains. Swelling in EP-450 starts first in ferrite grains and later in tempered martensite grains. The ODS variant, however, is composed primarily of ferrite grains. Therefore, it is not so surprising that the ODS variant might swell earlier and more than its base alloy.

2.5 Influence of pre-implanted helium and heavy ion-induced damage on deuterium trapping in austenitic and ferritic/martensitic steels using ion beam analysis techniques

We investigated the temperature intervals of helium and hydrogen retention and release from austenitic and ferritic-martensitic steels, the influence of radiation damage on accumulation and distribution of deuterium implanted in austenitic and ferritic/martensitic steels.

The implanted particle depth distribution was measured using the nuclear reaction $\text{D}({}^3\text{He,p}){}^4\text{He}$. The measurements were performed using forward and back scattering geometries. Deuterium release from stainless steel samples was investigated using the thermo-desorption mass-spectrometry technique. The microstructure of the implanted steels was examined by means of transmission electron microscopy at room temperature, employing standard bright-field techniques on the EM-125 electron microscope.

The specimens used were foils of austenitic 18Cr10NiTi (composition similar to AISI 321) and three ferritic-martensitic stainless steels EP-450 (Cr13Mo2NbVB), EI-852 (Cr13Mo2VS), and RUSFER-EK-181 (Fe-12Cr-2W-V-Ta-B). Before irradiation, the specimens were short-term annealed to either 1000°C (18Cr10NiTi) or 720°C (ferritic-martensitic steels) in an experimental chamber used for surface cleaning and degassing.

Influence of prior implantation of helium on trapping and retention of hydrogen in steel EP-450 was investigated by irradiation of specimens by helium ions with energy 12 keV to a dose of $1 \times 10^{17} \text{cm}^{-2}$, and then by hydrogen ions with energy 12 keV to a dose of $1 \times 10^{16} \text{H}_2^+ \cdot \text{cm}^{-2}$.

Argon implantation was used to obtain different levels of damage by irradiation with ions at 1.4 MeV to doses $0.5\text{--}2.5 \times 10^{17} \text{ cm}^{-2}$. By changing the angle of beam incidence on target from 0 to 60° relative to the surface perpendicular gave us the possibility to produce damage on the level of 20–200 dpa over a depth to 0–700 nm from the surface. Since Ar atoms are the closest to He atoms in their behavior in irradiated metals [19], high energy Ar ions were used to introduce, on the one hand, the high displacement damage, and on the other hand, to simulate helium effects. Deuterium (5keV/D^+) and helium are implanted perpendicular to the specimen surface.

The data analysis had showed that at high irradiation temperatures part ($\sim 30\%$) of the deuterium was trapped in the layer of defect displacement (Fig.10-curve 2). The remaining part ($\sim 70\%$) of retained deuterium is redistributed into the layer of maximum in damage and maximum of argon range profiles. Concentration of trapped deuterium in this case is two orders lower in comparison with 100% capture, but larger compared with deuterium only (Fig. 10, (curve 1)). Rutherford backscattering spectroscopy combined with channeling showed that the higher damage correlates with the area of depth between maxima of defects and ranges.

Investigation of the microstructural evolution of argon implanted steel after irradiation at different temperatures showed that bubble formation was clearly observed (Fig. 11).

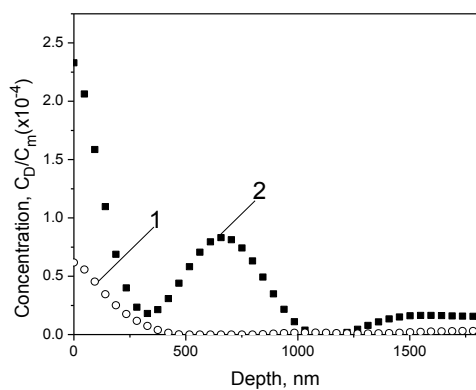


FIG. 10. Distribution profiles of 5 keV deuterium at 400°C to $1 \times 10^{17} \text{ cm}^{-2}$ (1) and simultaneously with 1.4 MeV argon ions to $7 \times 10^{16} \text{ Ar/cm}^2$ (2) in steel EP-450.

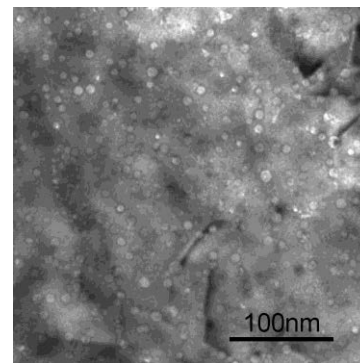


FIG. 11. Microstructure of EP-450 steel irradiated with 1.4 MeV argon ions at 400°C with $7 \times 10^{16} \text{ Ar/cm}^2$.

The amount of retained hydrogen (deuterium) was increased several times by the damage in the case of prior irradiation by argon ions. After annealing the temperature of depth profile evolution became higher ($\sim 200^\circ\text{C}$) compared with that of not-damaged sample (Fig. 12).

Recently it was shown that pre-implantation of helium produced additional traps for deuterium, and shifted the temperature range of its release from stainless steel 18Cr10NiTi from 20–300 to 200–600 $^\circ\text{C}$ [20]. Formation of helium bubbles in 18Cr10NiTi steel increased the retained deuterium by one order of magnitude in the range 20–300 $^\circ\text{C}$.

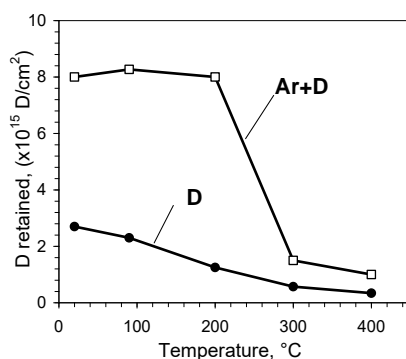


FIG. 12. Retention of deuterium implanted to $1 \cdot 10^{16} \text{ cm}^{-2}$ in EP-450 steel without and with pre-implantation of $5 \cdot 10^{16} \text{ Ar/cm}^2$.

Thermal desorption of ion implanted hydrogen from ferritic-martensitic steels was studied by irradiation at T_{room} only with hydrogen to $1 \times 10^{16} \text{ H}_2^+/\text{cm}^2$ and under irradiation of specimens first by helium ions to $1 \times 10^{17} \text{ He}^+/\text{cm}^2$ and then followed by hydrogen ions to $1 \times 10^{16} \text{ H}_2^+/\text{cm}^2$ (Fig. 13).

A desorption stage at around 20—300°C is typical in specimens without helium irradiation Fe-Cr based alloys, but this stage appeared at around 500°C, unique to ferritic-martensitic steels [21]. Pre-implantation of helium produced additional traps for deuterium and shifted the temperature range of its release. It is seen at this helium level in EI-852 steel, that up to temperatures of ~200°C, gas release is negligible, and only above this temperature does the hydrogen release start (see Fig. 13a), with a maximum rate of release near 350°C. For specimens implanted with H_2^+ gas release at temperatures higher than 800°C was actually caused by hydrogen release from the chamber components.

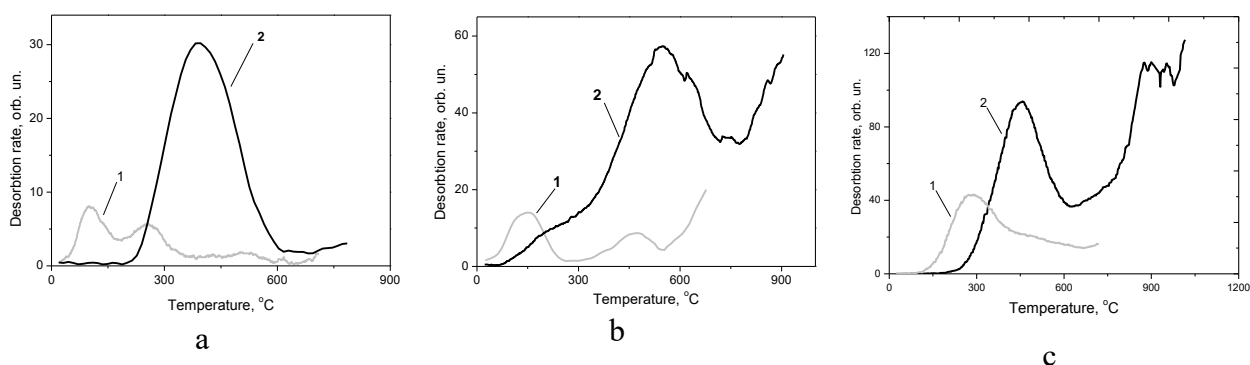


FIG. 13. Spectra of hydrogen thermal desorption from specimens of EI-852 (a), EP-450 (b) and EK-181 (c) irradiated at T_{room} only by hydrogen to dose $1 \times 10^{16} \text{ H}_2^+/\text{cm}^2$ (curve 1) and from specimens previously irradiated by helium ions to $1 \times 10^{17} \text{ He}^+/\text{cm}^2$ and then by hydrogen ions to $1 \times 10^{16} \text{ H}_2^+/\text{cm}^2$ (curve 2).

In this report we do not discuss some characteristic properties observed in spectra of thermal desorption for each studied steel. We will only note the common feature: gas evolution in the case of irradiation only by hydrogen starts practically at room temperature, has one wide (purely resolved) spike or two spikes in the region of temperatures 30—500°C. The main evolution occurs at annealing at temperature 300°C. Pre-implantation of helium shifted the temperature range of deuterium release. This shift moves to 300°C in EP-450, 200°C in EI-852 steel and 150°C in EK-181.

Therefore, helium and heavier ion implantation into austenitic stainless steel 18Cr10NiTi and ferritic-martensitic stainless steels EP-450, EP-852 and RUSFER-EK-181 causes the

formation of traps which retain hydrogen isotopes to temperatures of around 300°C. The interaction between deuterium and deuterium ion- and argon ion-induced displacement damages (~40 dpa, <20 appm/dpa) is not strong as compared with inert gas bubbles. Formation of inert gas bubbles in deuterium implanted steels increases the amount of retained deuterium by a factor of several times in the temperature range 20–600°C.

2.6 Kinetic modeling of He/H trapping in F/M steels

Controllable gas desorption from materials is the important method of studying the ability of a material to absorb and retain the gases. The experiments on the gas desorption are carried out in the following way: the annealing of samples with the linear or stepwise dependence of temperature on time is performed, and the residual gas in the material or the gas yield from the material as a function of time is controlled. This method is sensitive to the material structure on the atomic and microstructural level. The trapped gas is thermally released from the traps upon heating and diffuses to the specimen surface.

The problems of gas desorption are usually considered in the following formulation [22]. The gas atoms are able to diffuse comparatively fast with the diffusion coefficient D in the defect-free crystal. There are point and extended defects (vacancies, dislocations, grain boundaries, precipitations of new phases, etc.) in the bulk which can trap the gas atoms due to the positive binding energy E_b^k between the gas atom and the k -type defect. In other words, the crystal defects are traps for a gas, and their strength is determined from the solution of a separate problem of attaining equilibrium distribution of gas atoms in the vicinity of a certain trap resulting from the balance of gas atoms absorbed and emitted from this trap:

$$\frac{\partial C_F}{\partial t} = D\Delta C_F + \sum_k v_k(T)C_B^k - \beta DC_F \sum_i (C_{Tr}^k - C_B^k) \quad (2)$$

$$\frac{\partial C_B^k}{\partial t} = \beta DC_F (C_{Tr}^k - C_B^k) - v_k(T)C_B^k \quad (3)$$

where C_F is the concentration freely migrated gas, C_B^k is the concentration of k traps with gas, C_{Tr}^k is the total concentration of k -type traps, β and v_k are kinetics coefficients. The volume fraction of traps is assumed to be small in the mentioned type of approach.

The system separation on the defect-free region and the traps loses its sense in the case of highly defected crystals. The theory of the diffusion processes in disordered structures is applied for the solution of this problem. The master kinetic equations of the hopping diffusion which allow for the impossibility of more than one particle in the site are formulated based on this theory. As a result, a passage to the limit of the continuous medium we get a diffusion equation in partial differentials with diffusion coefficients which are determined self-consistently.

It was shown that if the particles of just one type diffuse, then the prohibition of the transition to the occupied site does not change the type of the diffusion in any structures, including the topologically disordered ones with the symmetrical over the sites transition probabilities, i.e. at $W_{nm} = W_{mn}$. Since the only reason of the onset of the concentration dependence of diffusion is the asymmetry of the transition frequencies from one site to the other and back or, in other words, the scatter of the energy levels of different sites, then the simplest model of the structure valid for the considered problem is the model of the lattice with random traps.

Fig. 14 shows the evolution of gas concentration in system with discrete distribution of traps on energies. Fig. 15 shows temperature dependence of gas flux for two different widths.

The obtained results can be used for theoretical modeling of accelerator irradiation experiments and description of radiation damage in high dose structural steels, and to analyze the mechanisms of helium influence on radiation behavior in the investigated alloys.

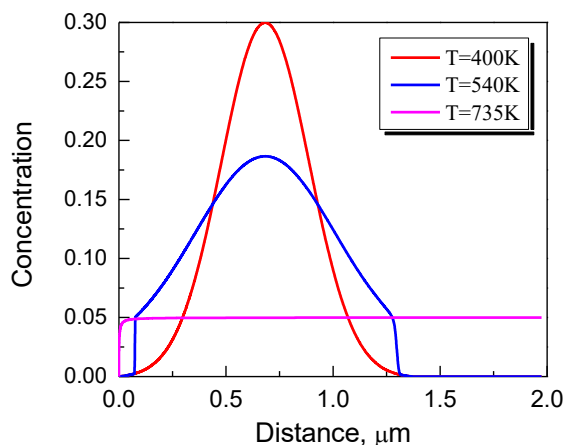


FIG. 14. Evolution of gas concentration in a film with discrete distribution of traps on energies.

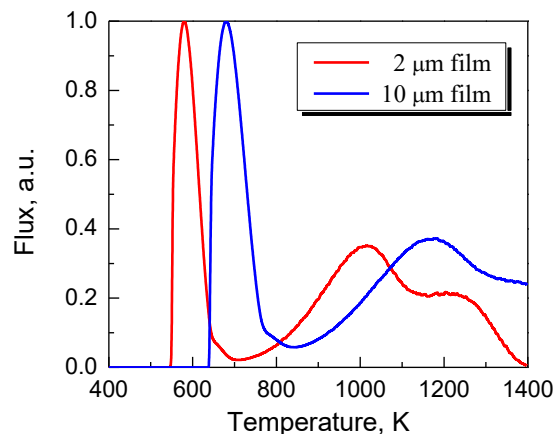


FIG. 15. Temperature dependence of gas flux over free external surface for films with two different widths (discrete trap distribution).

3. CONCLUSIONS

A system of irradiation by three ion beams was designed, fabricated and put into operation using the electrostatic accelerator with external injector of ions “ESUVI”. Irradiated specimens were examined using the modernized “ANT” plant with the thermal desorption mass-spectrometry technique and electrostatic accelerator “ESU-2” with ion beam analysis techniques. Improved methods were developed that increased the accuracy of the obtained results.

Employing simulation by heavy-ion irradiation it has been demonstrated that with a decrease in dose rate toward levels characteristic of WWERs, the temperature regime of swelling for 18Cr10NiTi steel will get broader and show a shift of the swelling peak toward lower temperatures. Increased swelling at lower dpa rates develops primarily from a decrease in the incubation period of swelling and an apparent increase in the post-transient swelling rate. Increases in irradiation temperature were found to decrease the post-transient swelling rate.

These findings were used to develop a swelling equation to predict the distribution of swelling in the very thick VVER baffle ring. On the basis of the developed empirical equation relatively large levels of swelling are anticipated to occur in the WWER baffle ring, especially at dose levels to be reached following plant life extension. Such information is crucial in making decisions concerning extended operation of WWERs, with or without replacement of the internals.

A study of porosity development during damage formation and simultaneous implantation of helium and hydrogen into austenitic stainless steel 18Cr10NiTi showed that void nucleation and swelling are suppressed in absence of gas injection at lower temperatures. Helium

injection leads to enhanced void nucleation at all temperatures examined, but depresses swelling somewhat at higher temperatures. Hydrogen injection is also very effective to nucleate voids, but exhibits different behavior with temperature, reflecting its higher mobility compared to helium.

The most significant results from this study concern the swelling of BCC alloys at very high dpa levels. It is shown that swelling of steel with BCC structure may reach 20% or higher. The Russian steel EP-450 can swell strongly, even in the absence of He and H injection. Ferrite grains begin to swell earlier than tempered martensite grains, but both eventually swell. The steady-state swelling rate appears to be $\sim 0.2\%/dpa$, similar to that observed in Fe-Cr binary alloys in the EBR-II and FFTF fast reactors. The ODS variant of EP-450 swells earlier and more than the non-ODS variant, probably due to its all-ferrite grain structure.

The damage created by heavy ion irradiation and pre-implantation of helium exert influence on the processes of trapping and accumulation of isotopes of hydrogen, especially deuterium, in austenitic steel and ferritic-martensitic stainless steels EP-450, EP-852 and RUSFER-EK-181. Such damage causes formation of traps which retain hydrogen isotopes to temperatures of around 300°C. Formation of inert gas bubbles increases the amount of retained deuterium in deuterium-implanted steels by several times in the temperature range 20—600 °C.

A physical model describing the kinetics of gas desorption from materials with arbitrary trap distribution has been formulated. A numerical algorithm has been developed for solving the underlying equations.

4. RECOMMENDATIONS

Works performed under the Project SMore 14935/RO are proposed to be continued in the following directions:

1. Study of the effect of different compositions and distributions (ferrite, tempered martensite) in the radiation behavior of steels of ferritic-martensitic grade.
2. Selection of the optimal composition of dispersion-strengthening precipitates in ferritic-martensitic steels.
3. Study of mechanisms of stability of dispersion-strengthening precipitates.
4. Influence of helium and hydrogen on stability of strengthening precipitates.

REFERENCES

- [1] F.A. GARNER, *J. Nucl. Mater.* **117** (1983) 177–197.
- [2] E. H. LEE, L. K. MANSUR, and M. H. YOO, *J. Nucl. Mater.*, **85 & 86** , 577–581 (1979).
- [3] D. L. PLUMTON and W. G. WOLFER, *J. Nucl. Mater.*, **120**, 245–253 (1984).
- [4] O. V. BORODIN, V. V. BRYK, A. S. KALCHENKO, V. V. MELNICHENKO, V. N. VOYEVODIN, F. A. GARNER, "Synergistic effects of helium and hydrogen on self-ion-induced swelling of austenitic 18Cr10NiTi stainless steel", accepted for publication in *J. Nucl. Mater.*, Proc. ICFRM-15.
- [5] A.S. KALCHENKO, V.V. BRYK, N.P. LAZAREV, I.M. NEKLYUDOV, V.N. VOYEVODIN, F.A. GARNER, *J. Nucl. Mater.* **399** (2010) 114–121.
- [6] A.S. KALCHENKO, V.V. BRYK, N.P. LAZAREV, V.N. VOYEVODIN and F.A. GARNER, "Prediction of void swelling in the baffle ring of WWER-1000 reactors for service life of 30–60 years", accepted for publication in *J. Nucl. Mater.*
- [7] N.I. BUDYLKIN, T.M. BULANOVA, E.G. MIRONOVA, N.M. MITROFANOVA, S.I. POROLLO, V.M. CHERNOV, V.K. SHAMARDIN and F.A. GARNER, *J. Nucl. Mater.* **329–333** (2004) 621–624.

- [8] J. L. SERAN and J. M. DUPOUY, Effects of Radiation on Materials: 11th Int. Symp., ASTM STP 782, 1982, pp. 5–16.
- [9] S.I. POROLLO, A.M. DVORIASHIN, YU.V. KONOBEV, A.A. IVANOV, S.V. SHULEPIN and F.A. GARNER, *J. Nucl. Mater.* **359** (2006) 41–49.
- [10] A. M. DVORIASHIN, S. I. POROLLO, YU. V. KONOBEV and F. A. GARNER, *J. Nucl. Mater.* **329–333** (2004) 319–323.
- [11] L.K. MANSUR, *Nuclear Technology* **40** (1978) 5–34.
- [12] Proceedings of the Thirteenth International Conference on Fusion Reactor Materials (ICFRM-13) Nice, France, December 10–14, 2007, *J. Nucl. Mater.* **386–388** (2009) pp. 1–1110.
- [13] O.V. BORODIN, V.N.VOYEVODIN, V.F.ZELENSKYI, I.M.NEKLYUDOV, *Physics of metals and metal science*, 1996, **81**, # 3.
- [14] S.I. POROLLO, A.M. DVORIASHIN, A.N. VOROBEEV, *J. Nucl. Mater.* **256** (1998) pp.247–253.
- [15] N.I. BUDYLKIN, E.G. MIRONOVA, V.M. CHERNOV, V.A. KRASNOSELOV, S.I. POROLLO, F.A. GARNER, *J. Nucl. Mater.* **375** (2008) 359–364.
- [16] F.A. GARNER, M.B. TOLOCZKO, B.H. SENCER, *J. Nucl. Mater.* **276** (2000) pp.123–142.
- [17] M.B. TOLOCZKO, F.A. GARNER, C.R. EIHOLZER, *J. Nucl. Mater.* **212–215** (1994) 604–607.
- [18] F.A. GARNER, O.V. BORODIN, V.V. BRYK, A.S. KALCHENKO, V.V. MELNICHENKO, V.N. VOYEVODIN, "Ion-induced swelling of HT9 to 600 dpa", manuscript submitted to *J. Nucl. Mater.*
- [19] N. MAROCHOV, P.J. GOODHEW, *J. Nucl. Mater.* **158** (1988) 81–86.
- [20] G.D. TOLSTOLUTSKAYA, V.V. RUZHYTSKIY, I.E. KOPANETZ, S.A. KARPOV, V.V. BRYK, V.N. VOYEVODIN, F.A. GARNER, *J. Nucl. Mater.* **356** (2006) 136–147.
- [21] D. HAMAGUCHI et.al, *J. Nucl. Mater.* **386–388** (2009) 375–378.
- [22] McNABB, P.K. FOSTER, *Trans. Met. Soc. AIME* **227** (1963) 618.

ION BEAM IRRADIATIONS ON STRUCTURAL MATERIALS FOR NUCLEAR APPLICATION

PETER HOSEMANN, NUCLEAR ENGINEERING, UC BERKELEY

Stuart A. Maloy MST-8 Los Alamos National Laboratory

Other contributors: D. Kiener, E. Stergar, Y. Wang, M. Pouchon, C. Hofer, A.M. Minor

1. INTRODUCTION

This Report is a summary of all activities at UCB and LANL related to the SMORE program organized by the IAEA. In the following chapters results of the ion beam irradiations conducted during the participation of LANL/UCB on the program are presented. This report is organized in different chapters according to the different activities started during the SMORE program. The focus of the UCB/LANL work is to perform ion beam irradiation on candidate structural materials, as well as basic simple materials to understand the effects of ion beam irradiation leading to a path-forward to use these techniques for accelerated materials testing and “pre-screening” of materials which can be used in nuclear applications.

The work presented here is centered around small scale mechanical testing after irradiation to gain property changes on materials due to ion beam irradiation needed to compare to neutron irradiation data. Also, it allows investigation to what extent these novel techniques can be useful to study large neutron irradiated materials so that less radioactive material need to be handled while gaining additional data to enhance the statistical value. As a result of these activities, UCB/LANL started several national and international collaborations on this topic since SMORE meetings led to new contacts in the community. In the last chapter these new collaborations are discussed based on the proposals submitted to the funding agencies.

1.1 Project 1: Ion beam irradiation on simple materials (single crystal) to evaluate the small scale materials testing technique and ion beam damage

One of the key techniques to evaluate material's property changes after accelerated materials testing in an ion beam is mechanical property testing in the ion beam irradiated areas. However, these small scale testing techniques are novel and complicated, and a detailed evaluation needs to be conducted in order to understand what it is that is truly sampled and what is the smallest sample size one can reliably test. In the following several experiments are performed on simple materials (single crystal Cu) to gain a better understanding what is actually measured. In the following, three experiments are briefly described that were conducted to get a fundamental insight into this type of Post Irradiation Examination (PIE).

1.1.1 *Issues to consider using nano-indentation on shallow ion beam irradiated materials*

Ion beam irradiation is a widely used method to cause radiation damage in materials in order to study materials degradation under radiation in a laboratory setting. Nano-indentation has become an often-used tool to measure the mechanical property changes due to ion beam irradiation. While the combination of ion beam irradiation and nano-indentation is a powerful tool, difficulties arise and need to be discussed in detail. This work intends to draw attention to the potential issues one might face if nano-indentation is used to evaluate radiation induced hardening, especially if compared to other mechanical tests such as yield strength from tensile tests on irradiated materials and others.

In this work we focus on issues associated with size and dose effects associated with quasi-static nano-indentation on shallowly irradiated Cu [100] single crystal material. It is shown that on irradiated material that is 1 μm deep it is not possible to correlate a single dose to a specific hardness value, rather a dose range has to be considered. However, deeper indents will always sample contributions of the unirradiated material. Moreover, the correlation between the indentation hardness and macroscopic properties is not straight-forward. While it

is a valuable tool to assess the qualitative change of materials properties due to the ion beam irradiation, it is rather difficult to extrapolate macroscopic properties such as yield strength and work hardening rate based on these measurements. In fact, one has to be particularly careful of how the data is analyzed, since a range of effects can contribute to the actual data gained as described in the introduction chapter.

A single crystal Cu sample was used in a 200keV proton irradiation at room temperature. For this experiment the Danphysik ion implanter located at Los Alamos National Laboratory was used. Half the sample was irradiated with protons while the other half of the sample was shielded by a Cu foil. The sample was mounted on a large temperature-controlled Cu block ensuring that the irradiation temperature stayed below 50°C. A thermocouple mounted on the Cu block was monitored during the entire experiment. The sample was mounted on the Cu block using silver paste, ensuring good thermal conductivity. The total beam current was 11uA/cm² while the experiment lasted a full day. A total dose of ~1dpa in the near area surface was achieved. The dose was calculated using SRIM-2008.04 code.

After irradiation the sample was tested using the Hysitron indenter at the CINT user facility at Los Alamos National Laboratory. Several indents to different indentation depths were performed (see Fig. 1). The indents were performed in a depth-controlled mode in quasi-static condition using a load rate of 20nm/sec. For each depth, 15 indents were performed to gain good statistical data. The Hysitron data analysis tool was used and the area function was gained on fused silica in accordance with the Hysitron manual procedure. The hardness vs. depth indentation curves are presented in Fig. 1. It is obvious in this figure that at a depth of 200nm the hardness of the irradiated material is significantly higher than in the unirradiated region of the sample.

Note: This work was submitted and accepted in 2011 for publication in the Journal of Nuclear Materials; JNM-D-11-00257R1, by P. Hosemann, D. Kiener, Y. Wang, S.A. Maloy

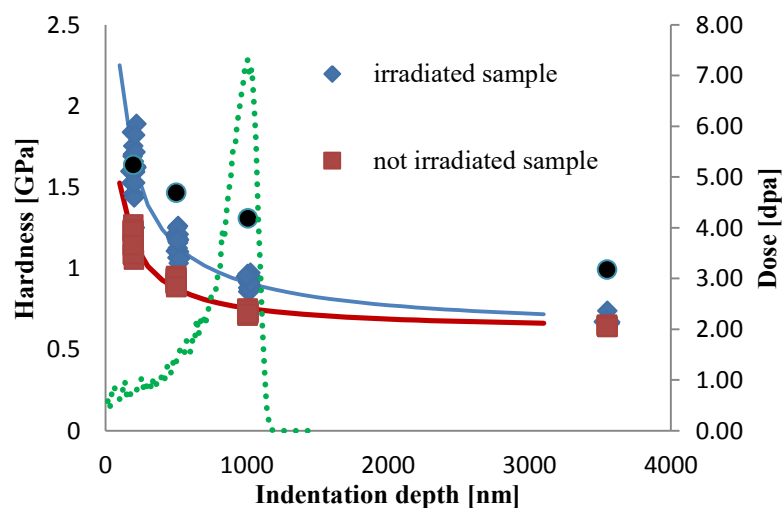


FIG. 1. The hardness vs. depth indentation curves.

2. ION BEAM IRRADIATION ON A CU SINGLE CRYSTAL AND POST-IRRADIATION INDENTATION IN CROSS SECTION WITH A DETAILED ANALYSIS OF THE INDENTS IN A TEM

Previously, several publications were written where cross section nano-indentation was conducted in order to assess the change in hardness as a function of dose induced by ion beam irradiations. Several experiments were made where 1–2 MeV proton-irradiated materials

(ODS steels, HT-9, Ta, etc.) were characterized using cross section nano-indentation to examine surface effects, dose variations, etc. However, many fundamental questions are still unsolved using this technique developed by P. Hosemann, especially on how to correlate them to macroscopic properties.

In the past it was assumed that the "size effect" is the same in the irradiated and unirradiated region, and therefore size effect studies were conducted in order to correlate the nano-scale hardness measurements to the macroscopic properties. Also, surface effects were neglected while it was not known the volume of material actually being sampled using this technique. A summary of the overlapping effects found in surface nano-indentation can be seen in the introduction technique chapter.

Therefore a basic study was conducted in order to verify the results on a clean pristine sample. Single crystal Cu was irradiated using 1 MeV Protons for 30h (reaching ~1 dpa), while cross section nano-indentation was conducted afterwards. The new FIB techniques allow cutting TEM foils from specific locations leading to the fact that one is able to cut TEM foils from the cross section indents. This information will allow us to understand better what is it that we are truly sampling and thereby allow us to put the gained information into FEM models.

Fig. 2 presents the results gained from the cross section nano-indentation experiment. It can be seen that the first three rows of indents are located in the irradiated part of the material. Indent 4 and higher are in the not-irradiated region. A significant hardness increase can be seen in these results. It has to be noted that the hardness increases from row 1 to row 3, which is probably due to the increased dose with depth.

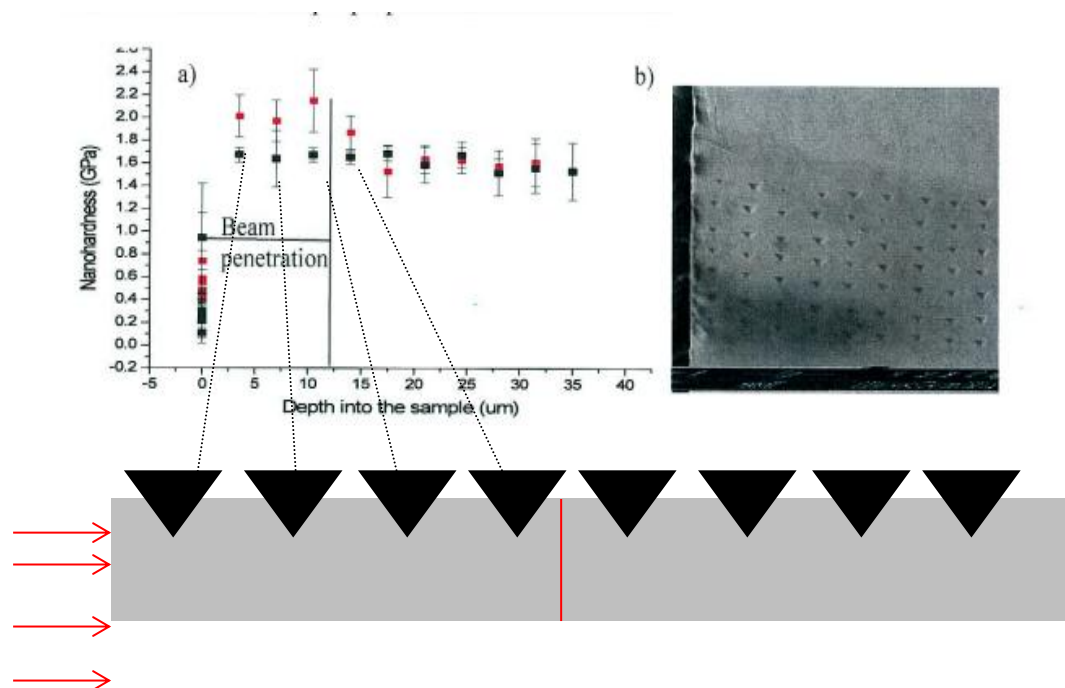


FIG. 2. Indentation vs. irradiation depth results on single crystal Cu a) two sets of measurements are shown. The red data show the indents made in the irradiated region while the black data indicate the indents performed in the not-irradiated edge. A post-indentation SEM image is shown in b).

Note: This work has not yet been submitted for publication and was performed by P. Hosemann, O. Anderoglu and Y. Wang.

2.1 In situ nano-compression testing on irradiated Cu

Here we show that yield strengths approaching macroscopic values were measured from ~ 400 nm diameter irradiated copper specimens. Quantitative *in situ* nano-compression testing in a transmission electron microscope reveals that the strength of larger samples is controlled by dislocation–irradiation defect interactions, yielding size-independent strengths. Below ~ 400 nm, size-dependent strength arises from dislocation source limitation. This transition length-scale should be universal, but depends on material and irradiation conditions. We conclude that for irradiated copper, and presumably related materials, nano-scale *in situ* testing can determine bulk-like yield strengths and simultaneously identify deformation mechanisms.

Materials Irradiation: A melt-grown single crystal of Cu with a (100) orientation was purchased, and 3 mm \times 3 mm wedges were prepared using mechanical and electrical polishing. The subsequent experimental procedure is shown in Schematic 1 and explained in the following section. A 5 μ m thick and 200 μ m long lamella was machined onto the single crystal wedge using a focused ion beam (FIB) microscope (FEI Strata 235; FEI, Hillsboro, OR, USA) operated with Ga⁺ ions at 30 keV. The whole wedge was then irradiated with a 1.1 MeV proton beam, having a Bragg peak at 7 μ m depth. Therefore, the proton beam passes through the FIB lamella, as seen from the dose profile in Schematic 1, thereby avoiding hydrogen implantation in the relevant region of the specimen. The irradiation temperature was continuously monitored on the sample holder and was found to be 80°C.

Sample fabrication: After irradiation of the lamella, nano-pillars with diameters ranging from 80 nm to 1500 nm, and heights at least five times the diameter, were fabricated by cutting annular trenches, again using the FIB microscope. Final milling currents were 10 pA and the samples had an inevitable axial taper of 2.5°. From the dose profile and the position of the pillars, the resultant dose for the nano-compression samples is estimated to be 0.8 dpa.

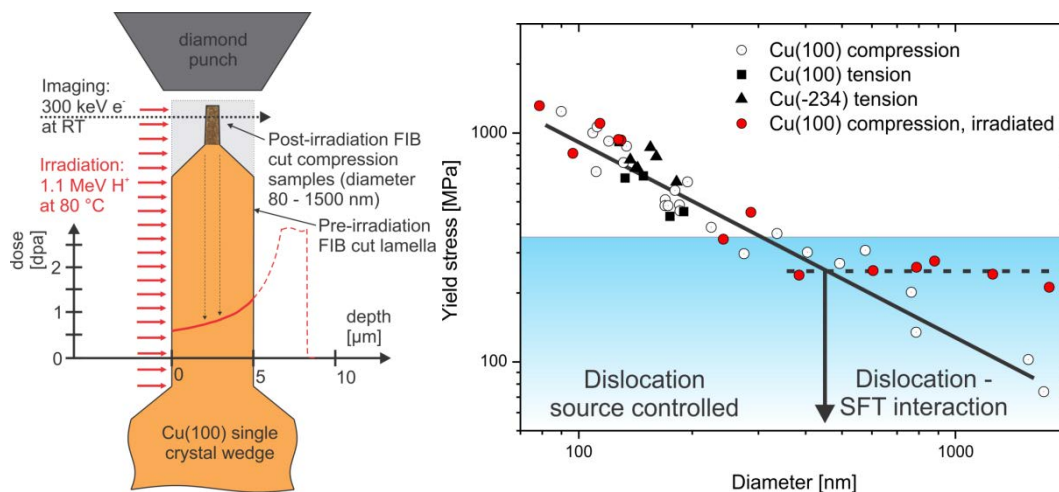


FIG. 3. Schematic of the experimental setup and condition a) size effect study on the irradiated and unirradiated Cu material.

Sample testing: Sample testing was performed *in situ* in a TEM (JEOL 3010, Tokyo, Japan) operated at 300 keV using a Hysitron Picoindenter (Hysitron, Minneapolis, MN, USA) in displacement-controlled mode with a nominal displacement rate of ~ 1 nm \cdot s⁻¹, resulting in strain rates of $\sim 10^{-3}$ s⁻¹. Digital videos were recorded during each test with a charge-coupled

device (CCD) camera (Gatan Orius SC200D; Gatan, Pleasanton, CA, USA) at 30 frames per second.

Results: Still images extracted from a video recorded during *in situ* TEM compression testing of an irradiated (100) Cu pillar with 130 nm diameter are shown in Fig. 4 along with the recorded load – displacement data and post testing TEM investigation. Before contact between the flat diamond punch and the sample (Fig. 4a), dots indicate the strain contours caused by the irradiation induced SFTs. After yield, plasticity and hardening, to a large extent, governed by the bowing and escape of short dislocation segments, as indicated in Fig. 4b, resemble a pinning – de-pinning-like motion on the radiation-induced obstacles. Note that several SFTs are still visible within the pillar, as indicated by arrows.

In Fig. 4c and Fig. 4d dislocations extend across the sample cross sectional area, resulting in pronounced load drops which were not seen before. Further deformation is then localized to a single slip plane with a spiral source acting, leading to the formation of a large slip step (Fig. 4e). Studying the deformation behaviour for sample sizes ranging from 80 – 1500 nm, we consistently observed this localized slip behaviour, which was not the case for unirradiated Cu, where even for the smallest specimens, slip preceded on adjacent planes. Note that there is a slight difference in contrast, seen especially in the low intensity Figs 1c and d, between the upper third of the image and the lower part.

The size-dependent yield strengths determined from the *in situ* compression tests for samples ranging from 80 to 1500 nm are shown in comparison to yield strengths determined for unirradiated material in tension and compression in Fig. 3b. Clearly, while the non-irradiated material exhibits a well-established, size-dependent strength over the whole investigated size range, the irradiated samples follow this trend only for sample diameters up to ~400 nm. Above this, the measured yield strengths were in the range of 220 – 280 MPa, seemingly independent of specimen size. The dashed line in Fig. 3 is added to guide the eye. The blue-shaded regime in Fig. 3 marks the range of maximum obstacle strength for interaction between 70 nm long dislocation segments of various character impinging on different heights of and with different orientation relations with respect to 4.7 nm large SFTs in Cu.

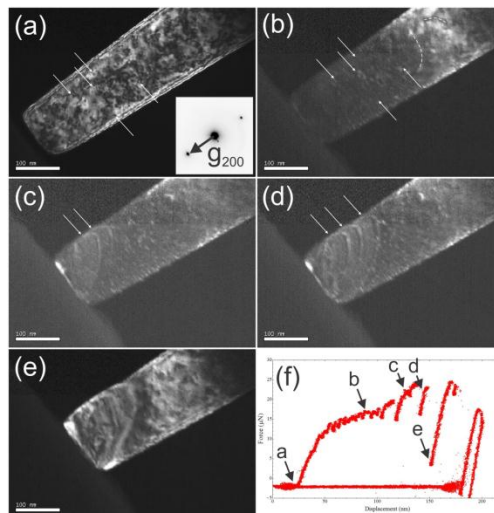


FIG. 4. (a-e) Dark field still images with g_{200} diffraction condition extracted from an *in situ* TEM compression test of an 130 nm diameter (100) oriented Cu pillar irradiated to 0.8 dpa and the measured load – displacement data (f). (TEM image of the deformed pillar g) and high resolution image of the SFT in the pillar h).

Summary of Ion beam irradiation on simple materials (single crystal) to evaluate the small scale materials testing technique and ion beam damage:

This series of experiments lead to the following conclusions.

- Surface indentation samples a range of doses and not a single dose due to the relatively large volume sampled in the material.
- Overstating the hardness occurs by performing indents of constant load on an irradiated versus un-irradiated sample due to the ISE.
- Measuring false size effects occurs by conducting the measurements in the beam direction and therefore sampling a dose range and un-irradiated material at the same time.
- Issues associated with surface changes and ion deposition in the material must be addressed.
- It is necessary to develop a method to investigate what deformation occurs under an indent in an irradiated and un-irradiated area.
- The smallest pillar size at which a difference in yield strength can be observed between irradiated and un-irradiated single crystal Cu is ~400 nm.
- The interaction of dislocations with SFT can be observed directly and agrees well with modeling.

Note: This work was published in: Nature Materials; 10, 608–61 (2011) by Daniel Kiener, Peter Hosemann, Stuart .A. Maloy, Andrew M. Minor

3. SMALL SCALE MECHANICAL TESTING AND LOCAL ELECTRODE ATOM PROBE MEASUREMENTS ON NOVEL MATERIALS FOR NUCLEAR APPLICATION

Structural materials for nuclear applications suffer a wide range of basic property changes such as embrittlement, swelling, etc. in an irradiation environment. The reason for the changes in properties can be due to the formation of gas in the material (n-alpha reaction) and/or to the creation of a large number of point defects which further evolve into larger defects, leading to a change in microstructure, dislocation density, void formation, or phase composition. The formation of cascades due to particle irradiation and the formation of a large number of point defects cannot be avoided initially. However, the recombination rate of the created defects can be enhanced by choosing materials with a small net bias, and/or by enhancing the recombination of defects by trapping. Recent studies have shown that the formation of large defects can be delayed or avoided by trapping the initial defects at a large number of defect sinks where the defects then annihilate, preventing their accumulation within the lattice.

The most effective defect sinks and traps have been proven to be interfaces such as grain boundaries or phase boundaries. This result encourages creation of materials with extremely high interface densities to allow for a more radiation-tolerant system. One example of this approach is Nano-structured Ferritic Alloys (NFA), where extremely large numbers, 10^{23} - 10^{24} m^{-3} , of nano-scaled oxide particles are distributed in mechanically-alloyed oxide dispersion strengthened steels. This microstructure allows the radiation-induced point defects or nuclear reaction products to “heal” or become trapped at interfaces.

It has been shown in the past that heat treatments on specialized tool steels (Maraging steels) also lead to the formation of finely dispersed intermetallic precipitates. As these precipitates are produced by solution annealing and a subsequent heat treatment, the advantage of these materials would therefore be that no mechanical alloying step is necessary to introduce a high

amount of nanometer sized precipitates. The methods described in the experimental chapter are applied to this experiment leading to the results described below. This study applies such an approach to evaluate the nucleation, growth, and stability of intermetallic precipitates in Maraging steels as well as their ability to act as defect sinks under irradiation.

3.1 Experimental

A commercially available corrosion-resistant Maraging steel from Uddeholm (Corrax) was investigated in this study. The material was delivered in the solution annealed state. No additional solution annealing heat treatment was applied prior to the aging and irradiation experiments. The material was irradiated using a 200 keV proton beam to a total dose of 1 dpa. During irradiation a part of the sample was masked by Al foil. This region was used as an unirradiated control sample. The irradiation temperature on the sample was held constant at $80\pm 10^\circ\text{C}$. After irradiation the sample was cut into four parts in order to perform several post irradiation heat treatments on each part. One sample was isolated for representation of the as-irradiated state, while the remaining three sections were annealed at 300°C , 400°C , and 500°C for 3 hours.

The nano-indentation experiments were carried out on a Hysitron Triboindenter, performing 25 indents per sample at distances of $10\ \mu\text{m}$ apart from each other were performed. For atom probe investigations focused ion beam (FIB) preparation methods were used to prepare atom probe tips as described in the previous chapters. Several atom probe samples were prepared using a Helios dual beam FIB instrument. Atom probe experiments were conducted on a local electrode atom probe (LEAP) Imago LEAP 3000X-HR system in voltage mode with a pulse repetition rate of 200 kHz. The sample temperature was kept constant at 38 K with an evaporation rate of 0.005 Atoms/pulse applied. Isoconcentration surfaces were calculated for Ni+Al levels of 23 at%. Applied cluster analysis is based on the maximum separation method. All given errors are based on counting statistics and reflect a one-sigma error.

3.2 Results and analysis

Fig. 5 displays a comparison of the hardness curves obtained following isothermal aging of unirradiated and irradiated material at three temperatures.

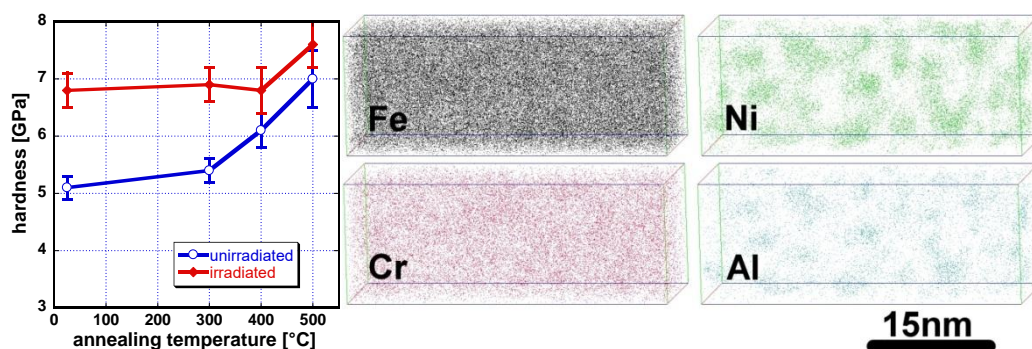


FIG. 5. Hardness curves for solution annealed and isothermally aged irradiated and not-irradiated. The given values are averaged values of 25 indents a). Elemental maps of atom probe analysis of the irradiated and annealed at 500°C sample b).

The hardness is strongly affected by irradiation. An increase of about 1.8 GPa compared to the solution annealed state can be noticed due to the applied irradiation. The unirradiated material shows a slight increase in hardness when annealed at 300°C , while the hardness value of the irradiated material stays fairly constant at about 6.8 MPa. Annealing to 400°C leads to a strong increase in hardness for the unirradiated sample (from about 5.4 GPa to

6.1 GPa) while the hardness values of the irradiated material still stay constant. Further increase of the annealing temperature leads to a significant increase in hardness for both materials to 7.0 GPa for the unirradiated material and to 7.5 GPa for the irradiated material. Atom probe investigations on the irradiated and annealed at 500°C material are shown in Fig. 6b. While distribution of Fe and Cr appears fairly continuous, enrichments of Ni and Al are clearly visible. It is possible to analyze these enrichments in detail by use of methods like isoconcentration surfaces and cluster detection algorithms.

3.3 Conclusions

Irradiation of solution annealed Corrax leads to a significant hardness increase before annealing treatment. A significant hardness increase cannot be found until the annealing temperatures exceed 400°C. In the unirradiated state an increase in hardness can already be found at temperatures higher than 300°C. Comparing the chemical composition of the detected enrichments with compositions given in literature show similar compositions. This implies that the occurring precipitates in the irradiated material should be from the same type as in the unirradiated material.

Note: This work is currently unpublished. It was performed by E. Stergar, C. Hofer, P. Hosemann.

4. LOW ENERGY ION BEAM IRRADIATION OF ODS ALLOY PM2000 AND POST-IRRADIATION INDENTATION CREEP AND TEM CHARACTERIZATION.

In recent years oxide dispersion strengthened (ODS) alloys become of interest to the nuclear community as a structural material. These alloys were originally designed as creep-resistant materials for high temperature applications. It is known that radiation damage causes an increase in structural defects such as vacancies, interstitials and dislocation loops and voids. Having radiation damage in a material might make it easier for dislocations to climb over obstacles such as oxide particles. It is the aim of this work to investigate if nano-indentation creep experiments can be used to investigate the effects of the developed defects on the dislocation-obstacle interaction.

4.1 Experimental

The commercially available Fe-based PM 2000™ oxide dispersion strengthened (ODS) alloy with nominal composition of Fe 19%Cr 5.5%Al 0.5%Ti 0.5%Y₂O₃ (by weight) was chosen for the irradiation using the 200keV Danfysik implanter at the Ion Beam Materials Laboratory at Los Alamos National Laboratory. Half the sample was masked using a 25 μm thick foil of Al during irradiation, leading to both an irradiated and a control sample on the same specimen. A 200keV proton beam was used to cause radiation damage to a depth of ~1 μm and a dose of 1dpa. The temperature of this irradiation was measured to be 80°C on the sample holder. The dose was calculated using the SRIM code.

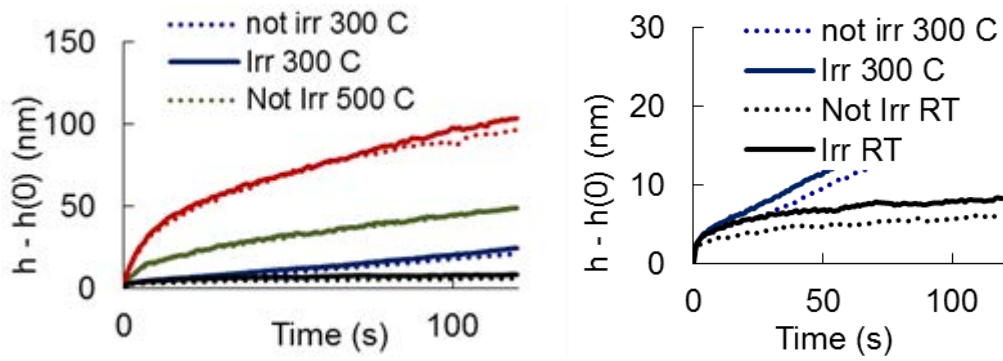


FIG. 6. Schematic sketch of the ion beam irradiation. Half the sample was masked, while half the sample was irradiated using 200keV protons.

After irradiation quasi-static nano-indentation measurements at different temperatures were performed using the Micromaterials nano-indenter instrument. The load-unload profile is shown in Fig. 2c. The holding time was set to 120seconds in order to measure the creep underneath the indenter during holding. A CBN Berkovich indenter was used for the indentation measurements. Drift measurements were performed before and after each indent and the data are corrected for these measurements. This insures good and accurate data from measurement to measurement.

4.2 Results and Discussion

It was found that the creep rate significantly increases with temperature. The room temperature creep was only 5 nm while the creep at 600°C was 100 nm in 120 seconds. Fig. 6a presents the average of all the creep data taken on both the irradiated side and the unirradiated side of the sample. The measurements were always performed on the same run to ensure no calibration variations or other influences. Fig. 6b shows the data for the RT and 300°C indentation more closely. The depth increase over time, $h-h_0$, is plotted over the holding time. It is obvious that the irradiated materials have a higher creep rate. It is assumed that at this point in the measurement stage 2 creep has been reached. This allows us to make the statement that a significant difference between the unirradiated and irradiated sample can be seen in stage I creep, while the slope in stage 2 is identical, whether irradiated or not.

Note: This work is currently unpublished. It was performed by P. Hosemann, A. Harris

5. ATOM PROBE TOMOGRAPHY ANALYSIS AFTER ION BEAM IRRADIATION ON PM2000

5.1 Introduction / Experimental

Several samples of PM2000 were received from PSI after intense ion beam irradiation. The material was cut using standard FIB processing at PSI and sent to UCB for APT analysis. The data gained are from three specimens; a reference sample (no irradiation), P3 irradiation with He-beam 0–24MeV at 300°C up to 3000 appm He which equals 0.8dpa, P7 irradiation with He beam 0–24 MeV at 500°C up to 2500ppm He which equals about 0.5dpa.

Due to the nm scale on which the alpha-alpha' decomposition occurs, atom probe tomography (APT) with its resolution near the atomic scale gives the possibility to describe the influence of He irradiation on the nanostructure and the decomposition behavior of this material. In this study the APT measurements were done using an Imago 3000X-HR system situated at the University of California at Santa Barbara. Laser and voltage modes were used. In both modes a pulse repetition rate of 200 kHz was applied. The temperature was 30 K for laser measurements and 60 K for voltage measurements. In voltage mode a pulse fraction of 20%

of the standing voltage was used. The laser energy was 0.08nJ. Analysis was done using the Imago IVAS software package.

5.2 Results

An overview of an atom probe measurement of the P3 state is shown in Fig. 7. Distinct enrichments of Cr can be found. Regions with almost no Al can be found as well. No oxides are visible. The Cr enrichments have a spherical appearance and seem to be homogeneously distributed.

Note: This work is currently unpublished but was performed by E. Stergar, M. Pouchon, and P. Hosemann

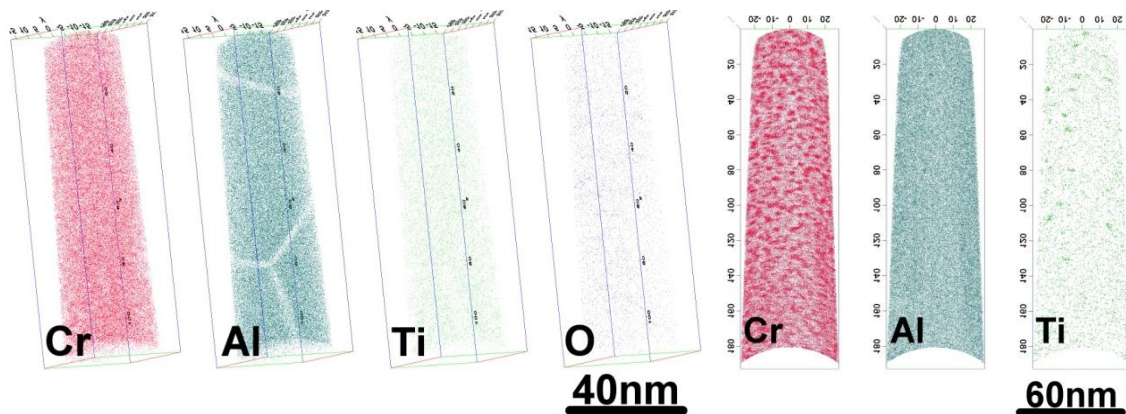


FIG. 7. APT elemental maps of sample P3 (left) and sample P7 (right)

Fig. 7 (right) shows an overview of an atom probe measurement of p7 material. Clustering of cr and ti is obvious. The overlay of the positions of cr and the positions of ti atoms shown in error! Reference source not found. Reveals no correlation between cr clusters and ti clusters found in the atom probe measurement. Comparing al distribution and ti distribution, however, shows a correlation between al enrichments and ti enrichments.

5.3 Summary

Significant amounts of Cr-rich precipitates were found after ion beam irradiation. It is assumed that alpha prime precipitates were formed. No oxide precipitates were found in the needles because the low oxide particle density of PM2000 reduces the chance to hit an oxide-containing area. Significant amount of Al depletion was found at the grain boundaries as well. It appears that no alpha prime precipitates are in the area of Al depletion, but Cr segregation was not observed. The results shown here are preliminary and detailed analysis needs to be performed.

6. LIST OF DIRECT COLLABORATIVE EFFORTS DEVELOPED DURING THE SMORE CRP

- (a) UCB-LLNL: Ion beam irradiation and small scale mechanical testing on candidate materials for fusion application. M. Fluss and P. Hosemann developed a 3-year program to investigate the property changes due to high dose multi-beam ion irradiation.
- (b) Collaboration with PSI and UCB: UCB and PIS (Hosemann and Pouchon) investigated the segregation of alloying elements in PM2000 after intense ion beam irradiation. The initial results are presented in this report.
- (c) Collaboration between UCB/LANL and KAERI

- (d) UCB and KAERI developed a INERI proposal together for investigation of the limits of small scale testing of materials on ion beam-irradiated samples, a program which was successfully awarded in 2012.
- (e) UCB and LANL made several pieces of ODS alloys available to the participants at the beginning of the Project. These materials were brought to previous meetings and distributed among the participants immediately. Several publications have resulted from these samples.

DUAL AND TRIPLE ION-BEAM IRRADIATIONS OF FE, FE(CR) AND FE(CR)-ODS FINAL REPORT: IAEA SMORE CRP#

Michael J. Fluss, Chief Scientific Investigator
Michael J. Fluss, Luke L. Hsiung and Jaime Marian, Authors

Lawrence Livermore National Laboratory, Livermore, California 94550 USA

Abstract

Structures of nanoparticles in Fe-16Cr-4.5Al-0.3Ti-2W-0.37Y₂O₃ (K3) and Fe-20Cr-4.5Al-0.34Ti-0.5Y₂O₃ (MA956) oxide dispersion strengthened (ODS) ferritic steels produced by mechanical alloying (MA) and followed by hot extrusion have been studied using high-resolution transmission electron microscopy (HRTEM) techniques to gain insight about the formation mechanism of nanoparticles in MA/ODS steels. The observations of Y-Al-O complex-oxide nanoparticles in both ODS steels imply that decomposition of Y₂O₃ in association with internal oxidation of Al occurred during mechanical alloying. While the majority of oxide nanoparticles formed in both steels is Y₄Al₂O₉, a few oxide particles of YAlO₃ are also occasionally observed. These results reveal that Ti (0.3 wt %) plays an insignificant role in forming oxide nanoparticles in the presence of Al (4.5 wt %). HRTEM observations of crystalline nanoparticles larger than ~2 nm and amorphous or disordered cluster domains smaller than ~2 nm provide an insight into the formation mechanism of oxide nanoparticle in MA/ODS steels, which we believe from our observations involves a solid-state amorphous precursor followed by recrystallization. Dual ion-beam irradiations using He⁺+Fe⁺⁸ ions were employed to gain more detailed insight about the role of nanoparticles in suppressing radiation-induced swelling. This is elaborated through TEM examinations of cavity distributions in ion-irradiated Fe-14Cr and K3-ODS ferritic steels. HRTEM observations of helium-filled cavities (helium bubbles) preferably trapped at nanoscale oxide particles and clusters in ion-irradiated K3-ODS are presented. Finally, we describe the results from triple ion-beam irradiations using H⁺+He⁺+Fe⁺⁸ ions to emulate fusion first wall radiation effects. Preliminary work is reported that confirms the existence of significant hydrogen synergistic effects described earlier by Tanaka et al., [1] for Fe(Cr) and by Wakai et al., [2, 3] for F82H reduced activation ferritic martensitic (RAF/M) steel. These previous results combined with our data suggest a complex new “catalytic” mechanism whereby H interacts with the steady state population of defects and the embryonic cavities so as to accelerated cavity (void) growth in both Fe(Cr) and under special conditions in ODS steels.

This work performed in part under the auspices of the U.S. Department of Energy by Lawrence Livermore National Laboratory under Contract DE-AC52-07NA27344.

1. RATIONALE FOR THE PROJECT

One of the major challenges in designing future fusion reactors is to develop the high-performance structural materials for first wall and breeder blanket, which will be exposed to the displacement damage from fusion neutrons (≤ 14 MeV) from the deuterium-tritium fusion, and to the bulk production of helium (He) and hydrogen (H) from the (n, α) , (n, p) , and (n, np) transmutation reactions. The choice of structural materials dictates the design and purpose of the fusion reactor system. As an example consider the sequence of materials choices for ITER, DEMO, and a commercial fusion system. ITER's structural components are standard steels, DEMO will likely utilize RAF/M steels, and while a future fusion commercial plant may use refractory alloys or even ceramics such as SiC/SiC_{fiber}. In particular, the allowable power plant operating temperature, the choice of coolant, and the power conversion system are critically dependent on the performance characteristics of the materials. The selection of suitable structural materials is based on conventional properties (such as thermophysical, mechanical, and corrosion and compatibility), low neutron-induced radioactivity, and resistance to radiation-induced damage phenomena such as material hardening/embrittlement and/or dimensional instability caused by void- and helium-driven swelling [4, 5].

Oxide dispersion strengthened (ODS) steels, which are produced by mechanical alloying (MA) of elemental powders or prealloyed metallic powder with yttria (Y₂O₃) powder and consolidated by hot extrusion or hot isostatic pressing, are a class of advanced structural materials with a potential to be used at elevated temperatures due to the metallurgical

enhancements from the dispersion of thermally stable oxide nanoparticles into the matrix. ODS steels are resistant to radiation-induced swelling and have improved creep strength and oxidation/corrosion resistance at elevated temperatures compared to conventional steels. Thus an operating temperature of the first wall in future fusion reactors of $>700\text{ }^{\circ}\text{C}$ [6] is possible, resulting in an improved energy efficiency $\geq 40\%$ [7].

Although significant progress has been made recently on the processing-microstructure-property relationships of RAF/M and ODS steels [8, 9], it remains to understand the role of fusion-relevant helium and hydrogen transmutation gases on their deformation, fracture, and cavity swelling. Since no prototype fusion reactors currently exist, it is difficult to directly evaluate the effects of high-energy neutron and transmutation gases on the first wall and blanket of a fusion reactor. One technique commonly used to study the evolution of defect structures and the kinetics of cavity formation utilizes transmission electron microscopy (TEM) examinations of specimens simultaneously bombarded by heavy ions and helium and/or hydrogen ions through so-called “dual-beam” and/or “triple-beam” accelerated experiments [1]. The heavy ions create atomic displacements while the implanted gas ions emulate transmutation gases, helium (~ 10 appm/dpa) and hydrogen ($\sim 40\text{--}45$ appm/dpa) [4, 10].

2. OVERVIEW OF THE INITIAL PROJECT PLAN

While some modifications of the initial project plan were required the overall project proceeded along the lines originally outlined and produced significant new data.

2.1 Dual beam irradiation

The ODS steels used for this investigation were Fe-16Cr-4Al-2W-0.3Ti-0.3Y₂O₃ (designated as K3) [11] and Fe-20Cr-4.5Al-0.34Ti-0.5Y₂O₃ designated as MA956 [12]. A full description of the fabrication procedure for the ODS steels can be found elsewhere [13, 14]. For the purpose of investigating the role of nanoparticles in radiation tolerance of ODS steels, an Fe-14 wt % Cr alloy was also prepared using a vacuum arc-melting method followed by hot rolling at $1050\text{ }^{\circ}\text{C}$. Dual-beam irradiation of Fe-14Cr alloy and K3-ODS steel loaded in a stainless-steel specimen holder using 24 MeV Fe⁺⁸ ions for displacement damage and energy-degraded 1.7 MeV He⁺ ions for helium implantation was conducted at the JANNUS facility, Saclay, France. Homogeneity of the irradiation was obtained by rastering of a Gaussian shaped 2mm fwhm (full width at half maximum) beam. The irradiation temperature was controlled at $425\pm 5^{\circ}\text{C}$ using a proportional-integral-derivative referenced thermocouple located on the specimen holder (Fig. 1). The specimen temperature uniformity was estimated by monitoring the surface temperature of the specimen using a digital infrared camera during heating and ion irradiation. The surface temperature was uniform within $\sim 2.5\text{ }^{\circ}\text{C}$ and tracked well with the controlling thermocouple. The displacement damage in dpa (displacement per atom) from Fe⁸⁺ as a function of depth into the specimen, and the He⁺ implantation profile were deduced using the SRIM code [15].

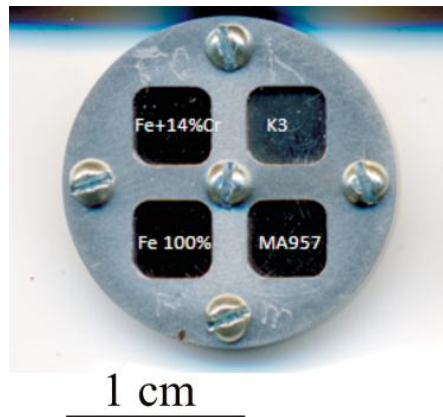


FIG. 1 Specimen holder for JANNUS heating stage indicating the types of specimens irradiated in these studies.

The implantation depth of helium was over a region extending from 1.5 to 2.6 μm beneath the specimen surface to avoid overlapping with the Fe^{8+} ion implanted region that extended from 2.75 to 3.6 μm beneath the specimen surface. The displacement damage at the peak position was 65 dpa and the specimens were irradiated in the region under test at $\sim 5 \times 10^{-4}$ dpa/s. The nominal time integrated radiation conditions for the volume under test are as follows: the displacement damage increases from 10 dpa at 1.5 μm to 40 dpa at 2.75 μm , and there are two peaks for the helium implantation (100 appm/dpa at 2.1 μm and 25 appm/dpa at 2.6 μm) that defined the volume under test. Most of the analyses was done in the region associated with the larger He peak. The dose parameters were 80 appm He/dpa, and an average of 40 dpa in the middle of the region under test.

2.2 Triple beam irradiation

A triple beam (H+He+Fe) irradiation was performed on four specimens soon after the three-beam facility came on-line at JANNUS-Saclay. The irradiation was conducted at 625°C using the same beam energies and dose rate as for the dual beam irradiation but with the addition of hydrogen (680 keV) such that the hydrogen was implanted in the same volume (depth) as the helium. Again, the volume under test was a region of ~ 0.5 micron thick from 2.1 to 2.6 microns in depth. The dose parameters were, 40 appm H/dpa, 16 appm He/dpa, and an average of 40 dpa in the middle of the region under test.

2.3 High resolution transmission electron microscopy (HRTEM)

Thin foils of the as fabricated ODS steels for TEM examination were prepared by a standard procedure that includes slicing, grinding, and polishing. Final thinning of the foils was performed using a standard twin-jet electro-polishing technique in an electrolyte (90 vol % acetic acid, 10 vol % perchloric acid) at 30 V and room temperature. Cross-section TEM foils (10 μm x 6 μm x < 0.1 μm) of irradiated Fe-14Cr and K3-ODS were prepared using a focused ion-beam method. The foils were lifted out using a micro-pickup system and mounted onto a copper grid. TEM characterizations were performed using a Phillips CM300 field-emission transmission electron microscope (accelerating voltage of 300 kV). A software package, CARINE CRYSTALLOGRAPHY 3.1 [16] was used to simulate electron diffraction patterns to identify the crystal structure of oxide nanoparticles.

3. MODIFICATION AND DEVIATIONS FROM INITIAL PLAN

The initial project plan was modified to accommodate operational aspects of the multi-ion beam facility at JANNUS-Saclay [17] resulting in carrying out experiments to dose of < 40 dpa. Additionally, plans to perform micro-mechanical measurements on the irradiated materials were deferred to the future. The irradiated specimens are still available for future

post irradiation examination with micro-mechanical techniques as well as 3D atom probe.

3.1 Collaborations within the project

The successes in this project are the result of the work and contributions of many collaborators. They are listed in Table 1 by institution.

TABLE 1 COLLABORATORS

Collaborators	Institution
Michael J. Fluss Luke L. Hsiung B. William Choi Scott Tumey Jaime Marian Paul Ehrart Vasily Bulatov	Lawrence Livermore National Laboratory Physical and Life Sciences Directorate Livermore, CA 94566 USA
Yves Serruys Estelle Meslin Francois Willaime	Service de Recherches de Métallurgie Physique, CEA, Gif-sur-Yvette 91191 France
Akihiko Kimura	Institute of Advanced Energy, Kyoto University, Gokasho, Uji, Kyoto 611-0011, Japan

4. RESULTS

4.1 As manufactured TEM characterization of Fe(Cr) alloy and ODS steel

4.1.1 Inclusions in Fe(Cr) alloy

An interesting aspect of the Fe(14at%Cr) alloy used in this study was the revealing of small “impurity” sites upon exposure to the dual beam irradiation. We believe that these sites are present in the as manufactured material but are at the resolution limit of the TEM and hence difficult if not impossible to observe. Fig. 2 elaborates this observation by showing the nucleation of helium bubbles in association with dislocations and then at high magnification highlighting the core inclusions at the center of two of the bubbles.

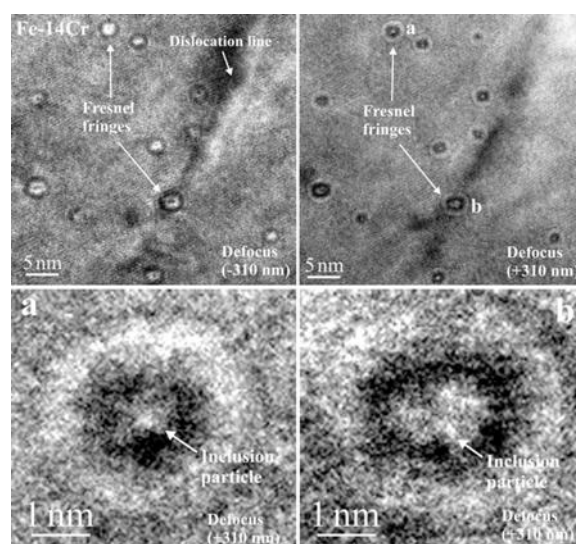


FIG. 2. Bright-field TEM images show the heterogeneous nucleation of helium bubbles in association with dislocation lines and inclusion particles. The high-magnification TEM images taken from the bubbles labeled a and b reveal that inclusion particles of ~1 and ~2 nm can be readily seen within these two bubbles, which appear as black contrasts surrounded by a white Fresnel fringe in overfocus images. From [18]

4.1.2 ODS particle morphology and crystallization

The larger ($> 1\text{nm}$) ODS particles crystallize during consolidation and heat treatment of the mechanically alloyed powder. This crystallization process is determined not only by the energetics, but by complex kinetics. We have observed that the precursor to the crystallization, and the formation of the so-called core shell structure, is an amorphous aggregation of the oxide materials. The experimental evidence for this is found in Fig. 3 and Fig. 4. In Fig. 3 we show the presence of an amorphous domain in the midst of a particle that was in the process of crystallizing. This feature was quite common in both the K3 and MA956 specimens investigated. In Fig. 4 is the strongest evidence for the existence of an amorphous precursor to crystallization, the formation of multiple domains in the oxide particle, which can only happen if the particle is preceded by an amorphous cluster of the oxide material. A discussion of sub-nanometer ODS particles discovered in the as manufactured steels is deferred to section 6.2.

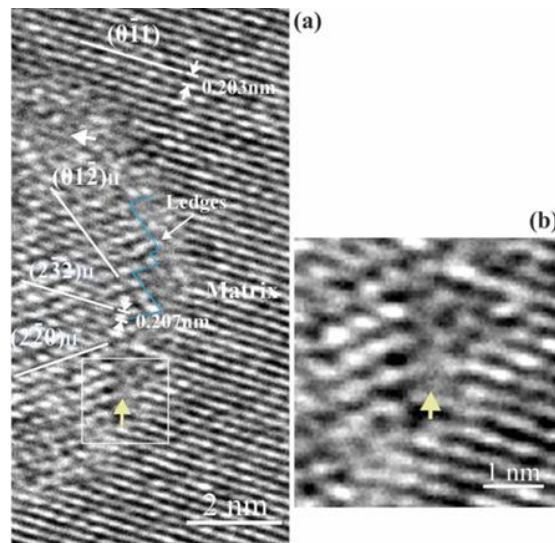


FIG. 3. HRTEM image shows the interfacial structure of an ODS nanoparticle in K3. (a) Facets, ledges, and remnant of amorphous domains (marked by arrows) can be found at the oxide (domain II)/matrix interface and (b) a higher magnification view of an amorphous domain in the framed area in (a). From [18]

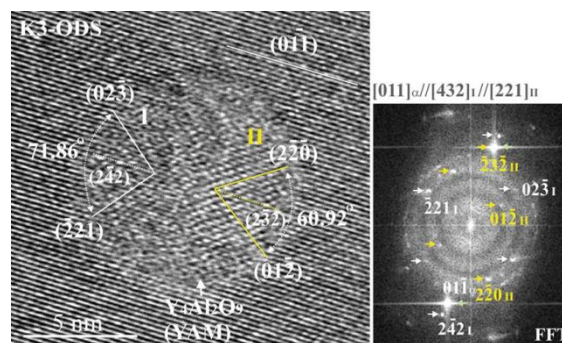


FIG. 4 HRTEM image shows the formation of multiple $Y_4Al_2O_9$ domains in an oxide nanoparticle. Two different orientation relationships between $Y_4Al_2O_9$ oxide and the matrix can be readily derived from the FFT image. From [18]

4.2 Dual beam experiments with He and Fe ions with TEM PIE

Oxide dispersion strengthened (ODS) steels, which are produced by mechanical alloying (MA) of the elemental, or prealloyed, metallic powder with yttria (Y_2O_3) oxide powder and then consolidated by hot extrusion or hot isostatic pressing, are a class of advanced structural

materials with a potential for use at elevated temperatures due to the dispersion of thermally stable oxide nanoparticles into the matrix. ODS steels are resistant to radiation-induced swelling and have improved creep strength and oxidation/corrosion resistance at elevated temperatures compared to conventional steels. Thus an operating temperature of the first wall in future fusion engines of as much as 650°C [6] may be possible.

Structures of nanoparticles in Fe-16Cr-4.5Al-0.3Ti-2W-0.37 Y₂O₃ (K3) and Fe-20Cr-4.5Al-0.34Ti-0.5Y₂O₃ (MA956) oxide dispersion strengthened (ODS) ferritic steels have been studied using high-resolution transmission electron microscopy (HRTEM) techniques to understand the formation mechanism of nanoparticles. The observation of Y-Al-O complex-oxide nanoparticles in both ODS steels imply that decomposition or amorphization of Y₂O₃ in association with internal oxidation of Al occurred during mechanical alloying. While the majority of oxide nanoparticles formed in both steels is Y₄Al₂O₉, a few oxide particles of YAlO₃ are occasionally also observed. These results reveal that Ti (0.3 wt %) plays an insignificant role in forming oxide nanoparticles in the presence of Al (4.5 wt %). HRTEM observations of crystalline nanoparticles larger than ~2 nm and amorphous or disordered cluster domains smaller than ~2 nm provide an insight into the formation mechanism of oxide nanoparticle in MA/ODS steels, which we believe from our observations involves solid-recrystallization from an amorphous precursor. More details can be found in a comprehensive paper published recently [18].

The role of nanoparticles in suppressing radiation-induced swelling is revealed through TEM examinations of cavity distributions in ion-irradiated Fe-14Cr and K3-ODS ferritic steels. HRTEM observations of helium-filled cavities (helium bubbles) preferably trapped at nanoscale oxide particles and clusters in ion irradiated K3-ODS were observed. The difference between the sequestration of He in an ODS alloy and in a ferritic martensitic alloy is shown in Fig. 5. This work is described in more detail in Phys. Rev. paper [18].

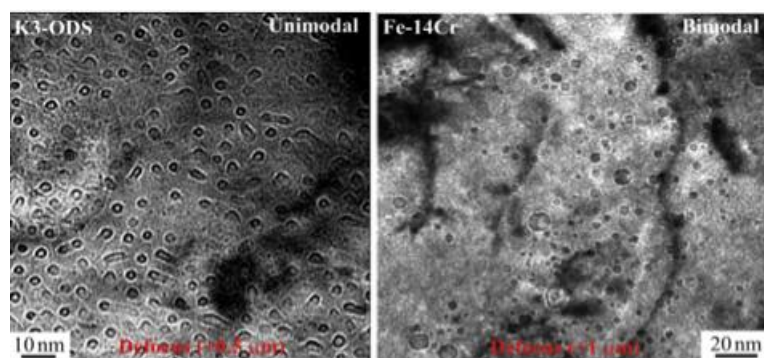


FIG. 5. A comparison is shown of a steel with nanoparticles (left) and a steel without nanoparticles (right) both irradiated with Fe and He under the same conditions. The specimen with nanoparticles exhibits small bubbles all below the critical size, and hence no void growth. The specimen without particles shows the start of deleterious void growth. From [18]

A discovery we made in this work is that sub-nanometer size particles sequester He in such a way as to form He clouds around the particle. Larger particles sequester He by forming small bubbles at the particle matrix interface. This comparison is shown in Figs 6 and 7. It is interesting to note that the sub-nanometer particles were not observable with TEM until they became decorated with He (Fig. 7). This observation explains why the 3D atom probe technique counts many more particles than TEM observations. The very small particles are actually the dominant source of He sequestration by virtue of their numbers. This suggests that the optimal size distribution for ODS particles is a bimodal one, consisting of sub-nanometer particles for He management and larger (>2 nm) diameter particles for improved

high temperature mechanical properties nanometer particles for He management and larger (>2 nm) diameter particles for improved high temperature mechanical properties.

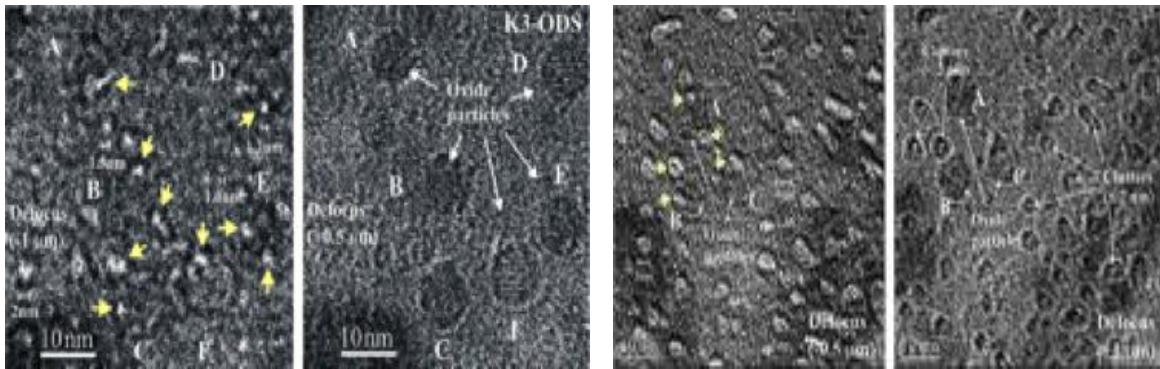


FIG. 6. TEM images from [18].

TEM images (Fig. 6) show (left) many spherical cavities ($d=1-2$ nm), which are mostly located at the oxide/matrix interfaces, can be clearly seen in an underfocus condition: -1 μm ; the crystalline-oxide particles appeared an underfocus condition: -1 μm ; the crystalline-oxide particles appeared with lattice fringes (labeled A through F; $d=5-10$ nm) can be more readily seen under an overfocus condition of $+0.5$ μm ; (right)- shows the formation of cavities in association with crystalline-oxide particles (labeled A, B, C; $d\approx 10$ nm) and clusters ($d<2$ nm), both can be more readily seen under an overfocus condition of $+0.5$ μm - From [18].

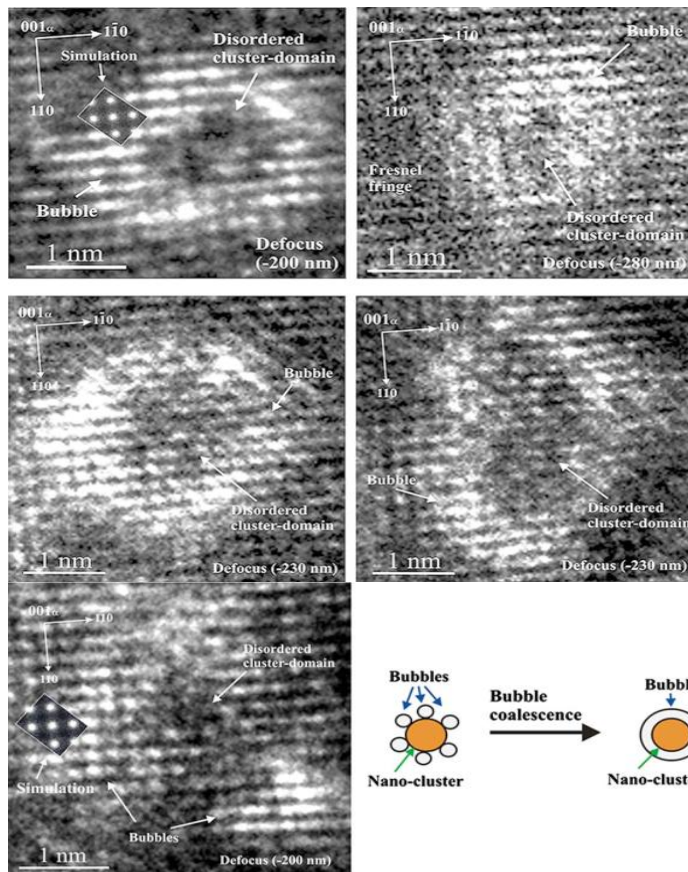


FIG. 7. (a) HRTEM images of helium bubbles in association with cluster domains of various shape. Here each helium bubble appears as white contrast surrounded by a dark Fresnel fringe in each underfocused image; (b) HRTEM image shows the trapping of several individual bubbles at a disordered cluster domain, which suggests that the appearance of cluster core/bubble shell is a result of the coalescence of small bubbles as conceptualized in the illustration. From [18]

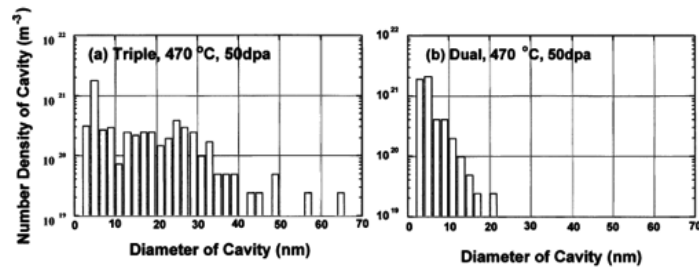


FIG. 8. Size distributions of cavities formed in F82H steel irradiated at 470°C to 50 dpa with the triple and dual ion beams under fusion condition. It was measured at depths from 0.9 to 1.1 μm . From [2]

4.3 Triple beam experiments with H, He, and Fe ions.

The synergistic aspects of simultaneous implantation of hydrogen along with He and displacement damage have been performed for Fe(Cr) and K3-ODS steel using triple beam irradiation at the CEA-Saclay JANNUS facility. A previously unreported void structure is seen in Fe(Cr) irradiated specimens that may explain the anomalously large swelling seen during triple ion beam irradiations by Tanaka et al.,[1].

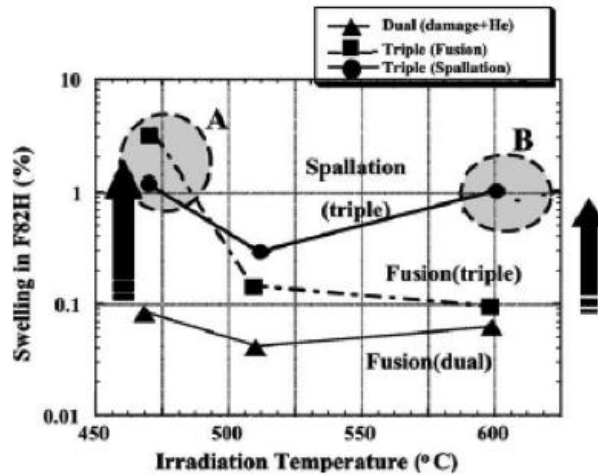


FIG. 9. The dependence of swelling of F82H steels on irradiation temperature under these conditions. In the area A the synergistic effect of displacement damage, helium and hydrogen occurred, and in the area B the enhancement of swelling was caused by the synergistic effect of displacement damage and high concentration helium. From [3]

Wakai and co-workers have addressed the question of anomalous swelling associated with H implantation in triple beam experiments focused on the technically relevant alloy F82H [2, 3]. In their two papers they confirmed the synergistic effect reported in [1] for Fe(Cr) model alloys, and have even demonstrated the neutron spectral dependence by varying the H and He to dpa ratio to simulate fusion and spallation conditions at 50 dpa at three temperatures (470, 510 and 600°C) and at 1 μm depth into the specimen. Figs 8 and 9 show a summary of the cavity statistics and the swelling data respectively. The dpa dose of 50 dpa is relevant for what one would want for a DEMO structural. Two very important issues are raised by this work:

- (1) First is the underlying mechanism resulting in the synergistic effect of hydrogen. Wakai and co-workers measured the hydrogen content of the triple beam irradiated specimens that showed a large synergistic swelling. They report no hydrogen present in the volume of material under test. What this means is that while there is evidence

for a synergistic effect from hydrogen the hydrogen itself does not remain in the specimen. One might say that the hydrogen is acting like a catalyst.

- (2) With this in mind, there is a very important question regarding the reaction kinetics that must be asked. Could the observed synergistic effect be strongly rate dependent in addition to its observed temperature dependence, and can it be expected to greatly diminish or even disappear at the much lower dose rates that would exist in a fusion neutron environment? In addition, one might also ask if there is a peak in the temperature dependence for a given dose rate and spectral condition such as one observes for other swelling phenomena?

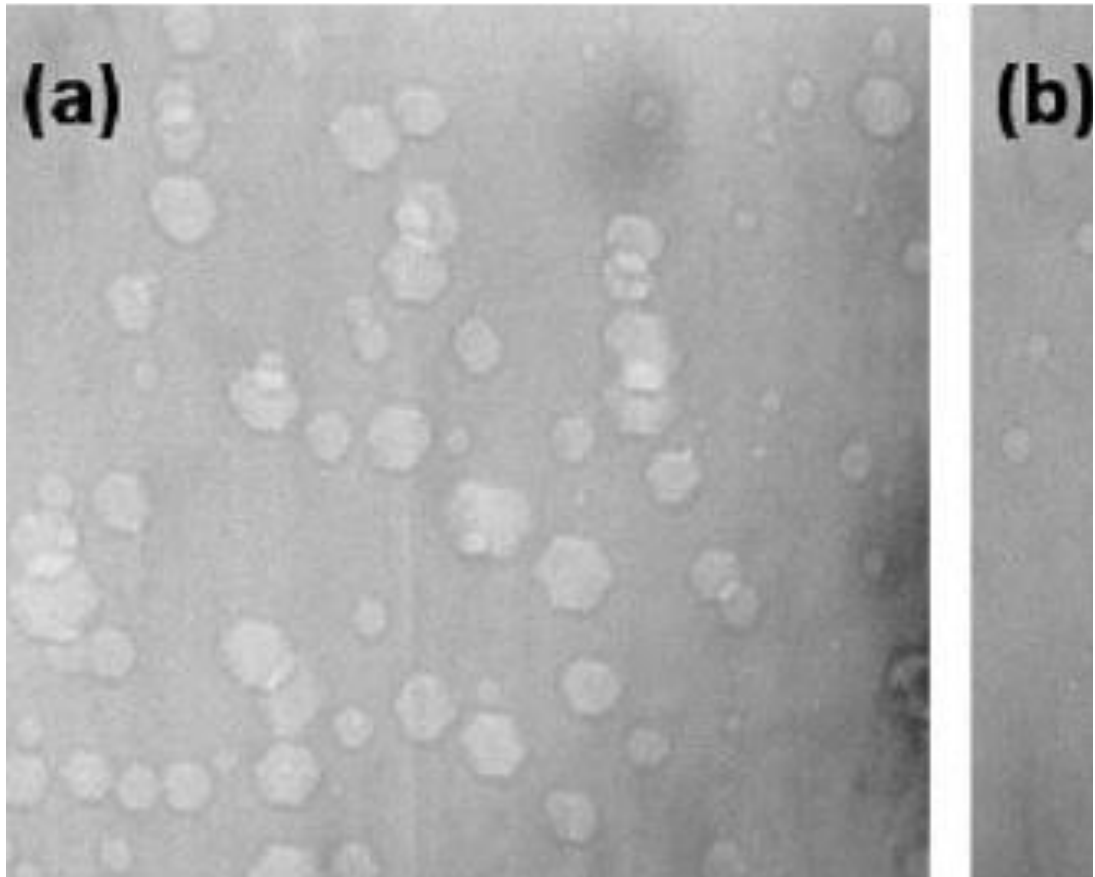


FIG. 10. Cavities formed in F82H steel irradiated at 470 °C to 50 dpa at the depth of around 1 μm under (a) triple beams of Fe⁺, He⁺ and H⁺ ions and (b) dual beams of Fe³⁺ and He⁺ ions. From Wakai et al., [3].

In our first triple beam experiment on Fe(14at%Cr) at 625°C we observed new cavity features that appear to be a consequence of the synergistic effect of hydrogen. We note that the temperature of this triple beam experiment was the same as that used by Tanaka earlier [1]. What is interesting is a comparison of our high resolution images for Fe(14at%Cr) dual and triple beam irradiations at 625°C and 40 dpa with the TEM images shown by Wakai for F82H at 470°C and 50 dpa. This is seen by comparing Fig. 10 with Fig. 11. We note that both of these are the product of irradiations where synergistically large void swelling is extant. The faceted void-like structures appear to be a common element of the two irradiations, and may hold clues to the kinetics/mechanism for this hydrogen synergistic swelling effect.

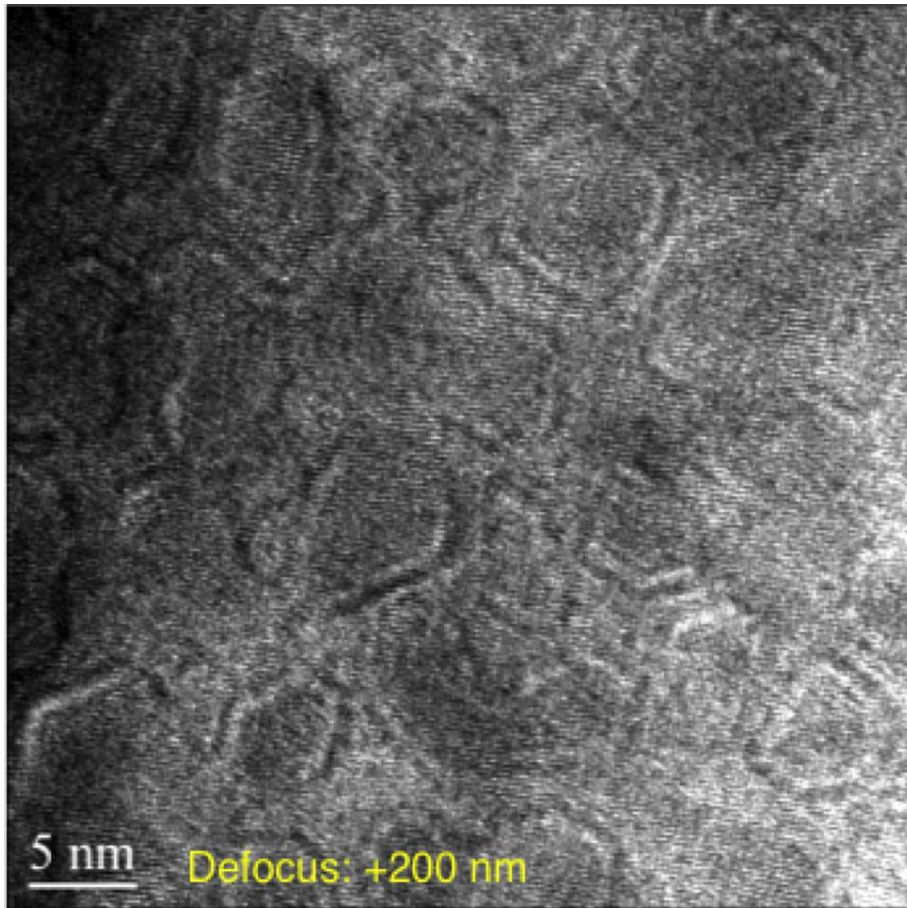


FIG. 11. New void like structure is seen in 625°C triple beam irradiation of Fe14Cr, 40dpa, 40 appm H/dpa, and 15 appm He/dpa. Note the similar faceting and large size of the cavities shown to those in Fig. 10, both of which are the product of a synergistic hydrogen effect. From: P'vt communication: L. Hsiung et. al.,

4.4 Theory, simulation, and modeling (TSM)

Theory, simulation, and modeling (TSM) efforts in the last three years have been focused on developing an integrated multiscale methodology to study damage accumulation in *nanostructured* ferritic steels (*nanoparticles dispersed in the matrix*) under fusion irradiation conditions. The behavior of these materials, at relatively high temperatures and neutron doses, is exceedingly complicated, and a comprehensive coverage of all their microstructural features, their coupled behavior, and their evolution with irradiation was simply impractical. Encouraged by the results described above, but constrained by finite resources, we thus chose to select among all the topics of interest, three critical areas of TSM research:

- (i) Nature of He ions and α particles upon implantation and transmutation, (respectively).
- (ii) Volumetric aspects of metallic oxide particles (ODS-type) on He-atom retention.
- (iii) Accumulation of complex irradiation species containing He and H up to high irradiation doses.

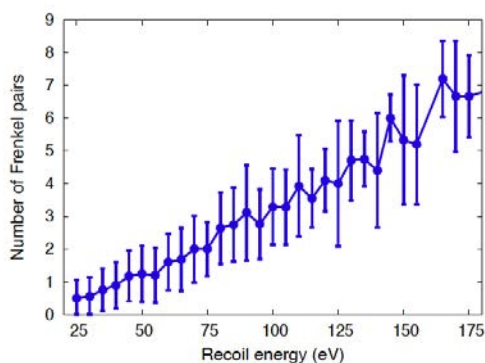


FIG. 12. Production of stable Frenkel pairs by He atoms implanted with energies between 0.33 and 4.5 MeV. P Erhart and J Marian, [19].

The objective was twofold: first, we strived to fill knowledge gaps where the understanding (per the existing literature) was too limited for our purposes; second, the goal was to produce important contributions in terms of high impact papers in the specialized literature. Along the way, our approach was enriched by the concurrent experimental observations taking place and, thus, modified accordingly in a very dynamic and mutually informing fashion.

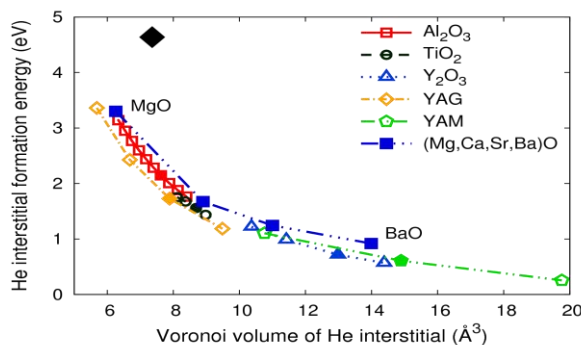


FIG. 13. Scaling of the He interstitial formation energy for a number of oxide structures. Yttria substructures produce very low formation energies, which render ODS particles effective thermodynamic volumetric sinks. P Erhart and J Marian, [20].

Regarding (i), the question was the following: when He ions are implanted in a ferritic matrix, are they inserted as substitutional or as interstitial He? The answer is most important due to the enormous difference in mobility between the two species. Interestingly, this question had not been conclusively answered in over three decades of modeling of He effects in steels. As Fig. 12 shows, we found that He atoms implanted with energies from 0.33 to 4.5 MeV create their own cascade of defects, which may result in correlated recombination of the He atom with a vacancy of its own creation, giving rise to substitutional He [19]. From calculations, we find that up to 3% of all He, either ion implanted or from an (n,α) reaction ends up as substitutional before uncorrelated long-range diffusion occurs. This means that cavity growth can begin almost immediately with these He-vacancy pairs as the seed.

Item (ii) refers to a systematic study of the stability of He atoms within metallic oxide particles (akin to ODS particles) and at their surface. Fig. 13 illustrates the formation energy of a He interstitial atom in several oxide structures [20]. The black diamond symbolizes a pure Fe matrix. Clearly, He interstitials will be thermodynamically attracted to oxide particles. In addition, we find that the formation energy scales universally based on the interstitial Voronoi volume of each oxide structure. *Helium formation energies can be predicted across a wide range of oxides based on the volume of the interstitial site.* This “first-of-a-kind” calculation will be very useful to quantify He sequestration at ODS particles.

Finally, (iii) has led to the development of a novel technique never before used for materials science and/or nuclear materials. The so-called *Stochastic Cluster Dynamics* (SCD) method easily permits the treatment of complex species containing more than two types of defects. In addition, by including beneficial aspects of both Monte Carlo and rate theory, our technique lends itself to efficient volume rescaling and long simulated dose periods. Fig. 14 shows the first calculations of damage, He, and H accumulation in an Fe(Cr) alloy at 300K up to 50 dpa [21]. The curve shows the formation of He and H bubbles and shows the corresponding incubation doses. We expect SCD to become a leading simulation technique for nuclear materials allowing us to effectively deal with the variations in dpa-dose rate between ion-beam experiments and neutron experiments.

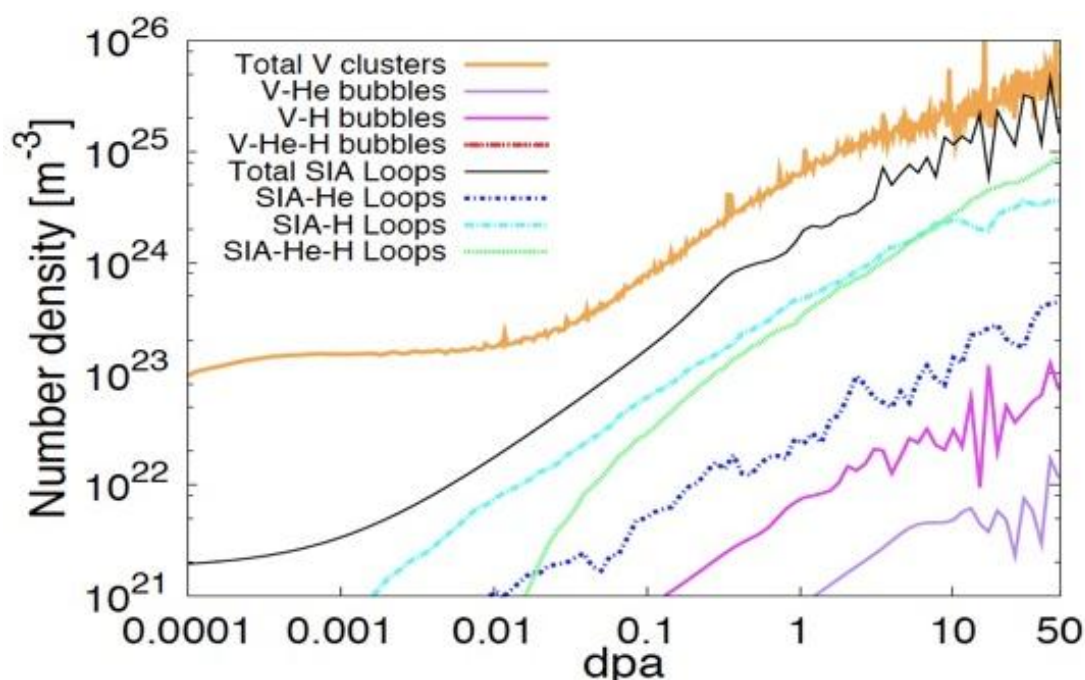


FIG. 14. Accumulation of damage in a triple implanted FeCr alloy (Fe, He and H ions). *P'vt comm., T. Hoang, J Marian and VV Bulatov, also after [21].*

5. CONCLUSIONS

The following conclusions were obtained in the work described here:

- ODS particles crystallize during mechanically alloyed powder consolidation and heat treatment from an amorphous precursor.
- ODS particles less than a critical size ~ 1 nm do not crystallize but they are efficient sequesters of helium
- The critical cavity size for Fe(14%Cr) ($d \sim 2.5$ nm) was determined from dual beam irradiations with Fe+He, and is consistent with other measurements using sequential ion beams and neutron irradiations.
- The presence of hydrogen in triple ion beam irradiations of Fe(Cr) alloys and steels leads to anomalously large cavity growth rates but this effect is likely temperature and possibly dose-rate dependent.

6. RECOMMENDATIONS

Multi-ion-beam experiments can emulate the production of displacement damage and the simultaneous production of helium and hydrogen over a broad range of absolute and relative doses. This includes the ability to emulate different neutron spectra by changing the ratio of

He and H injected relative to the dpa produced by ballistic collisions. However, because ion beam experiments are performed at dpa rates that are 2 to 3 orders of magnitude greater than those that will be encountered in a fusion environment there remains the reasonable question as regards dose rate effects. While carefully designed triple beam experiments can discover important key mechanisms, such as the anomalously large swelling due to hydrogen synergy [1, 2, 3], it is not always clear if these mechanisms are relevant to the much lower dose rate (lower dpa rate and lower transmutation rate) encountered in a fusion reactor. For some conditions, particularly where vacancy and interstitials are the only species of interest, it is reasonable to accelerate the interstitial and vacancy transport by raising the temperature to compensate for the higher dpa rate. Invariant equations have been developed for this procedure by Mansur [22] and are often employed to estimate the elevated temperature that will yield the same microstructure in an ion-beam experiment as in a neutron experiment.

The introduction of multiple beams, incubation periods, and non-linear changes in the accumulating and changing microstructure make such simple ideas problematic. However, we are not helpless experimentally because we can vary three important parameters in ion-beam irradiation experiments; dose, dose-rate, and temperature. Variations in the evolved microstructure associated with these three variables will lead to improved simulation and modeling because this parametric space will bracket the observed microstructural features. Moreover by exploring this three dimensional space subsequent comparisons with neutron irradiated specimens can be made in such a way as to experimentally determine the invariant set of parameters that yield equivalent microstructural features, or we can expect to eliminate some evolved microstructural features found in ion-beam experiments as irrelevant to the conditions of lower rate neutron irradiations.

REFERENCES

- [1] T. TANAKA, K. OKA, S. OHNUKI, S. YAMASHITA, T. SUDA, S. WATANABE, E. WAKAI, *J. Nucl. Mater.* **329–333** (2004) 294–298.
- [2] E. WAKAI, T. SAWAI, K. FURUYA, A. NAITO, T. ARUGA, K. KIKUCHI, S. YAMASHITA, S. OHNUKI, S. YAMAMOTO, H. NARAMOTO, S. JISTUKAWA, *J. Nucl. Mater.* **307–311** (2002) 278.
- [3] E. WAKAI, K. KIKUCHI, S. YAMAMOTO, T. ARUGA, M. ANDO, H. TANIGAWA, T. TAGUCHI, T. SAWAI, K. OKA, S. OHNUKI, *J. Nucl. Mater.* **318** (2003) 267.
- [4] K. EHRLICH, *Philos. Trans. R. Soc. London, Ser. A* **357** (1999) 595.
- [5] E. E. BLOOM, S. J. ZINKLE, AND F. W. WIFFEN, *J. Nucl. Mater.* **329–333** (2004) 12.
- [6] S. UKAI and M. FUJIWARA, *J. Nucl. Mater.* **307–311** (2002) 749.
- [7] KOHYAMA, M. SEKI, K. ABE, T. MUROGA, H. MATSUI, S. JITSUKAWA, and S. MATSUDA, *J. Nucl. Mater.* **283–287** (2000) 20.
- [8] E. E. BLOOM, J. T. BUSBY, C. E. DUTY, P. J. MAZIASZ, T. E. MCGREEVY, B. E. NELSON, B. A. PINT, P. F. TORTORELLI, and S. J. ZINKLE, *J. Nucl. Mater.* **367–370** (2007) 1.
- [9] J. BOUTARD, A. ALAMO, R. LINDAU, and M. RIETH, *C. R. Phys.* **9** (2008) 287.
- [10] E. E. BLOOM, *J. Nucl. Mater.* **85–86** (1979) 795.
- [11] K. YUTANI, H. KISHIMOTO, R. KASADA, and A. KIMURA, *J. Nucl. Mater.* **367–370** (2007) 423.
- [12] R. KASADA, N. TODA, K. YUTANI, H. S. CHO, H. KISHIMOTO, and A. KIMURA, *J. Nucl. Mater.* **367–370** (2007) 222.
- [13] S. UKAI, T. NISHIDA, H. OKADA, T. OKUDA, M. FUJIWARA, and K. ASABE, *J. Nucl. Sci. Technol.* **34** (1997) 256.

- [14] S. UKAI, T. NISHIDA, T. OKUDA, and T. YOSHITAKE, *J. Nucl. Sci. Technol.* **35** (1998) 294.
- [15] J. F. ZIEGLER, J. P. BIRSACK, M.D. ZIEGLER, *SRIM: The Stopping and Range of Ions in Matter*, Lulu Press Co.; 860 Aviation Parkway; Suite 300; Morrisville, NC, 27560 USA
- [16] C. BOUDIAS and D. MONCEAU, *The crystallographic software for research and teaching*, Senlis, France, 1989–1998.
- [17] Y. SERRUYS et al., *JANNUS: experimental validation at the scale of atomic modeling*, *C. R. Physique* **9** (2008) 437–444, and Y. Serruys et al., *J. Nucl. Mater.* **386–388** (2009) 967–970.
- [18] L. HSIUNG, M. FLUSS, S. TUMEY, B. CHOI, Y. SERRUYS, F. WILLIAMS, AND A. KIMURA, *Phys. Rev.*, **B 82** (2010) 184130.
- [19] P ERHART and J. MARIAN, *J. Nucl. Mater.* **414** (2011) 426–430.
- [20] P ERHART and J MARIAN, “Helium affinity of metallic oxide particles in bcc Fe”, manuscript in preparation.
- [21] J. MARIAN, V. V. BULATOV, *J. Nucl. Mater.* **415** (2011) 84–95.
- [22] L.K. MANSUR, *J. Nucl. Mater.* **206** (1993) 306–323.